Static and Seismic Responses of Pile-Supported Marine Structures under Scoured Conditions

by

Wenyu Jiang

B.Eng., Southwest Jiaotong University, China, 2015

M.A.Sc., Southwest Jiaotong University, China, 2018

A Dissertation Submitted in Partial Fulfillment of the

Requirements for the Degree of

DOCTOR OF PHILOSOPHY

in the Department of Civil Engineering

University of Victoria

We acknowledge and respect the lək̓ʷəŋən peoples on whose traditional territory the university stands and the Songhees, Esquimalt and W̱SÁNEĆ peoples whose historical relationships with the land continue to this day.

Static and Seismic Responses of Pile-Supported Marine Structures under Scoured Conditions

by

Wenyu Jiang

B.Eng., Southwest Jiaotong University, China, 2015

M.A.Sc., Southwest Jiaotong University, China, 2018

Supervisory Committee

Dr. Cheng Lin, Supervisor

Department of Civil Engineering

Dr. Min Sun, Departmental Member

Department of Civil Engineering

Dr. Sanat Pokharel, Outside Member

Stratum Logics

Abstract

Scour is a process of removing soils around foundations by currents and waves. For the pile-supported marine structures such as the monopile-supported offshore wind turbines (OWTs) and the pile-supported bridges, scour can decrease the pile capacities and alter the dynamic responses of the structures. At present, there is not a widely accepted method to estimate pile axial or lateral capacity under scoured conditions. For example, different recommendations are used among the existing design standards for estimation of the vertical effective stress and the resulting capacities for single piles under different scour conditions. None of the existing standards or design practice has even considered the scour effects on the behavior of pile groups. Furthermore, the investigation into the responses of piles under multiple hazards of scour and earthquakes is rarely reported.

To address the foregoing limitations, this study first introduces an analytical solution to determining the vertical effective stress of soils around single isolated piles under scoured conditions and uses it to examine the limitations of the existing standards in estimation of pile tensile capacity (Chapter 1). The effect of soil-pile interface friction is highlighted. Next, the study proposes new approaches to investigating the combined effects of scour and earthquakes on the lateral responses of the monopile-supported OWTs in sand (Chapter 2) and soft clay (Chapter 3). Lastly, simple and practical methods are developed based on the *p*-*y* curve framework for analyzing the lateral responses of pile groups in sand (Chapter 4) and soft clay (Chapter 5) subjected to static lateral loading.

The proposed methods in this study were encoded into a series of open-source computer scripts for engineering practice. They were verified with the 3D continuum finite element (FE) analyses. Using the proposed methods, standard methods, and 3D FE method, parametric analyses were conducted to investigate the scour effects on the lateral behavior of the monopile-supported OWTs under crustal earthquakes and that of the pile groups under static loading. The factors considered in the parametric study included effects of scour-hole dimensions, soil stress history, soil density, soil-pile interface behavior, soil liquefaction potential, pile group configurations, etc. Through the parametric analyses, the standard methods were critically assessed by comparing

the results to those calculated by the proposed methods and 3D FE methods, and some design-related issues were also discussed.

Table of Contents

List of Tables

List of Figures

Acknowledgements

I would like to express my special gratitude to my research supervisor, Dr. Cheng Lin, for providing me with the opportunity to complete a Ph.D. at the University of Victoria. Without his patient and supportive guidance, this dissertation would not be possible. His commitment to excellence and wealth of experience in industry and academy are admirable and inspiring. I appreciate that Dr. Lin creates valuable opportunities (e.g., cooperative research project, academic conference, internship, teaching assistant, etc.) for me to develop my academic and professional skills.

I wish to thank my supervisory committee members, Dr. Min Sun and Dr. Sanat Pokharel, for providing me with insightful suggestion for my research proposal and dissertation. I also appreciate Dr. Zhe Luo for serving on my oral examination.

I would also like to thank Dr. Bengt H. Fellenius and Dr. Tuna Onur for their suggestion and guidance when just I started my research into this area. I also appreciate Dr. Benjamin Turner, Dr. Wu-Sheng Lu, and Dr. Raffaele De Risi for their helpful comments on my numerical models.

Special thanks go to the Natural Sciences and Engineering Research Council of Canada (NSERC) for sponsoring my research at the University of Victoria. I am sincerely grateful to the staff at the University of Victoria for providing me with a supportive and enjoyable work atmosphere. Appreciation is extended to the following institutes for generously providing the open-source research tools and data: the University of California (for providing OpenSees), the University of Illinois Urbana-Champaign (for providing DEEPSOIL), the Pacific Earthquake Engineering Research Center (for sharing ground motion records), and the Center for Geotechnical Modeling at the University of California, Davis (for sharing centrifuge test data).

Finally, I would like to thank my families, friends, and colleagues for their endless love, support, and encouragement.

Dedication

In dedication to my families, teachers, and friends

♡

Chapter 1 Evaluation of Vertical Effective Stress and Pile Tension Capacity in Sands Considering Scour-Hole Dimensions

1.1 Abstract

Evaluation of vertical effective stress of soils around piles is essential to calculation of pile capacities. However, the widely-used design manuals such as FHWA and API recommend different methods for calculating the vertical effective stress under scour conditions, which thus lead to different calculations of pile capacities. This paper was to evaluate the suitability of the existing methods and the proposed analytical solution for estimation of pile tension capacity by comparing them with FE analyses under different scour-hole dimensions. Based on the comparisons, recommendations were developed for selecting an appropriate method to calculate pile tension capacity under different scour-hole conditions.

1.2 Introduction

Pile foundations in river and ocean can suffer enormous loss of soil supports due to scour. To ensure the safety of bridges and marine structures, pile foundations should be designed with adequate capacities against scour in floods or hurricanes. Scour generally consists of general scour (erosion across the riverbed) and local scour (developing a scour hole at the foundation). General scour causes the uniform reduction of vertical effective stress in the remaining (or unscoured) soils; however, the stress reduction due to local scour is nonuniform and highly dependent on the dimensions of a scour hole. Currently, the widely used design manuals including American Petroleum Institute (API) (API, 2011), US Federal Highway Administration-Driven Piles (denoted as FHWA-DP) (Patrick et al., 2016), and FHWA-Drilled Shafts (denoted as FHWA-DS) (Brown et al., 2010) specify different methods to estimate vertical effective stress of remaining soils at piles under local scour (Lin and Wu, 2019). The different stress calculations lead to the pronounced difference in calculated pile lateral or axial capacity, which thus confuses the engineer on selecting an appropriate method for the design.

Lin and Wu (2019) compared the existing methods (i.e., FHWA-DP, FHWA-DS, and API) with their proposed closed-form solution and quantified the difference in terms of pile lateral capacity. They found that FHWA-DP and FHWA-DS overestimated pile lateral capacity by 34%-47% and 12%-22%, respectively, while API gave the most agreeable estimation but was only applicable in limited scour-hole conditions.

Extensive research efforts have been focused on scour effects on the behavior of laterally loaded piles considering various scour-hole dimensions (Achmus et al., 2010; Lin et al., 2016, 2014a; Søren and Lars Bo, 2013; Tseng et al., 2017; H. Zhang et al., 2017). However, limited attention has been paid to variations of pile axial capacity including both compression and tension capacities with scour-hole dimensions. In particular, almost no effort has been made to evaluate the difference in pile compression or tension capacity due to the different stress calculations recommended by the existing methods.

The objective of this paper was to investigate how the different stress calculations by the existing methods (i.e., FHWA-DS, FHWA-DP, and API) and an analytical solution proposed by the authors (Lin, 2017) would affect the calculations of pile tension capacity under local scour. A series of FE analyses (65 cases) was run on single piles in both loose and dense sands under a wide range of scour-hole dimensions. The FE results including vertical effective stress and pile tension capacity were compared with those from the existing methods and the analytical solution (Lin, 2017). Based on the comparisons and discussions, recommendations for selecting a proper method were developed.

1.3 Pile tension capacity under local scour conditions

In general design practices, pile tension capacity is often estimated as the ultimate tensile load according to various design methods such as Reese and O'Neil (1988) and Fleming et al. (1992). In this study, the method of Fleming et al. (1992) was adopted as it yielded the agreeable prediction to in-situ testing data for bored piles (Krabbenhoft et al., 2008). It can be expressed as

$$R_{\mathrm{s}} = \int_0^{L_{\mathrm{e}}} (\pi D K \sigma_{\mathrm{v}}' \tan\delta)\,\mathrm{d}z \tag{1-1}$$

The value of K is typically chosen as 0.9 for sands and 0.6 for silts. The value of

δ was chosen as peak friction angle of soils in this study (Krabbenhoft et al., 2008), equal to 28° and 39° for loose and dense sands, respectively. The detailed soil and pile properties are summarized in Table 1.1. It should be noted that the present study was focused on the effect of scour-hole dimensions on pile tension capacity and the effect of stress history changes in remaining soil due to scour on soil properties (e.g., K and ϕ') and pile capacities (Liang et al., 2018, 2015; Lin et al., 2014b, 2010) was not considered in this study. The value of σ'_v was chosen as $\sigma'_v=\gamma' Z$ before scour occurred but as σ'_{va} after scour occurred. The value of σ'_{va} for local scour conditions was determined using FHWA-DP, FHWA-DS, API, and the analytical solution (Lin, 2017) as discussed later. The value was taken as $\sigma'_{va}=\gamma' z$ when local scour evolved into general scour (i.e., $S_{wb}=\infty$).

In finite element (FE) analyses, two-dimensional axisymmetric FE models were built in the commercial software, Plaxis. The vertical boundary was set 50D from the pile center and the bottom horizontal boundary was 20D below the pile tip. These boundaries were found to have a negligent effect on the results of numerical modelling. A "medium size" meshing function in Plaxis was selected, which automatically created a large number of 15-node triangular elements (approximately 1500 to 3500). The computational results become less sensitive to meshing density when soil-pile interface is created (Wehnert and Vermeer, 2004). In the FE models, soil-pile interface was established and the "medium-size" mesh was sufficient to achieve computational accuracy. In the soil-pile interface, shear strength was chosen as that of the adjacent soil (i.e., $R_{int}=1.0$ in Table 1.1). Soils were simulated using the elastic perfectly plastic Mohr-Coulomb model and piles as an elastic material. Soil parameters used in FE analyses varied with the density of sands. As shown in Table 1.1, a larger elastic modulus, a slightly higher unit weight, and a lower void ratio were used for dense sand than loose sand. Dilatancy was considered in dense sand but not in loose sand. The dilatant angle was computed using $\psi=\phi'-30°$ as suggested by Plaxis. The numerical calculation proceeded with the initial equilibrium of the model, followed by imposing tensile displacement on the pile head. The pile tensile loads were computed at the corresponding imposed tensile displacements. The pile tension capacity was taken as the tensile load that corresponded to a pile tensile displacement of 5%D. The shaft resistance is typically mobilized at a pile axial displacement of 0.5%-2%D (Fleming et al., 2009; Mullins et al., 2006). The higher pile displacement of 5%D was chosen herein mainly to account for the potential rebound of piles after scour.

Table 1.1 Soil and pile parameters

Soil parameters	Loose sand	Dense sand
Soil (Mohr-Coulomb)		
Saturated unit weight, γ_s (kN/m^3)	19	21
Elastic modulus, E_s (MPa)	20	100
Poisson's ratio, ν_s	0.3	0.3
Void ratio, e_{int}	0.7	0.4
Effective friction angle, ϕ' (°)	28	39
Dilatant angle, ψ (°)	0	9
Soil-pile interface		
Reduction factor, R_{int}	1	
Pile (linear elastic)		
Unit weight, γ_p (kN/m^3)	24	
Elastic modulus, E_p (GPa)	24	
Poisson's ratio, ν_p	0.15	
Pile diameter, D (m)	1	
Pile length (fully embedded), L ($\times D$)	20	

As described previously, pile tension capacity determined by FEM was based on the serviceability limit state, which is different from the ultimate limit state used in Eq. (1-1) (Fleming et al., 1992). To make the results computed by both methods comparable, tension capacity ratio was used instead of the absolute value of tension capacity. It is defined as a ratio of pile tension capacity calculated after scour to that before scour, i.e., tension capacity ratio=$R_{s(post\text{-}scour)}/R_{s(pre\text{-}scour)}$.

1.4 Approaches for evaluation of vertical effective stress at piles under local scour

Local scour forms a scour hole around the piles. In general design practices, the scour hole is simplified as an inverted truncated cone with the dimensions defined by S_d, S_{wb}, and S_θ in Figure 1.1(a). For foundations in river, FHWA HEC-18 (Arneson et al., 2012) recommends the top width of scour hole be twice the scour depth (i.e., $S_{wt}=2S_d$) which corresponds to $S_{wb}=0$ and $S_\theta=26.6°$, and the value of S_d can be varied. For foundations in ocean, similar dimensions of the scour hole (i.e., $S_{wb}=0$ and $S_\theta=30°$) are used (Whitehouse, 1998) but $S_d=1.5D$ is often suggested (API, 2011).

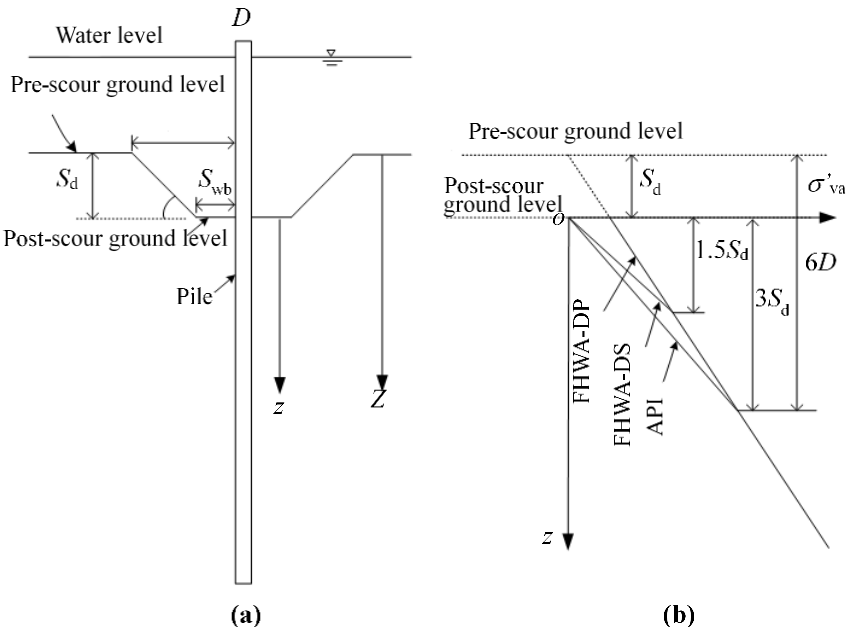

Figure 1.1 (a) Scour-hole dimensions and (b) schematic of stress distribution by different methods

The formation of a scour hole reduces the vertical effective stress in the remaining soils around piles and the reduction rate of the stress becomes smaller at greater depths. The existing methods account for this in different ways. FHWA-DP ignores the scour-induced stress reduction, so its vertical effective stress follows a linear line calculated from the pre-scour ground as illustrated in Figure 1.1(b), whereas FHWD-DS and API consider the stress reduction but only to a limited depth, so their vertical effective stress follows two lines. Before the limited depth, the stress is calculated from the post-scour ground; however, below this depth, no further reduction in the stress occurs and therefore the stress is calculated from the pre-scour ground in Figure 1.1(b). Lin and Wu (2019) defined this limited depth as the influence depth. It is equal to $1.5S_d$ below the post-scour ground according to FHWA-DS (i.e., $z_i=1.5S_d$) and $6D$ below the pre-scour ground according to API. Since API recommends $S_d=1.5D$, its influence depth is $z_i=3S_d$ below the post-scour ground. The detailed stress calculation using the existing methods can be referenced to Lin and Wu (2019). Note that although API's recommendation is based on only one scour depth, the influence depth $z_i=3S_d$ was extended to other scour depths in this paper.

The above methods can consider various S_d but only a constant S_{wb} and S_θ (i.e., $S_{wb}=0$ and $S_\theta=26.6°$or 30°). To consider various scour-hole dimensions, the authors (Lin, 2017) proposed a closed-form equation based on Boussinesq's point load equation,

which is dubbed the analytical solution throughout this paper,

$$\sigma'_{va} = \gamma' z \left[1 + (\tan S_\theta) \left(\frac{S_d \cot S_\theta + S_{wb}}{\sqrt{(S_d \cot S_\theta + S_{wb})^2 + z^2}} - \frac{S_{wb}}{\sqrt{S_{wb}^2 + z^2}} \right) \right] \quad (1\text{-}2)$$

The above-mentioned methods including FHWA-DP, FHWA-DS, API, and the analytical solution (Lin, 2017) yielded different σ'_{va} for different scour-hole dimensions. The calculated σ'_{va} was then substituted for σ'_{v} in Eq. (1-1) to calculate pile tension capacity under different scour-hole dimensions. As with tension capacity ratio, a stress ratio equal to $\sigma'_{va}/\sigma'_{va}$ was adopted to represent the stress results. The obtained stress ratio and tension capacity ratio were compared with those from FE analyses. The results are discussed next.

1.5 Results and discussion

Figure 1.2 shows the stress ratio distribution obtained for S_d=1.5D, S_{wb}=0, and S_θ=26.6°. From the figure, the analytical solution (Lin, 2017) agreed with API, both yielding the lowest stress ratio among the methods considered. The stress ratio from FHWA-DP was the highest and equal to 1.0 as it ignores the scour-induced stress reduction. Surprisingly, FHWA-DS produced the most agreeable results with the FEM except at shallow depths (i.e., z<0.75D). Unlike the monotonic decrease found in other methods, the stress ratio from FEM reached a peak before following a continuous decrease with depth. This was due to the soil-pile interface friction that suppressed the rebound of the remaining soils near the piles after scour. Neither the analytical solution nor the existing methods could capture this. If the pile was replaced by soil and the pile stickup was removed in the FE model, the calculated stress ratio matched well that of the analytical solution. These results indicate that the soil-pile interactions played a favorable role in preventing the scour-induced reduction in vertical effective stress at piles. It explains why the analytical solution yielded a lower stress ratio than FEM. To evaluate effects of S_d, S_{wb}, and S_θ on pile tension capacity, a wider range of scour-hole dimensions was considered and the results are discussed next.

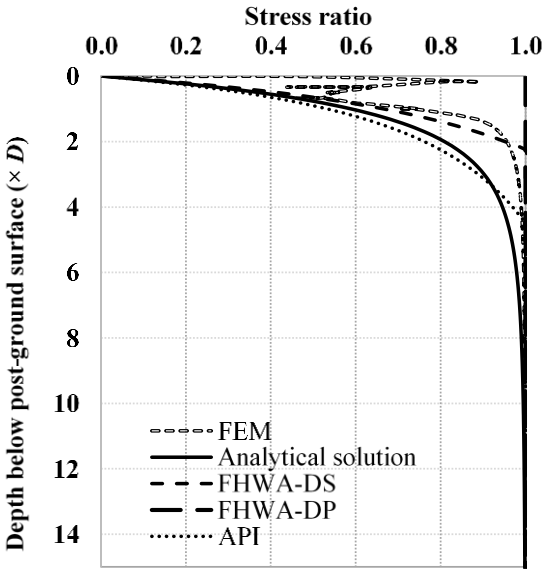

Figure 1.2 Vertical effective stress distribution calculated by different methods (S_d=1.5D, S_{wb}=0, S_θ=26.6°)

1.5.1 Effect of scour depth

The effect of scour depth on pile tension capacity was evaluated by setting S_d=0, 1D, 1.5D, 2D, 3D, and 5D, and S_{wb}=0, and S_θ=26.6°. Figure 1.3(a) depicts variation of tension capacity ratio with S_d when S_{wb}=∞. It shows that the tension capacity ratio decreased linearly with scour depth. Moreover, the tension capacity ratio calculated by Eq. (1-1) (Fleming et al., 1992) was independent of soil friction angle whereas that determined by FEM decreased as soil friction angle increased. Figure 1.3(b) demonstrates that local scour had little effect on pile tension capacity at small scour depths (e.g., $S_d \leq 2D$) but the effect became remarkable at large scour depths (e.g., $S_d \geq 4D$). Unlike the linear decrease in Figure 1.3(a) (general scour), the curves in Figure 1.3(b) (local scour) appeared in a concave shape. The concave curves also differed from the convex curves of lateral capacity ratio versus S_d (Lin and Wu, 2019). Such a difference is attributed to that the pile tension capacity was dependent on the soil resistance at all depths but the pile lateral capacity was controlled by the soil resistance at shallow depths.

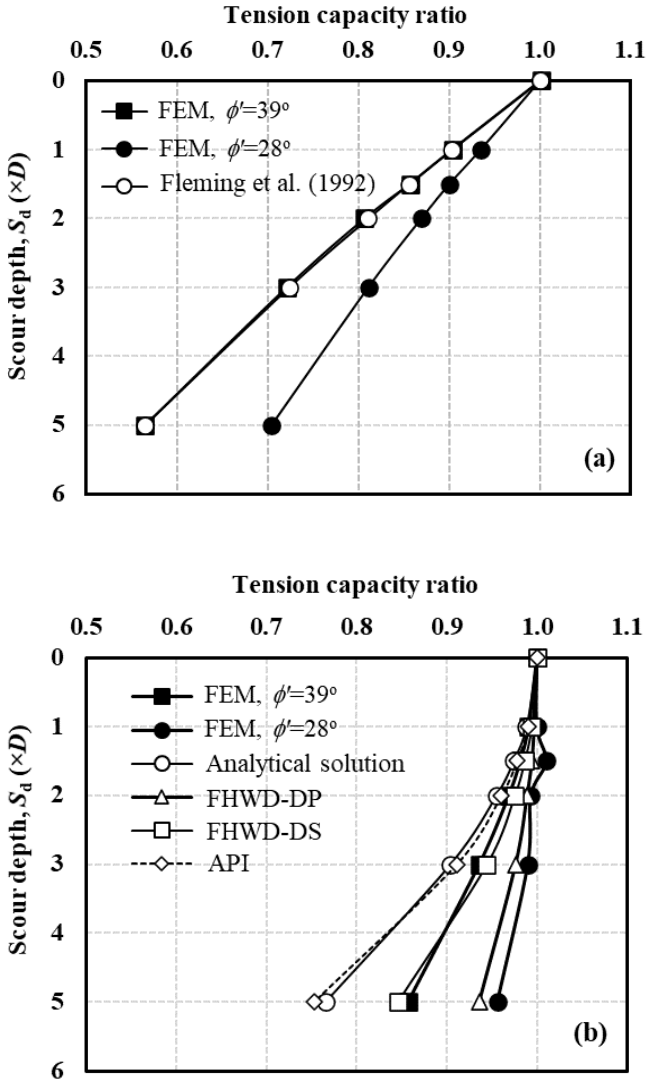

Figure 1.3 Tension capacities at different scour depths: (a) S_{wb}=∞, S_θ=26.6°; (b) S_{wb}=0, S_θ=26.6°

Figure 1.3(b) also shows that the analytical solution (Lin, 2017) and API yielded lower tension capacity than FEM. FE results agreed with those of FHWA-DS in dense sands but with those of FHWA-DP in loose sands. Note that since Eqs. (1-1) and (1-2) are independent of soil friction angle, the pile tension capacity calculated using the existing methods and the analytical solution was also independent of soil friction angle. When scour depth increased from 0 to 5D, the loss of pile tension capacity calculated by the analytical solution, API, FHWA-DS, and FHWA-DP was 24%, 25%, 16%, and 6%, respectively. In FE analyses, the pile tension capacity loss was more severe in dense sands (approximately 14%) than loose sands (approximately 4%). Overall, the loss of pile tension capacity (4%-25%) was much smaller than the loss of pile lateral capacity (approximately 77%) for the same amount of increase in scour depth (Lin and

Wu, 2019). This result indicates that for a scour hole with S_{wb}=0, piles suffered much less loss in tension capacity than in lateral capacity.

1.5.2 Effect of scour width

To understand the effect of scour width on pile tension capacity, a total of 11 bottom widths of scour hole were considered, i.e., S_{wb}=0, 1D, 2D, 4D, 6D, 8D, 10D, 15D, 20D, and ∞, while S_d=1.5D and S_θ=26.6°. Note that the existing methods (FHWA-DP, FHWA-DS, and API) are only feasible for the scour holes having S_{wb}=0. However, they may be used mistakenly by the engineer for the cases of S_{wb}>0. Therefore, the results for S_{wb}=0 were extrapolated to the cases of S_{wb}>0, as shown in Figure 1.4.

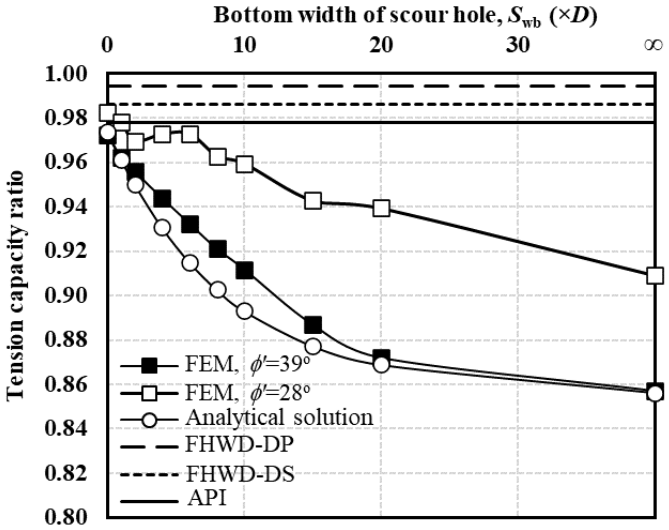

Figure 1.4 Tension capacities at different scour widths (S_d=1.5D, S_θ=26.6°)

The tension capacity ratio calculated by FEM was much smaller in dense sands than in loose sands. The results from the analytical solution compared well with FE results in dense sands. From FE analyses, the increase in S_{wb} caused the loss of pile tension capacity to increase by approximately 7% in loose sands and 11% in dense sands when S_d=1.5D, S_θ=26.6°. However, if the existing methods were used, the increase in S_{wb} caused no change in pile tension capacity, which is apparently unreasonable and unsafe. Overall, the existing methods are unable to consider the effect of scour width. The analytical solution can be used to estimate pile tension capacity under various scour width as it yielded agreeable results in dense sands and conservative results in loose sands as compared with FEM.

1.5.3 Effect of scour-hole slope angle

The effect of scour-hole slope angle on pile tension capacity was investigated using seven S_θ values (0°-38°) when ϕ'=39°, and five S_θ values (0°-26.6°) when ϕ'=28°. In both cases, the other two dimensions were fixed, i.e., S_d=1.5D and S_{wb}=0. The case of S_θ=0° indicates the case of general scour. The tension capacity ratio calculated by the existing methods was independent of S_θ, showing a horizontal line in Figure 1.5. FEM yielded a smaller tension capacity ratio in dense sands than in loose sands. The calculated results based on the analytical solution were in good agreement with FE results in dense sands. Overall, pile tension capacity increased nonlinearly with S_θ. As S_θ increased from 0° to 38°, pile tension capacity was increased by 14%. The majority of the capacity increase (i.e., 11%) occurred in the range of S_θ=0°-12°. Further increasing S_θ (S_θ =12° -38°) led to a negligent change in pile tension capacity (e.g., 2%-5%). It is worth noting that the range of S_θ =12° -38° has been observed in the bridge foundations (Butch, 1996) and this range of S_θ is more likely to occur in the field. Therefore, in practical applications, the effect of S_θ on pile tension capacity may be ignored.

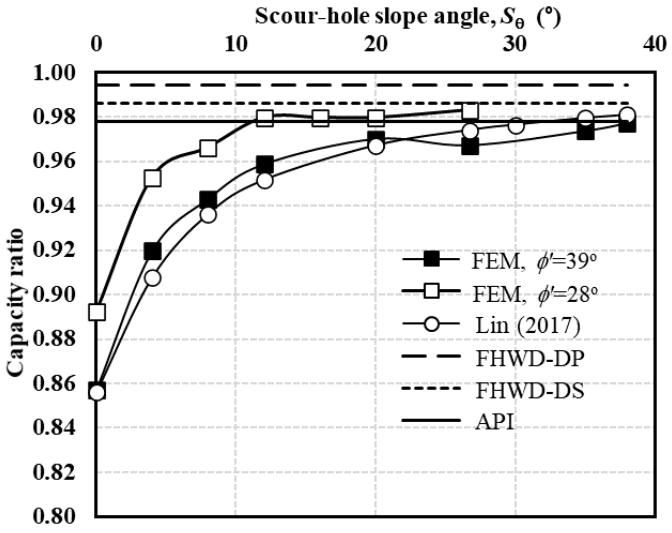

Figure 1.5 Tension capacities at different scour-hole slope angles (S_d=1.5D, S_θ=26.6°)

1.6 Conclusions

(1) FE results indicated that scour-induced loss of pile tension capacity was more

significant in dense sands than in loose sands. However, the existing methods (FHWA-DS, FHWA-DP, and API) and the analytical solution (Lin, 2017) were unable to capture this effect.

(2) The analytical solution (Lin, 2017) yielded a conservative result of vertical effective stress and pile tension capacity compared with FEM. This is probably due to the soil-pile interactions that prevent the scour-induced reduction in vertical effective stress at piles.

(3) For a scour hole with varying scour depths but S_{wb}=0 and S_{θ}=26.6°, FHWA-DS may be used to estimate pile tension capacity in dense sands but FHWA-DP is preferred in loose sands.

(4) The analytical solution is recommended for use when considering the effect of various scour width on pile tension capacity. It produced comparable results with FEM in dense sands and conservative results in loose sands.

(5) The decrease of scour-hole slope angle causes the loss of pile tension capacity, which is more significant at the smaller slope angles (0°-12°) than at the larger slope angles (12°-38°). As the slope angle is more likely in the range of 12°-38°, the effect of scour-hole slope angle on pile tension capacity may be ignored in practical applications.

1.7 Notation

API = American Petroleum Institute, Geotechnical and Foundation Design Considerations

D = pile diameter

e_{int} = initial void ratio of soils

E_s = Elastic modulus of soils

E_p = Elastic modulus of piles

FHWA-DP = US Federal Highway Administration, Driven Pile Manual

FHWA-DS = US Federal Highway Administration, Drilled Shaft Manual

K = coefficient of lateral earth pressure at piles

L = pile length

L_e = embedded length of piles

R_s = ultimate tension capacity

S_{wt} = top width of scour hole

S_{wb}= bottom width of scour hole

S_d = scour depth due to local scour

S_θ= scour-hole slope angle

z = depth below post-scour ground level

Z = depth below pre-scour ground level, equal to S_d+z

z_i = influence depth below which the reduction of vertical effective stress due to local scour vanishes and the effective stress is computed from the pre-scour ground level

δ = friction angle of soil-pile interface

ϕ' = friction angle of soil

ψ = dilation angle of soil

γ' = effective unit weight of soils

γ_s = saturated unit weight of soils

γ_p = total unit weight of piles

ν_s = Poisson's ratio of soils

ν_p = Poisson's ratio of piles

σ'_v = vertical effective stress of soils at piles

σ'_{va} = vertical effective stress of soils at piles after scour

σ'_{vb} = vertical effective stress of soils at piles before scour

$\sigma'_{va}/\sigma'_{vb}$ = stress ratio, or normalized vertical effective stress

Chapter 2 Seismic Responses of Monopile-Supported Offshore Wind Turbines in Sands under Scoured Conditions

2.1 Abstract

Offshore wind turbines (OWTs) supported by monopiles can be vulnerable to scour and liquefaction triggered by waves and earthquakes. However, the combined effects of scour and earthquakes on the monopile-supported OWTs in sands are not fully appreciated. This study proposes a practical method to evaluate the post-scour seismic responses of piles in sands and applies it to analyze the monopile-supported OWTs. This method introduces a new concept that relates scour-hole geometric conditions to soil liquefaction potential. Using the proposed method, a parametric study was conducted to evaluate the effects of scour-hole dimensions, sand relative densities, and input ground motions on the lateral responses of OWTs. The results showed that scour shifted the fundamental frequency of the OWT system into the rotor frequency range, causing resonance. An increase in scour depth increased the dynamic responses of the monopile and tower, which was less significant in liquefied than in non-liquefied condition.

2.2 Introduction

The number of offshore wind turbines (OWTs) has been significantly increased with a global endeavor to tap into more sustainable wind energy (GWEC, 2021) to battle climate change. Among the potential foundations under the OWTs, monopile is the most common type of foundation used in practice. It is a steel tubular pile with an outside diameter of 3-7 m and an embedded length of 25-40 m. A monopile-supported OWT system generally consists of monopile, transition piece, tower, and rotor-nacelle assembly (RNA), and it is typically used for water depths up to 35 m (Bhattacharya, 2019; Doherty and Gavin, 2012). The design of the OWT system can be dictated by its dynamic behavior since it is subjected to waves, winds, turbine rotation, and earthquakes. Based on a soft-stiff design rule (DNV, 2014; GL, 2012), the fundamental

frequency of the OWT system is required to fall within a range between the rotor frequency, f_{1P}, and the blade-passing frequency to avoid resonance.

Affected by currents and waves, monopile-supported OWTs are also vulnerable to scour (Van den Brink, 2014; Whitehouse, 1998). Scour around a monopile can be classified into two types: general scour (uniform erosion across the seabed) and local scour (development of a scour hole around the monopile). The local scour hole is typically simplified as an inverted truncated cone in design practice, and thus it can be characterized by scour-hole depth, S_d (typically taken as $1.3D_{op}$-$2.5D_{op}$, D_{op}=outside diameter of monopile), scour-hole bottom width, S_{wb} (typically taken as 0), and side slope angle, S_θ (typically taken as 30° in marine environment) (API, 2011; DNV, 2014; GL, 2012; Whitehouse, 1998). Scour can decrease the pile capacity and change the natural frequency and dynamic responses of the integrated OWT system. Note that scour may shift the fundamental frequency of the OWT system into the f_{1P} resonance range and cause failures of structural and/or non-structural components (Jiang et al., 2021).

In a seismically active area, the damage to the monopile-supported OWT can increase under the combined effects of scour and earthquakes, in particular for fully liquefied soils that experience a drastic loss of soil strength by earthquakes, thus reducing the pile capacity (Esfeh and Kaynia, 2020; Jia et al., 2017; Miyamoto et al., 2021; Yang et al., 2019a). Moreover, the scour hole at a monopile caused by currents or waves can also be varied by the state of soil liquefaction. For example, the scour hole may collapse and vanish in a liquefied condition during earthquakes, causing the local scour to turn into the general scour (Taboada-Urtuzuastegui et al., 2002; Van den Brink, 2014). On the contrary, the scour hole at the monopile may remain to exist after an earthquake in non-liquefied soils. The different interrelation between scour-hole shape and liquefaction potential in sands can cause different dynamic behavior of the OWT system under scoured conditions. It has been reported that both scour and liquefaction can influence the participation of kinematic and inertial interactions in the pile-supported bridges, and this coupling effect is also dependent on the bedrock input motion (Khosravifar et al., 2014; Shang et al., 2016; Tokimatsu et al., 2005; Turner et al., 2017; Wang et al., 2015, 2020, 2019). However, at present, only a dearth of research is focused on analyses of the responses of OWTs in sands (both liquefiable and non-liquefiable) under the combined effects of scour and earthquakes. In the limited studies reported in literature (Jia et al., 2017; Zhu et al., 2020), only 3D continuum FE analyses

or experimental model tests are adopted; however, no simple and practical approach is available, which can be used by practicing engineers in routine design analyses.

This study aimed to propose a practical method for analyzing the lateral responses of the monopile-supported OWTs in sands under the combined effects of scour and earthquakes. The proposed method was established based on the framework of the dynamic-beam-on-nonlinear-Winkler-foundation (DBNWF) method (Boulanger et al., 1999) that has been widely used for analyses of the monopile-supported OWTs under no-scour conditions (Ali et al., 2020; De Risi et al., 2018; Haldar and Patra, 2021; Van de Putte, 2018). The proposed method also defines the different scour-hole geometric conditions in non-liquefiable and liquefiable sands: i.e., local-scour hole for the former but general scour for the latter. Using the proposed method, 102 nonlinear time-domain parametric analyses were performed for a selected monopile-supported OWT system considering varying scour-hole dimensions, soil relative densities, and input earthquake motions. Through the parametric study, the combined effects of scour and earthquakes on the lateral responses of the monopile-supported OWTs in sands were assessed, and some design-related issues were also discussed.

2.3 Proposed method

This section proposes the procedures to develop a new method based on the DBNWF framework (Boulanger et al., 1999) to account for the combined effects of local scour and earthquakes in sands. The DBNWF framework involves the analysis of soil-monopile interactions in sands using the soil springs that can capture the softening effect of the soil stiffness caused by the increase in the excess pore water pressure (Brandenberg et al., 2013) and the radiation damping that is simulated as dashpots in parallel with the soil springs. To address the scour effect, the post-scour vertical effective stress was first determined, which was then incorporated into the DBNWF framework to determine the post-scour springs and dashpots in both vertical and lateral directions. The post-scour vertical effective stress at piles was estimated by defining different scour-hole geometric conditions for liquefied and non-liquefied sands: i.e., a local-scour hole in a non-liquefiable condition while the local scour turned into the general scour in a liquefiable condition. The initiation of soil liquefaction was determined based on the excess pore water pressure ratio, r_u, developed in the free-field soil, which is the ratio of the excess pore water pressure, Δu, to the initial mean effective

stress of soil, σ'_{mo}. If r_u was close to unity (e.g., ≥0.8) (Haldar and Patra, 2021) in the shallow depths of soil deposit (depth ≤2.5D_{op}), the soil would be deemed liquefied and vice versa.

2.3.1 Post-scour vertical effective stress

In design practice, the vertical effective stress of soil around a monopile needs to be determined before the evaluation of vertical and lateral pile capacities (API, 2011; DNV, 2014; GL, 2012). Therefore, an appropriate calculation of the post-scour vertical effective stress in the remaining soil around monopile, $\sigma'_{\mathrm{v,sc}}$, is critical to estimate the response of the monopile-supported OWT under scoured conditions. As discussed previously, the calculation of $\sigma'_{\mathrm{v,sc}}$ varies between liquefied and non-liquefied soils that are associated with differently defined scour-hole geometric conditions.

2.3.1.1 Non-liquefied case

In non-liquefied sands, a scour hole is present around the pile, which is usually simplified as an inverted truncated cone with its dimensions defined by the scour-hole depth, S_{d}, bottom width, S_{wb}, and side slope angle, S_{θ}, as illustrated in Figure 2.1. Based on the Boussinesq point load solution, the post-scour vertical effective soil stress, $\sigma'_{\mathrm{v,sc}}$, at a monopile for different scour-hole dimensions (Jiang et al., 2021; Lin and Wu, 2019) can be expressed as

$$\sigma'_{\mathrm{v,sc}} = \gamma' z \left\{ 1 + \tan S_{\theta} \left[\frac{S_{\mathrm{wb}} + S_{\mathrm{d}} \cot S_{\theta} + 0.5 D_{\mathrm{op}}}{\sqrt{\left(S_{\mathrm{wb}} + S_{\mathrm{d}} \cot S_{\theta} + 0.5 D_{\mathrm{op}}\right)^2 + z^2}} - \frac{S_{\mathrm{wb}} + 0.5 D_{\mathrm{op}}}{\sqrt{\left(S_{\mathrm{wb}} + 0.5 D_{\mathrm{op}}\right)^2 + z^2}} \right] \right\} \quad (2\text{-}1)$$

where γ' is the submerged unit weight of soil, and z is the depth below the scour-hole bottom.

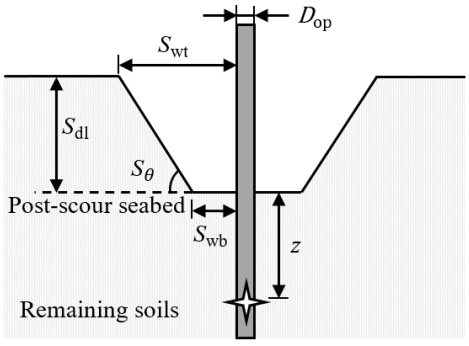

Figure 2.1 Scour hole around a monopile foundation

2.3.1.2 Liquefied case

When soil liquefaction is triggered, the scour hole is deemed unstable, causing the local scour to become the general scour. As such, in liquefied soils, local scour is simply simulated as general scour, defined only by scour depth (i.e., $S_{wb}=\infty$ or $S_{\theta}=0°$). Accordingly, the post-scour vertical effective soil stress in this case is simply calculated as

$$\sigma'_{v,sc} = \gamma' z \tag{2-2}$$

2.3.2 Post-scour springs and dashpots in vertical direction

The post-scour vertical springs are developed by modifying liquefiable *t-z* and *q-z* curves to account for scour effects through incorporating the $\sigma'_{v,sc}$ determined in Section 2.3.1 into the vertical ultimate soil resistance of the *t-z* and *q-z* curves. Similarly, the post-scour vertical dashpots are also developed by including the $\sigma'_{v,sc}$. The post-scour vertical springs and dashpots are then attached to the structural element simulating the monopile, which constitutes the vertical component of the proposed numerical model under the DBNWF framework.

The vertical soil-monopile interaction in sands (i.e., a near-field problem) is evaluated using the liquefiable soil springs (in parallel with a dashpot) defined by liquefiable *t-z* and *q-z* curves, which can be used for both liquefied and non-liquefied sands. As such, there is no separate discussion on the liquefied and non-liquefied cases as with Section 2.3.1. As discussed above, the liquefaction state is dependent on the excess pore water pressure developed in the free-field soil (i.e., a far-field problem). The decay of the soil resistance by the increase in excess pore water pressure, i.e., this softening effect, is incorporated into the liquefiable soil springs for both liquefied and non-liquefied conditions (Brandenberg et al., 2013). For non-liquefied soil, the resistance would be partially reduced by shaking but does not reach the residual strength, while for fully liquefied soil, the resistance would be decreased to the residual strength. The mathematical description of this along with scour effect is discussed as follows.

The calculated $\sigma'_{v,sc}$ in Section 2.3.1 is used to determine the ultimate soil resistances on the pile shaft and at the pile tip ($\beta\sigma'_{v,sc}$ and $N_q\sigma'_{v,sc}$, respectively) for the liquefiable soil springs where β and N_q are the friction factor and end bearing factor suggested by API (2011), respectively. The calculated post-scour ultimate soil

resistance along the shaft is incorporated into the liquefiable *t-z* springs to generate post-scour springs along the shaft. The liquefiable *t-z* springs are formulated in a similar manner to the sand *t-z* curves of Mosher (1984) but with a lower ultimate soil resistance to account for the softening effect. A first-order approximation is considered to capture the softening effect (Boulanger et al., 2003; Brandenberg et al., 2013), as expressed in Eq. (2-3).

$$t_{\mathrm{u,sl}} = t_{\mathrm{u,res}} + (\beta\sigma'_{\mathrm{v,sc}} - t_{\mathrm{u,res}})\sigma'_{\mathrm{m}}/\sigma'_{\mathrm{mo}} \tag{2-3}$$

where $t_{\mathrm{u,sl}}$ is the ultimate soil resistance of the modified *t-z* curve that accommodates for both scour and liquefaction effects; $t_{\mathrm{u,res}}$ is the residual soil resistance in a fully liquefied condition (i.e., when the excess pore water pressure ratio, r_u, equals unity or σ'_{m} reduces to zero), $t_{\mathrm{u,res}} = f_{\mathrm{m}}\beta\sigma'_{\mathrm{v,sc}}$; f_{m} is a multiplier (less than 1.0) that can be evaluated based on the relative density of soil, D_{r} (Boulanger et al., 2003); σ'_{m} and σ'_{mo} are the mean effective stress in the free-field soil at the current and initial time instants, respectively; and they can be calculated using a free-field soil column with a pressure-dependent multi-yield (PDMY) material (Yang, 2000) based on effective stress analysis, as will be discussed in Section 2.5.1. When soil is fully liquefied, $\sigma'_{\mathrm{m}} = 0$ and thus $t_{\mathrm{u,sl}} = t_{\mathrm{u,res}}$ in Eq. (2-3). Since the excess pore water pressure is typically negligible in the end bearing stratum (Brandenberg et al., 2013), the post-scour ultimate soil resistance at the pile tip is directly incorporated into the *q-z* curve (Vijayvergiya, 1977) without considering the softening effect to generate the post-scour springs at the pile tip. In general, the post-scour springs along the pile shaft and tip comprise the post-scour springs in the vertical direction.

Besides, the post-scour dashpots in the vertical direction are developed by substituting the damping coefficient, $c_{\mathrm{v,sc}}$ in Eqs. (2-4) and (2-5) that can consider scour-hole dimensions into the conventional vertical dashpots (Berger et al., 1977).

$$c_{\mathrm{v,sc}} = 2\pi D_{\mathrm{op}}\rho_{\mathrm{sat}}V_{\mathrm{s,sc}}\Delta z \tag{2-4}$$

$$G_{\mathrm{max,sc}} = 1000K_{2,\mathrm{max}}\sqrt{\sigma'_{\mathrm{v,sc}}(1+2k_{\mathrm{o}})/3} \tag{2-5}$$

where Δz is the discretized element size of monopile; ρ_{sat} is the saturated mass density of soil; $V_{\mathrm{s,sc}}$ is the post-scour shear wave velocity of soil, $V_{\mathrm{s,sc}} = \sqrt{G_{\mathrm{max,sc}}/\rho_{\mathrm{sat}}}$; $G_{\mathrm{max,sc}}$ is the small-strain shear modulus of soil after scour; $k_{\mathrm{o}} = (1 -$

$\sin\varphi'$) $\mathrm{OCR}^{\sin\varphi'}$ is the coefficient of lateral earth pressure; φ' is the effective friction angle of soil; OCR is the overconsolidation ratio of soil; $K_{2,\max}$ is a dimensionless factor dependent on D_r (Seed et al., 1986). Note that the units of $G_{\max,sc}$ and $\sigma'_{v,sc}$ are lb/ft^2 in Eq. (5), and the shear wave velocity is often taken as 10% of the pre-earthquake value in a liquefied condition (Khosravifar et al., 2014).

2.3.3 Post-scour springs and dashpots in lateral direction

The development of the post-scour springs and dashpots in the lateral direction is similar to that in the vertical direction as described in the preceding section. Firstly, the ultimate lateral soil resistance under scoured conditions may be written in Eq. (2-6), where C_1, C_2, and C_3 are three constants dependent on D_r (API, 2011).

$$p_{u,sc} = \min\left[\left(C_1\sigma'_{v,sc}/\gamma' + C_2 D_{op}\right)\sigma'_{v,sc}, C_3 D_{op}\sigma'_{v,sc}\right] \tag{2-6}$$

Subsequently, the $p_{u,sc}$ is further modified to account for the liquefaction-induced softening effect, as given in Eq. (2-7).

$$p_{u,sl} = p_{u,res} + (p_{u,sc} - p_{u,res})\sigma'_m/\sigma'_{mo} \tag{2-7}$$

where $p_{u,res} = f_m p_{u,sc}$ is the residual lateral soil resistance in a fully liquefied condition. The computed $p_{u,sl}$ is then substituted into the *p-y* curves for sand (API, 2011) to form the post-scour liquefiable *p-y* curves (or springs). The initial modulus of subgrade reaction used in the API *p-y* curves is dependent on D_r or φ' (API, 2000; Isenhower et al., 2020), and a modification multiplier of $\sqrt{50\ \mathrm{kPa}/\sigma'_{v,sc}}$ is applied to the initial modulus to account for the overburden effective stress (Boulanger et al., 1999; Brandenberg et al., 2013; Khosravifar et al., 2014). Furthermore, the post-scour lateral dashpots are developed by substituting the lateral damping coefficient expressed in Eq. (2-8) into the lateral dashpot proposed by Gazetas and Dobry (1984).

$$c_{h,sc} = 4 D_{op}\rho_{sat} V_{s,sc}\Delta z \tag{2-8}$$

Likewise, the shear wave velocity of soil is taken as 10% of the pre-earthquake value to consider the liquefaction-induced softening effect (Khosravifar et al., 2014).

The above-mentioned procedures for the post-scour lateral springs and dashpots are then attached to the monopile, which constitute the lateral component of the

proposed numerical model under the DBNWF framework. Overall, Sections 2.3.2 and 2.3.3 allow for development of post-scour liquefiable springs and post-scour dashpots in both vertical and lateral directions. These springs and dashpots are further incorporated into the structural models (displacement-based beam) that simulate a pile under axial and lateral dynamic loading. The above procedures constitute the proposed method for analyzing both axial and lateral dynamic responses of piles in sands under the combined effects of scour and earthquakes.

2.4 Implementation and validation

The procedures described in Section 2.3 were used to analyze the responses of the monopile-supported OWT in sands under the combined effects of scour and earthquakes, with consideration of both liquefied and non-liquefied conditions. The analysis was performed using the finite-element (FE) numerical solution in an open-source platform OpenSees (McKenna, 2011). Figure 2.2 illustrates the implementation of the proposed approach; the developed computer codes are provided as supplementary materials. Given the input parameters, the proposed soil springs and dashpots, free-field soil column, and structural components are established. Meanwhile, water-monopile interaction can be considered using the hydrodynamic added mass (Goyal and Chopra, 1989a, 1989b). The hydrodynamic added mass is calculated from a pre-processing MATLAB program and then added to the submerged portion of the monopile, and greater details are discussed in Section 2.5.1. During the nonlinear dynamic analysis, the mean effective stress of the free-field soil is simultaneously applied to the ends of the spring-dashpot elements to capture the softening effect of liquefaction. The outcomes of the time-domain analysis are processed in a post-processing MATLAB program, from which the envelopes of the free-field and structural responses (e.g., the lateral acceleration of free-field soils, the lateral acceleration, deflection, rotation, and bending moment of the OWT structure) are extracted and normalized for discussion.

The DBNWF method for the evaluation of dynamic responses of pile-supported structures has been extensively validated against centrifuge experiments (Boulanger et al., 2003; Ilankatharan, 2008) and 3D continuum FE analysis (Kampitsis et al., 2013). The liquefiable soil springs and free-field soil material were also validated against centrifuge experiments (Brandenberg et al., 2013; X. Wang et al., 2017; Yang, 2000).

This demonstrates the rationale of the proposed method for dynamic loading under no-scour conditions. The capability of the proposed method for simulating scour effects (i.e., scour-hole dimensions) has been confirmed with the results of 3D continuum numerical modeling for static loading by the authors (Lin et al., 2014a; Lin and Jiang, 2019; Lin and Lin, 2019). Therefore, these indirectly confirm the validity of the proposed method for analyzing the monopile-supported OWTs under the combined effects of scour and earthquakes.

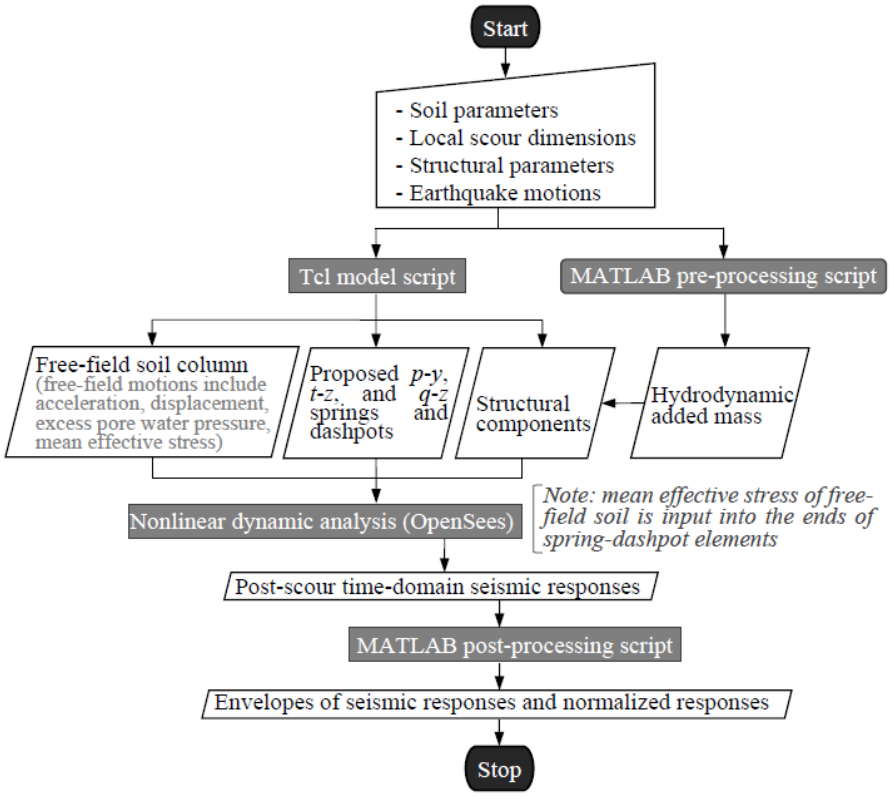

Figure 2.2 Implementation of the proposed procedure

To confirm the above statement and correctness of the developed computer scripts, a centrifuge model test (Wilson et al., 1997) for a seismically loaded pile-superstructure system in liquefiable sands under a no-scour condition was simulated here. The pipe pile (outside diameter=0.67 m, wall thickness=72 mm) was modeled as an elastic beam with a bending stiffness of 417 MN·m since it was not yielded during the test, and the superstructure was modeled as a mass block (49.14 ton). The soil deposit consisted of two layers: an upper layer of loose Nevada sand (D_r=35%) and a lower layer of dense Nevada sand (D_r=75%-80%). Table 2.1 shows the soil parameters used for the numerical analysis. The soil parameters were taken as the suggested values according to the PDMY material manual in OpenSees (McKenna, 2011; Yang, 2000). Since the

base of the model box in the centrifuge test was sufficiently rigid, a rigid bedrock (3.7 m below the pile bottom) condition was adopted in the numerical model. Correspondingly, the recorded acceleration (i.e., motion J in the centrifuge test with a peak bedrock acceleration, PBA, of 0.45g) in the soil near the base of the model box (i.e., within motion) was applied to the bottom of the free-field soil column following the uniform excitation method (Chopra, 2011; X. Wang et al., 2017). Greater details of the numerical model are discussed in Section 2.5.1.

Table 2.1 Soil parameters

Soil layer	D_r (%)	Thickness (m)	ρ_{sat} (ton/m^3)	φ' (°)	f_m	c_{drag}
Loose Nevada sand	35	9.1	1.9	32	0.18	0.1
Dense Nevada sand	75	11.4	2.0	38	0.30	0.1

Note: f_m is the p-multiplier that considers softening effect of liquefaction (Boulanger et al., 2003); c_{drag} is the drag coefficient that accounts for gapping effect (Brandenberg et al., 2013). The other soil parameters of the pressure-dependent multi-yield (PDMY) material used for the free-field soil column were taken as the suggested values in OpenSees based on D_r, detailed description and values are given in McKenna (2011) and Yang (2000) and are not repeated here for brevity.

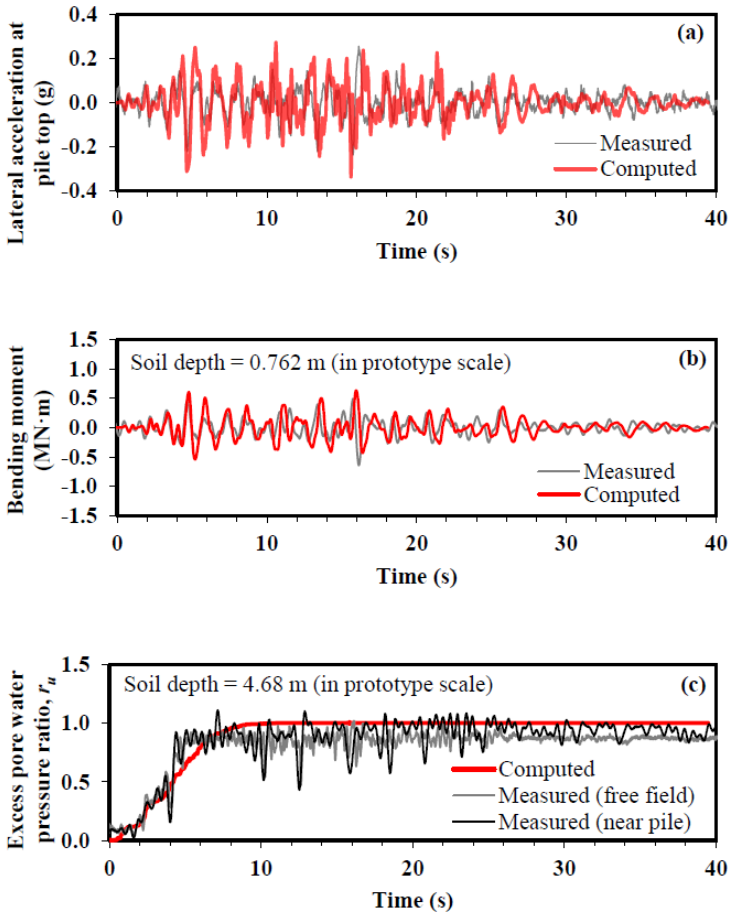

Figure 2.3 Measured and computed time histories: (a) lateral acceleration, (b) bending moment, and (c) excess pore water pressure ratio

Figure 2.3 shows the measured and computed time histories of responses in pile

and soil, including the (a) lateral acceleration and (b) bending moment of the single pile, and the (c) excess pore water pressure ratio (r_u) in the center of the loose sand layer. Overall, the predicted responses agreed reasonably with the measured values. In the following sections, the proposed method is used for the parametric analyses to investigate the combined effects of scour and earthquakes, in which the soil parameters in Table 2.1 were used while the structure was replaced by a selected monopile-supported OWT.

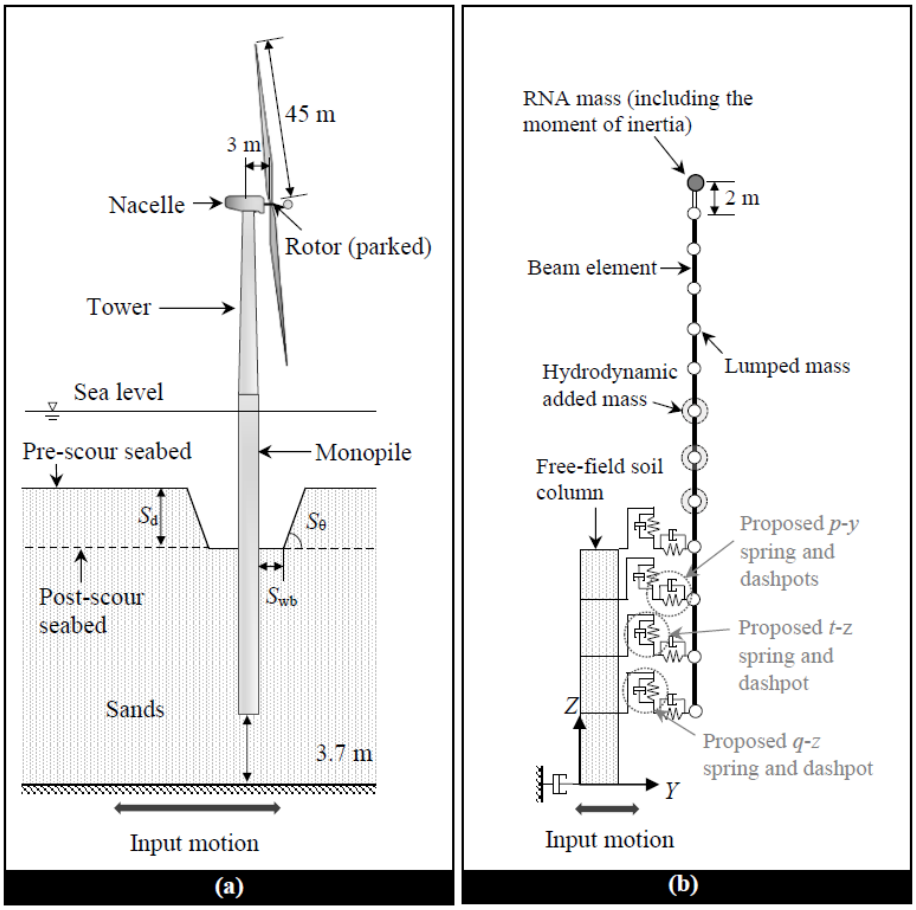

Figure 2.4 The monopile-supported OWT under the combined effects of scour and earthquake: (a) physical model and (b) numerical model

2.5 Parametric analyses

2.5.1 Numerical model

Figure 2.4 illustrates the numerical model for the monopile-supported OWT in sands under the local scour condition following the proposed method. In the numerical

model, the analysis started with the upward propagation of shear waves in a free-field soil column by inputting earthquake motions at its base, from which the free-field motions at different depths of the soil column were determined. The calculated free-field motions (expressed as the time history of the mean effective stress, σ'_{m}) were simultaneously applied to the ends of the post-scour springs and dashpots, which would result in the vibration of the monopile and superstructure. This integrated model allows for incorporation of kinematic and inertial interactions in evaluation of the dynamic responses of OWT structures.

A 3-MW wind turbine was selected as the case study, and the parameters of structural components were extracted from Jiang et al. (2021) and are summarized in Table 2.2. The rotor-nacelle assembly (RNA) in a parked state was modeled as the translational and rotational masses atop the tower (De Risi et al., 2018). The tubular tower and monopile were modeled as nonlinear displacement-based beam elements, with two translational degrees of freedom (DOFs) and one rotational DOF assigned to each beam-element node. The tapered tower was discretized into small elements with different-sized cross-sections. Moreover, the hydrodynamic added mass was used to consider the effect of hydrodynamic loading for a horizontally vibrating monopile in water (Goyal and Chopra, 1989a, 1989b). Therefore, the total lateral dynamic mass of the submerged monopile included the hydrodynamic added mass and buoyant material mass. Since monopile is an open-ended steel pipe, the hydrodynamic added mass inside and outside the monopile ($m_{\mathrm{a}}^{\mathrm{i}}$ and $m_{\mathrm{a}}^{\mathrm{o}}$) can be expressed as

$$m_{\mathrm{a}}^{\mathrm{i}}(h_{\mathrm{s}}) = \rho_{\mathrm{w}}\pi r_{\mathrm{ip}}^2\left[\frac{16h_{\mathrm{i}}}{\pi^2 r_{\mathrm{ip}}}\sum_{m=1}^{\infty}\frac{(-1)^{m-1}}{(2m-1)^2}\frac{I_1(\alpha_m r_{\mathrm{ip}}/h_{\mathrm{i}})}{I_0(\alpha_m r_{\mathrm{ip}}/h_{\mathrm{i}})+I_2(\alpha_m r_{\mathrm{ip}}/h_{\mathrm{i}})}\cos(\alpha_m h_{\mathrm{s}}/h_{\mathrm{i}})\right] \quad (3\text{-}9)$$

$$m_{\mathrm{a}}^{\mathrm{o}}(h_{\mathrm{s}}) = \rho_{\mathrm{w}}\pi r D_{\mathrm{op}}^2\left[\frac{8h_{\mathrm{o}}}{\pi^2 D_{\mathrm{op}}}\sum_{m=1}^{\infty}\frac{(-1)^{m-1}}{(2m-1)^2}\frac{K_1(\alpha_m D_{\mathrm{op}}/2h_{\mathrm{o}})}{K_0(\alpha_m D_{\mathrm{op}}/2h_{\mathrm{o}})+K_2(\alpha_m D_{\mathrm{op}}/2h_{\mathrm{o}})}\cos(\alpha_m h_{\mathrm{s}}/h_{\mathrm{o}})\right] \quad (3\text{-}10)$$

where ρ_{w} is the mass density of water, $\alpha_m = (m-0.5)\pi$ is a dimensionless factor, and m is an integer ranging from unity to infinity; h_{s} is the distance from the post-scour seabed to the pile node i; h_{i} and h_{o} are water depths inside and outside monopile, respectively; I_n is the modified Bessel function of order n (n=0, 1, 2) of the first kind, while K_n is the modified Bessel function of order n (n=0, 1, 2) of the second kind; r_{ip} is the inside radius of monopile. The added mass at node i was obtained by multiplying $m_{\mathrm{a}}^{\mathrm{i}}(h_{\mathrm{s}})$ and $m_{\mathrm{a}}^{\mathrm{o}}(h_{\mathrm{s}})$ by the tributary length. Note that the hydrodynamic added mass

was derived assuming a leveled seabed. Since the water volume in the scour hole is relatively small, its inertial effect on the monopile is negligible (Jiang et al., 2021). Correspondingly, in a non-liquefied scenario in which a local-scour hole was considered, no m_a^o was added to the monopile within the range of local scour depth.

Table 2.2 Parameters of structural components

Monopile (nonlinearity)	Pile length (m)	58
	Pre-scour embedded length (m)	35
	Outside diameter (m)	3.5
	Wall thickness (m)	0.075
	Poisson's ratio	0.3
	Elastic modulus (GPa)	210
	Yield strength (Gpa)	0.408
	Mass density (ton/m^3)	8.5
Tower (nonlinearity)	Height (m)	56
	Outside diameter (m)	2.8-3.5
	Wall thickness (m)	0.02-0.075
	Poisson's ratio	0.3
	Elastic modulus (Gpa)	210
	Yield strength (Gpa)	0.408
	Mass density (ton/m^3)	8.5
Rotor-nacelle assembly	Height above mean sea level (m)	60
	Rotor diameter (m)	90
	Rotor mass (ton)	41
	Nacelle mass (ton)	70
	Three-blade mass (ton)	19

At the soil-pile interface, the zero-length interface elements that contained the post-scour springs and dashpots were set up to connect the pile nodes and the free-field soil nodes. Besides, a free-field soil column in plane-strain condition was created using four-node quadratic elements (Boulanger et al., 2003). A fully undrained condition was assumed for the soils around the monopile in water under seismic loading. The free-field motions were calculated based on effective stress analysis, and the time history of the mean effective stress, σ'_m, in the free-field soil was applied to the ends of the post-scour springs and dashpots. The soils were simulated with the fluid-solid porous material and the PDMY material (Boulanger et al., 2003; Yang, 2000) in OpenSees. The out-of-plane thickness of the soil column was set as 500 m to sufficiently preclude the influence of monopile on the free-field response (Boulanger et al., 2003; Khosravifar et al., 2014). Moreover, a dashpot (Lysmer and Kuhlemeyer, 1969) was placed at the base of the free-field soil column to account for the finite rigidity of the underlying bedrock (or firm ground). Accordingly, the seismic loading was applied as

a force time history (Joyner and Chen, 1975), which is the product of the velocity time history recorded on a rock outcrop or firm ground (i.e., outcropping motions) and the Lysmer-Kuhlemeyer dashpot coefficient. The dashpot coefficient is evaluated as $A_{\mathrm{b}}\rho_{\mathrm{b}}V_{\mathrm{b}}$, where A_{b} is the cross-section area at the base of the free-field column, ρ_{b} and V_{b} are the mass density (taken as 2.2 ton/m^3) (Uthayakumar and Naesgaard, 2004) and shear wave velocity (taken as 760 m/s) (NRCC, 2015) of the bedrock (or firm ground), respectively. Note that if the input ground motions were recorded on the embedded bedrock or firm soils (i.e., within motions), a rigid bedrock condition would be adopted by removing the dashpot from the base of the free-field soil column. Correspondingly, the recorded acceleration time history would be applied to the free-field base following the uniform excitation method. Furthermore, the energy dissipation in the integrated system including the soil, monopile, tower, and RNA was simulated using Rayleigh damping, and a total damping ratio of 3% (Bhattacharya, 2019) was assigned to the integrated system for its first and second modes of natural frequencies (Mo et al., 2017). To reduce numerical oscillations that can potentially develop in viscous dashpot forces under transient loading, the equation of motions was integrated using the Hilbert-Hughes-Taylor (HHT) algorithm with a coefficient of 0.7 (Boulanger et al., 2003; Brandenberg et al., 2013).

2.5.2 Earthquake motions

Table 2.3 summarizes the input bedrock motions applied to the base of the free-field soil column at a depth of 3.7 m below the pile tip as with the centrifuge test (Wilson et al., 1997). These records were scaled and selected as the bedrock outcropping motions (Baker et al., 2011; FEMA, 2009). The use of amplitude scaling rather than spectral matching was to reveal the inherent variabilities of the ground motions. These records were associated with different mean square frequencies (Rathje et al., 1998) ranged from 2.85 Hz to 7.54 Hz and significant duration (and thus different equivalent cyclic numbers) ranged from 11.66 s to 25.20 s (Hashash et al., 2017; Kramer, 1996). Therefore, it is anticipated that the seismic responses corresponding to these six motions would exhibit certain variations besides some general trends, in particular for liquefied soils that involved marked nonlinearity.

Table 2.3 Information about bedrock input motions

Earthquake event	Moment magnitude	Mechanism	Record sequence number	Component	Significant duration (s)	Mean frequency (Hz)
San Fernando, 1971	6.61	Reverse	72	111	12.78	7.54
Landers, 1992	7.28	Strike slip	832	090	25.20	3.85
Northridge, 1994	6.69	Reverse	1042	270	16.02	3.50
Duzce, Turkey, 1999	7.14	Strike slip	1618	531E	14.88	3.06
Kocaeli, Italy, 1999	7.51	Strike slip	1165	090	13.26	2.85
Hector Mine, 1999	7.13	Strike slip	1787	000	11.66	3.15

2.5.3 Parametric analysis arrangement

Table 2.4 shows the details of the parametric analyses, three cases (A, B, and C) were considered to account for different scour-hole dimensions and liquefaction states. As discussed in Section 2.3, the initiation of liquefaction herein was determined by checking the calculated profile of r_u under a pre-scour condition, i.e., if r_u was close to unity (e.g., ≥0.8) (Haldar and Patra, 2021) in the upper range of soil (depth≤$2.5D_{op}$), the case would be treated as a liquefied case, otherwise, it would be considered as a non-liquefied case.

Case A involved no liquefication, in which the local scour characterized with a typical scour-hole shape (i.e., varying S_d, S_{wb}=0, and S_θ=30°) was considered. In contrast, Cases B and C involved liquefication, in which the local scour turned into the general scour (i.e., varying S_d while S_θ=0°). Thereinto, Case C considered layered soils (i.e., a loose sand layer overlying dense sands). The thickness of the loose sand layer (9.1 m or $2.6D_{op}$) was kept the same as that in prototype in the centrifuge test (Wilson et al., 1997). Since the seismic responses of the monopile-supported OWT under local scour conditions are primarily dependent on the scour-hole depth (Jiang et al., 2021), only scour depth was varied to evaluate the scour effects. In each of the three cases, six scour depths were investigated while maintaining constant S_{wb} and S_θ in Table 2.4. In design practice, scour depth is typically taken as $1.3D_{op}$-$2.5D_{op}$ (API, 2011; DNV, 2014; GL, 2012). Therefore, the investigated range of scour depth was taken to be from

$0.5D_{op}$ to $2.5D_{op}$, and the corresponding embedded length of the monopile was $7.5D_{op}$-$9.5D_{op}$.

Table 2.4 Summary of parametric analyses

Case	Soil deposit	Local scour dimensions			Embedded length of monopile ($\times D_{op}$)	Input motion	
		S_d ($\times D_{op}$)	S_{wb} ($\times D_{op}$)	S_θ (°)		Earthquake event	Scaled PBA (g)
A	Dense Nevada sand (D_r=75%)	0, 0.5, 1.0, 1.5, 2.0, 2.5	0	30	10.0, 9.5, 9.0, 8.5, 8.0, 7.5	San Fernando, Landers; Northridge; Duzce, Turkey; Kocaeli, Italy; Hector Mine	0.1
B	Dense Nevada sand (D_r=75%)	0, 0.5, 1.0, 1.5, 2.0, 2.5	∞	0	10.0, 9.5, 9.0, 8.5, 8.0, 7.5	Landers; Northridge; Duzce, Turkey; Kocaeli, Italy; Hector Mine	0.5
C	Loose Nevada sand (D_r=35%) in the upper 9.1 m; dense Nevada sand (D_r=75%) in the lower layer	0, 0.5, 1.0, 1.5, 2.0, 2.5	∞	0	10.0, 9.5, 9.0, 8.5, 8.0, 7.5	San Fernando, Landers; Northridge; Duzce, Turkey; Kocaeli, Italy; Hector Mine	0.5

The scaled PBA values of 0.1g and 0.5g were used, as also adopted by other studies (Haldar and Patra, 2021; Jiang et al., 2021; D. H. Kim et al., 2014). A smaller PBA value of 0.1g in Case A was to achieve a non-liquefied condition, while a greater PBA value of 0.5g was used in Cases B and C to trigger liquefaction. Note that the ground motion of the San Fernando earthquake was not included in Case B since the soil was found to be non-liquefied in a pre-run analysis, which was due to the short significant duration of this motion (as shown in Table 2.3). In total, 102 cases of analyses were performed.

2.6 Results and discussion

2.6.1 Effects of scour depth on natural frequencies of OWT

Before presenting the results of dynamic responses, the effect of scour depth on the

natural frequency of the integrated monopile-supported OWT system is discussed here. Figure 2.5(a) shows the fundamental frequency, f_1, associated with the first fore-aft bending mode varied by scour depth for the three cases listed in Table 2.4. As with Zhu et al. (2020), the increase in S_d from 0 to $2.5D_{op}$ decreased f_1 by up to 13%-19% due to a slenderer system. Note that the eigenvalue analysis is linear and only the initial stiffness of the soil spring is used; therefore, the computed natural frequency is momentary and does not reflect the state during seismic shaking or liquefaction (Bhattacharya, 2019; Mo et al., 2017). In Cases A and B, post-scour f_1 fell into the f_{1P}±10% range (f_{1P}=0.14-0.3 Hz for the 3 MW turbine investigated here) (Bhattacharya et al., 2021) when S_d was greater than $0.8D_{op}$ and $0.9D_{op}$, respectively, causing resonance with the turbine rotation. The post-scour f_1 could cause resonance with the turbine rotation in Case C for all the scour depths examined. For the monopile-supported OWT in the same soil condition, f_1 appeared to be slightly larger in the local-scour hole condition (Case A) than in the general scour condition (Case B). Under the same scour condition, dense sand (Case B) was associated with a larger f_1 (up to 5% larger) than loose sand (Case C), but the difference vanished when $S_d \geq 2.0D_{op}$, which was due to the decreased thickness of the loose sand layer. At the prescribed maximum scour depth of $2.5D_{op}$, the entire loose sand layer ($2.6D_{op}$) in Case C was almost removed by the scour. In general, driving the monopile into denser sands is beneficial to avoid resonance dictated by the soft-stiff design rule.

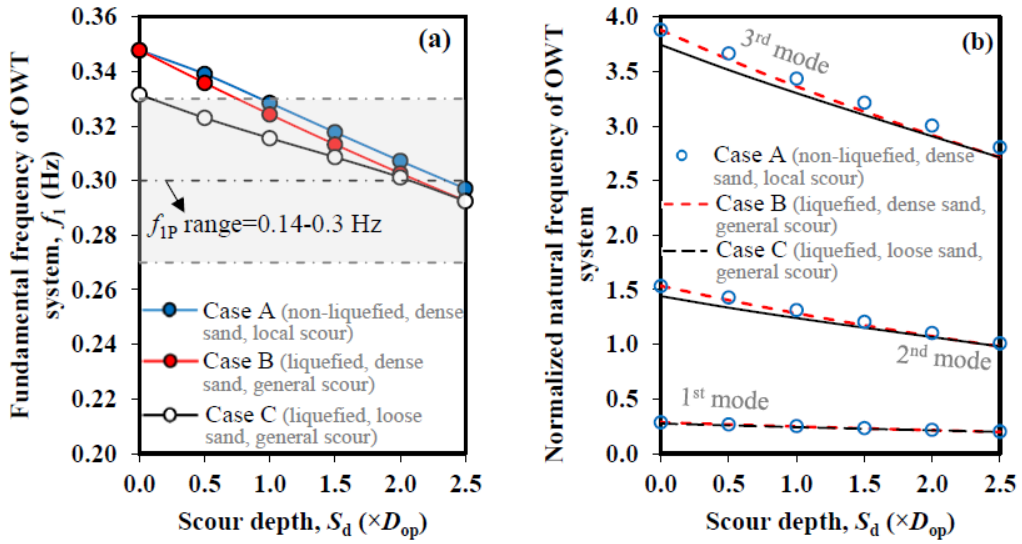

Figure 2.5 Effects of scour depth on the (a) fundamental frequency and (b) normalized natural frequency of the integrated monopile-supported OWT system

Figure 2.5(b) shows the natural frequency, f_n, normalized to the site characteristic frequency (1.2-1.5Hz when S_d increased from 0 to $2.5D_{op}$ in the three cases) (Kramer, 1996). The site characteristics frequency increased by 21% as S_d increased from 0 to $2.5D_{op}$, which is consistent with Shang et al. (2016). The f_n is the n^{th} natural frequency corresponding to the n^{th} natural mode of vibration. The frequency ratio for the first two modes (i.e., f_2/f_1) was 5.4-5.0 in Cases A and B but 5.2-5.0 in Case C when S_d increased from 0 to $2.5D_{op}$, consistent with a typical range of 4.0-6.0. This indicates that the first two natural modes of vibration are widely spaced. Although f_1 dominates the dynamic response of the OWT system, the higher mode contribution should also be considered in evaluation of the total dynamic responses of a monopile-supported OWT system (Jiang et al., 2021). As shown in Figure 2.5(b), the normalized f_2 approached unity as S_d increased, while f_1 shifted away from the site characteristic frequency. Moreover, the mean square frequencies of the bedrock input motions (listed in Table 2.3) were generally close to f_3 when S_d=$1.5D_{op}$-$2.5D_{op}$. Therefore, the above comparison indicates that a peak amplification of dynamic response might occur at S_d=$1.5D_{op}$-$2.5D_{op}$ due to the resonance effect between the soil-structure system and the bedrock motions.

2.6.2 Effects of scour depth on dynamic responses of OWT

The following discussion focuses on the effects of scour depth on the maximum dynamic responses under each earthquake motion including the lateral acceleration, lateral displacement, rotation, and bending moment of the monopile-supported OWT. The maximum response is presented in a normalized way by comparing it to the pre-scour response using the three steps:

(1) Determine the peak of time-histories of responses at different locations on the monopile and tower (e.g., Figure 2.6), which allows profiling the peak response envelope along the monopile and tower (e.g., Figure 2.7).

(2) From the peak response envelopes along the monopile and tower, determine the maximum value at two locations and two portions: tower top, tower portion, monopile at the post-scour seabed, and embedded portion of monopile.

(3) Calculate the normalized responses by dividing the maximum responses at the four selected locations after scour by those before scour. Therefore, the normalized

values greater than one indicate scour-induced amplification of the dynamic response and vice versa.

To elaborate on the above procedure, the results of Case A under the input motion of 1992 Landers earthquake are presented here. Figure 2.6 shows the calculated time histories of the lateral displacements at the tower top and pile top before and after scour (S_d=1.5D_{op}, S_{wb}=0, and S_θ=30°), from which the peak values were identified.

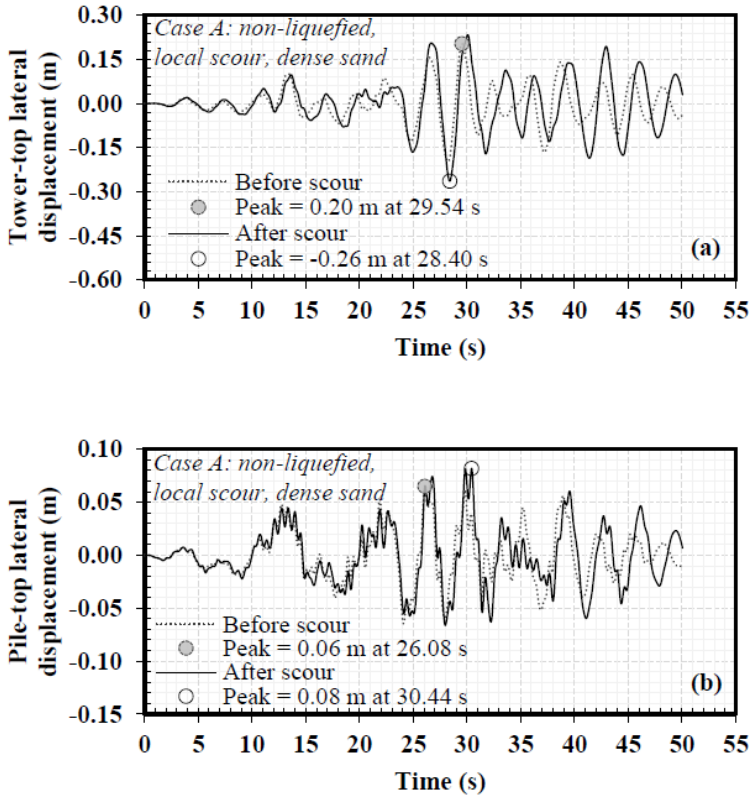

Figure 2.6 Pre-scour and post-scour (S_d=1.5D_{op}, S_{wb}=0, S_θ=30°) lateral displacements at (a) tower top and (b) pile top (Case A)

Likewise, the time histories of displacement were also determined for other locations of the monopile-supported OWT system, from which the peak values were also identified. The plots of the identified peak displacement and other responses (e.g., acceleration, rotation, and bending moment) along the lengths of tower and monopile form the peak response envelopes as shown in Figure 2.7. Figure 2.7(a) shows the largest peak lateral acceleration occurred in the tower, which was 5% greater after scour than before scour. As with Jia et al. (2017), the peak lateral acceleration increased from the pile tip to location slightly above the pile top, and then decreased to locations near the tower top, which was attributed to the effect of structural damping from the heavy

RNA.

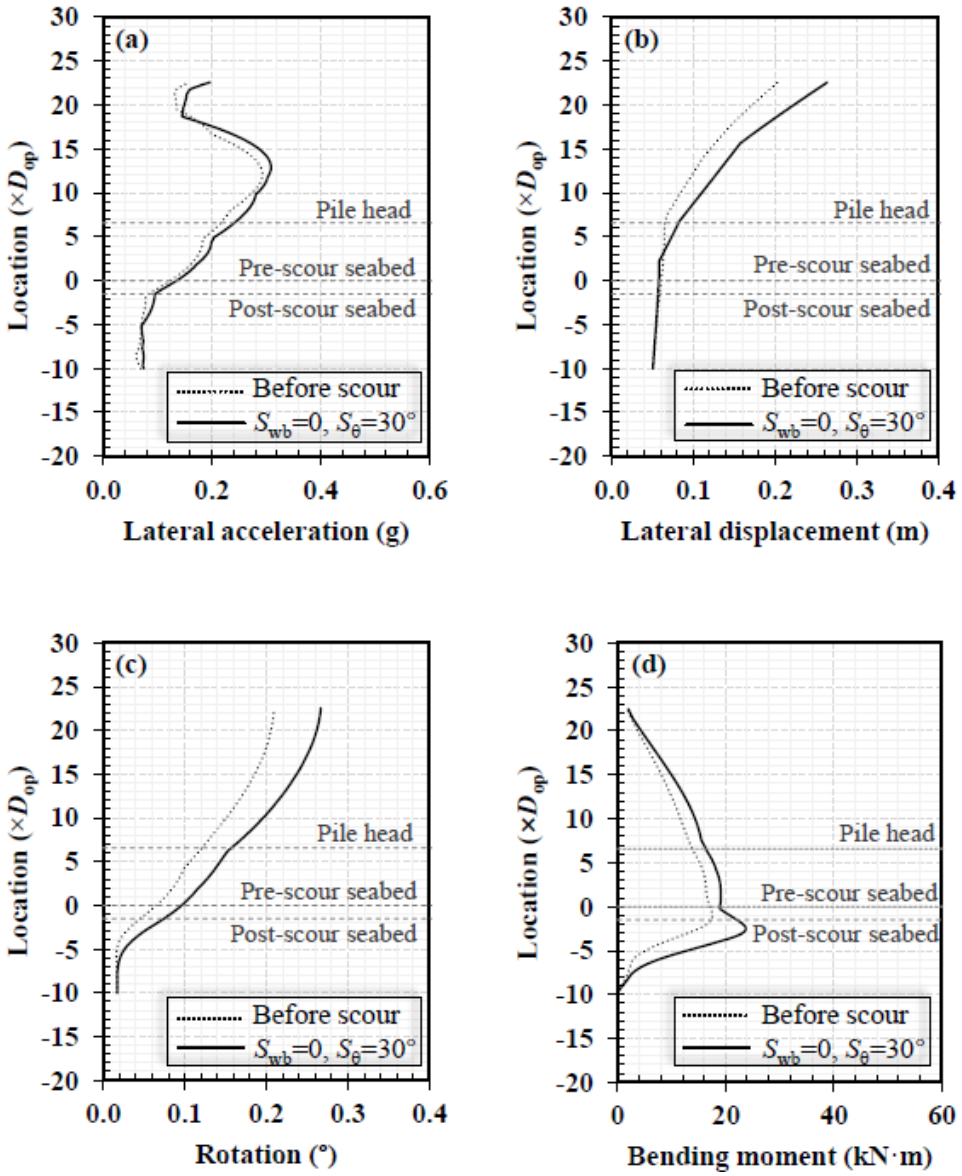

Figure 2.7 Pre-scour and post-scour response envelopes: (a) lateral acceleration, (b) lateral displacement, (c) rotation, and (d) bending moment under motion Landers for Case A (non-liquefied, dense sand, local scour: S_d=1.5D_{op}, S_{wb}=0, S_θ=30°)

Figures 2.7(b) and 2.7(c) show that the peak response envelopes of the lateral displacement and rotation appeared to be larger at a higher structural element (e.g., from the pile tip to the tower top) regardless of the occurrence of scouring due to a cantilever system. Therefore, the largest peak displacement and rotation were found at the tower top. The peak lateral displacement and rotation at the tower top were amplified by 30% and 27%, respectively due to scour. Figure 2.7(d) indicates that the largest peak

bending moment was located in the embedded portion of monopile, which increased by 35% as compared to the pre-scour one. In comparison, the rotation response was most sensitive to scour than the other dynamic responses examined. This implies that the rotation of pile or tower may be a good indicator to monitor scour extent.

Since the largest values for different peak response envelopes occurred at different locations of the OWT system, two locations and two portions were selected herein, from which the maximum peak dynamic responses were determined: tower top (lateral acceleration, lateral displacement, and rotation), monopile at the post-scour seabed level (lateral displacement and rotation), tower portion (lateral acceleration and bending moment), embedded portion of monopile (bending moment). It is apparent that the maximum peak dynamic responses at the two locations (tower top and monopile at the post-scour seabed) are also peak dynamic responses. In the following sections, the maximum peak dynamic responses are simply termed as the maximum responses for brevity. The scour effect on the dynamic responses was then presented in a normalized form. The results of Case A (non-liquefied scenario) are presented in Section 2.6.2.1, while the results of Cases B and C (liquefied scenarios) are presented in Section 2.6.2.2.

2.6.2.1. Non-liquefied case (Case A)

Figure 2.8 shows the normalized maximum lateral acceleration at the tower top and that of the tower portion with varying S_d while keeping S_{wb}=0 and S_θ=30°. In Figure 2.8(a), the normalized maximum acceleration at the tower top on average increased from 1.0 to 1.13 as S_d increased from 0 to $2.0D_{op}$, indicating that the maximum acceleration at the tower top increased by 13%, while this increase tended to be weakened when S_d was greater than $2.0D_{op}$. The peak increase occurring at S_d=$2.0D_{op}$ could primarily result from the resonance effect between the soil-structure system and the input bedrock motions, as discussed in Figure 2.5(b) (Shang et al., 2016). However, as shown in Figure 2.8(b), the increase in S_d caused negligible changes in the maximum acceleration of the tower portion, particularly for $S_d \leq 1.5D_{op}$. This indicates that more energy was absorbed by the rotor-nacelle assembly atop the tower top. The different trends could also manifest the scour-induced changes in the inertial interaction: e.g., affecting the participation of vibration modes (Liang et al., 2020).

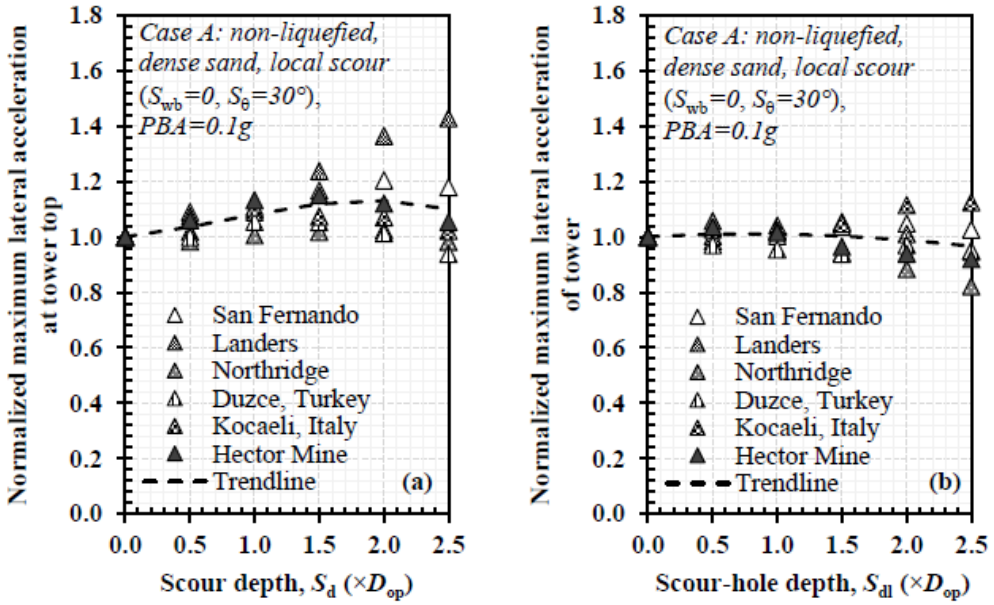

Figure 2.8 Normalized maximum lateral accelerations (a) at tower top and (b) of tower varied with scour depth (Case A)

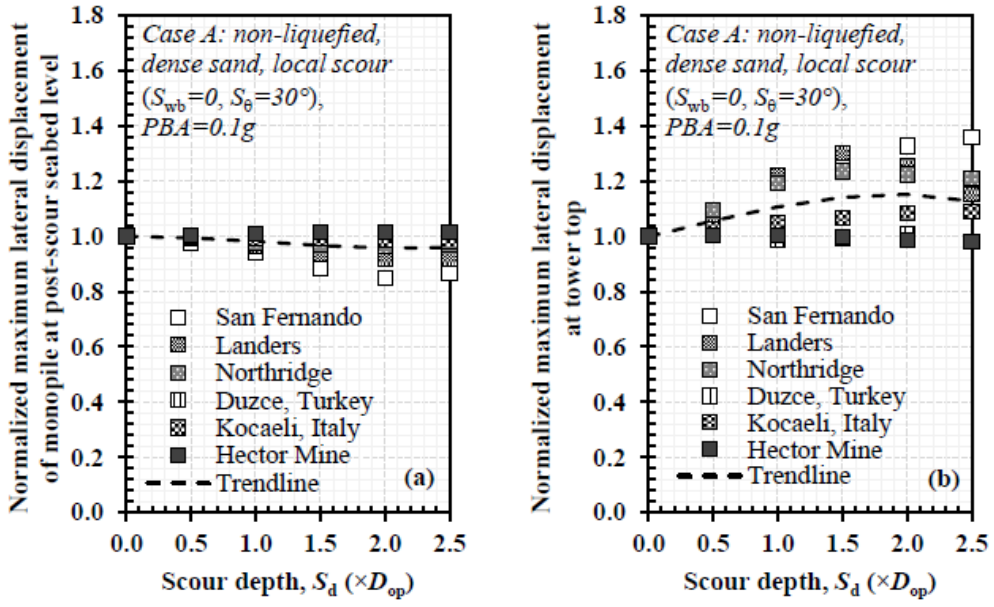

Figure 2.9 Normalized maximum lateral displacements of (a) monopile at post-scour seabed and (b) tower top varied with scour depth (Case A)

Figures 2.9 and 2.10, respectively, show the effect of local scour depth on the maximum lateral displacement and rotation of the monopile at the post-scour seabed level and the tower top (S_{wb}=0 and S_θ=30°). The effect of S_d on the maximum lateral displacement was more significant at the tower top than that of the monopile at the post-scour seabed level. From the mean trendline, the maximum lateral displacement of the monopile at the post-scour seabed level decreased by 4% as S_d increased from 0 to

2.5D_{op}. Contrarily, the maximum lateral displacement at the tower top was increased by up to 15% at S_d=1.5D_{op}-2.5D_{op}, and the peak increase generally occurred at S_d=2.0D_{op}. In comparison to the maximum displacement, scour effect on the maximum rotation was more significant. The maximum rotation of the monopile at the post-scour seabed level was amplified due to scour, showing a peak amplification of 16% at S_d=1.5D_{op}. Likewise, a peak amplification (19%) of the maximum rotation at the tower top generally occurred at S_d=1.5D_{op}-2.0D_{op}.

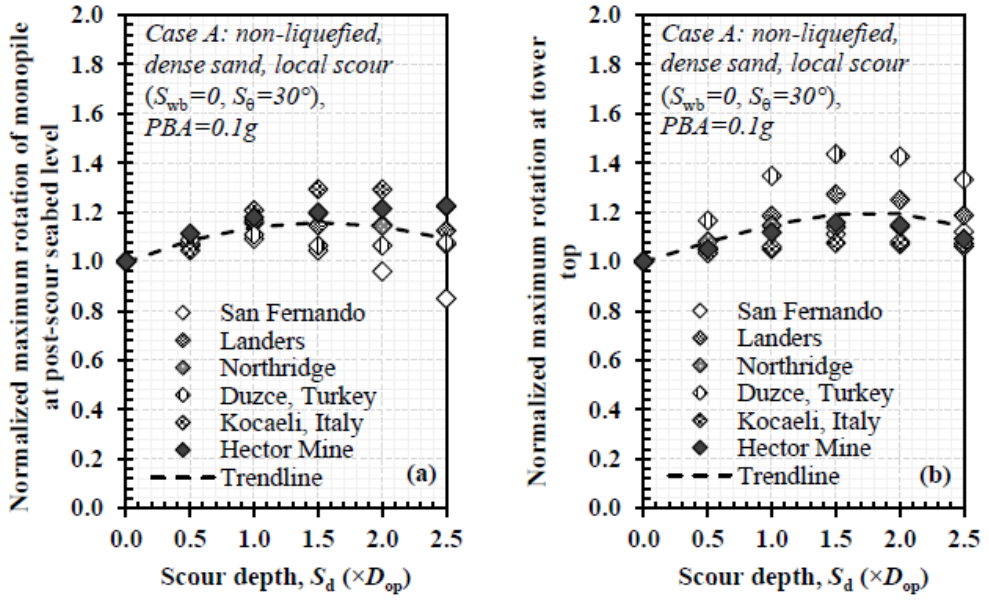

Figure 2.10 Normalized maximum rotations of (a) monopile at post-scour seabed level and (b) tower top varied with scour depth (Case A)

Figure 2.11 shows the normalized maximum bending moment of the embedded portion of monopile and that of the tower varied with S_d while S_{wb}=0 and S_θ=30°. In Figure 2.11(a), the maximum bending moment of the embedded monopile on average increased by up to 29% as S_d increased from 0 to 2.5D_{op}, which was agreeable with the shake-table/centrifuge tests (Shang et al., 2016; Wang et al., 2015; Zhu et al., 2020). A similar trend was also observed at the tower portion but with a smaller increase [Figure 2.11(b)]. As with Jiang and Lin (2020), the peak increase in the maximum bending moments of monopile and tower generally occurred at S_d=2.0D_{op}, which could result from the resonance effect between the integrated OWT system and the bedrock motions.

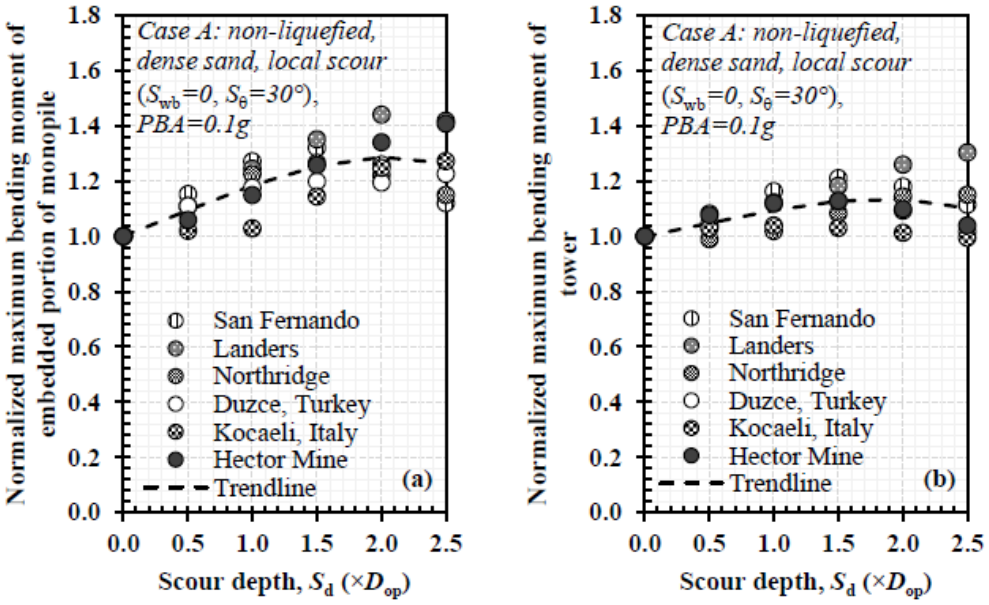

Figure 2.11 Normalized maximum bending moments of (a) embedded portion of monopile and (b) tower varied with scour depth (Case A)

2.6.2.2. Liquefied cases (Cases B and C)

This section discusses the dynamic responses of the OWT structures in the liquefied condition. In comparison to the non-liquefied case (Case A), more scattered results were found because liquefaction usually introduces marked nonlinearity and causes variable responses under different ground motions (Turner et al., 2017; Wang et al., 2020, 2019). For example, liquefaction-induced changes in soil stiffness, soil-monopile stiffness contrast, and frequency and wavelength of free-field excitation could affect soil-monopile interactions and therefore total dynamic responses of the entire OWT system.

Figure 2.12 shows the normalized maximum lateral acceleration at the tower top and that of the tower portion under different S_d while S_{wb}=∞ or S_θ=0°. Although more variable responses occurred in Case B than Case C due to the different density of soils (and thus kinematic interactions), the mean trendlines were agreeable. The maximum lateral acceleration at the tower top [Figures 2.12(a) and (c)] was amplified by up to 10% (Case B) and 5% (Case C) by scour and the peak amplification generally occurred at S_d=1.5D_{op}, which was consistent to non-liquefied case [Case A in Figure 2.8(a)]. Besides, the maximum lateral acceleration of the tower portion [Figures 2.12(b) and (d)] on average decreased as S_d increased, showing a similar trend to the non-liquefied case [Case A in Figure 2.8(b)]. The normalized maximum accelerations that were more

scatter in Case B than in Case C could be due to two reasons: (1) unlike Case B where the depth of liquefaction (i.e., r_u value and the depth range of liquefied soils) was varied with different ground motions, the entire layer of loose sand in Case C was fully liquefied (r_u=1.0) under different ground motions, which somehow "filtered" out certain high-frequency contents in the seismic input that could interact with the OWT system and produce evident amplifications as occurred in Case B; (2) the effect of scour-induced changes in overburden (and thus the response acceleration of structure) was relatively smaller in loose sands (Case C) than in dense sands (Case B).

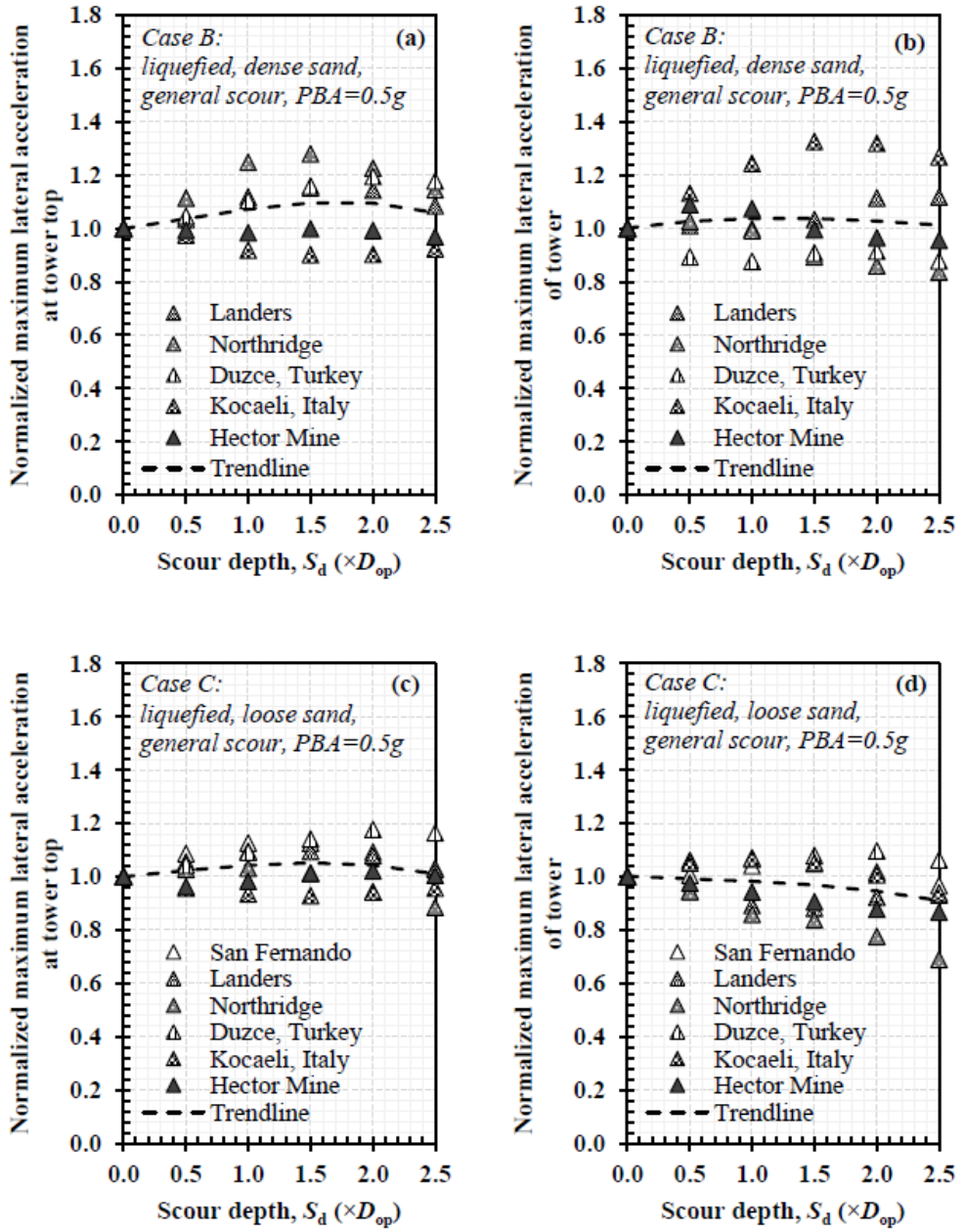

Figure 2.12 Normalized maximum lateral accelerations varied with scour depth in liquefied cases: (a) and (c) for tower top; (b) and (d) for tower portion

Figure 2.13 shows the normalized maximum lateral displacement of the monopile at the post-scour seabed level and at the tower top under different S_d while $S_{wb}=\infty$ or $S_\theta=0°$. In comparison, the effect of scour on the maximum lateral displacement was similar between Case B and Case C, and the results for both liquefied cases (Cases B and C) were less affected by scour than those for non-liquefied soil (Case A). This is attributed to that the scour-induced loss of stiffness and strength in non-liquefied soil was more pronounced than in liquefied soils as the stiffness and strength of the liquefied soil were already very small.

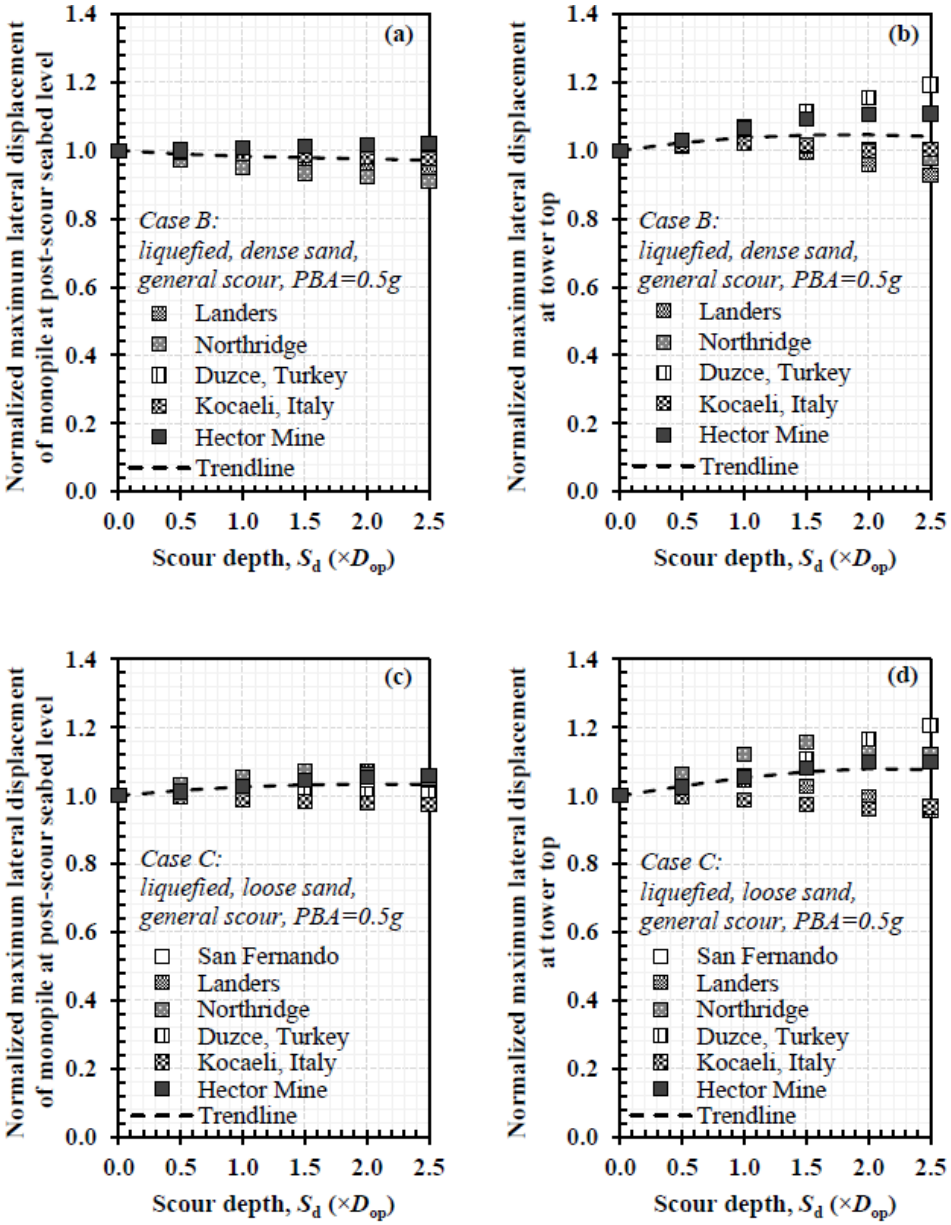

Figure 2.13 Normalized maximum lateral displacements varied with scour depth in liquefied cases: (a) and (c) for monopile at post-scour seabed level and (b) and (d) for tower top

Figure 2.13 also shows that the effect of S_d on the maximum lateral displacement was more remarkable at the tower top [Figure 2.13(b) and (d)] than monopile at the post-scour seabed level [Figure 2.13(a) and (c)]. From the mean trendline, the maximum lateral displacement at the tower top increased by up to 8% for S_d=0 to 2.5D_{op} in the liquefied cases, which was much smaller than 15% in the non-liquefied case [Figure 2.9(b)]. As with Jia et al. (2017) and Zhu et al. (2020), the increase in S_d generally increased the maximum displacement at the tower top. It is also noted that the variability of the maximum displacement at the tower top was more noticeable at greater scour depths (e.g., $S_d \geq 1.5D_{op}$), featuring both increase and decrease in the displacement with the increased scour depth. This could be due to the nonlinearity of liquefaction (Khosravifar et al., 2014; Wang et al., 2019) and the inherent variability of different input motions (as shown in Table 2.3) (Shang et al., 2016; Turner et al., 2017; Wang et al., 2020, 2019). For example, the liquefaction-induced softening effect could intensify the phase difference between the kinematic and inertial interactions, which could further influence the dynamic responses (Tokimatsu et al., 2005). Moreover, the effect of Rayleigh damping on the lateral displacement at the tower top was found to be more significant than the other locations of the OWT structure due to a heavy rotor-nacelle assembly (Jia et al., 2017). The changes in the Rayleigh damping concerning the stiffness-proportional component caused by the softening effect of liquefaction could introduce more nonlinearity and render a mixed response.

Figure 2.14 shows the normalized maximum rotation of monopile at the post-scour seabed level and that at the tower top under various S_d while S_{wb}=∞ or S_θ=0°. As indicated by Wang et al. (2019), a relatively strong correlation between pile curvature and inertial interaction could be identified in a non-liquefied scenario. Contrarily, in a liquefied scenario, such a correlation tended to be weak, and it is difficult to identify whether the pile curvature was more affected by the inertial interaction or the kinematic interaction under different ground motions. As discussed in Figure 2.7, affected by the nonlinear kinematic interaction, the rotation response was more sensitive to scour effect for the non-liquefied soil. This, however, was not noticeable in the liquefied soils as shown in Figure 2.14. It is also noted that the rotation results for monopile at the post-scour seabed were increasingly scatter with increased scour depth, showing both scour-induced amplification and attenuation (up to ±20% variation) [Figures 2.14(a) and (c)]. The mean trendline for the rotation at this location was almost not changed by scour depth, which was different from the trend in Figure 2.10(a). In contrast, the maximum

rotation at the tower top was less scatter at a greater scour depth [Figures 2.14(b) and (d)], showing a relatively consistent trend because the response at the tower top was more affected by the inertial interaction. Overall, the maximum rotation at the tower top was increased by up to 6% (Case B) or 10% (Case C) as S_d increased from 0 to $2.5D_{op}$, which was less than that in Case A (19%). However, the peak increase was found to occur at the same scour depth of S_d=$1.5D_{op}$ for all the three cases.

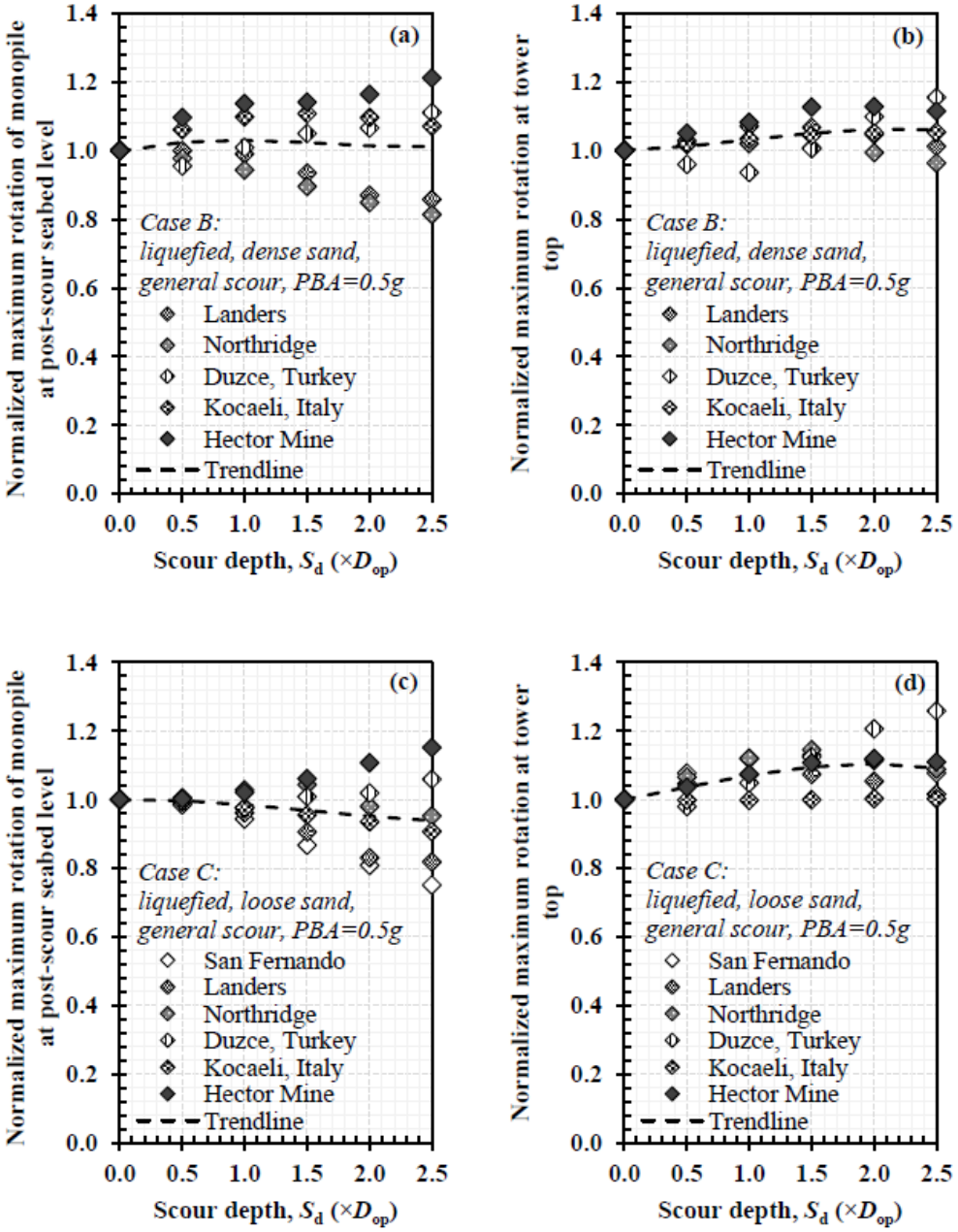

Figure 2.14 Normalized maximum rotations varied with scour depth in liquefied cases: (a) and (c) for monopile at post-scour seabed level and (b) and (d) for tower top

Figure 2.15 shows the normalized maximum bending moment of the embedded portion of monopile and that of the tower portion with varying S_d for Cases B and C. The effect of S_d on the maximum bending moment in the liquefied cases was less significant than in the non-liquefied case (Figure 2.11), which was consistent to other dynamic responses observed and the reason was also explained previously.

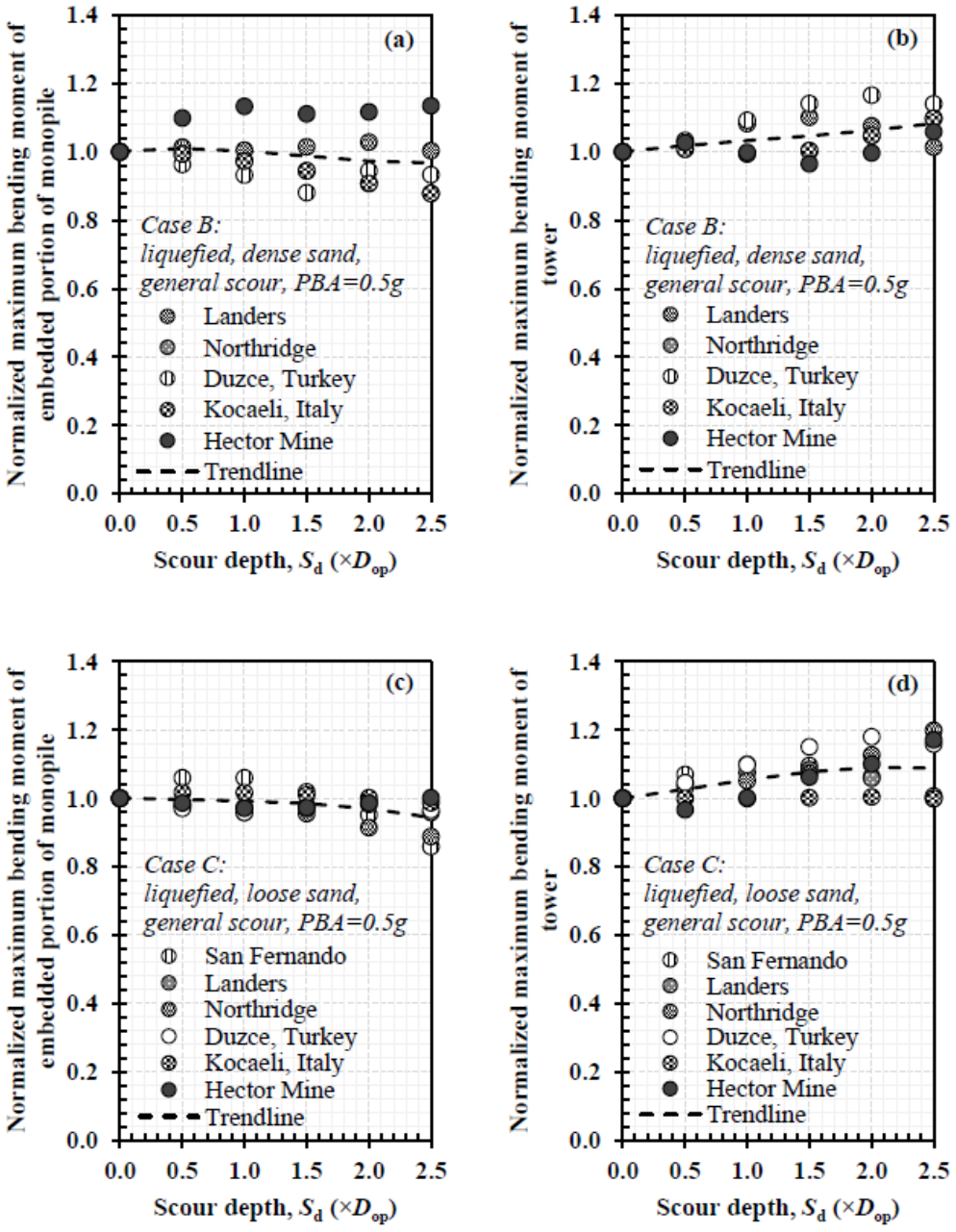

Figure 2.15 Normalized maximum bending moments varied with scour depth in liquefied cases: (a) and (c) for embedded portion of monopile and (b) and (d) for tower portion

It is also observed that the maximum bending moment of the embedded portion of monopile [Figures 2.15(a) and (c)] tended to decrease slightly with scour depth while the maximum bending moment of the tower portion [Figures 2.15(b) and (d)] was increased as S_d increased from 0 to $2.5D_{op}$, with the peak increase being up to 6% (Case B) or 9% (Case C). The reason for the different responses at the two locations was that the former was primarily affected by kinematic interaction which was varied insignificantly by scour as the soil stiffness and strength in liquefied condition were already very small. In contrast, the latter was affected by both kinematic and inertial interactions and the inertial interaction tended to be amplified by scour as the cantilever portion of the OWT system was increased.

In summary, the preceding comparison between the non-liquefied condition (Case A) and the liquefied condition (Cases B and C) highlighted the effect of soil liquefaction on the post-scour seismic responses of the monopile-supported OWT system. Overall, dynamic responses of the OWT structure in liquefiable soils exhibited more nonlinear features under different bedrock input motions, which were consistent with other studies (Khosravifar et al., 2014; Shang et al., 2016; Wang et al., 2019). In the liquefied soils, the increase in S_d imposed less impact on the maximum dynamic responses of the OWT system. This could be due to two reasons: (1) the seismic energy associated with the high-frequency components of the bedrock motion was precluded to be transmitted to the ground (Kramer, 1996; Kramer et al., 2016; Mehrzad et al., 2018); and (2) the scour-induced loss of stiffness and strength in liquefied soil was smaller than in non-liquefied soil as the stiffness and strength of the liquefied soil were already very small.

2.7 Conclusions

This study proposed a practical approach to evaluating the responses of piles in sands under the combined effects of scour and earthquakes. This approach is novel in that it realistically captured the difference in scour-hole geometric conditions between liquefied and non-liquefied conditions. The proposed procedure was encoded into a set of open-source computer scripts for analyzing the post-scour dynamic responses of the monopile-supported OWTs in sands. A total of 102 parametric analyses were performed by varying scour depth, soil relative densities, and crustal earthquake input motions. The following conclusions were obtained from the study:

(1) In the non-liquefied condition, local scour around piles was characterized by

typical scour-hole dimensions including scour-hole depth, bottom width, and side slope; in the liquefied condition, the local scour turned into the general scour with the dimensions only defined by scour depth.

(2) The first-mode fundamental frequency, f_1, of the integrated soil-monopile-tower-RNA system decreased by 13%-19% as scour depth, S_d, increased from 0 to $2.5D_{op}$. Scour could shift f_1 into the rotor frequency range, causing resonance. The ratio between the first two natural frequencies (f_2/f_1) ranged from 5.0-5.4, indicating a distinct difference in the natural modes of the integrated OWT system. The decrease of higher-mode frequencies (f_2, f_3) should be evaluated in the OWT design against scour due to the increased slenderness of the system.

(3) For a non-liquefied case (Case A), the maximum lateral acceleration, lateral displacement, and rotation at the tower top, and the maximum bending moments of the embedded monopile and the tower portion were all increased with increasing scour depth. Besides, the peak increase of these responses with scour depth generally occurred at S_d=$1.5D_{op}$-$2.0D_{op}$ due to the resonance effect between the soil-structure system and the bedrock input motions at this range of scour depth.

(4) For liquefied cases (Cases B and C), the dynamic responses of the monopile-supported OWTs in sands with different relative densities exhibited similar trends. The increase in S_d caused the increase in the maximum lateral displacement and rotation at the tower top and the maximum bending moment of the tower, while the scour effect on the maximum bending moment of the embedded portion of monopile was minor. For the given variable input motions, the results were more scatter with increased scour depth due to the marked nonlinearity of liquefaction and the inherent variability of different bedrock motions.

(5) The difference in the liquefaction state (Case A vs. Cases B & C) produced different responses of the OWT system under increased scour depth, with the results being more variable in liquefied soil (Cases B and C) than in non-liquefied soil (Case A). In general, the scour effect was more remarkable in the non-liquefied case than in the liquefied case. Within the typical range of scour depth (i.e., $1.3D_{op}$-$2.5D_{op}$) adopted in design practice, scour depths of $1.5D_{op}$-$2.0D_{op}$ could be appropriate for use in a non-liquefied case, while a greater general scour depth (e.g., $2.5D_{op}$) would be more suitable for use in a liquefied case when assessing the maximum seismic responses of the monopile-supported OWT under scoured conditions.

2.8 Notation

A_b = cross-section area at the base of the free-field soil column

C_1, C_2, C_3 = three constants dependent on D_r (API, 2011)

c_{drag}= drag coefficient accounting for gapping effect between pile and soil

$c_{h,sc}$= post-scour lateral damping coefficient

$c_{v,sc}$= post-scour vertical damping coefficient

D_{op} = outside diameter of monopile

D_r= relative density of soil

f_m = a multiplier (≤1.0) to calculate post-liquefaction residual soil resistance

f_n = the n^{th} natural frequency corresponding to the n^{th} natural mode of vibration of the integrated soil-monopile-tower-turbine system, n=1, 2, 3

f_{1P} = rotor frequency of the turbine

$G_{max,sc}$ = post-scour small-strain shear modulus of soil

g = gravitational acceleration

h_o= water depth outside monopile

h_i = water depth inside monopile

I_n= modified Bessel function of order (n=0, 1, 2) of the first kind

K_n= modified Bessel function of order (n=0, 1, 2) of the second kind

$K_{2,\,max}$ = dimensionless factor dependent on D_r

k_o = coefficient of lateral earth pressure at rest, k_o=1-sinφ'

m_a^o = outside added mass per unit length of a pile

m_a^i = inside added mass per unit length of a pile

N_q = end bearing factor suggested by API (2011)

p = lateral soil resistance per unit length of a pile

$p_{u,sc}$ = ultimate lateral soil resistance considering scour dimensions

$p_{u,sl}$ = ultimate lateral soil resistance considering the combined effects of scour dimensions and liquefaction-induced softening

$p_{u,res}$ = residual soil resistance of the modified p-y curve in a fully liquefied condition (r_u=1)

q = unit end bearing in stress units

r_{ip} = inside radius of monopile

r_u = excess pore water pressure ratio

S_d = scour depth

S_{wb} = scour-hole bottom width

S_{wt} = scour-hole top width, $S_{wt}=S_{wb}+S_d/\tan S_\theta$

S_θ = scour-hole side slope angle

t = unit shaft friction in stress units

$t_{u,res}$ = residual soil resistance of the modified t-z curve in a fully liquefied condition (i.e., r_u=1)

$t_{u,sl}$ = ultimate soil resistance of the modified t-z curve that accounts for scour and liquefaction effects

V_b = shear wave velocity of the bedrock (or firm ground)

$V_{s,sc}$ = pos-scour shear wave velocity of soil, $V_{s,sc}=(G_{max,sc}/\rho_{sat})^{0.5}$

y = lateral soil displacement

z = depth below post-scour seabed

α_m = dimensionless factor, taken as $(2m-1)\pi/2$ with m being an integer ranging from one to infinity

β = friction factor suggested by API (2011)

γ' = submerged unit weight of soil

Δu= excess pore water pressure in free-field soil

Δz= element size of monopile

ρ_b = mass density of the bedrock (or firm ground)

ρ_{sat}= saturated mass density of soil

ρ_w= mass density of water

$\sigma'_{v,sc}$ = post-scour vertical effective stress of soil at monopile

σ'_m = mean effective stress in free-field soil at a time instant of interest

σ'_{mo} = mean effective stress in free-field soil at initial time instant

φ' = effective friction angle of soil

Chapter 3 Seismic Responses of Monopile-Supported Offshore Wind Turbines in Soft Clays under Scoured Conditions

3.1 Abstract

For the monopile-supported offshore wind turbine (OWT), scour can significantly affect the seismic responses of the structure. However, the combined effects of scour and earthquakes are not fully appreciated. This study proposed a new method to evaluate the post-scour seismic responses of monopole-supported OWTs, considering various scour-hole dimensions and soil stress-history changes due to different scour levels. Using the developed computer scripts, a parametric study was conducted, including 198 cases on a monopile-supported OWT in soft clays under different scoured conditions and six crustal earthquakes. The results showed that scour significantly changed the seismic responses of the selected OWT structure. Use of an overpredicted scour depth in the post-scour analysis underestimated the seismic response while simplifying local scour as general scour and ignoring soil stress history overestimated the seismic response of OWT. This research recommends in analysis the use of a cone-shape scour hole with side slope angle of 30°.

3.2 Introduction

The number of offshore wind turbine (OWT) farms has been increasing globally, due to the great potential to produce sustainable energy. In particular, the popularity of monopile-supported OWT has increased significantly over the years due to the ease of fabrication, installation, and operation (GWEC, 2020; REN21, 2019, p. 21; WindEurope, 2019). Typically, a monopile is a tubular steel pile with an outside diameter of four to six meters for supporting tower and rotor-nacelle assembly (RNA) in water depths up to 35 m (Doherty and Gavin, 2012; Klinkvort and Hededal, 2013; Søren and Lars Bo, 2013). The OWT system is often designed against the cyclic lateral loads due to waves, winds, and rotor vibration. Affected by currents and waves, the OWT is also vulnerable to scour. In the active seismic zones, damage to the OWT can

be magnified by the combined effects of scour and earthquake (Zheng et al., 2015). In extreme conditions, the occurrence of both scour and earthquake can exist when: (1) the newly deposited sediments in the scour hole are liquefied or softened during the earthquake; and (2) a large earthquake produces a tsunami-induced scour followed by aftershocks, such as the 2011 Tohoku earthquake (Yim et al., 2014). Scour not only reduces the monopile capacity but also changes the dynamic characteristics of the OWT system. It is, therefore, worthwhile to investigate the scour effects on the seismic responses of monopile-supported OWT that often has no redundancy in the structural system (Myers et al., 2012).

The design of monopile-supported OWTs is mainly dictated by their dynamic characteristics, among which the fundamental frequency is the key (Bhattacharya et al., 2013; Dean, 2010). Generally, the design follows a soft-stiff design rule (DNV, 2014; GL, 2012) such that the fundamental frequency, f_1, of the OWT system falls between the zone of rotor frequency, f_{1P}, and the zone of blade-passing frequency to avoid the resonance (Bhattacharya et al., 2011). This narrow frequency band requires a careful assessment of foundation stiffness over a typical design life of 20-25 years (Carter, 2007). Hence, considering scour is essential as it may shift the fundamental frequency into the f_{1P} resonance range and amplify the structural dynamic responses. Scour around monopile includes general scour (erosion across the seabed) and local scour (development of a scour hole around the pile), which can occur not only in cohesionless soils but also in cohesive soils (Couldrey et al., 2020; Harris and Whitehouse, 2014, 2017; Mueller and Wagner, 2005; Whitehouse, 1998; Whitehouse et al., 2011). The consequence of scour includes removal of soil supports to pile and an increase in over-consolidation ratio (OCR) of the remaining soils that are unloaded due to the removal of overburden (Lin et al., 2014b). That is, scour effects include changes to both seabed geometry around the pile and stress history of the remaining soils, which are anticipated to affect the natural frequency and seismic responses of the OWTs.

At present, only limited research is focused on the responses of OWTs or piles under combined effects of earthquakes and scour, which mostly evaluates the scour process as a general scour. Guan et al. (2019) examined the interaction between the scouring process and monopile vibration in a flume test, where the monopile top was excited by simple harmonic motions. Prendergast et al. (2015) measured variations of the fundamental frequency with general scour depths and evaluated the scour effect on the shift of the fundamental frequency. Jia et al. (2017) analyzed dynamic responses of

bucket-supported OWTs using continuum finite elements (Fes) under combined effects of general scour and one earthquake record. In addition to the full continuum FE analyses, the dynamic-beam-on-nonlinear-Winkler-foundation (DBNWF) method (Boulanger et al., 1999) is often adopted to analyze the combined effects of earthquakes and scour, in which a general scour is simply simulated by removing the *p-y* springs within an estimated maximum scour depth (Abhinav and Saha, 2016; Li et al., 2018; Rezaei et al., 2018; Tempel et al., 2004).

Previous research on the effects of scour-hole dimensions and soil stress history has mainly focused on the static responses of OWTs or piles (Achmus et al., 2010; He et al., 2019; Li et al., 2020; H. Ma et al., 2018; Tseng et al., 2018); however, there is almost no study on their effects on the dynamic responses of OWTs or piles. The evaluation of scour-hole dimensions was highlighted by a recent centrifuge test (Li et al., 2020) to investigate the effects of both local and general scour on the monotonic lateral monopile response. To investigate the lateral response under static wind-wave loads, several studies (Achmus et al., 2010; H. Ma et al., 2018) explicitly modeled three-dimensional local scour using continuum FE method but neglected soil stress-history changes. Contrarily, He et al. (2019) considered and highlighted the effects of soil stress-history changes on the structural responses. Recent studies (Tseng et al., 2018, 2017) adopted the post-scour *p-y* springs (Lin et al., 2014a) to account for the scour-hole dimensions, but no soil stress history was included. Overall, the above literature review indicates two research gaps: (1) lack of understanding of the combined effects of earthquakes and scour where multiple recorded earthquakes are considered, and (2) lack of research on the effects of scour-hole dimensions and soil stress history on seismic responses of OWTs.

This study aimed to propose a simple method for investigating the combined effects of earthquakes and scour on OWTs in soft clays, in which the effects of both scour-hole dimensions and soil stress history were incorporated into the framework of dynamic soil-structure interaction [i.e., DBNWF (Boulanger et al., 1999)]. The proposed processes were encoded into a set of open-source scripts via MATLAB (MATLAB, 2019) and OpenSees (McKenna, 2011) and validated against the existing results. Using this method, 198 nonlinear time-domain parametric analyses were conducted for six crustal earthquake motions. Through the parametric analyses, scour effects including the scour-hole dimensions and soil stress-history changes on the dynamic responses of the monopile-supported OWT in soft clays were illuminated, and some design-related

issues were also discussed.

3.3 Overview of dynamic soil-structure interaction

Dynamic soil-structure interactions essentially include kinematic interaction and inertial interaction. Kinematic interaction is mainly affected by soil movements and soil-pile interface behaviors, while inertial interaction is mainly related to the mass of the superstructure. In general, nonlinear soil behaviors under strong ground motions and soil-pile interface behaviors (e.g., slip, gap, and closure, etc.) represent the essential responses of the entire OWT system. The method of DBNWF is commonly used to evaluate the dynamic soil-structure interaction, where the pile is simplified as a series of massless beams with lumped mass, and soil-pile interactions are represented by a series of uncoupled nonlinear springs in parallel with dashpots.

The governing equation of DBNWF for a pile under lateral dynamic loading can be written as Eq. (3-1), where the pile is discretized into n elements and nodes i=1 to n+1.

$$k_i^{\mathrm{p}}(u_{i+1}-u_i)+k_i^{\mathrm{s}}(u_i-u_{si})+c_i^{\mathrm{p}}(\dot{u}_{i+1}-\dot{u}_i)+c_i^{\mathrm{s}}(\dot{u}_i-\dot{u}_{si})+m_i\left(\ddot{u}_g+\ddot{u}_i\right)=0 \tag{3-1}$$

From Eq. (3-1), pile lateral dynamic responses are dependent on free-field motions (u_{si} and $\dot{u}_{si}$). In nonlinear analyses, k_i^{s} is often evaluated using the p-y curves (Matlock, 1970). Material damping (c_i^{p}), is often simulated using Rayleigh damping, which is proportional to the mass and stiffness. Soil damping (c_i^{s}), includes hysteresis damping and radiation damping, where the latter can be simulated using a linear dashpot in parallel to the elastic component of spring to account for high-frequency energy dissipation. Scour that removes soil supports and changes soil OCRs can affect all the above-mentioned parameters ($\dot{u}_{si}$, u_{si}, k_i^{s}, and c_i^{s}) in Eq. (3-1) and therefore the lateral dynamic responses of piles. Likewise, scour can also affect the vertical dynamic responses of piles.

3.4 Proposed method

The proposed method includes: (1) improvement of DBNWF to consider effects of

both scour-hole dimensions and soil stress history, dubbed modified DBNWF method, and (2) a practical procedure that integrates scour effects into 1D site response analysis to compute post-scour free-field motions. A flowchart of the implementation of the proposed method is shown in Figure 3.1.

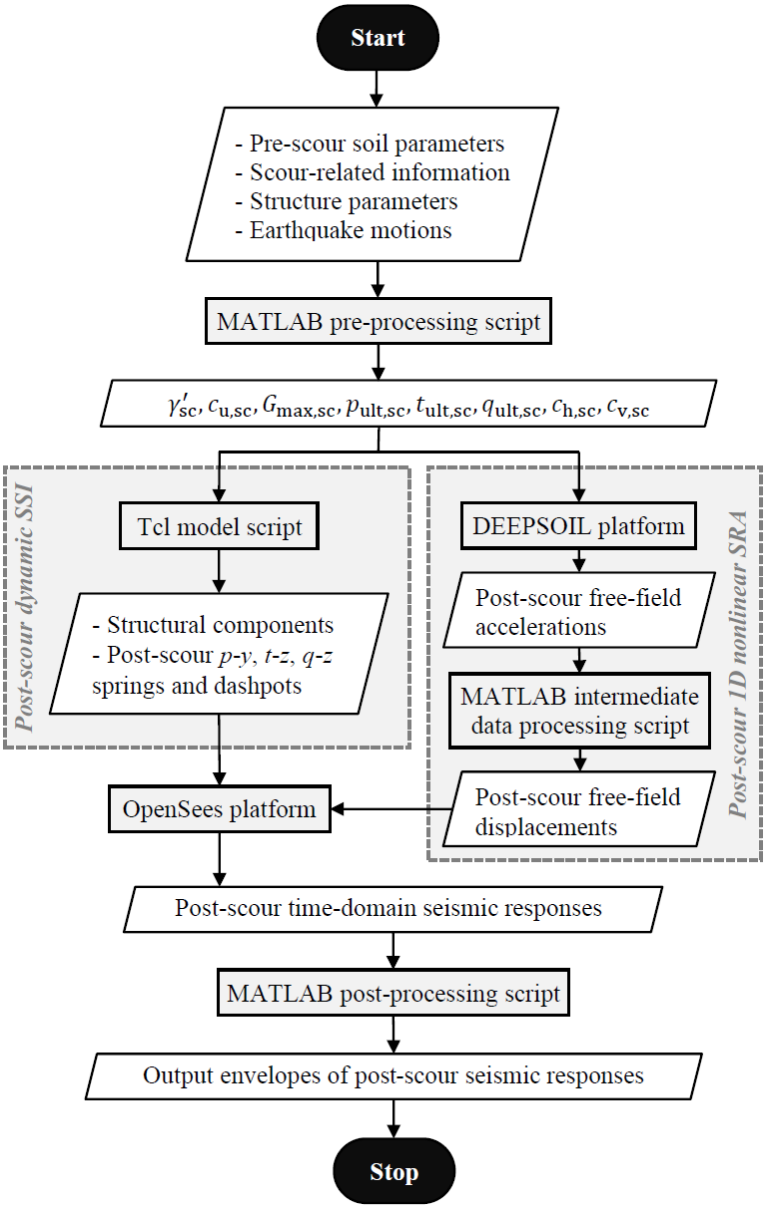

Figure 3.1 Implementation of the proposed approach

3.4.1 Modified DBNWF method

For the pre-scour cases where the seabed is leveled, the horizontal and vertical soil-pile interactions in soft clays are often represented by the Matlock *p-y* springs (Matlock, 1970), API *t-z* and *q-z* springs (API, 2011) and these springs are mainly dependent on

the ultimate resistances. Besides, soil radiation damping is usually simulated by a linear dashpot (i.e., constant damping coefficient) in parallel with the springs (Berger et al., 1977; Gazetas and Dobry, 1984). Therefore, to consider the effects of soil stress history and scour-hole dimensions, post-scour springs and dashpots are determined by modifying the ultimate resistances and radiation damping coefficients, which forms the basis of the modified DBNWF method.

3.4.1.1 Effects of soil stress history on soil parameters

Because scour is an unloading process for the remaining soils, it increases soil OCR and changes other soil properties. To evaluate soil properties after scour, the authors established correlations for effective unit weight between before and after scour (γ' and γ'_{sc}) through changes in void ratio I and overburden, and for undrained shear strength between before and after scour (c_u and $c_{u,sc}$) through OCR according to the critical state soil mechanics (Lin et al., 2014b). That is, post-scour effective unit weight, and undrained shear strength of soft clays are calculated by

$$\gamma'_{sc} = \gamma'(1+e)/[1+e+C_s \log \mathrm{OCR}] \tag{3-2}$$

$$c_{u,sc} = c_u \mathrm{OCR}^{-C_s/C_c} \tag{3-3}$$

$$\mathrm{OCR} = \min\left(\frac{\gamma'\chi}{\gamma'_{sc}\chi_{sc}},\ \mathrm{OCR}_{limit}\right) \tag{3-4}$$

$$\mathrm{OCR}_{limit} = [(1+\sin\phi')/(1-\sin\phi')^2]^{1/\sin\phi'} \tag{3-5}$$

In the equations above, C_c and C_s are compression index and swell index of soil, respectively; χ_{sc} is the depth below the scour-hole bottom. OCR_{limit} is the maximum OCR accounting for the passive failure of soils near the post-scour seabed due to the removal of overburden (Kulhawy and Mayne, 1990; Schofield and Wroth, 1968). Furthermore, soil dynamic properties after scour, such as post-scour maximum shear modulus ($G_{max,sc}$) can be determined by modifying the equation of Hardin and Drnevich (1972).

$$G_{max,sc} = 625(\mathrm{OCR})^{\epsilon}\sqrt{p_a\sigma'_{m,sc}}/\{0.3+0.7[e+C_s \log \mathrm{OCR}]^2\} \tag{3-6}$$

$$\sigma'_{m,sc} = \gamma'_{sc}\chi_{sc}\left[1+2(1-\sin\phi')\mathrm{OCR}^{\sin\phi'}\right]/3 \tag{3-7}$$

For a typical range of scour depth ($1.3D_{op}$-$2.5D_{op}$), the calculated $G_{max,sc}$ of soft clays using Eq. (3-6) was 19.79 Mpa-19.94 Mpa in this study, which is within the range (18.06 Mpa-40.89 Mpa) suggested by Santos (2000), indicating the rationality of Eq. (3-6).

3.4.1.2 Soil-pile interaction analysis considering scour effects

Post-scour soil-pile interactions are evaluated for both axial and lateral dynamic loads through deriving the post-scour springs and dashpots. The effects of both scour-hole dimensions and soil stress history are considered in deriving the post-scour springs and dashpots. The extent of general scour is defined by general scour depth, while that of local scour by scour-hole dimensions as illustrated in Figure 3.2 where the scour hole is idealized as a truncated cone.

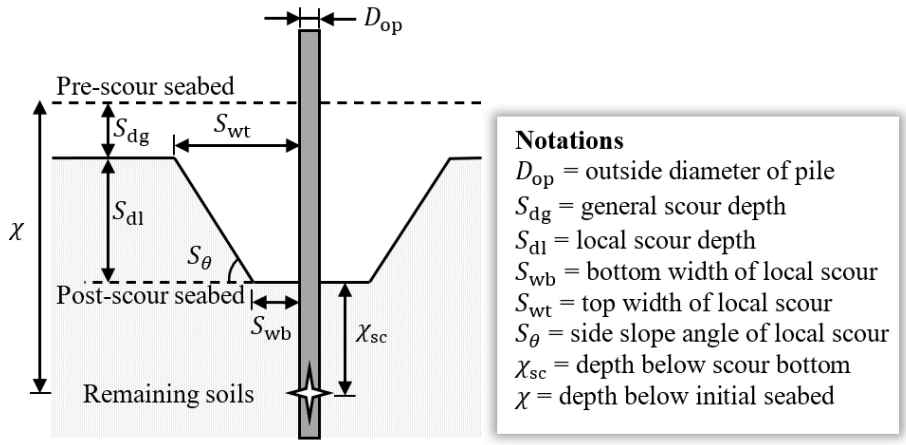

Figure 3.2 General scour and local scour hole at a monopile foundation

3.4.1.2.1 Post-scour vertical springs and dashpots

For the vertical soil-pile interactions, post-scour *t-z* and *q-z* springs are achieved by modifying the ultimate resistances. The ultimate resistance of the *q-z* springs is mainly dependent on the undrained shear strength; therefore, post-scour ultimate resistance of the *q-z* spring was simply given by $q_{ult,sc}=9c_{u,sc}$. However, the ultimate resistance of the *t-z* springs ($t_{ult,sc}$) is related to both undrained shear strength and soil effective stress using Eq. (3-8). To account for scour-hole effects, the remaining soils above post-scour seabed are treated as surcharge load and vertical effective stress of soil surrounding the

pile induced by the surcharge load is calculated using Boussinesq's solution (Lin and Jiang, 2019; Lin and Wu, 2019). To account for the effect of soil stress history, the post-scour soil properties determined in Section 3.4.1.1 are used. Finally, $t_{ult,sc}$ calculated by Eq. (3-8) is substituted into API *t-z* curves (API, 2011) so that the modified *t-z* curves can consider effects of scour-hole dimensions and soil stress history.

$$t_{\mathrm{ult,sc}} = \begin{cases} 0.5\left(c_{\mathrm{u,sc}} p'_{\mathrm{v,sc}}\right)^{0.5} \text{ for } c_{\mathrm{u,sc}} \le p'_{\mathrm{v,sc}} \\ 0.5 {c_{\mathrm{u,sc}}}^{0.75}\left(p'_{\mathrm{v,sc}}\right)^{0.25} \text{ for } c_{\mathrm{u,sc}} > p'_{\mathrm{v,sc}} \end{cases} \text{ and } t_{\mathrm{ult,sc}} \le c_{\mathrm{u,sc}} \quad (3\text{-}8)$$

$$p'_{\mathrm{v,sc}} = \gamma'_{\mathrm{sc}} \chi_{\mathrm{sc}} \left\{ 1 + \tan S_\theta \left[\frac{S_{\mathrm{wt}} + 0.5D_{\mathrm{op}}}{\sqrt{\left(S_{\mathrm{wt}} + 0.5D_{\mathrm{op}}\right)^2 + \chi_{\mathrm{sc}}^2}} - \frac{S_{\mathrm{wb}} + 0.5D_{\mathrm{op}}}{\sqrt{\left(S_{\mathrm{wb}} + 0.5D_{\mathrm{op}}\right)^2 + \chi_{\mathrm{sc}}^2}} \right] \right\} \quad (3\text{-}9)$$

Furthermore, vertical radiation damping after scour is considered by substituting the post-scour vertical damping coefficient given by Eq. (3-10) into the conventional vertical dashpot (Berger et al., 1977).

$$c_{\mathrm{v,sc}} = \Delta\chi\left[2\pi D_{\mathrm{op}} \sqrt{\left(\gamma'_{\mathrm{sc}}/g + \rho_{\mathrm{w}}\right) G_{\mathrm{max,sc}}}\right] \quad (3\text{-}10)$$

3.4.1.2.2 Post-scour lateral springs and dashpots

The post-scour *p-y* curves are developed by substituting the post-scour ultimate soil resistance, $p_{ult,sc}$, into Matlock *p-y* curves (Matlock, 1970). The $p_{ult,sc}$ is determined using Eq. (3-11), in which the effect of scour-hole dimensions is considered using the equivalent depth method (Lin et al., 2016) and the effect of soil stress history post-scour is considered using post-scour soil properties determined in Section 3.4.1.1.

$$p_{\mathrm{ult,sc}} = \min\left[\left(3 + \gamma'_{\mathrm{sc}} \chi_{\mathrm{eq}}/c_{\mathrm{u,sc}} + 0.5\chi_{\mathrm{eq}}/D_{\mathrm{op}}\right) c_{\mathrm{u,sc}} D_{\mathrm{op}},\ 9c_{\mathrm{u,sc}} D_{\mathrm{op}}\right] \quad (3\text{-}11)$$

where the equivalent depth (χ_{eq}) is back-calculated from Eq. (3-12) given the post-scour ultimate soil resistance force, F_{sc}.

$$F_{\mathrm{sc}} = 0.5\gamma'_{\mathrm{sc}} D_{\mathrm{op}} \chi_{\mathrm{eq}}^2 + 2c_{\mathrm{u,sc}} D_{\mathrm{op}} \chi_{\mathrm{eq}} + \sqrt{2} c_{\mathrm{u,sc}} \chi_{\mathrm{eq}}^2 \quad (3\text{-}12)$$

where the F_{sc} is calculated based on the scour-hole slope angle as follows:

$$F_{sc} = \begin{cases} F_0 & (0 < \chi_{sc} \le S_{wb}) \\ F_1 & (S_{wb} < \chi_{sc} \le S_{wb} + \Theta S_{dl}) \\ F_2 & (\chi_{sc} > S_{wb} + \Theta S_{dl}) \end{cases} \quad \text{when } S_\theta < 45° \tag{3-13a}$$

$$F_{sc} = \begin{cases} F_0 & (0 < \chi_{sc} \le S_{wb}) \\ F_2 & (\chi_{sc} > S_{wb}) \end{cases} \quad \text{when } S_\theta \ge 45° \tag{3-13b}$$

$$F_0 = 0.5\gamma'_{sc} D_{op} \chi_{sc}^2 + 2c_{u,sc} D_{op} \chi_{eq} + \sqrt{2} c_{u,sc} \chi_{sc}^2 \tag{3-14a}$$

$$F_1 = 0.5\gamma'_{sc} D_{op} [\chi_{sc}^2 + \Theta(\chi_{sc} - S_{wb})^2] + 2c_{u,sc} D_{op} [\chi_{sc} + \Theta(\chi - S_{wb})] + \sqrt{2} c_{u,sc} [\chi_{sc}^2 + \Theta(\chi_{sc} - S_{wb})^2] \tag{3-14b}$$

$$F_2 = 0.5\gamma'_{sc} D_{op} [(\chi_{sc} + S_{dl})^2 - S_{dl}(S_{wb} + S_{wt})] + 2c_{u,sc} D_{op} (\chi_{sc} + S_{dl}) + \sqrt{2} c_{u,sc} [(\chi_{sc} + S_{dl})^2 - S_{dl}(S_{wb} + S_{wt})] \tag{3-14c}$$

Furthermore, lateral radiation damping after scour is considered by substituting the post-scour lateral damping coefficient given by Eq. (3-15) into the lateral dashpots proposed by Gazetas and Dobry (1984).

$$c_{h,sc} = \Delta\chi \left[4 D_{op} \sqrt{(\gamma'_{sc}/g + \rho_w) G_{max,sc}} \right] \tag{3-15}$$

3.4.2 Site response analysis considering scour effects

Seismic excitation for DBNWF analysis is achieved by applying the free-field displacements to the ends of spring-dashpot elements. The free-field displacements are obtained from the site response analysis (SRA). The earthquake motions recorded on the embedded bedrock/firm soils (i.e., within motion) or on the rock outcrop or firm ground (i.e., outcropping motion) can be input directly to the SRA model. However, if the earthquake motions are recorded on the soft ground, deconvolution is implemented to back-calculate the within motions or the outcropping motions (Kramer, 1996). Once the input earthquake motion (either within motion or outcropping motion) is known, one-dimensional nonlinear SRA is performed to simulate the shear wave propagating upward from the bedrock to the overlying soft clays. From this analysis, the free-field displacement time histories at different depths in soft clays are calculated.

Herein, a practical method is proposed to incorporate the scour effects into the 1D

nonlinear SRA. Scour effects on changes in the soil stress history are considered to be only due to general scour, and those caused by local scour are neglected. The reasons are that local scour is a near-field problem while general scour is a far-field problem. The influence of local scour on the free-field soil properties is considered to be negligible (Meymand, 1998; Shang et al., 2016). The nonlinear SRA employs the general quadratic/hyperbolic (GQ/H) model (Groholski et al., 2016) with the shear strength and damping controls (Afacan et al., 2019; Yee et al., 2013). The GQ/H model uses the reference modulus reduction and damping curves proposed by Darendeli (2001). To account for the effect of soil stress history, scour-induced changes in OCR and post-scour soil parameters are explicitly included in Darendeli's curves. It is worth noting that the post-scour soil parameters used for the 1D site response analysis are calculated only for general scour depth, and therefore in Eqs. (3-2)-(3-7), $\chi_{sc}+S_{dl}$ is replaced by χ_{sc}. Furthermore, the ground surface of the 1D soil column is set at the general scour bottom, and the computed time-domain soil motions are extracted from the pile tip to the scour-hole bottom.

3.4.3 Implementation

The foregoing processes proposed to compute the post-scour soil-pile interactions and free-field displacements are encoded using MATLAB (MATLAB, 2019) and implemented in open-source platforms of OpenSees (McKenna, 2011) and DEEPSOIL (Hashash et al., 2017). Figure 3.1 shows the flowchart of the implementation of the proposed method (the developed codes are provided as supplementary materials). Given the input parameters, a pre-processing MATLAB program developed based on Sections 3.4.1 and 3.4.2 can generate post-scour soil parameters, which are sent to the Tcl script in OpenSees to develop post-scour time-domain dynamic soil-pile interaction (SSI) model and to DEEPSOIL to develop post-scour 1D nonlinear SRA. The post-scour 1D nonlinear SRA produces free-field accelerations, which are processed using a signal processing script in MATLAB and then integrated to generate free-field displacements. The free-field displacements are used as seismic excitations for post-scour dynamic SSI analysis performed in the OpenSees platform. The outcomes of the time-domain SSI analyses are further processed in a post-processing MATLAB program, from which the envelopes of specific responses (e.g., lateral displacement, lateral acceleration, and bending moment, etc.) are extracted.

3.5 Validation

To the best of the authors' knowledge, no experimental data is available for verifying seismic responses of the monopile-supported OWT considering both scour-hole dimensions and soil stress history. Nevertheless, the DBNWF method was extensively validated by comparing the results with the centrifuge test data (Boulanger et al., 1999; Wang et al., 1998) and with the results obtained with continuum elements and sophisticated constitutive models (Kampitsis et al., 2013) under the pre-scour conditions. Besides, the pre-scour DBNWF method has been widely adopted to investigate the seismic responses of the pile-soil-structure system due to its computational efficiency and effectiveness in the analysis of soil-pile interactions (Ghosn et al., 2003; Hochi et al., 2019; Wang et al., 2018, 2013). Furthermore, the *p-y* springs have been improved to consider the scour-hole dimensions and scour-induced stress history changes, which were verified by the authors (Lin et al., 2014b; Lin and Jiang, 2019; Lin and Wu, 2019). Therefore, the validated foregoing models confirm the validity of the proposed method for analysis of the monopile-supported OWTs considering the combined effects of earthquakes and scour.

To ensure the correctness of the scripts (Tcl model script and several MATLAB scripts) used for implementing the proposed method (Figure 3.1), two sets of analyses were conducted. Firstly, a published pre-scour case (Wang et al., 2018) involving eigenvalues for a seismically loaded monopile-supported OWT in soft clays was referenced to verify the developed script of the DBNWF model. Secondly, a published post-scour case (Lin et al., 2016) involving a pile in soft clays subjected to static lateral loads was referenced to verify the developed scripts in accommodating scour effects. Figure 3.3(a) shows the calculated fundamental frequencies of the entire system varied with different undrained shear strength. The calculated values agreed well with the published data (Wang et al., 2018). Figure 3.3(b) shows the calculated pile-top displacement curves varied with scour-hole depths, in which two values (30 kN and 50 kN) of the lateral load applied at the pile top were examined. From Figure 3.3(b), the results of the present study were compared well to Lin et al. (2016) that were obtained based on the 3D continuum finite difference model. Overall, based on the comparisons in Figure 3.3(a) and (b), credence is given to the proposed processes in Figure 3.1.

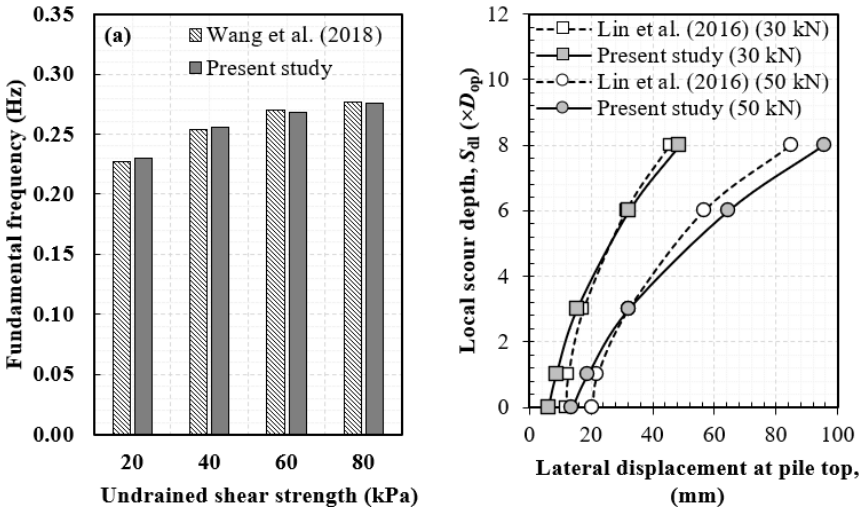

Figure 3.3 Comparisons of (a) fundamental frequencies and (b) lateral pile-top displacements calculated using different methods

3.6 Parametric analyses

To investigate the effects of scour-hole dimensions and soil stress history on the seismic responses of a monopile-supported OWT in soft clays, a 3-MW wind turbine that is often adopted for soft soil conditions (Bhattacharya, 2019; Lombardi et al., 2013; Wang et al., 2018; Zaaijer, 2006) was selected as the case study, as illustrated by Figure 3.4.

The geometric and material properties of the structural components (Wang et al., 2018; Zaaijer, 2006) and the pre-scour soil parameters (Baffer, 2013) used in this study are listed in Table 3.1 and Table 3.2, respectively. The monopile was an open-ended steel pipe pile. It should be noted that the pre-scour embedded length of the monopile was taken as 35 m (or $8.75D_{op}$), which fell in the typical design range of the embedded length ($5D_{op}$-$10D_{op}$) (Gilbert et al., 2015).

Table 3.3 summarizes earthquake motion records corresponding to six different crustal earthquakes. These records were scaled and selected as the bedrock outcropping motions for general cases of analyses (Capraro, 2018; Mo et al., 2017).

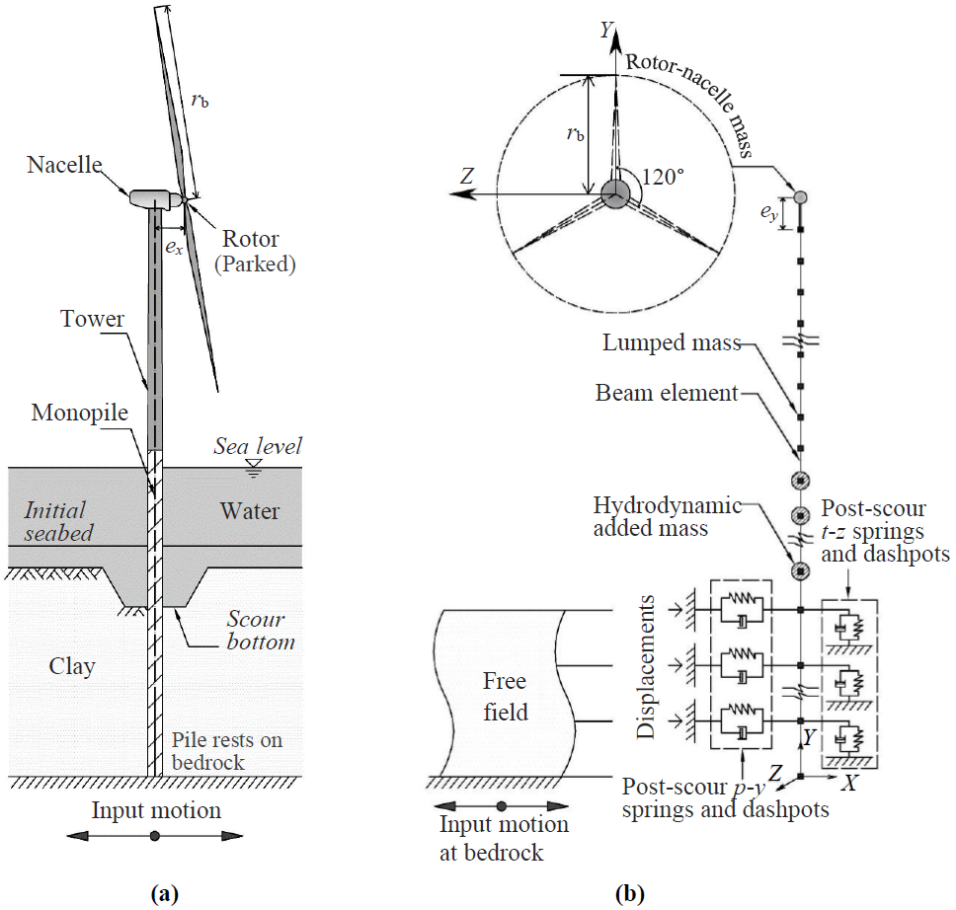

Figure 3.4 The monopile-supported OWT under combined effects of scour and earthquake: (a) physical model and (b) numerical model

Table 3.1 Parameters of structural components

Monopile (Nonlinearity)	Pile length (m)	58
	Pre-scour embedded length (m)	35
	Outside diameter (m)	4
	Wall thickness (m)	0.075
	Poisson's ratio	0.3
	Elastic modulus (Gpa)	210
	Yield strength (Gpa)	0.408
	Mass density (kg/m^3)	8500
Tower (Nonlinearity)	Height (m)	56
	Outside diameter (m)	2.8-3.5
	Wall thickness (m)	0.02-0.075
	Poisson's ratio	0.3
	Elastic modulus (Gpa)	210
	Yield strength (Gpa)	0.408
	Mass density (kg/m^3)	8500
Rotor-nacelle assembly[1]	Height above mean sea level (m)	60
	Rotor diameter (m)	90
	Rotor mass (ton)	41
	Nacelle mass (ton)	70
	Three-blade mass (ton)	19

Note: [1]the rotor diameter and mass, nacelle mass, and blade mass were referenced to the online resource: https://en.wind-turbine-models.com/turbines/603-vestas-v90-3.0.

Table 3.2 Pre-scour soil parameters

Soil property	Value
Effective unit weight (kN/m^3)	6.18
Undrained shear strength/effective vertical stress	0.30
Plasticity index (%)	41
Specific gravity	2.70
Moisture content (%)	68
Void ratio	1.83
Compression index	0.52
Swell index	0.13

Details of earthquake motions are discussed in Section 3.6.2. To evaluate the effects of scour-hole dimensions, 26 scenarios of scour-hole dimensions in Table 3.4 were analyzed with consideration of soil stress history. General scour depth (S_{dg}) was taken as 10% of the local scour depth (Fischenich and Landers, 1999) (i.e., S_{dg}=0.1S_{dl}). Note that in design practice, the typical scour-hoe dimensions used are: S_{wb}=0, S_{θ}=30°, and S_{dl}=1.3D_{op}-2.5D_{op} (API, 2011; DNV, 2014; GL, 2012; Whitehouse, 1998). In our analysis, the maximum local scour depth was taken as 3.0D_{op}, which is larger than 2.5D_{op}. The use of a larger upper-bound scour depth was to consider effects of potential extreme weather conditions (e.g., hurricanes), uncertainty of scour-depth measurement and prediction, and turbine vibration that all can contribute to additional scour depth. The post-scour embedded length of the monopile investigated in the study ranged from 5.45D_{op} to 8.2D_{op} when S_{dl}=0.5D_{op}-3.0D_{op}. In the special case where S_{wb}=∞ or S_{θ}=0°, a local scour turned into a general scour. To evaluate the effect of soil stress history, seven more cases with scour-hole dimensions of S_{wb}=0, S_{θ}=30° and S_{dl}=0.5D_{op}-3.0D_{op} were analyzed without consideration of the changes in soil stress history. One earthquake motion was used for 33 cases of analyses, and therefore, for six earthquake motions, a total of 198 cases were analyzed in this study.

Table 3.3 Information about bedrock input motions

Earthquake event	Moment magnitude	Mechanism	Record sequence number	Component	Significant duration (s)
Chalfant Valley-02, 1986	6.19	Strike slip	549	180	12.55
Loma Prieta, 1989	6.93	Reverse oblique	779	000	10.18
Landers, 1992	7.28	Strike slip	832	090	25.20
Northridge, 1994	6.69	Reverse	1042	270	16.02
Kobe,1995	6.90	Strike slip	1111	000	9.59
Chi-Chi, 1999	7.62	Reverse oblique	1521	089	24.86

Table 3.4 Summary of parametric analyses on scour effects

Investigated factor	S_{dl} (×D_{op})	S_{wb} (×D_{op})	S_{θ} (°)	Embedded length of monopile (×D_{op})
Effect of scour depth	0, 0.5, 1.3, 1.5, 2.0, 2.5, 3.0	0	30	8.75, 8.20, 7.32, 7.10, 6.55, 6.00, 5.45
Effect of side slope angle	1.5	0	10, 20, 30, 40, 50, 60	7.10
Effect of bottom width	1.5	0, 0.5, 1.0, 1.5, 2.0 2.5, 3.0	30	7.10
Effect of simplified scour condition	0, 0.5, 1.3, 1.5, 2.0, 2.5, 3.0	0, ∞	0, 30	8.75, 8.20, 7.32, 7.10, 6.55, 6.00, 5.45

To demonstrate the effect of soil stress history on soil parameters as discussed in Section 3.4.1.1, the post-scour soil properties at S_{dl}=1.5D_{op} were calculated and presented in Table 3.5. By comparing submerged unit weight, undrained shear strength, and maximum shear modulus before and after scour, it is apparent that the soil stress-history effects were significant at shallower soil depths but were minor at greater depths.

Table 3.5 Initial and post-scour soil parameters (S_{dg}=0.1S_{dl}, S_{dl}=1.5D_{op})

χ_{sc} (×D_{op})	OCR	γ' (kN/m^3)	γ'_{sc} (kN/m^3)	c_u (kPa)	$c_{u,sc}$ (kPa)	G_{max} (Mpa)	$G_{max,sc}$ (Mpa)
0.06	27.33	5.99	5.62	12.32	5.39	13.32	8.58
0.19	10.29	5.99	5.73	13.21	7.38	13.79	10.07
0.44	4.94	5.99	5.81	15.00	10.07	14.70	11.75
1.06	2.61	5.99	5.88	19.48	15.33	16.75	14.58
1.56	2.09	5.99	5.91	23.07	19.19	18.23	16.36
2.06	1.82	5.99	5.92	26.65	22.93	19.59	17.93
3.05	1.55	5.99	5.94	33.82	30.29	22.07	20.67
4.05	1.42	5.99	5.95	40.99	37.57	24.29	23.06
5.04	1.33	5.99	5.96	48.16	44.80	26.33	25.22
6.04	1.28	5.99	5.96	55.32	52.02	28.22	27.20
7.04	1.24	5.99	5.97	62.49	59.22	30.00	29.04

3.6.1 Numerical model

Rotor-nacelle assembly (RNA) in a parked state was modeled by the translational and rotational masses atop the tower. This simplified approach can effectively incorporate the moment of inertia of the blades [Eqs. (3-16)-(3-18)]. For more details about this approach, the reader can refer to De Risi et al. (2018) and Ali et al. (2020).

$$I_x = m_b r_b^2 \tag{3-16}$$

$$I_y = 0.5 m_b r_b^2 + 3 m_b e_x^2 \tag{3-17}$$

$$I_z = 0.5m_b r_b^2 + 3m_b e_x^2 \quad (3\text{-}18)$$

The eccentricity (e_x) between the centroids of rotor and nacelle was taken as 3 m here (i.e., half of the 6 m-long nacelle perfectly aligned with the axis of the tower) (De Risi et al., 2018).

According to Passon et al. (2015) and Arany et al. (2017), the tubular tower and monopile were modeled as the nonlinear displacement-based beam elements with three-dimensional fiber sections. Three translational degrees of freedom (DOFs) and three rotational DOFs were designated to beam-element nodes. At the pile tip, the monopile was assumed to rest on the bedrock in the parametric study, in which the interface between the bedrock and the pile tip was assumed to be frictionless. Similar pile-tip condition is used by others for numerical analyses and centrifuge tests (D. H. Kim et al., 2014; Wang et al., 2018; Yu et al., 2015). In this case, the pile tip was restrained in the vertical movement but free in horizontal movement. The tower, which is tapered, was discretized into small elements with different sized cross-sections. The co-rotational formulation was used for the coordinate transformation in OpenSees to capture potential global instability of the structure (De Risi et al., 2018). At the soil-pile interface, the interface element involved a pair of three-DOF nodes sharing identical coordinates: master (i.e., soil) node and slave (i.e., pile) node. The slave nodes were initially free at the vertical DOF in the gravity analysis, while slave and master nodes were in equal DOFs during the seismic analysis. The energy dissipation of the OWT system corresponding to the hysteresis behaviors was simulated using Rayleigh damping (De Risi et al., 2018). It generally results from aerodynamic damping, hydrodynamic damping, structural damping, and soil material damping (DNV, 2014), and a total damping ratio of 3% was adopted for a parked turbine (Ali et al., 2020; Bhattacharya, 2019; De Risi et al., 2018).

Besides the dynamic soil-pile interactions, the effects of hydrodynamic loading were considered for a horizontally vibrating monopile in water. Interactions with seawater outside and inside of a monopile produce a longer structural fundamental period and hydrodynamic pressures on the monopile due to the inertial effect of water (Liaw and Chopra, 1974). Monopile-water interactions are often simulated by hydrodynamic added masses distributed on the submerged pile in conventional dynamic analyses (Goyal and Chopra, 1989a, 1989b). Hence, the lateral nodal mass of the submerged monopile contained buoyant material mass and hydrodynamic added

mass. The outside and inside added mass functions were written as

$$m_{\mathrm{a}}^{\mathrm{o}}(h_{\mathrm{s}}) = \rho_{\mathrm{w}}\pi r D_{\mathrm{op}}^2 \left[\frac{8h_{\mathrm{o}}}{\pi^2 D_{\mathrm{op}}}\sum_{m=1}^{\infty}\frac{(-1)^{m-1}}{(2m-1)^2}\frac{K_1(\alpha_m D_{\mathrm{op}}/2h_{\mathrm{o}})}{K_0(\alpha_m D_{\mathrm{op}}/2h_{\mathrm{o}})+K_2(\alpha_m D_{\mathrm{op}}/2h_{\mathrm{o}})}\cos(\alpha_m h_{\mathrm{s}}/h_{\mathrm{o}})\right] \tag{3-19a}$$

$$m_{\mathrm{a}}^{\mathrm{i}}(h_{\mathrm{s}}) = \rho_{\mathrm{w}}\pi r_{\mathrm{ip}}^2 \left[\frac{16h_{\mathrm{i}}}{\pi^2 r_{\mathrm{ip}}}\sum_{m=1}^{\infty}\frac{(-1)^{m-1}}{(2m-1)^2}\frac{I_1(\alpha_m r_{\mathrm{ip}}/h_{\mathrm{i}})}{I_0(\alpha_m r_{\mathrm{ip}}/h_{\mathrm{i}})+I_2(\alpha_m r_{\mathrm{ip}}/h_{\mathrm{i}})}\cos(\alpha_m h_{\mathrm{s}}/h_{\mathrm{I}})\right] \tag{3-19b}$$

The added mass to monopile was obtained through multiplying $m_{\mathrm{a}}^{\mathrm{o}}(h_{\mathrm{s}})$ and $m_{\mathrm{a}}^{\mathrm{i}}(h_{\mathrm{s}})$ at node *I* by the tributary length. It should be noted that Eqs. (3-19a) and (3-19b) were derived assuming a leveled seabed. Because the horizontal extent of a scour hole is relatively small, the inertia effect of water in the scour hole on the monopile is negligible; therefore, no $m_{\mathrm{a}}^{\mathrm{o}}(h_{\mathrm{s}})$ was added to the pile within the local scour zone. The model assumed that the soil was fully plugged inside the monopile below the seabed according to Liu et al. (2009) and the water surface inside the monopile was set at the mean sea level.

In the nonlinear site response analysis, the GQ/H model fitting procedure for the modulus reduction curves was conducted for shear strains up to 0.3% (Groholski et al., 2016). Meanwhile, the fitting of damping ratios was conducted for all available levels of shear strains (Phillips and Hashash, 2009). Besides, unit weight and shear wave velocity of the firm ground were taken as 21.58 kN/m^3 (Uthayakumar and Naesgaard, 2004) and 760 m/s (NRCC, 2015), respectively.

3.6.2 Earthquake motions

Figure 3.5 plots the acceleration time histories and Fourier spectra of the six input earthquake motions. The acceleration time histories were scaled to a peak bedrock acceleration (PBA) of 0.5g and then input as bedrock outcropping motions in DEEPSOIL to calculate free-field motions (Bhattacharya, 2019; NRCC, 2015). Scaling of the amplitude to PBA=0.5g is generally consistent to previous studies regarding the seismic design of the OWT (Mo et al., 2017; Wang et al., 2018; Yang et al., 2019a, 2019b; Yu et al., 2015; Zhu et al., 2020).

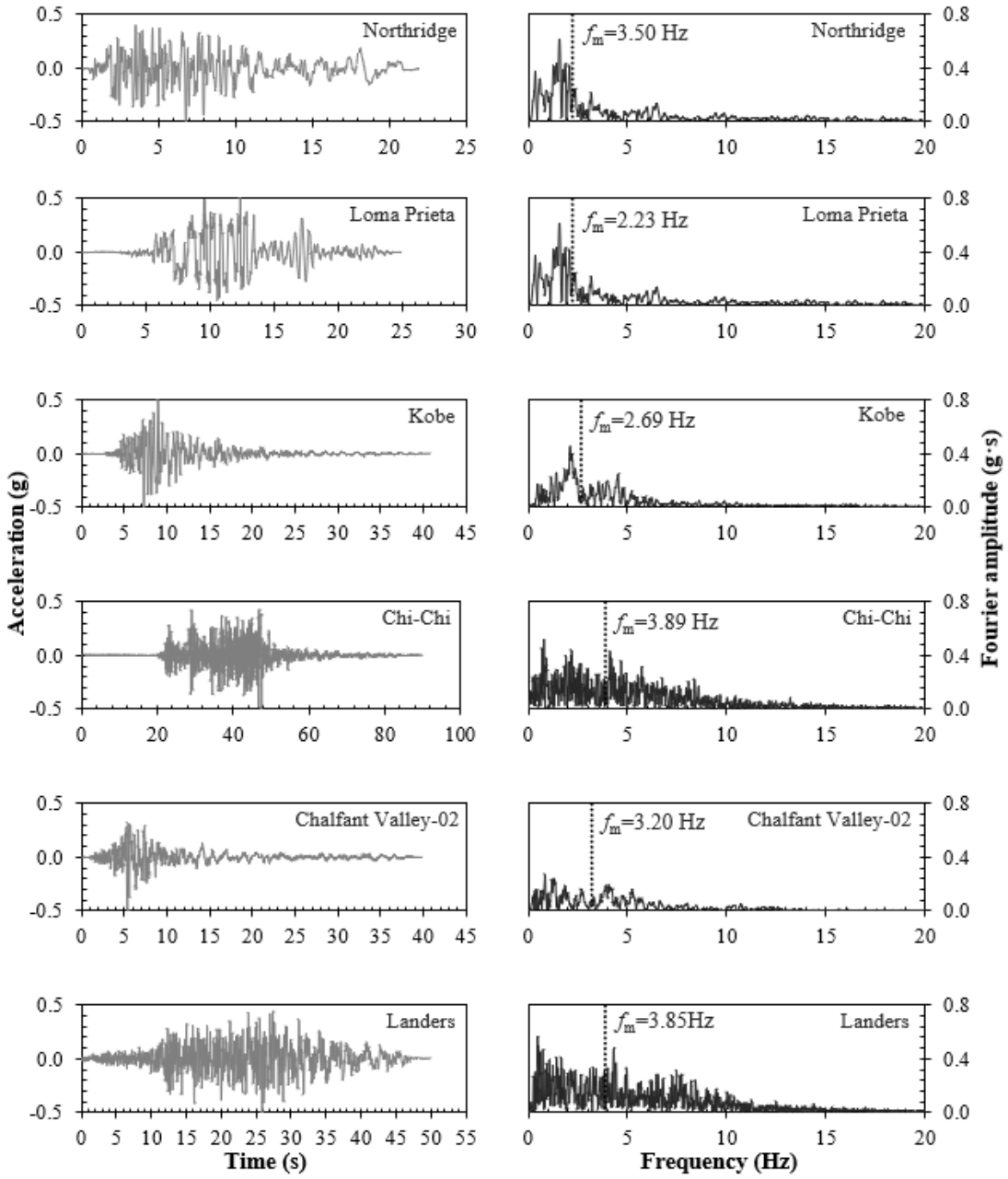

Figure 3.5 Accelerograms (left column) and Fourier spectra (right column) of the six earthquake motions

Furthermore, since 2005 the National Building Code of Canada requires increasing PBA from 0.23g to 0.5g for the seismically active area (e.g., Fraser River delta) (Uthayakumar and Naesgaard, 2004). It also reflects more severe shaking conditions that are important for evaluation as most of the existing turbines are relatively newly constructed and sparsely distributed and have not experienced critical shaking (Bhattacharya, 2019; De Risi et al., 2018; Myers et al., 2012). The use of amplitude scaling instead of spectral matching was to reveal the inherent variabilities of the

earthquake records. Therefore, it is anticipated that the computed seismic responses corresponding to these six motions would exhibit certain variations besides some general trends. Figure 3.5 also shows that the mean square frequency (f_m) of these records (Rathje et al., 1998) ranged between 2.23 Hz and 3.89 Hz, indicating intermediate/low-frequency contents (Di Laora and de Sanctis, 2013). In comparison, the frequency range of interest for a 3-MW OWT system is 0.16-2.07 Hz (0.5-6.7 times the fundamental frequency of OWT with the fundamental frequency being 0.31 Hz) (NRCC, 2015). The difference in the frequency range between soils and OWT in pre-scour conditions confirms that the scaled earthquake motions would be appropriate for use in the seismic analyses.

3.7 Results and discussion

Prior to presenting the results of scour effects on seismic responses of the OWT, the scour-induced changes in the free-field motions shown in Figure S3.1-Figure S3.8 (supplementary figures) are first discussed here. In Figure S3.1-Figure S3.8, the normalized free-field acceleration is a ratio of the maximum free-field acceleration to the peak bedrock acceleration of 0.5g. From these figures, the maximum free-field acceleration decreased as the soil depth decreased. The attenuation of acceleration at the shallower depth was due to smaller shear strength and modulus of soils near the ground surface that constrained the increase of shear stress. This effect was found to be more significant in soft clays subjected to strong bedrock motions (Garala and Madabhushi, 2019; Idriss, 1991; D. H. Kim et al., 2014; Zhou et al., 2017). Figure S3.9 shows profiles of the mean normalized accelerations obtained at different scour depths, indicating that scour did not significantly affect the propagation of seismic waves in comparison with the pre-scour condition. In other words, scour effects on variations of free-field motions were similar under different scoured levels.

Subsequently, the post-scour seismic responses of the OWT system, including the lateral displacement, lateral acceleration, and bending moment under different scour-hole dimensions are presented in a normalized form with respect to the respective pre-scour seismic responses using the following three steps:

(1) Determine maximum time-domain responses at different locations of the structure (e.g., Figure 3.6) and plot them as the response envelopes (e.g., Figure 3.7).

(2) Determine the maximum responses of the monopile at the seabed level, the

cantilever and embedded parts of the pile, the tops of the tower and monopile from the response envelopes.

(3) Determine the normalized responses by dividing the maximum post-scour response by the corresponding pre-scour value, and thus a normalized response greater than one represents an amplification effect due to scour and vice versa.

To demonstrate the foregoing steps, the results from the 1989 Loma Prieta earthquake are presented and discussed as representative results of the six crustal earthquakes. For the convenience of discussions, the post-scour case with $S_{wb}=\infty$ or $S_{\theta}=0°$ is referred to as the simplified scour condition while the post-scour case with $S_{wb}=0$ and $S_{\theta}=30°$ as the standard scour condition. Figure 3.6(a) and (b) depict the lateral displacement time histories at the tower top and monopile top under the standard scour condition where $S_{dl}=1.5D_{op}$.

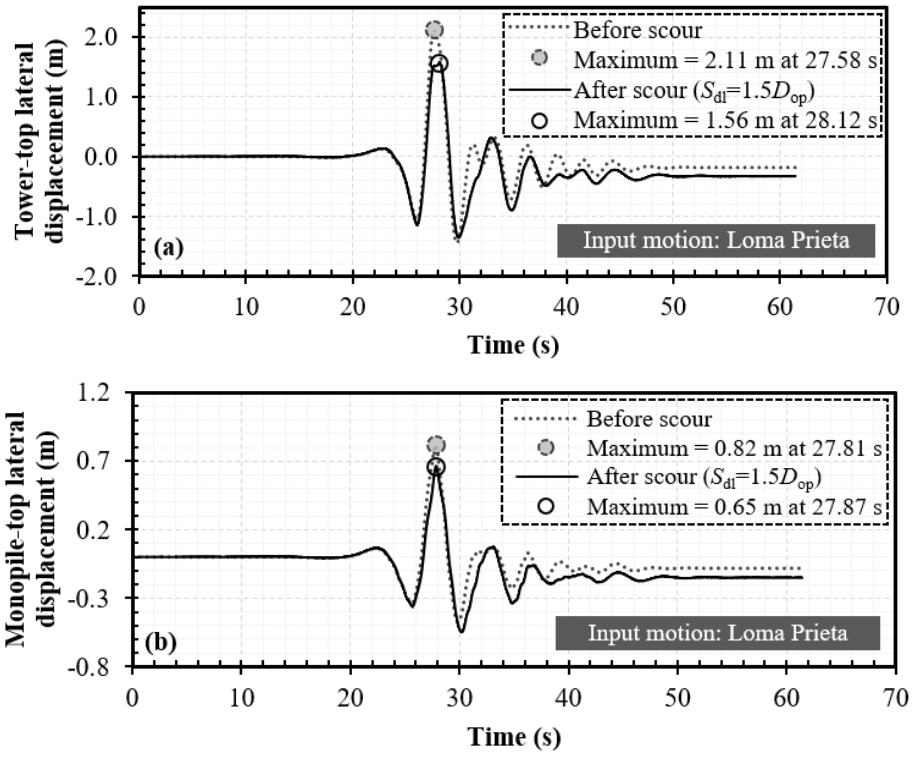

Figure 3.6 Pre-scour and post-scour ($S_{dl}=1.5D_{op}$, $S_{wb}=0$, $S_{\theta}=30°$) lateral displacements of (a) tower top and (b) monopile top

In comparison to pre-scour cases, scouring increased the permanent (residual) lateral displacements by 46% and 45% at the tower top and the pile top, respectively but decreased the maximum lateral displacements by 26% and 20%, respectively. Likewise, these maximum time-domain responses before and after scour could be

determined for other locations of the OWT system.

The plots of these maximum responses along length of tower and pile formed the response envelopes in Figure 3.7, where one pre-scour and two post-scour cases (simplified and standard scour conditions) were included.

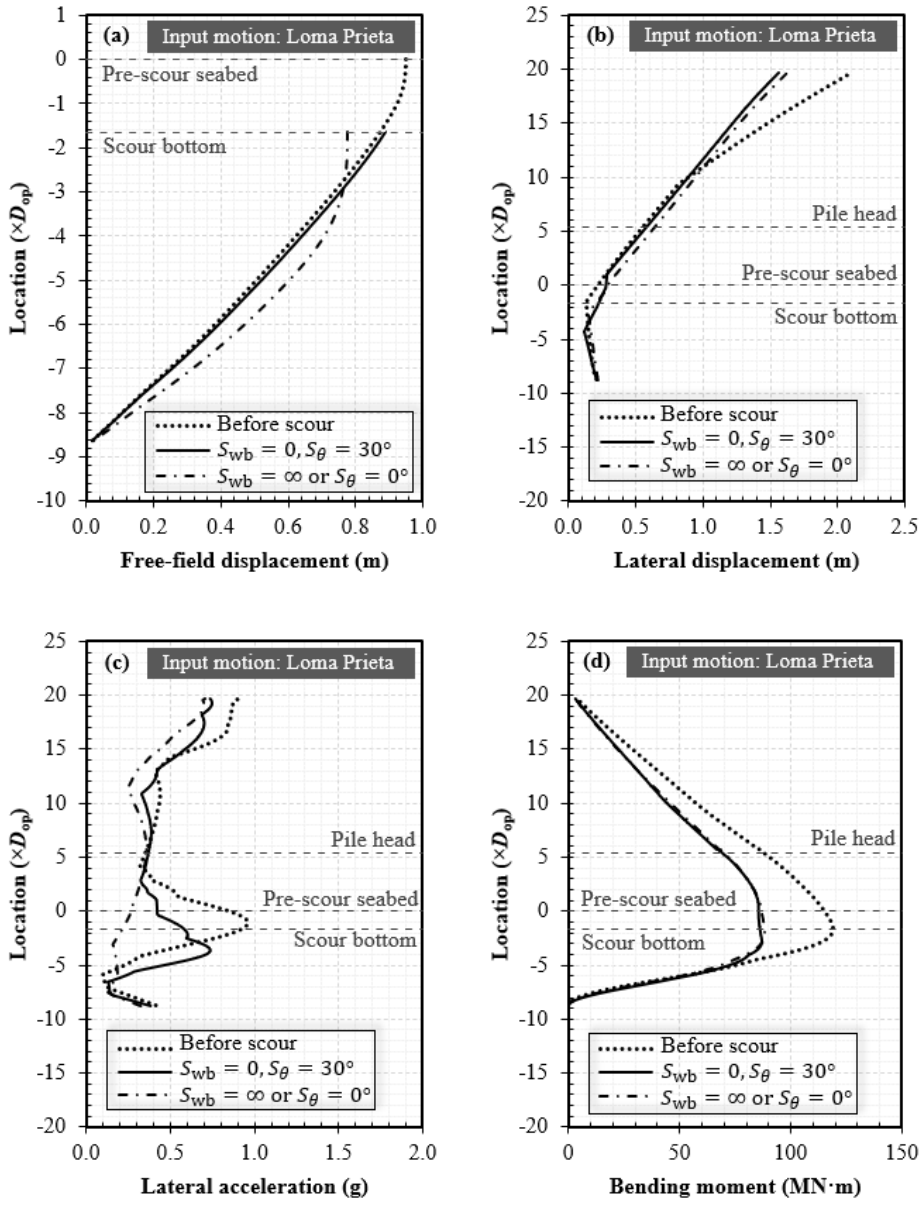

Figure 3.7 Pre-scour and post-scour (S_{dl}=1.5D_{op}) response envelopes: (a) free-field displacement and structural (b) displacement, (c) acceleration, and (d) bending moment

Figure 3.7(a) shows that the maximum free-field displacements of soils at the local scour bottom decreased by 11% under the simplified scour condition but slightly increased by 2% under the standard scour condition. Figure 3.7(b) shows the maximum

lateral displacements at the tower top decreased by 25% under both simplified and standard scour conditions. Figure 3.7(c) reveals relatively minor differences in the lateral acceleration envelopes above the pile head but greater differences below it. This indicates that the dynamic response of tower was more affected by the inertial effect; however, both kinematic and inertial effects were evident on the monopile, particularly at the seabed level. Besides, Figure 3.7(d) indicates the maximum bending moments decreased by up to 26% under both simplified and standard scour conditions.

Based on the response envelopes, normalized maximum responses at selected locations are presented. The normalized maximum responses were then plotted against different scour depth, scour bottom width, and scour-hole slope angle to investigate the effects of scour-hole dimensions. Moreover, the normalized maximum responses obtained under simplified and standard scour conditions were compared to assess the effect of simplifying local scour as general scour. Lastly, the cases considering and ignoring the changes to soil stress history were analyzed to evaluate the effect of soil stress history.

3.7.1 Effects of scour-hole depth

3.7.1.1 Variations of natural frequencies against scour depths

As shown in Figure 3.8(a), natural frequencies of the OWT system (f_n) decreased as S_{dl} increased due to a slenderer system. Compared with the pre-scour values (i.e., S_{dl}=0), the first fore-aft bending mode of natural frequency (f_1) decreased by 12%-30% when S_{dl}=1.3D_{op}-2.5D_{op}. This amount of frequency reduction was greater than that in sands (6%-9% when S_{dl}=1.3D_{op}-2.5D_{op}) (Li et al., 2018; Prendergast et al., 2015; Tseng et al., 2018), indicating that the increase of S_{dl} in soft clays is more likely to shift f_1 into the range of the rotor frequency of the turbine (f_{1P}), causing resonance. In this study, post-scour f_1 values (0.25-0.20 Hz) fell into the typical f_{1P} range of 0.14-0.30 Hz (Bhattacharya et al., 2011) when S_{dl}=0.5D_{op}-3.0D_{op}.

Figure 3.8(b) shows f_n normalized to the site characteristic frequency (0.73-0.75 Hz when S_{dl} increased from 0 to 3.0D_{op}) (Kramer, 1996). The normalized frequencies of the second and third bending modes tended to approach one as S_{dl} increased, while f_1 shifted away from the site characteristic frequency. This result confirms that the higher-mode contribution should be considered in the total dynamic responses for

slender structures (Chopra, 2011; De Risi et al., 2018; Yang et al., 2019a).

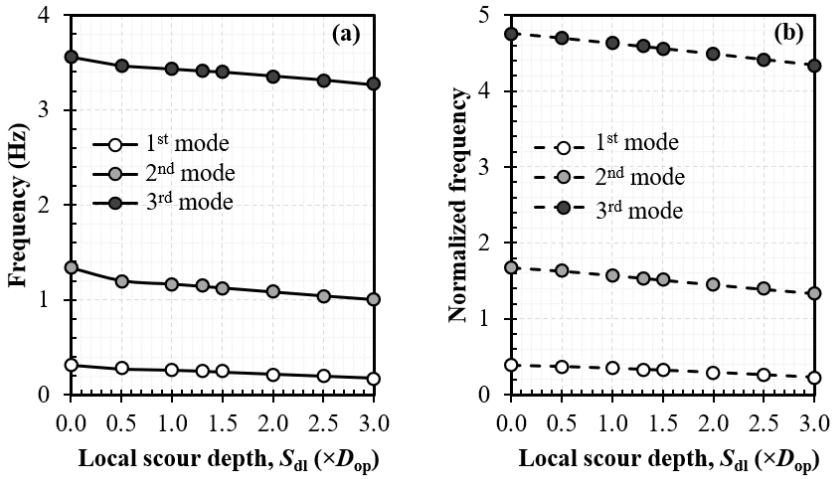

Figure 3.8 (a) Natural frequencies and (b) normalized natural frequencies under various local scour depths

3.7.1.2. Variations of maximum responses against scour depths

Figure 3.9 shows the normalized maximum lateral accelerations of the monopile at the post-scour seabed level and that of the tower under various scour depths. The maximum acceleration of the tower showed a smaller dispersion than those of the monopile at the post-scour seabed because the former was mainly affected by the inertial effect although under different kinematic inputs, as indicated by Figure 3.7. In Figure 3.9(a), the maximum acceleration of the monopile at the seabed on average increased by up to 14% as S_{dl} increased to $1.5D_{op}$, followed by a gradual decrease by up to 16% as S_{dl} reached $3.0D_{op}$. The peak amplification generally occurred at S_{dl}=$1.0D_{op}$-$1.5D_{op}$ with a maximum increase of 67%, which might be due to the contribution of the higher modes as previously discussed with Figure 3.8(b). Contrarily, the maximum acceleration of the tower (occurred at the tower top) in general monotonically decreased with the increased S_{dl} as shown in Figure 3.9(b).

Figure 3.10 (a) and (b) show the normalized maximum lateral displacements of the monopile and tower, which were found to occur at the pile top and tower top, respectively. The maximum pile-top displacement on average decreased by 42% when S_{dl} increased to $3.0D_{op}$, although that from the Chi-Chi earthquake exhibited a slight amplification when S_{dl}=$2.0D_{op}$, which might be attributed to greater significant duration of the Chi-Chi earthquake motion. Likewise, as shown in Figure 3.10(b), increasing

scour depth generally decreased the maximum tower-top displacement by 15%-33% when S_{dl}=1.3D_{op}-2.5D_{op}. In all, the maximum displacement after scour was lower than that before scour, showing a beneficial effect of scour on the tower lateral displacement under seismic loading.

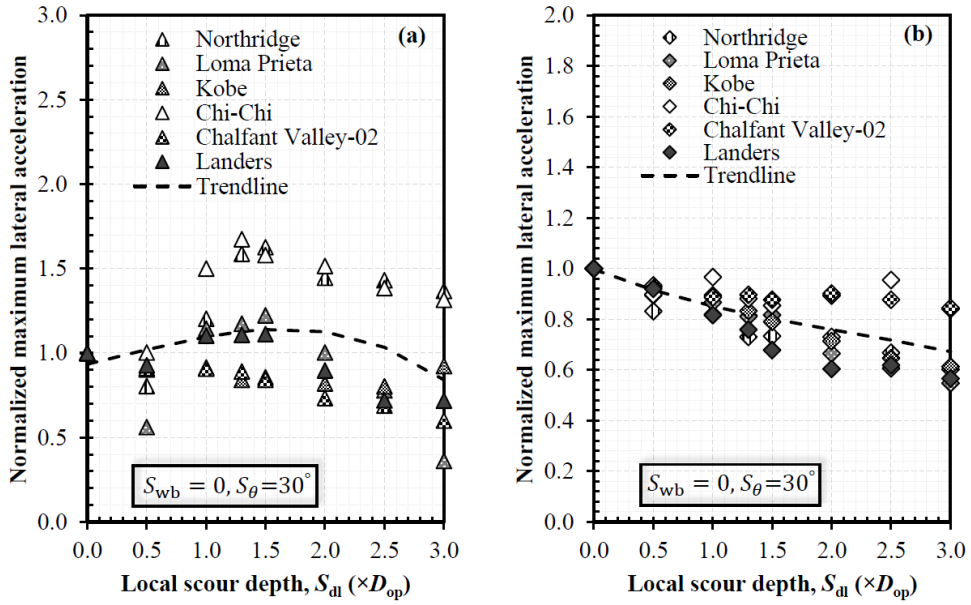

Figure 3.9 Normalized maximum lateral accelerations of (a) monopile at post-scour seabed level and (b) tower under various local scour depths

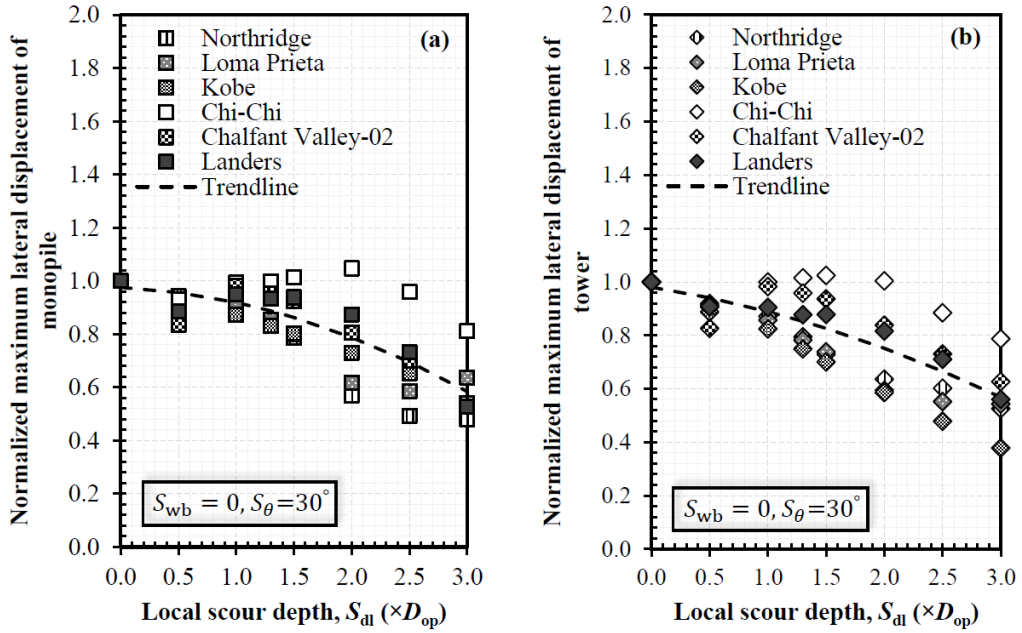

Figure 3.10 Normalized maximum lateral displacements of (a) monopile and (b) tower under various local scour depths

The normalized maximum bending moments of the monopile below and above the post-scour seabed were plotted in Figure 3.11(a) and (b), respectively. The former decreased almost linearly with S_{dl} and the decrease was up to 51% when S_{dl} increased from 0 to 3.0D_{op}. This result also demonstrates a beneficial scour effect on the decrease in the maximum bending moment of the embedded monopile. Likewise, the maximum bending moment of the cantilever part of monopile generally decreased by 17%-38% when S_{dl}=1.3D_{op}-2.5D_{op}. Based on the results from Figure 3.9 to Figure 3.11, application of an overestimated S_{dl} value (which often occurs in design practice) in the OWT design against scour could cause unconservative estimates of the seismic demand. Similar results were also observed by Ghosn et al. (2003) in their study of a pile-supported bridge.

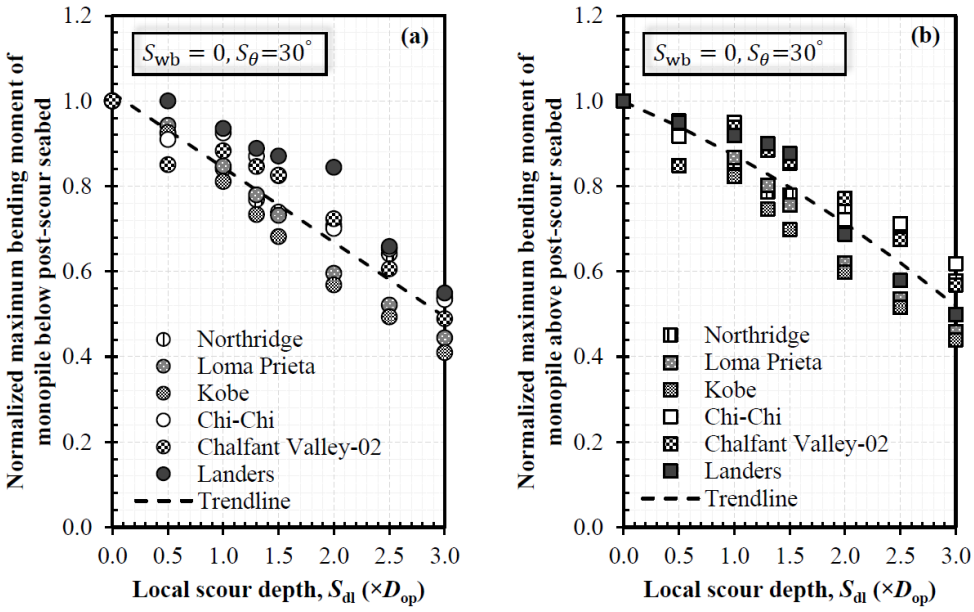

Figure 3.11 Normalized maximum bending moments of (a) the embedded part and (b) the cantilever part of the monopile under various local scour depths

3.7.2 Effects of scour-hole slope angle

To evaluate effects of scour-hole slope angle, a range of S_θ=10°-60° was considered, which covered a typical range of S_θ observed in the field (Butch, 1996) and used in practice (Arneson et al., 2012; Whitehouse, 1998). The effects of scour-hole slope angle on the normalized maximum responses were found to be minor when S_θ=10°-60°. Therefore, only two representative results including the maximum lateral displacement of the tower and the maximum bending moment of the monopile under different S_θ are

discussed herein. As shown in Figure 3.12(a), the maximum tower displacement decreased by 11% as S_θ decreased from 60° to 10°. It indicates that an enlarged scour hole could decrease the maximum tower-top displacement.

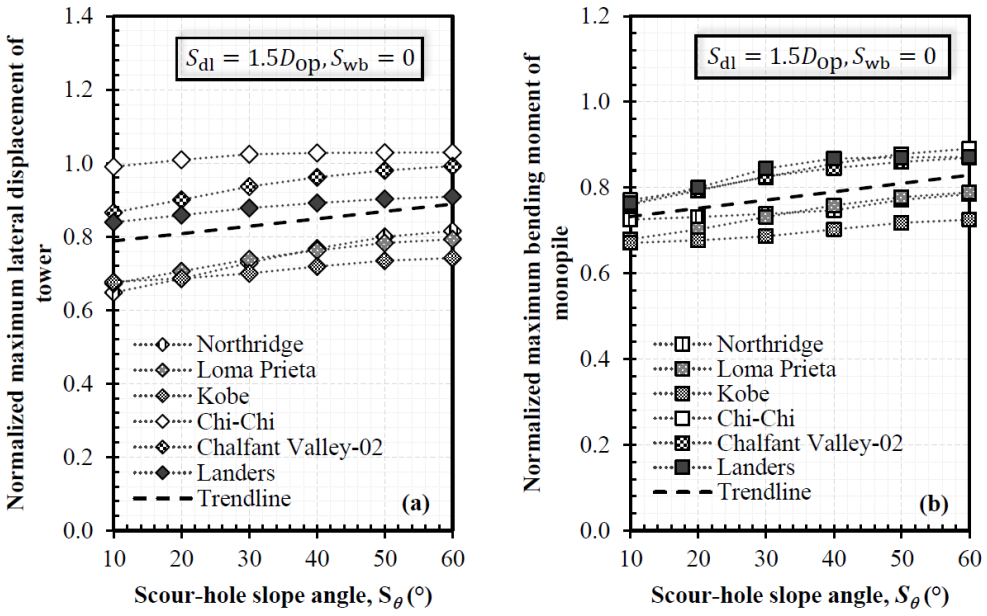

Figure 3.12 Effects of scour-hole slope angle on normalized maximum responses: (a) tower lateral displacement and (b) monopile bending moment

Likewise, Figure 3.12(b) shows that the maximum pile bending moment averagely decreased by 12% when S_θ decreased from 60° to 10°. The above results indicate that the use of an underestimated S_θ value in the dynamic analysis could underestimate the seismic demand. Overall, the effects of scour-hole slope angle on the seismic responses of OWT were relatively small and the relationship was in general linear. The results obtained at S_θ=30° deviated less than 7% from the results obtained from the range of S_θ=10°-60°. Therefore, from this perspective, it would be reasonable to adopt S_θ=30° for a design purpose.

3.7.3 Effects of scour-hole bottom width

In general, effects of scour-hole bottom width on the maximum tower displacement and pile bending moment were less noticeable than those of the scour-hole slope angle. Two representative results including the maximum lateral displacement of the tower and the maximum bending moment of the monopile when S_{wb}=0-3.0D_{op} are discussed. The upper bound of S_{wb}=3.0D_{op} was used as a larger value showed no effect on the pile

lateral responses under static loads (Lin et al., 2016). Figure 3.13(a) and (b) show the normalized maximum displacement of the tower and the normalized maximum bending moment of the monopile under different S_{wb}.

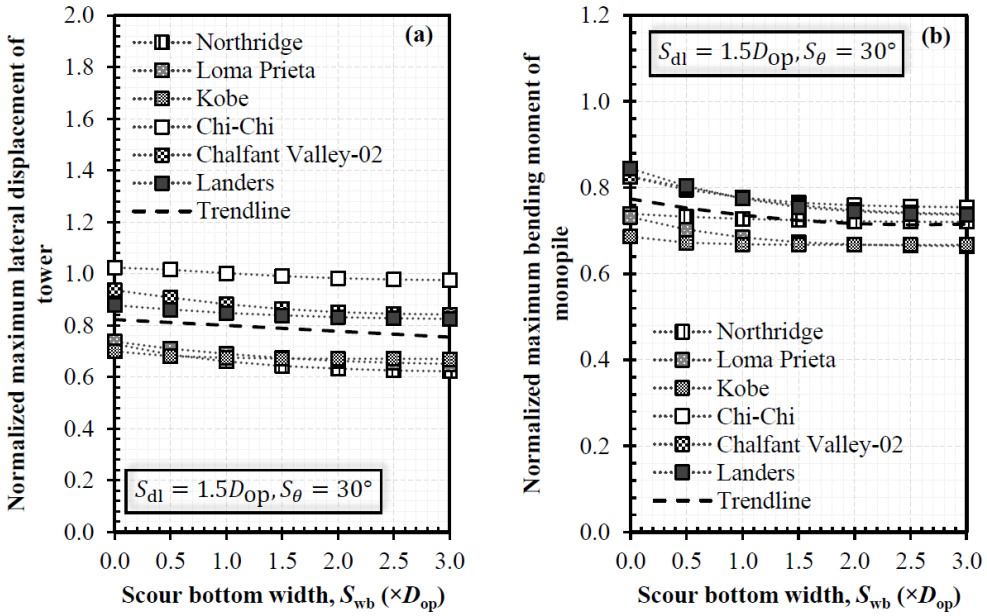

Figure 3.13 Effects of scour-hole bottom width on normalized maximum responses: (a) tower lateral displacement; (b) monopile bending moment

In general, the threshold value of S_{wb} was found to be $1.5D_{op}$ under the seismic excitations, above which the normalized maximum responses exhibited minor changes. This value is smaller than that (S_{wb}=$3.0D_{op}$) obtained at the static loads (Lin et al., 2016). In Figure 3.13(a), the maximum tower displacement generally decreased by 8% when S_{wb} increased from zero to $3.0D_{op}$, indicating that the increase in S_{wb} reduced the maximum tower displacement occurring at the tower top. Furthermore, as shown in Figure 3.13(b), the maximum pile bending moment decreased by 7% when S_{wb} increased from zero to $3.0D_{op}$. Overall, since the changes in S_{wb} had a trivial effect on the seismic responses, it would be appropriate to choose S_{wb}=0 for a seismic analysis, as it is used in design practice.

3.7.4 Effects of simplifying local scour as general scour

Effects of simplifying local scour as general scour were evaluated by comparing the results between simplified scour condition (i.e., S_θ=0° or S_{wb}=∞) and standard scour condition (i.e., S_θ=30° and S_{wb}=0). As mentioned previously, the simplified scour

condition corresponds to simplifying a local scour as a general scour. Scour depth including S_{dg}=0.1S_{dl} and S_{dl}=0-3.0D_{op} was used. To quantify the effects, ratios of responses obtained from the simplified scour condition to those from the standard scour condition were used. Therefore, a ratio greater than one represents an overestimate by using the simplified scour condition and vice versa.

3.7.4.1 Effects on natural frequencies

Figure 3.14 shows the normalized natural frequencies under various scour depths. Overall, the simplified condition caused small effects on the natural frequencies. Compared with the standard scour condition, simplified scour condition led to underestimation of f_1, f_2, and f_3 by 8%, 5%, an 7%, respectively when S_{dl} increased to 3.0D_{op}.

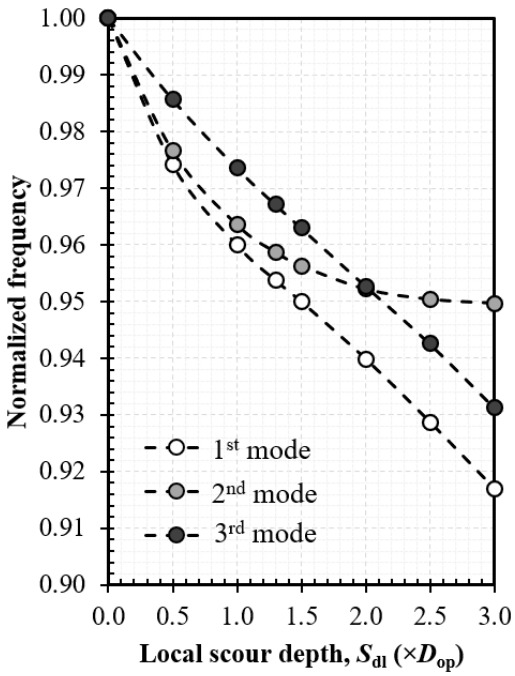

Figure 3.14 Effects of simplified scour condition on normalized natural frequencies (simplified vs. standard scour condition)

3.7.4.2 Effects on the maximum responses

Figure 3.15(a) exhibits ratios of the maximum tower accelerations between the simplified and standard scour conditions, where the solid line represents the mean trend. It depicts that as S_{dl} increased, the normalized acceleration in general increased while the results were more dispersed. Simplified scour condition resulted in negligible differences in the maximum tower acceleration as compared with the standard scour

condition when $S_{dl} \leq 1.0D_{op}$ but the difference became more evident when $S_{dl} \geq 1.3D_{op}$. Overall, simplifying local scour as general scour overestimated the maximum tower acceleration by up to 15%. Figure 3.15(b) shows the negligible effect on the maximum bending moment resulting from the simplified scour condition, with slight overestimation by 3%-8% when $S_{dl}=0.5D_{op}$-$1.3D_{op}$. The variation of data in each box essentially resulted from the inherent variations of the ground motions (e.g., frequency contents, durations, etc.), and this dispersion generally became more significant (i.e., larger interquartile range) as S_{dl} increased.

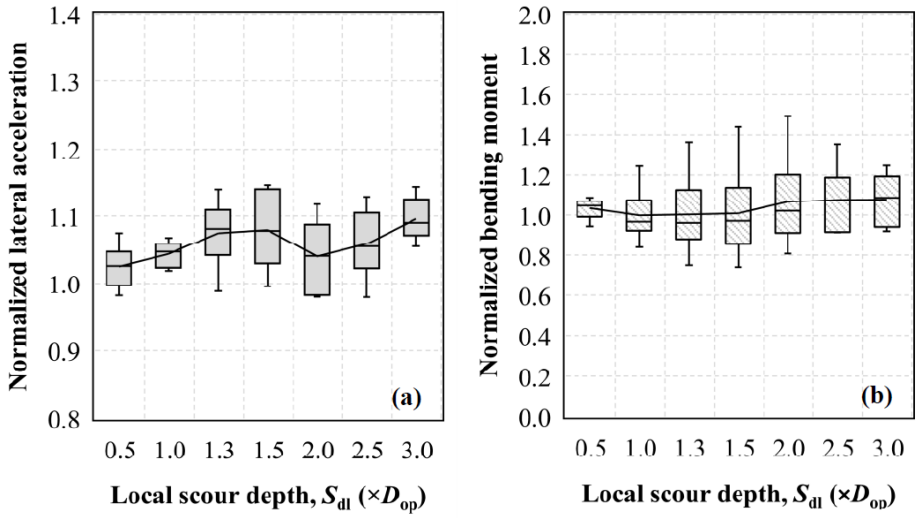

Figure 3.15 Effects of simplified scour condition on normalized maximum responses (simplified vs. standard scour condition): (a) tower lateral acceleration and (b) monopile bending moment

3.7.5 Effects of soil stress history

In Sections 3.7.1-3.7.4, the effects of scour-hole dimensions and simplified scour condition were examined, in which soil stress history was considered. To quantify the effect of soil stress history, scour-induced soil stress history was intentionally ignored in this section so that the results obtained by considering and ignoring the soil stress history could be compared. Ignoring the stress-history changes was evaluated using the pre-scour parameters in Table 3.2, which involved no OCR. A ratio of calculated results between ignoring and considering soil stress history was defined and the ratio greater than one means an overestimate by ignoring soil stress history and vice versa.

3.7.5.1 Effects on natural frequencies

Ignoring soil stress history overestimated f_1 by 4%-8% while f_2 and f_3 by approximately 2% when S_{dl}=1.3D_{op}-2.5D_{op}. This indicates that the effect of soil stress history was more evident on the lower-mode natural frequency than on the higher-mode natural frequency, although this effect was small in general.

3.7.5.2 Effects on the maximum responses

Figure 3.16(a) and (b) respectively show the normalized maximum pile-top displacement and maximum bending moment of the embedded part of the monopile under various S_{dl}. A higher normalized value indicates a more appreciable effect of ignoring soil stress history on the monopile responses. The mean trend of the normalized values indicates that ignoring soil stress history overestimated the maximum pile-top displacement by 7%-16% when S_{dl}=1.5D_{op}-3.0D_{op}.

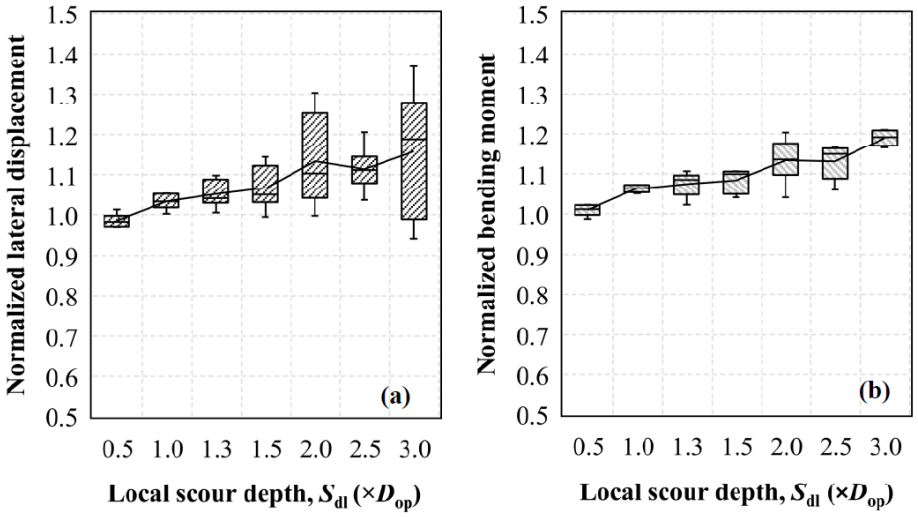

Figure 3.16 Effects of soil stress history on normalized maximum responses (ignoring vs. considering stress history): (a) lateral displacement of monopile top and (b) bending moment of embedded monopile

Similarly, ignoring soil stress history averagely overestimated the maximum bending moment of the embedded monopile by 8%-19% when S_{dl}=1.5D_{op}-3.0D_{op}. These results are different from those obtained under static loads. It is reported that under static loads, lateral pile-head displacement and the maximum bending moment of monopile were underestimated by up to 49% and 7%, respectively when the soil stress history was ignored (He et al., 2019; Lin et al., 2014b).

3.8 Conclusions

This study proposed a new method to incorporate the scour-hole dimensions and scour-induced changes in soil stress history into the framework of dynamic soil-structure interactions. The proposed processes were encoded into a set of open-source scripts to analyze the post-scour seismic responses of the monopile-supported OWTs in soft clays. A total of 198 parametric analyses for an OWT system were performed by varying scour-hole dimensions and soil stress-history effects under six crustal earthquake motions. The following conclusions were obtained from this study:

(1) The natural frequencies and seismic responses of the soil-monopile-tower-RNA system (i.e., OWT system) were primarily affected by the scour depth and secondarily by the scour-hole slope angle and bottom width. The first-mode fundamental frequency (f_1) of the OWT system could descend to the turbine rotor frequency range (f_{1P}), causing resonance when the local scour depth (S_{dl}) was $0.5D_{op}$-$3.0D_{op}$ and the corresponding embedded length of the monopile was $5.45D_{op}$-$8.20D_{op}$. Higher modes of fundamental frequencies (f_2 and f_3) should also be evaluated in the OWT design against scour due to the increasing slenderness of the OWT system.

(2) Increase in scour depth caused consistent decrease in the maximum bending moment of the monopile above and below the seabed. Use of an overestimated scour depth (i.e., $S_{dl} \geq 1.5D_{op}$) in the OWT design against scour caused unconservative design, as it underestimated the maximum lateral acceleration and displacement of the tower, and the maximum lateral displacement and bending moment of the monopile.

(3) Standard scour condition (S_θ=30° and S_{wb}=0) was found to be appropriate for use in seismic design analyses. Nevertheless, simplified scour condition (i.e., S_{wb}=∞ or S_θ=0°) underestimated the fundamental frequency of the OWT system but in general overestimated the maximum lateral acceleration of the tower and the maximum bending moment of the pile.

(4) Ignoring the scour-induced change in the soil stress history overestimated the fundamental frequency of the OWT system, the maximum lateral displacement of the pile top, and the maximum bending moment of the pile below the post-scour seabed.

3.9 Notation

c_i^{p} = damping coefficient of the pile at node i

c_i^{s} = damping coefficient of soil at node i

C_s = swell index of soil

C_c = compression index of soil

c_u = undrained shear strength of soil

$c_{u,sc}$ = post-scour undrained shear strength of soil

$c_{h,sc}$ = post-scour horizontal radiation damping coefficient

$c_{v,sc}$ = post-scour vertical radiation damping coefficient

D_{op} = outside diameter of monopile

e = void ratio of soil

e_x = distance between the centroids of rotor and nacelle, taken as 3 m in this study

e_y = distance between rotor centroid and tower top, taken as 2 m in this study

F_{sc} = post-scour ultimate soil resistance in force units

F_0 = post-scour ultimate soil resistance force when $0 < \chi_{sc} \leq S_{wb}$

F_1 = post-scour ultimate soil resistance force when $S_{wb} < \chi_{sc} \leq S_{wb}+\Theta S_{dl}$ and $S_\theta < 45°$

F_2 = post-scour ultimate soil resistance force when $\chi_{sc} > S_{wb}+\Theta S_{dl}$ and $S_\theta < 45°$ or when $\chi_{sc} > S_{wb}$ and $S_\theta \geq 45°$

f_m = mean square frequency of an acceleration time history

f_n = natural frequency corresponding to the n^{th} (n=1, 2, 3) bending mode of the integrated soil-pile-tower-turbine system

f_{1P} = rotor frequency of the turbine

f_{3P} = blade-passing frequency of the turbine, taken as $3f_{1P}$ for a three-blade turbine

G_{max} = maximum shear modulus of soil

$G_{max,sc}$ = post-scour maximum shear modulus of soil

G_s = specific gravity of soil solids

g = gravitational acceleration

h_o = water depth outside monopile

h_I = water depth inside monopile

h_s = distance between the seabed and pile node of interest

I_x, I_y, I_z= moment of inertia of three blades applied to the centroid of the RNA with respect to X, Y, and Z axis, respectively

I_n = modified Bessel function of order n (n=0, 1, 2) of the first kind

k_i^{p} = lateral stiffness of pile element at node *i*

k_i^{s} = lateral stiffness of soil at node *i*

K_n = modified Bessel function of order *n* (*n*=0, 1, 2) of the second kind

$m_{\mathrm{a}}^{\mathrm{o}}$ = outside added mass per unit length of a pile

$m_{\mathrm{a}}^{\mathrm{I}}$ = inside added mass per unit length of a pile

m_{b} = mass of a blade

m_i = lumped mass of node *i*

OCR = overconsolidation ratio of soil

$\mathrm{OCR}_{\mathrm{limit}}$ = upper-bound value of OCR

p = lateral soil resistance per unit length of a pile

$p_{\mathrm{ult,sc}}$ = post-scour ultimate lateral soil resistance per unit length of a pile

p_{a} = atmospheric pressure, usually taken as 101.325 kPa

PI = plasticity index of soil

q = unit end bearing in stress units

$q_{\mathrm{ult,sc}}$ = post-scour ultimate end bearing in stress units

r_{b} = length of a blade

r_{ip} = inside radius of monopile

S_{dg} = general scour depth

S_{dl} = depth of local scour

S_{wb} = bottom width of local scour hole

S_{wt} = top width of local scour hole, $S_{\mathrm{wt}} = S_{\mathrm{wb}}+S_{\mathrm{dl}}/\tan S_{\theta}$

S_{θ} = side slope angle of local scour hole

t = unit shaft friction in stress units

$t_{\mathrm{ult,sc}}$ = post-scour ultimate shaft friction in stress units

u_i = lateral pile displacement at node *i*

u_{si} = lateral displacement of free-field soil at node *i*

$\dot{u}_{si}$ = lateral velocity of free-field soil at node *i*

$\dot{u}_i$ = lateral pile velocity at node *i*

$\ddot{u}_i$ = lateral pile acceleration at node *i*

$\ddot{u}_g$ = lateral acceleration of bedrock motion

y = lateral soil displacement

z = vertical soil displacement

α_m = dimensionless factor, taken as $(2m\text{-}1)\pi/2$ with *m* being an integer ranging from one to infinity

γ' = effective unit weight of soil

γ'_{sc} = post-scour effective unit weight of soil

$\Delta\chi$ = pile element size

ϵ = a constant value hinging on the plasticity index of soil, taken as 0.31 herein

Θ = dimensionless parameter dependent on scour-hole slope angle, $\Theta = \tan S_\theta/(1-\tan S_\theta)$

ρ_w = mass density of water

$\sigma'_{m,sc}$ = post-scour mean principal effective stress

ϕ' = effective friction angle of clay under the drained condition

χ = soil depth below pre-scour seabed

χ_{sc} = soil depth below the local scour bottom

χ_{eq}= equivalent soil depth to consider local scour hole

Chapter 4 Scour Effects on Lateral Responses of Pile Groups in Sands

4.1 Abstract

For pile-supported structures, scour is a major threat as it removes soils around foundations and causes structural damages. Scour effects on the performance of the pile foundation have been well studied. However, most of these studies are focused on lateral responses of single piles, while very limited research is focused on lateral responses of pile groups. Therefore, prevailing design standards only recommend scour design procedures for single piles. Here, we proposed an improved analytical method (IAM) to analyze laterally loaded pile groups considering various scour-hole dimensions. The IAM was validated against the results of 3D finite element (FE) models calibrated against a full-scale load test. A series of parametric analyses were conducted to investigate the effects of scour-hole depth, scour-hole slope angle, sand relative density, pile spacing, number of piles, and pile group configuration on both post-scour vertical effective stresses and lateral responses of pile groups. Based on the IAM, a simple practical approach called the influence depth method (IDM) was also developed for use in routine design. The feasibility of applying the standard methods for the scoured pile groups was evaluated by comparing them with the 3D FE analyses and the proposed methods (IAM and IDM).

4.2 Introduction

Scour is a process of soil removal caused by waves, currents, and ship propeller jets, etc. (Chin et al., 1996; Whitehouse, 1998), which decreases the soil resistance to the foundation. It is a major cause for intolerable stresses in offshore structures (Watson, 1974) and bridge collapse worldwide (Briaud, 2015; Coleman and Melville, 2001; Liang et al., 2017; Mueller and Wagner, 2005; Zhang et al., 2015). Scour includes general scour that causes a uniform decrease in mudline elevation across a riverbed or a seabed and local scour that causes a localized decrease in mudline elevation, primarily located at piles. For a pile group, local scour can be further classified into global scour (shallow wide depression across the pile group) and localized pit (steep-sided pits

located at individual piles). In the past decades, the mechanisms and characteristics of scour at pile groups in different flow conditions have been extensively investigated by flume tests (Amini et al., 2012; Ataie-Ashtiani and Beheshti, 2006; Ji et al., 2018; Lança et al., 2013; Liang et al., 2017; L. Ma et al., 2018; Ni et al., 2021; Sheppard, 2003; Solaimani et al., 2017; Sumer et al., 2005; Sumer and Fredsøe, 1998; Wang et al., 2016; Yagci et al., 2017; Yifan Yang et al., 2020; Yilin Yang et al., 2020) and field surveys (Bayram and Larson, 2000; Palmer, 1969; Sun et al., 2007). Moreover, numerical simulations based on computational fluid dynamics are adopted to investigate complex flow structures in different pile groups (Hamidi and Siadatmousavi, 2018; H. S. Kim et al., 2014; Liang et al., 2019; C. Wang et al., 2017; Q. Zhang et al., 2017). As indicated by these studies, scour at a pile group is rather complicated compared to that at a single isolated pile due to hydraulic group effects, and a greater detailed review of the scour-hole characteristics of pile group is presented in Section 4.3.

Currently, there is no generally accepted practical approach for determining pile vertical or lateral capacity under local scour conditions, probably due to uncertainty in characterizing sizes and shapes of scour holes at piles or pile groups, and lack of considering scour-induced changes in soil stress history (Lin and Wu, 2019). In design practices, estimation of vertical effective stress of soils around piles is required before calculation of pile capacities. However, the prevailing standards such as American Petroleum Institute (API, 2011), U.S. Federal Highway Administration-Drilled Shaft (FWHA-DS) (Brown et al., 2010) and Driven Pile (FHWA-DP) (Patrick et al., 2016) specify inconsistent approaches to computing the vertical effective stress under local-scour conditions, termed as post-scour vertical effective stress. The different calculations of post-scour vertical effective stress would lead to a discrepancy of the calculated pile axial or lateral capacity and thus confuse practicing engineers when designing pile foundations against scour damage. To improve the standard methods, both closed-form solutions derived from Boussinesq's solution (Lin and Jiang, 2019; Lin and Wu, 2019) and numerical solution using Mindlin's solution (H. Zhang et al., 2017) are developed to estimate the post-scour vertical effective stress, which are further used to calculate the axial or lateral capacity of scoured single piles. The drawbacks of these solutions and standard methods (API, FWHA-DS, and FHWA-DP) are that they are recommended only for single piles. However, piles are commonly installed in groups rather than single piles, and scour effects are more severe in pile groups than single piles as a result of the double group effect (Lin and Lin, 2020):

geotechnical group effect that reduces the pile capacity of individual piles in a group as compared with the single isolated piles and hydraulic group effect that intensifies the flow in a pile group as compared with a single isolated pile. Despite its importance, research concerning the capacities of scoured pile groups is highly scarce. For example, as of this writing, there are only one experimental study and two numerical studies reported on the investigation into the local scour effects on the behavior of pile groups. Liang et al. (2020) investigated the seismic responses of the pile group using centrifuge tests, in which only two scour-hole dimensions and one pile group configuration were examined and no static loading was concerned. Lin and Lin (2020) and H. Ma et al. (2018) employed 3D continuum finite element method (FEM) to investigate laterally loaded pile groups under local-scour conditions, which enabled evaluating a wider range of scour-hole dimensions and pile group configurations than model tests.

In practice, none of 3D FEM, centrifuge test, or shake table test is widely used in routine design and analysis. Therefore, it necessitates efforts to develop a simple and practical method for evaluating post-scour vertical effective stress and behavior of a pile group under local-scour conditions. Lin and Lin (2020) initiate such an effort by extending the solution for a scoured single pile (Lin and Wu, 2019) to that for a scoured pile group; however, this method involves several simplifications such as assuming a square pile group, assuming equal soil vertical effective stresses between individual piles in a group, and ignoring the effect of soil-pile interface friction on the change in post-scour vertical effective stress. These assumptions lead to an unnecessarily conservative estimate of the lateral capacity of the pile group and an incorrect prediction of the pile group response to scour-hole slope angle.

The objectives of this study are threefold. Firstly, we proposed a rigorous analytical solution for calculating post-scour vertical effective stresses for pile groups, which overcomes the limitations of Lin and Lin (2020) that is simply extended from the solution for scoured single piles. The proposed solution for post-scour vertical effective stress was further integrated into the existing *p*-*y* curve framework to form a new method for the lateral behavior of pile groups under local-scour conditions. This proposed process is called the improved analytical method (IAM). A MATLAB program (attached as a supplementary file) was developed to implement the proposed IAM. It was validated against 3D FE analyses whose baseline model (i.e., unscoured condition) was calibrated against a full-scale load test reported in the literature. With the IAM, 288 parametric analyses were performed to elucidate the effects of scour-hole

depth, scour-hole slope angle, soil relative density, pile spacing, number of piles, and pile group configuration on lateral responses of pile groups. The second objective of this study was to assess the suitability for applying the standard methods to analyze the laterally loaded pile groups under local-scour conditions. Note that although the standard methods are developed only for scoured single piles, they may be mistakenly used for scoured pile groups as no corresponding specifications are available for scoured pile groups. Lastly, drawing on the IAM, we proposed a simple and practical approach, called the influence depth method (IDM) for practicing engineers to analyze laterally loaded pile groups under local-scour conditions.

This paper starts with a synthesis of an extensive literature review on the characteristics of the scour hole at the pile group and the existing methods for analyzing the post-scour vertical effective stresses and lateral responses of group piles, followed by the development and validation of the proposed methods (IAM and IDM). After that, the results of parametric analyses are presented, in which the standard methods are critically assessed, and some design-related issues are discussed.

4.3 Review of scour-hole dimensions at a pile group

In contrast to scour at a single isolated pile, scour at a pile group is influenced by pile group conditions and hydraulic conditions. The hydraulic mechanism involves not only downflow, horseshoe vortices, and wake vortices that are common to the single isolated pile, but also the hydraulic group effect that is unique to the pile group. In general, the hydraulic group effect includes reinforcement, sheltering, shed vortices, and jetting effects (Hannah, 1978; Hosseini and Amini, 2015) that are dependent on the flow skew angle, α_f, center-to-center pile spacing, s, and pile group configuration ($m \times n$, where m and n are the numbers of piles in-line with and normal to the lateral load direction, respectively). Most of the past studies focused on scour characteristics considering different pile group configurations (e.g., square, rectangular, and circular shapes) with various pile numbers and pile spacings (Amini et al., 2012; Ataie-Ashtiani and Beheshti, 2006; Bayram and Larson, 2000; Ji et al., 2018; Lança et al., 2013; Liang et al., 2017; Ni et al., 2021; Sheppard, 2003; Solaimani et al., 2017; Sumer et al., 2005; Sumer and Fredsøe, 1998; Wang et al., 2016; Yagci et al., 2017; Yifan Yang et al., 2020; Yilin Yang et al., 2020). Thereinto, the effects of hydraulic conditions including Froude number (Yilin Yang et al., 2020), Keulegan-Carpenter number (Sumer and Fredsøe,

1998; Yifan Yang et al., 2020), and flow direction (Lança et al., 2013; L. Ma et al., 2018; Sheppard, 2003; Sun et al., 2007; Yifan Yang et al., 2020) were also examined. Besides, Sumer et al. (2007) investigated the effect of relative density of soil on the time scale and depth of scour. Overall, under the given flow condition scour pattern is highly governed by pile spacing according to these flume tests and field surveys. For example, Amini et al. (2012) presented four photographs to exhibit the shapes of local scour at pile groups ($m \times n$=5×3) with different spacings (s/D=1, 2, 3.5, and 5). As summarized in Table 4.1, the scouring process at a pile group behaves like that at a single isolated pile when s=1D-1.15D (D = pile diameter) due to the negligible flow-pile interaction in the zero or narrow pile spacing.

Table 4.1 Effects of pile spacing on types of local scour at pile groups

Type	Reference	Flow condition	Lower-bound pile spacing[1]	Critical pile spacing[2]	Upper-bound pile spacing[3]
Field survey	Bayram and Larson (2000)	Wave dominated	N/A	5.5	N/A
Flume test	Solaimani et al. (2017)	Clear-water steady current	N/A	3	N/A
	Wang et al. (2016)		1	N/A	12
	Lança et al. (2013)	Clear-water steady current	1	3-4.5	6
	Amini et al. (2012)		1	3.5	N/A
	Ataie-Ashtiani and Beheshti (2006)	Live-bed wave	1.15	3.5	5
	Sumer and Fredsøe (1998)		1	2-4	N/A

Note: [1]pile spacing below which pile-group scour forms like a scour at an integrated single pile; [2]critical pile spacing below which pile-group scour is governed by a single global scour hole; [3]pile spacing above which there is no interaction between scouring at each pile.

Once s>1.15D, the flow-pile interaction starts to develop but decreases as s increases, and there is a critical pile spacing (approximately 2D-5.5D) below which only global scour is formed around the pile group without localized pits at individual piles. This is due to the strong interference of scouring at individual piles that wipes out the soils between the piles. However, when s is greater than the critical pile spacing, the localized pits at individual piles emerge as the waning interference of scouring between individual piles. When s exceeds the upper-bound pile spacing (5D-12D), scour interference ceases while the localized pits dominate the local scour at the pile group, i.e., the hydraulic group effect vanishes. The different result of critical pile spacing is mainly resulted from different flow conditions examined in these flume tests (Yilin Yang et al., 2020). It is worthwhile to mention that the flume tests may underestimate the critical pile spacing compared with the field observations, probably

due to the reduced scale and artificial flow used in the flume tests (Bayram and Larson, 2000; Palmer, 1969; Sun et al., 2007).

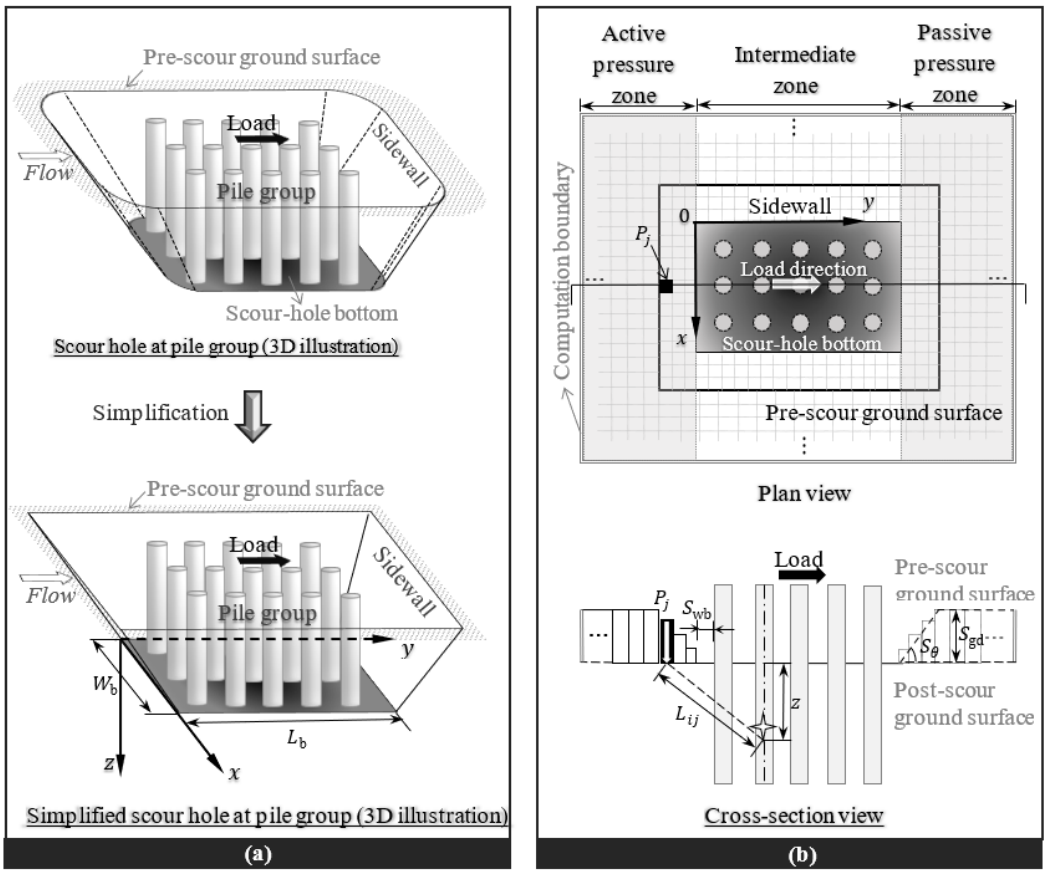

Figure 4.1 (a) Scour hole around a pile group and (b) proposed model for deriving post-scour effective vertical stresses around piles

In practice, pile groups are commonly constructed with s= 2.5D-5D (ASSHTO, 2012; Bowles, 1997); therefore, the local scour around a pile group can be reasonably represented by a large global scour hole, while the localized pits at individual piles can be neglected (or incorporated into the global scour hole) as indicated by the field surveys (Bayram and Larson, 2000; Palmer, 1969; Sun et al., 2007; Watson, 1974). According to Amini et al. (2014, 2012), the global-scour hole was found to be an inverted truncated pyramid with a rounded-quadrilateral cross section as illustrated in Figure 4.1.

The scour depth for a pile group is often normalized by an effective group diameter, D_e, so that the comparison between scour at a single pile and a pile group is possible, i.e., S_{gd}/D_e is comparable to S_{sd}/D. According to Sheppard (2003), D_e is the diameter of an equivalent single pile that can develop the same scour depth as the pile group

under the same flow and sediment conditions. It varies with the number of piles and pile spacing. For more details regarding D_e, readers should refer to Sheppard (2003). To advance the understanding of typical ranges of scour-hole dimensions for pile groups, an extensive literature review was conducted. The database of 120 samples of measurements (supplementary Table S4.1) is established based on field surveys or flume tests. A condensed version of the database is presented in Table 4.2.

Table 4.2 Measured dimensions of scour holes around pile groups in sands from literature

Type	Reference	Flow condition	α_f (°)	Pile group (m×n)	s (×D)	D_e (×D)	S_{gd} (×D)	S_{gd} (×D_e)	S_{wt} (×D)	S_θ (°)
Field survey	Sun et al., (2007)	Wave and current	N/A	2×2	N/A	N/A	1.7-1.9	N/A	7.5-10.9	12-15
	Bayram and Larson, (2000)	Oscillatory wave	<10	2×2 (rhombus shape)	4.5	1.3	1-3.5	0.8-2.6	3.8-11.3	5-15
Flume test	L. Ma et al. (2018)	Live-bed steady current	0	49 piles (dumbbell shape)	2.4	N/A	3.6	N/A	N/A	N/A
		Live-bed tidal current					2.4-2.9			
	Liang et al. (2017)	Clear-water steady current	0	1×2	4	1.2	1.1	0.9	N/A	N/A
				2×1	4	1.1	0.9	1.0		
				3×3	2	1.8	1.2	0.6		
	Amini et al. (2014)	Clear-water steady current	0	2×2	2	1.6	2.1	1.3	N/A	N/A
				4×2	2	1.8	2.6	1.4		
				4×2	2.5	1.8	2.3	1.3		
	Lança et al. (2013)	Clear-water steady current	15	4×2	3	2.5	3.7	1.5	N/A	N/A
			30			2.4	5.6	2.3		
			15	4×3		3.1	4.2	1.4		
			30			3.5	5.6	1.6		
	Sumer et al. (2005)	Live-bed steady current	0	1×2	5	1.8	1.5	1.3	N/A	N/A
				2×2		1.3	1.2	0.9		
				3×3		1.6	1.8	1.1		
				5×5		2.3	2.1	0.9		
	Zhao and Sheppard (1998)	Steady current	0	8×3	3	2.6	2.1	0.8	N/A	N/A

Overall, scour-hole slope angle for offshore pile groups is in a range of S_θ=5°-15° (Bayram and Larson, 2000; Sun et al., 2007), which is similar to the observed range of S_θ<15°for bridge piers (Butch, 1996). Surprisingly, these values are much smaller than the typical values (26.6°and 30°) used for scour at bridges (Arneson et al., 2012) and marine structures (Whitehouse, 1998). The scour depth for pile groups is mainly in the range of S_{gd}/D_e=1.2-2.0 (Figure 4.2), which is comparable to that for single piles, i.e.,

S_{sd}/D=1.3-2.5 (API, 2011; DNV, 2014; GL, 2012).

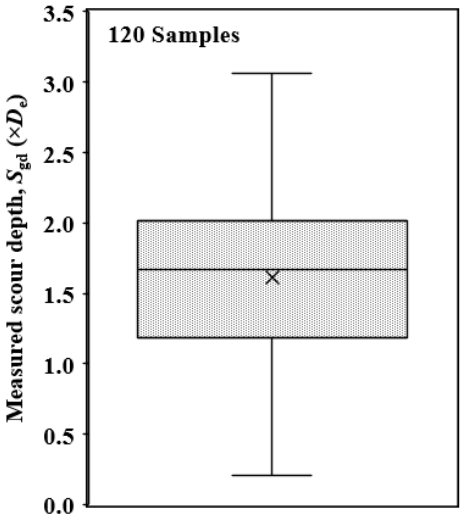

Figure 4.2 Measured maximum depths of scour holes around pile groups

4.4 Existing approaches for post-scour vertical effective stress

The post-scour lateral responses of pile groups can be practically evaluated by incorporating the post-scour vertical effective stress into the *p*-*y* curve framework. Although the standard methods (API, FHWA-DS, and FHWA-DP) are only applicable to single piles, they may be mistakenly used to analyze post-scour pile groups. This section gives a summary of the standard methods and the method of Lin and Lin (2020) regarding the estimation of post-scour vertical effective stress, while the integration of the post-scour vertical effective stress, $\sigma'_{z,\mathrm{sc}}$, to the *p*-*y* curves for pile groups are presented later.

The standard methods specify different procedures to estimate $\sigma'_{z,\mathrm{sc}}$ for single piles. Both API and FHWA-DS acknowledge the decrease in vertical effective stress by local scour, but the decrease is only limited to a certain depth below the post-scour ground surface, which is called the influence depth, z_i, below which $\sigma'_{z,\mathrm{sc}}$ is equal to the pre-scour vertical effective stress, $\sigma'_{z,\mathrm{int}}$, and above which $\sigma'_{z,\mathrm{sc}}$ is linearly increased from the post-scour ground surface, as illustrated in Figure 4.3(a) and mathematically expressed in Eq.(4-1).

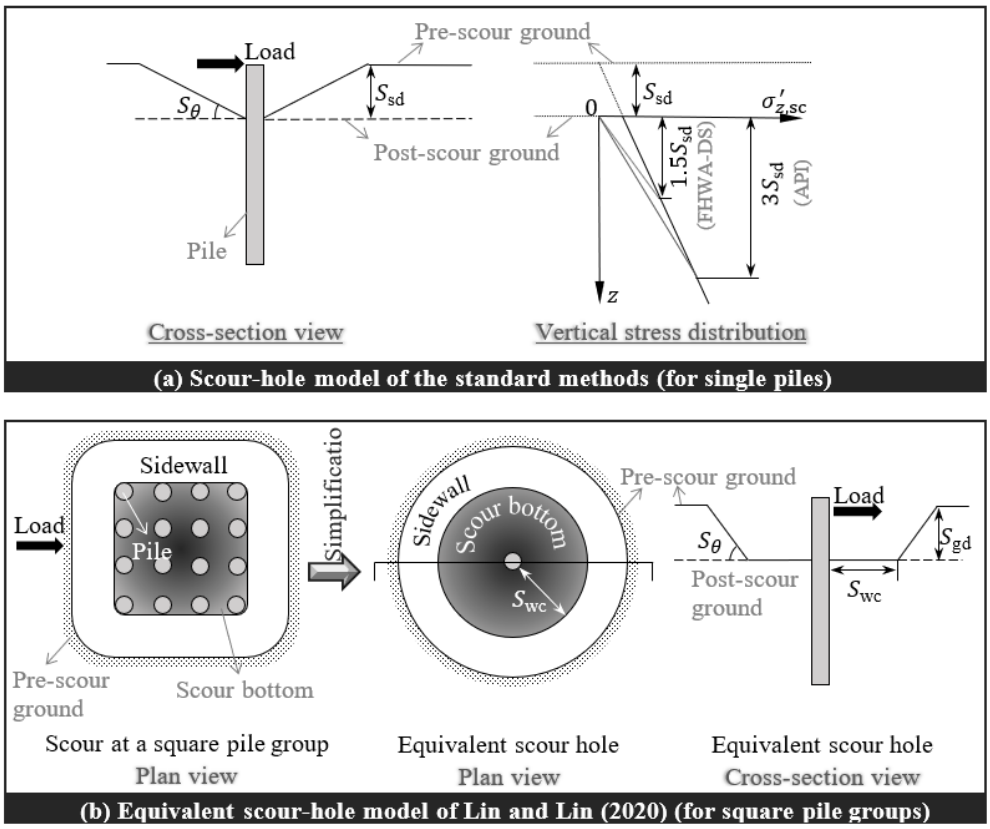

Figure 4.3 (a) Scour-hole model of the standard methods and (b) equivalent scour-hole model of Lin and Lin (2020)

For API, the influence depth is three times the local-scour depth below the post-scour ground surface (z_i=3S_{sd}), while z_I recommended by FHWA-DS is only half that suggested by API (z_i=1.5S_{sd}). However, FHWA-DP neglects the loss of vertical effective stress by local scour; therefore, z_i=0 and the depth distribution of $\sigma'_{z,sc}$ is identical to that of $\sigma'_{z,int}$.

$$\sigma'_{z,sc} = \begin{cases} \gamma' z(1 + S_{sd}/z_i) & \text{for } z < z_i \\ \gamma'(S_{sd} + z) & \text{for } z \geq z_I \end{cases} \quad (4\text{-}1)$$

Eq. (4-1) can also be presented in a normalized way using vertical stress ratio:

$$\frac{\sigma'_{z,sc}}{\sigma'_{z,int}} = \begin{cases} \frac{z(S_{sd}+z_i)}{z_i(S_{sd}+z)} & \text{for } z < z_i \\ 1.0 & \text{for } z \geq z_I \end{cases} \quad (4\text{-}2)$$

In Eqs. (4-1) and (4-2), S_{sd} is substituted with S_{gd} when they are used for scoured pile groups.

To extend the solution for $\sigma'_{z,sc}$ for single piles (Lin and Wu, 2019) to that for

square pile groups, Lin and Lin (2020) suggest an equivalent scour-hole model [an inverted truncated cone in Figure 4.3(b)], which has the same bottom area, A_b, and scour-hole slope angle, S_θ, as the scour hole at the pile group (an inverted rounded-truncated pyramid). The vertical effective stress for the pile in the center of the equivalent scour hole is calculated by Eq. (4-3) and used as $\sigma'_{z,sc}$ for all piles in the group.

$$\sigma'_{z,sc} = \gamma' z \left[1 + \left(\frac{S_{gd}/\tan S_\theta + S_{wc}}{\sqrt{\left(S_{gd}/\tan S_\theta + S_{wc}\right)^2 + z^2}} - \frac{S_{wc}}{\sqrt{S_{wc}^2 + z^2}} \right) \tan S_\theta \right] \quad (4\text{-}3)$$

where γ' is the effective unit weight of soil; z is the depth below the post-scour ground surface; S_{wc} is the distance from the scour-bottom perimeter to the center pile, $S_{wc}=(A_b/\pi)^{0.5}-0.5D$.

As mentioned in the introduction section, Lin and Lin's method involves several simplifications, which may limit its application and cause unnecessary conservatism. Firstly, it assumes a pile group to be square, which is not always true in practice since the pile group can be rectangular when supporting jetty pier structures and bridges. Secondly, it assumes equal $\sigma'_{z,sc}$ around individual piles within a group, leading to underestimated $\sigma'_{z,sc}$ at individual piles except the center pile, particularly for a large-scale pile group because when $S_{wc}>3D$ the local-scour effect is equivalent to a general-scour effect (Lin and Lin, 2020). This also leads to no difference in active or passive earth pressure between the back row and the leading row, and thus incorrect responses of the lateral capacity of pile group to the change in S_θ (Lin and Lin, 2020). Lastly, it neglects the soil-pile interface friction (Lin and Jiang, 2019) that can effectively retain the soil effective stress at the piles and prevent the scour-induced loss in $\sigma'_{z,sc}$. Therefore, it necessitates the development of a rigorous approach to overcoming the foregoing limitations.

4.5 Proposed methods

To appropriately analyze laterally loaded pile groups under local-scour conditions, an improved analytical method (IAM) is proposed. Based on the results of IAM, a practical approach called the influence depth method (IDM) is developed. The two methods are implemented in MATLAB, allowing for analyzing post-scour vertical

effective stresses and lateral responses of pile groups.

4.5.1 Post-scour vertical effective stresses around piles

As discussed in Section 4.3, a scour hole at a pile group can be featured by a frustum with a rounded-rectangle cross section (Amini et al., 2014, 2012) as shown in Figure 4.1(a). It is also possible that a more complicated scour-hole shape featuring uneven scour bottom and unequal slope angles can exist in large pile groups involving great pile spacings and/or pile numbers (Liang et al., 2017; Sumer et al., 2005; Yilin Yang et al., 2020). However, as will be discussed later, for most scour cases considered in this study, this simplified uniform scour-hole shape is considered to be proper, and the effect of the simplification is quantified through a comparative study in Section 4.5.3. In the proposed IAM, the scour-hole shape is slightly modified by substituting the rounded edges with the sharp edges for mathematical convenience [note that this simplified scour hole with sharp edges is also adopted by the centrifuge tests (Kariyawasam et al., 2020)] while both frustums sharing the same bottom area of the scour hole, A_b=$L_b W_b$, and scour-hole slope angle, S_θ. Thereinto, L_b and W_b are the length and width of the scour-hole bottom, respectively. Both frustums also share the same length-to-width ratio (L_b/W_b). A Cartesian coordinate system is established to define the scour-hole dimensions, with its origin being placed on the upper-left corner of the scour-hole bottom and y and z axes pointing to the lateral loading and downward direction, respectively in Figure 4.1(a). The post-scour vertical effective stress is calculated by superposition of two components of vertical effective stresses resulting from soil overburden below and above the post-scour ground surface: i.e., $\sigma'_{z,\mathrm{sc}} = \sigma'_z + \Delta\sigma'_z$. The former is easily calculated using $\sigma'_z = \gamma' z$; the latter, $\Delta\sigma'_z$, called additional vertical effective stress, is determined by a series of soil columns [Figure 4.1(b)], which have a width of Δx=Δy=0.02D and varied heights of h_j=0-S_{gd} within the sloping ground domain (sidewall) but a larger width of Δx=Δy=0.07D and a constant height of h_j=S_{gd} within the leveled pre-scour ground domain. Furthermore, individual piles are reduced to vertical lines as D is significantly smaller than the soil domain and the pile diameter effect was found to be negligible (Lin and Wu, 2019). The value of $\Delta\sigma'_z$ is then calculated using Boussinesq's point load solution by integrating the contribution from the weights of soil columns. The integration is done over a finite area with boundaries located 60.5W_b and 60.5L_b from the center of the scour-hole bottom on x and y

directions, respectively [Figure 4.1(b)], beyond which soil overburden has no contribution to $\Delta\sigma'_z$.

4.5.1.1 Consideration of entire overburden zone

Assuming the overburden (or remaining soils) above the post-scour ground is discretized into J soil columns, and all the soil columns contribute to $\Delta\sigma'_z$ at an individual pile according to Boussinesq's solution. Therefore, $\Delta\sigma'_z$ for different piles in an $m\times n$ group at a given depth, z, can be expressed as

$$\begin{bmatrix} \Delta\sigma'_{z,1} \\ \Delta\sigma'_{z,2} \\ \vdots \\ \Delta\sigma'_{z,mn} \end{bmatrix}_{mn\times 1} = \begin{bmatrix} \Psi_{1,1} & \Psi_{1,2} & \cdots & \Psi_{1,J} \\ \Psi_{2,1} & \Psi_{2,2} & \cdots & \Psi_{2,J} \\ \vdots & \vdots & \ddots & \vdots \\ \Psi_{mn,1} & \Psi_{mn,2} & \cdots & \Psi_{mn,J} \end{bmatrix}_{mn\times J} \begin{bmatrix} P_1 \\ P_2 \\ \vdots \\ P_J \end{bmatrix}_{mn\times J} \tag{4-4}$$

where P_j is the weight of the j^{th} soil column, $P_j=\gamma' h_j \Delta x \Delta y$. $\Psi_{I,j}$ is the influence factor depending on the distance ($L_{i,j}$) between the point of interest in the i^{th} pile to the center of the j^{th} soil column bottom.

$$\Psi_{i,j} = \frac{3z^3}{2\pi[(x_{\text{p}}-x_{\text{s}})^2+(y_{\text{p}}-y_{\text{s}})^2+z^2]^{2.5}} \quad (i = 1,2,\dots,mn \text{ and } j = 1,2,\dots,J) \tag{4-5}$$

where (x_{s}, y_{s}) and (x_{p}, y_{p}) represent the coordinates of the j^{th} soil column and the i^{th} pile, respectively; z is the depth of point of interest in the i^{th} pile below the post-scour ground. Once $\Delta\sigma'_z$ is determined from Eq. (4-4), post-scour vertical stresses at individual piles within a group for a given depth, z, can be calculated by

$$\begin{bmatrix} \sigma'_{z,\text{sc},1} \\ \sigma'_{z,\text{sc},2} \\ \vdots \\ \sigma'_{z,\text{sc},mn} \end{bmatrix}_{mn\times 1} = \eta \cdot \left\{ \begin{bmatrix} \Delta\sigma'_{z,1} \\ \Delta\sigma'_{z,2} \\ \vdots \\ \Delta\sigma'_{z,mn} \end{bmatrix}_{mn\times 1} + \begin{bmatrix} \gamma' z \\ \gamma' z \\ \vdots \\ \gamma' z \end{bmatrix}_{mn\times 1} \right\} \leq \begin{bmatrix} \sigma'_{z,\text{int}} \\ \sigma'_{z,\text{int}} \\ \vdots \\ \sigma'_{z,\text{int}} \end{bmatrix}_{mn\times 1} \tag{4-6}$$

Besides, the vertical stress ratios ($\sigma'_{z,\text{sc}}/\sigma'_{z,\text{int}}$) for individual piles at depth, z, are

$$\begin{bmatrix} \sigma'_{z,\text{sc},1}/\sigma'_{z,\text{int}} \\ \sigma'_{z,\text{sc},2}/\sigma'_{z,\text{int}} \\ \vdots \\ \sigma'_{z,\text{sc},mn}/\sigma'_{z,\text{int}} \end{bmatrix}_{mn\times 1} = \frac{1}{\gamma'(z+S_{\text{gd}})} \cdot \begin{bmatrix} \sigma'_{z,\text{sc},1} \\ \sigma'_{z,\text{sc},2} \\ \vdots \\ \sigma'_{z,\text{sc},mn} \end{bmatrix}_{mn\times 1} \leq \begin{bmatrix} 1 \\ 1 \\ \vdots \\ 1 \end{bmatrix}_{mn\times 1} \tag{4-7}$$

In Eq. (4-6), η is a semi-empirical correction factor to account for the effect of soil-

pile interface friction on retaining vertical effective stress in soils after scouring. This value is back-calculated by matching the $\sigma'_{z,\mathrm{sc}}/\sigma'_{z,\mathrm{int}}$ profile calculated from Eqs. (4-4)-(4-7) to that from 3D FEM (e.g., Figure 4.4). Through parametric analyses considering various scour-hole depth, scour-hole slope angle, sand relative density, pile spacing, and number of piles, η was found to primarily depend on the scour-hole depth and pile spacing and can be expressed as $\eta=f_{\mathrm{d}}f_{\mathrm{s}}$, where f_{d} and f_{s} are factors considering the effects of S_{gd} and s, respectively. For the typical ranges of S_{gd} and s encountered in practice, η can be determined by Table 4.3.

Table 4.3 Correction factor for considering soil-pile interface friction

S_{gd} ($\times D$)	f_{d}	
1.5	1.09	
3.0	1.13	
4.5	1.17	
6.0	1.20	$\eta=f_{\mathrm{d}}f_{\mathrm{s}}$
s ($\times D$)	f_{s}	
2	1.14	
3	1.00	
4	0.94	
6	0.94	

The preceding procedure invoking Eqs. (4-4)-(4-7) constitutes the first step of the proposed IAM concerning the calculation of $\sigma'_{z,\mathrm{sc}}$ considering the contribution of the entire overburden zone. The IAM can be further utilized to derive the influence depth, z_{i}, for different pile groups and scour-hole dimensions using equivalent stress ratio area: invoking Eq. (4-8), the stress ratio area, A_{e}, calculated using $\sigma'_{z,\mathrm{sc}}/\sigma'_{z,\mathrm{int}}$ determined from Eqs. (4-4)-(4-7) is equal to that calculated using $\sigma'_{z,\mathrm{sc}}/\sigma'_{z,\mathrm{int}}$ determined by Eq. (4-3).

$$A_{\mathrm{e}}=\int_0^{L_{\mathrm{e}}}\left(1-\frac{\sigma'_{z,\mathrm{sc}}}{\sigma'_{z,\mathrm{int}}}\right)\mathrm{d}z \tag{4-8}$$

where A_{e} represents the area enclosed by the right vertical axis and $\sigma'_{z,\mathrm{sc}}/\sigma'_{z,\mathrm{int}}$ profile (e.g., Figure 4.4).

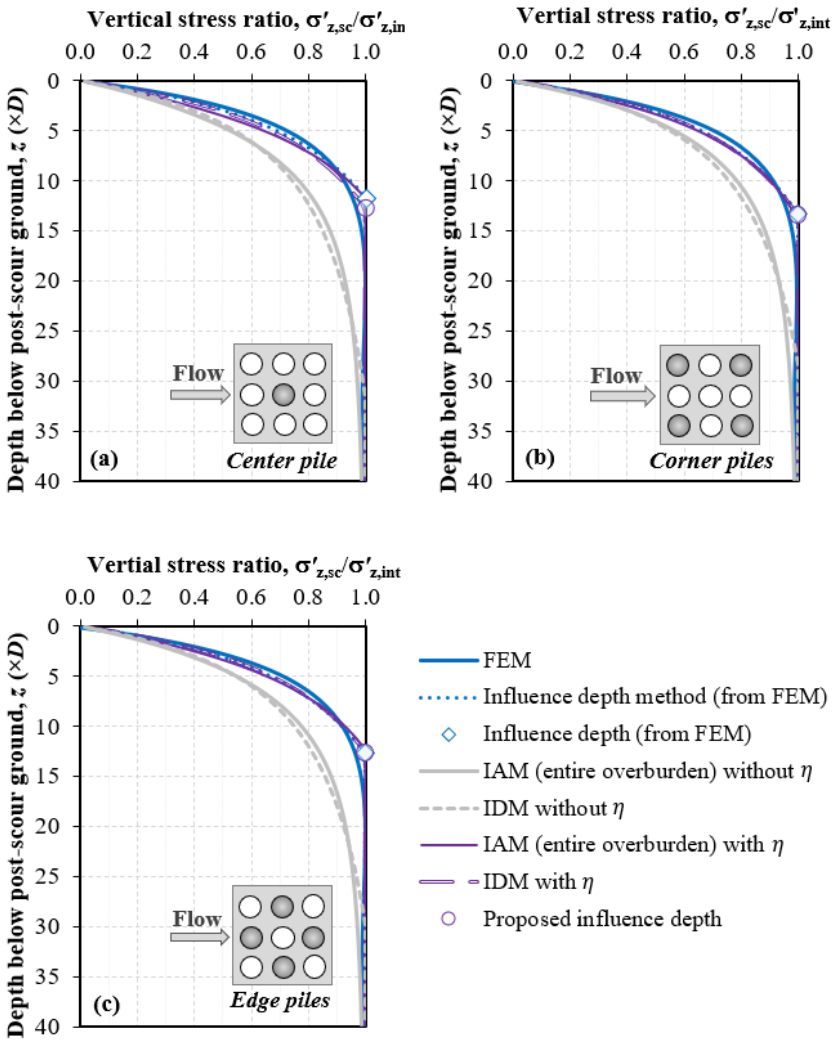

Figure 4.4 Profiles of vertical stress ratios of (a) center pile, (b) corner piles, and (c) edge piles in a 3×3 pile group with 3*D* spacing (S_{gd}=2.8D_e, S_{wb}=0, S_θ=26.6°)

Using this procedure, a typical range of z_i is obtained, as given in Figures 4.5 and 4.6 for a 3×3 pile group. For other sizes of pile groups, the values are presented in supplementary Tables S4.3-S4.8. By substituting z_i into Eq. (4-1), $\sigma'_{z,sc}$ at individual piles can be obtained. This forms part of the proposed IDM in relation to the calculation of post-scour vertical effective stress.

4.5.1.2 Consideration of separate overburden zones

In Eqs. (4-4)-(4-7), $\Delta\sigma'_z$ and $\sigma'_{z,sc}$ are calculated considering the total influence of the overburden above the post-scour ground surface; however, when integrating the calculated $\sigma'_{z,sc}$ into *p*-*y* curves, the calculated lateral soil resistances for the leading and back rows are identical, which is not reasonable. To capture the difference in lateral soil resistance, the wedge failure model was adopted for scoured single piles (Lin et al.,

2014a). However, the application of the wedge failure model for a pile group is untenable as the difficulty in considering the geotechnical group effect and scour-hole geometry. To address this issue, the preceding procedure for $\sigma'_{z,\mathrm{sc}}$ was improved by dividing the overburden above the post-scour ground surface into different zones and separately evaluating $\Delta\sigma'_z$ and $\sigma'_{z,\mathrm{sc}}$. As illustrated in Figure 4.1(b), when a pile group is under lateral load, the overburden pressure contributing to $\Delta\sigma'_z$ can be divided into a passive earth pressure zone, an active earth pressure zone, and an intermediate zone. Instead of calculating $\Delta\sigma'_z$ considering the entire overburden above the post-scour ground surface, $\Delta\sigma'_{z\mathrm{a}}$ and $\Delta\sigma'_{z\mathrm{p}}$ are separately evaluated considering the overburden within the intermediate-active pressure zone and the intermediate-passive pressure zone, respectively. Mathematically, $\Delta\sigma'_{z\mathrm{a}}$ and $\Delta\sigma'_{z\mathrm{p}}$ are calculated by substituting J_a (the number of soil columns within the intermediate-active pressure zone) and J_p (the number of soil columns within the intermediate-passive pressure zone), respectively, for J in Eq. (4-4). Subsequently, post-scour vertical effective stresses corresponding to the intermediate-active pressure zone and intermediate-passive pressure zone ($\sigma'_{z\mathrm{a,sc}}$ and $\sigma'_{z\mathrm{p,sc}}$) are obtained by substituting $\Delta\sigma'_{z\mathrm{a}}$ and $\Delta\sigma'_{z\mathrm{p}}$ into Eq. (4-6), respectively. This constitutes part of the proposed IAM in relation to the calculation of the post-scour vertical effective stresses considering the effects of the separate overburden zones.

4.5.2 Post-scour lateral responses of pile group

The next part of the proposed IAM and IDM is to incorporate the post-scour vertical effective stress into the *p*-*y* curve framework. This step requires calculating an equivalent depth, z_e, by dividing the post-scour vertical effective stress by soil effective unit weight. Substitution of z_e into existing *p*-*y* curves [e.g., Reese's *p*-*y* curves for sands (Reese and Van Impe, 2001)] for pile groups results in the modified *p*-*y* curves that can account for laterally loaded pile groups under different scour-hole dimensions. The above-mentioned step is also used when the standard methods are employed. The post-scour vertical effective stresses calculated considering the entire overburden zone will be used by the standard methods and the IDM, while those considering separate overburden zones are used by the IAM. Note that the IAM considering the entire overburden zone [Eqs. (4-4)-(4-7)] is only used for the purpose of deriving the IDM.

4.5.2.1 Consideration of entire overburden zone

The equivalent depths, z_e, of the IDM and the standard methods are calculated from Eq. (4-9), where $\sigma'_{z,sc}$ is calculated by substituting z_i developed in this study and suggested by the standard methods, respectively, into Eq. (4-1). The post-scour *p-y* curves for group piles are developed by substituting z_e for z in Reese's *p-y* relationship (Reese and Van Impe, 2001), as presented in Eqs. (4-10)-(4-14).

$$z_e = \sigma'_{z,sc}/\gamma' \tag{4-9}$$

$$p = \begin{cases} f_m k z_e y & y \le y_k \\ f_m \frac{p_m}{y_m{}^{\lambda}}\, y^{\lambda} & y_k < y \le y_m \\ f_m \left[p_m + \frac{(y-y_m)(p_u-p_m)}{y_u-y_m}\right] & y_m < y \le y_u \\ f_m p_u & y > y_u \end{cases} \tag{4-10}$$

where f_m is the *p*-multiplier that considers the geotechnical group effect; y_m=D/60; y_u=3D/80; k is the *p-y* modulus, taken as 34, 16.3, 5.4 MN/m^3 for the submerged dense, medium dense, and loose sands, respectively (API, 2011). The other parameters (p_u, p_m, y_k, λ) are related to the ultimate lateral soil resistance per unit length of a pile, p_{ult}.

$$p_u = \bar{A}_s p_{ult} \tag{4-11}$$

$$p_m = \bar{B}_s p_{ult} \tag{4-12}$$

where $\bar{A}_s$ and $\bar{B}_s$ are the static load-type factors that can be determined by substituting z_e/D for z/D in Reese's *p-y* curves. Y_k and λ are obtained from $y_k = \left(\frac{p_m}{k z_e y_m{}^{\lambda}}\right)^{\frac{1}{1-\lambda}}$ and $\lambda = \frac{y_m(p_u-p_m)}{p_m(y_u-y_m)}$, respectively. P_{ult} is taken as the smaller value of Eqs. (4-13) and (4-14).

$$p_{ult,s} = \gamma' z_e \left[\frac{\tan\beta(z_e \tan\beta \tan\alpha + D)}{\tan(\beta-\phi')} + \frac{K_0 z_e \tan\phi' \sin\beta}{\tan(\beta-\phi')\cos\alpha} + K_0 z_e \tan\beta\,(\tan\phi' \sin\beta - \tan\alpha) - K_A D\right] \tag{4-13}$$

$$p_{ult,d} = \gamma' z_e D[K_A(\tan^8\beta - 1) + K_0 \tan\phi' \tan^4\beta] \tag{4-14}$$

where $p_{ult,s}$ and $p_{ult,d}$ are ultimate soil resistance per unit length of a pile at shallow and great depths, respectively; α=ϕ'/2; β=45°+ ϕ'/2; K_A=tan^2(45°- ϕ'/2) and K_A=1-sinϕ' are active and at-rest earth pressure coefficients, respectively, for normally consolidated

soils.

4.5.2.2 Consideration of separate overburden zones

The proposed IAM employs $\sigma'_{\mathrm{za,sc}}$ and $\sigma'_{\mathrm{zp,\,sc}}$ to account for the differences in the active and passive earth pressures between the back row and the leading row in contributing to the lateral soil resistances. The corresponding equivalent depths are calculated using $z_{\mathrm{ea}}=\sigma'_{\mathrm{za,sc}}/\gamma'$ and $z_{\mathrm{ep}}=\sigma'_{\mathrm{zp,\,sc}}/\gamma'$, respectively. For the ultimate lateral resistance at shallow depths, $p_{\mathrm{ult,s}}$, a close examination of Eq. (4-13) reveals that it consists of the components related to the active and passive earth pressures; therefore, Eqs. (4-11)-(4-13) are modified to calculate $p_{\mathrm{ult,s}}$, incorporating $\sigma'_{\mathrm{za,sc}}$ and $\sigma'_{\mathrm{zp,\,sc}}$, given by

$$p_{\mathrm{u}} = \bar{A}_{\mathrm{sp}}\gamma' z_{\mathrm{ep}} K_0 \left[\frac{\tan\beta(z_{\mathrm{ep}}\tan\beta\tan\alpha+D)}{K_0\tan(\beta-\phi')} + \frac{z_{\mathrm{ep}}\tan\phi'\sin\beta}{\tan(\beta-\phi')\cos\alpha} + z_{\mathrm{ep}}\tan\beta\,(\tan\phi'\sin\beta - \tan\alpha)\right] - \bar{A}_{\mathrm{sa}}\gamma' z_{\mathrm{ea}} K_{\mathrm{A}} D \quad (4\text{-}15)$$

$$p_{\mathrm{m}} = \bar{B}_{\mathrm{sp}}\gamma' z_{\mathrm{ep}} K_0 \left[\frac{\tan\beta(z_{\mathrm{ep}}\tan\beta\tan\alpha+D)}{K_0\tan(\beta-\phi')} + \frac{z_{\mathrm{ep}}\tan\phi'\sin\beta}{\tan(\beta-\phi')\cos\alpha} + z_{\mathrm{ep}}\tan\beta\,(\tan\phi'\sin\beta - \tan\alpha)\right] - \bar{B}_{\mathrm{sa}}\gamma' z_{\mathrm{ea}} K_{\mathrm{A}} D \quad (4\text{-}16)$$

where $\bar{A}_{\mathrm{sa}}$ ($\bar{B}_{\mathrm{sa}}$) and $\bar{A}_{\mathrm{sp}}$ ($\bar{B}_{\mathrm{sp}}$) are the static load-type factors dependent on z_{ea}/D and z_{ep}/D, respectively (Reese and Van Impe, 2001). However, soil failure at a great depth typically follows a plane flow mode; therefore, the lateral soil resistance at a great depth, $p_{\mathrm{ult,d}}$ is influenced by the entire overburden above the post-scour ground surface, and in this case, Eq. (4-14) is still used.

In summary, for the IAM, the post-scour *p*-*y* curves are developed using Eqs. (4-10)-(4-12), and (4-14) when $p_{\mathrm{ult}}=p_{\mathrm{ult,d}}$ but Eqs. (4-10), (4-15) and (4-16) when $p_{\mathrm{ult}}=p_{\mathrm{ult,s}}$. For the IDM or the standard methods, Eqs. (4-10)-(4-14) are invoked.

4.5.3 Implementation and validation

The post-scour *p*-*y* curves developed from the above procedures were incorporated into the Euler-Bernoulli beam equation (Reese and Van Impe, 2001) to analyze the laterally loaded pile groups considering different scour-hole conditions. A central finite-difference algorithm with Newton's iteration was developed in MATLAB to

implement the calculations. The MATLAB code is attached as a supplementary file.

As discussed in the introduction, no field tests or centrifuge tests regarding scoured pile groups can be used to validate the proposed methods. Therefore, the proposed IAM and IDM were verified against a series of 3D continuum FE results computed by the authors (Lin and Lin, 2020) and compared with the standard methods (API, FHWA-DP, and FHWA-DS) and the method of Lin and Lin (2020). In the 3D FE model (Lin and Lin, 2020), the pile was simulated as an elastic material using continuum solid elements, while soil as an elastoplastic material with Mohr-Coulomb failure criterion. Soil parameters were back-calculated from a full-scale load test on a single pile (Brown et al., 1988), and the baseline 3D FE model for a pile group established using the calibrated soil parameters was verified against a full-scale test of a laterally loaded pile group (3×3, s=3D) at the same site as the single pile (Brown et al., 1988). The pile head of individual piles in the pile group was pin-connected through a frame and thus was free for rotation while moving equally horizontally. The baseline model was for a pre-scour condition while the scour hole was created from the baseline model by deactivating the soil elements that were intended to be scoured away. The scour depth ranged from 0 to 6D (0 to 2.8D_e) and scour-hole slope angle from 0° to 42° (one degree less than soil friction angle) while scour bottom width remained zero. Greater details of the 3D FE model can be referred to Lin and Lin (2020). Table 4.4 shows the soil and pile parameters, and the pile head was 0.305 m above the ground surface (corresponding to the pre-scour ground in this study).

Table 4.4 Sand and pile parameters of Reese's *p-y* curve framework

Parameters of Reese's *p-y* curve framework		Dense sand	Medium dense sand	Loose sand
Sands (different relative densities)[1]	Effective unit weight (kN/m^3)	9.83	9.83	9.83
	Effective angle of internal friction (°)	48	35	26
	p-y modulus (kN/m^3)	34000	16300	5400
Equivalent pile (linear elastic)[2]	Length (m)	12.81		
	Diameter (m)	0.273		
	Elastic modulus (Gpa)	75.713		

Note: [1]soil parameters of dense sand were back-calculated from field test results (Brown et al., 1988), while that of medium dense and loose sands were back-calculated from 3D FEM results (Lin and Lin, 2020); [2]equivalent pile with solid cross-section has the same flexural stiffness as the prototype test pile (Brown et al., 1988) including steel pipe and tube bounded by grout.

It is noted that Mohr-Coulomb constitutive model that adopts an elastic perfectly plastic relation has inherent limitations: for example, it could not evaluate the stress-

dependent soil stiffness, which however can be significant for sands (Gouw, 2014). Therefore, an advanced model such as strain hardening model may be more proper. However, the present study has validated the FE model using Mohr-Coulomb constitutive relation against the pile group test (Brown et al., 1988), with the soil parameters back-calculated from another field test (for a single isolated pile) at the same site. This indicates that the numerical model in this study is still acceptable. Besides, as discussed in Section 4.5.1, the scour-hole shape adopted by this study is, to some extent, simplified from a more complex scour scenario featuring uneven scour-hole bottom as well as unequal upstream and downstream side slope angles. Therefore, a preliminary comparative study was conducted herein using 3D FEM to quantify the difference between a complex scour-hole scenario and a simplified uniform scour-hole scenario in terms of the lateral capacity of pile group, where the lateral capacity was the lateral load causing 1-inch deflection at the pile head (Lin and Wu, 2019). The comparative study investigated the post-scour lateral capacities of the 3×3 pile group (Brown et al., 1988) under four different scour-hole scenarios illustrated in supplementary Figure S4.1, and the detailed scour-hole dimensions are summarized in supplementary Table S4.2. Meanwhile, the pile spacing was set to be 5D so that the localized pits could be formed at individual piles as discussed in Section 4.3**.** By comparing the lateral capacities corresponding to these four different scour-hole cases (Figure S4.2), simplifying an asymmetrical and uneven scour hole as a uniform scour hole could underestimate the post-scour lateral capacity of pile group by 10%-13%. This indicates that the simplification was conservative, and its effect was not significant. It is acknowledged that a further study is warranted to explore the limitations of the simplified scour-hole model for other sizes of pile group or improve the analytical method to directly account for the nonuniform scour-hole conditions.

Overall, using the proposed IAM and IDM, Lin and Lin's method, and standard methods (API, FHWA-DP, and FHWA-DS), a total of 288 parametric analyses were conducted to investigate the effects of scour-hole depth (0 to 6.0D or 2.8D_e), scour-hole slope angle (0°-42°), soil relative density (loose, medium, dense), pile spacing (2D-6D), number of piles (4-16 piles), and pile group configuration (square, rectangular) on the post-scour lateral responses of pile groups. The details of the parametric analyses are summarized in Table 4.5.

Table 4.5 Details of parametric analyses

Investigated factor	Scour-hole dimensions S_{gd} (×D)	S_{gd} (×D_e)	S_θ (°)	Sand Relative density	Pile group m×n	s (×D)	η^1
Scour-hole depth	1.5, 3.0, 4.5, 6.0	0.7, 1.4, 2.1, 2.8	26.6	Dense	3×3	3	1.09-1.20
Scour-hole slope angle	3.0	1.4	0, 12, 20, 26.6, 35, 42	Dense	3×3	3	1.13
Relative density of soil	1.5, 3.0, 4.5, 6.0	0.7, 1.4, 2.1, 2.8	26.6	Dense medium loose	3×3	3	1.09-1.20
Pile spacing	3.0	1.3,1.4,1.7,1.9,2.1	26.6	Dense	3×3	2, 3, 4, 5, 6	1.06-1.29
Number of piles	3.0	2.0 1.4 1.1	26.6	Dense	2×2 3×3 4×4	3	1.13
Pile group configuration	2.5, 5.1, 7.6, 10.2 1.8, 3.6, 5.4, 7.2 1.4, 2.8, 4.3, 5.7	0.7, 1.4, 2.1, 2.8	0, 12, 20, 26.6, 35, 42 when S_{gd}=2.8D_e	Dense	6×5 10×3 15×2	3	1.12-1.20 1.10-1.20 1.09-1.20

Note: [1] η was determined using Table 4.3.

4.6 Results and discussion

The results of post-scour vertical effective stress and lateral responses of pile groups are presented, focusing on the demonstration of the efficacy of the proposed methods (IAM and IDM) and the appraisal of the existing methods mentioned in Section 4.4. Note that the calibrated 3D FE model (Lin and Lin, 2020) was used to validate the IAM and IDM, and to evaluate the existing methods.

Prior to presenting the results, the effect of soil-pile interface friction quantified by η and the determination of influence depth, z_i, are discussed. Figure 4.4(a)-(c) show the computed $\sigma'_{z,sc}/\sigma'_{z,int}$ profiles of the center, corner, and edge piles, respectively, for the 3D spaced 3×3 pile group with S_{gd}=2.8D_e (6D), S_{wb}=0, and S_θ=26.6°. Also shown in Fig 4 is the influence depth, z_i. When the soil-pile interface friction effects were neglected [i.e., dropping out η in Eq. (4-6)], IAM that considers the entire overburden zone [Eqs. (4-4)-(4-7)] and IDM yielded smaller $\sigma'_{z,sc}/\sigma'_{z,int}$ than the 3D FEM. This is because the effect of soil-pile interface friction (Lin and Jiang, 2019) was ignored when η was precluded. Contrarily, with the inclusion of η, IAM and IDM yielded a

much better comparison with the 3D FEM. Therefore, for the following analyses, only IAM and IDM with η (Table 4.3) are considered. Figure 4.4 also reveals that the proposed influence depths (denoted by circles) determined from Eqs. (4-4)-(4-8) were $2.12S_{gd}$ (center pile), $2.25S_{gd}$ (corner pile), and $2.10S_{gd}$ (edge pile), which are similar to the benchmark values ($1.94S_{gd}$, $2.22S_{gd}$, and $2.13S_{gd}$) determined from the 3D FEM (denoted by rhombus symbols).

4.6.1 Post-scour vertical effective stresses around piles

The vertical effective stresses under local-scour conditions are discussed in terms of the influence depth. A greater z_i indicates a deeper influence and thus a greater loss in the vertical effective stress caused by the local scour.

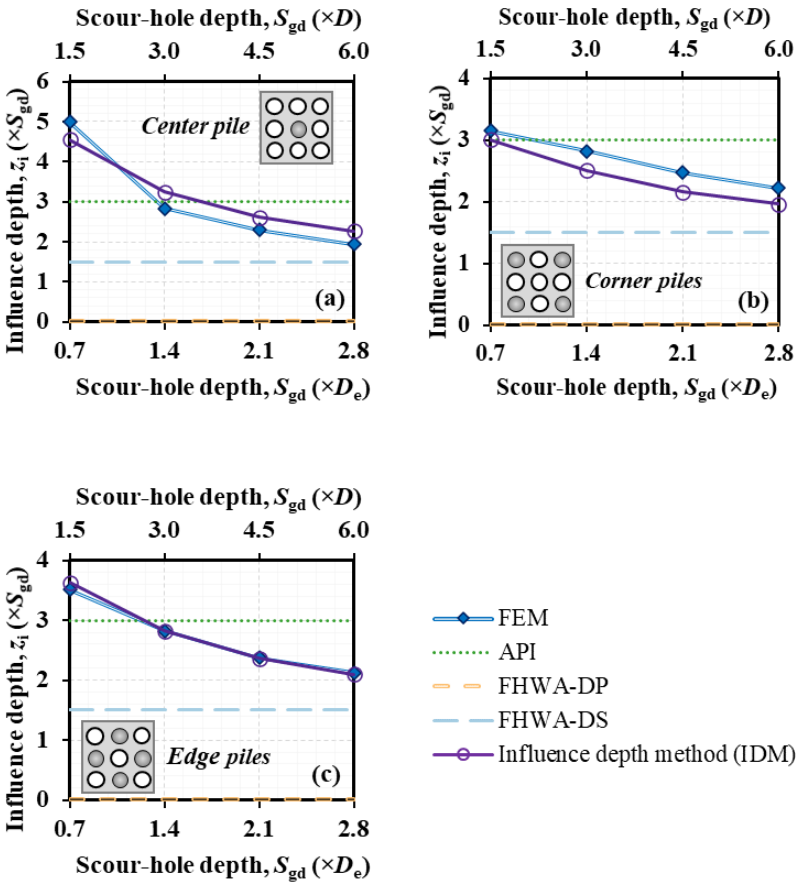

Figure 4.5 Influence depths of (a) center pile, (b) corner piles, and (c) edge piles in a 3×3 pile group (s=3D) varied with scour-hole depths (S_{gd}=0.7D_e-2.8D_e, S_w=0, S_θ=26.6°)

4.6.1.1 Effect of scour-hole depth on the influence depth

The proposed influence depths under different S_{gd} were determined by back-calculating from the results of IAM, and they were compared with those determined by the 3D FEM and recommended by the standard methods. As indicated in Figure 4.5, the results for different positions of piles agreed well with the 3D FE results, showing a nonlinear decrease in z_i with increased S_{gd}. For example, z_i decreased by 61%, 39%, and 30% for the center, edge, and corner piles, respectively, as S_{gd} increased from 0 to 2.8D_e 6D). The results further indicate that $\sigma'_{z,sc}$ (reflected by z_i) varied with the pile position in the pile group, with deeper z_i at the center pile than the edge piles and corner piles. This means that local scour caused a larger loss and a deeper influence in the vertical effective stress at the center pile than the perimeter piles. In contrast, the standard methods that recommend a constant z_i failed to capture the nonlinear relationship and the variation of z_i with the pile position. However, the influence depth suggested by API (z_i=3S_{gd}) was comparable to that from IDM and 3D FEM when S_{gd}=1.4D_e. The influence depth suggested by FHWA-DS (z_i=1.5S_{gd}) served as a lower bound of IDM and 3D FEM, showing increasing agreement as S_{gd} increased, while that by FHWA-DP was incorrect as it ignored the local-scour effects on the soil stress reduction.

4.6.1.2 Effect of pile spacing on the influence depth

Figure 4.6 presents variations of influence depth with pile spacing when S_{gd}=3D, S_{wb}=0, S_θ=26.6°. Note that S_{gd} is normalized by D since the effective diameter, D_e, is no longer constant under varied pile spacing.

Overall, z_i increased as s increased, with that at the center pile increasing more significantly than at the edge and corner piles. This result is attributed to the reduced soil-pile interactions with increased s (as indicated by f_s in Table 4.3). Again, this was captured by the IDM and 3D FEM but not by the standard methods. In comparison, FHWA-DS (z_i=1.5S_{gd}) and API (z_i=3S_{gd}) only agreed with IDM and 3D FEM when s=*2D* and 3D, respectively.

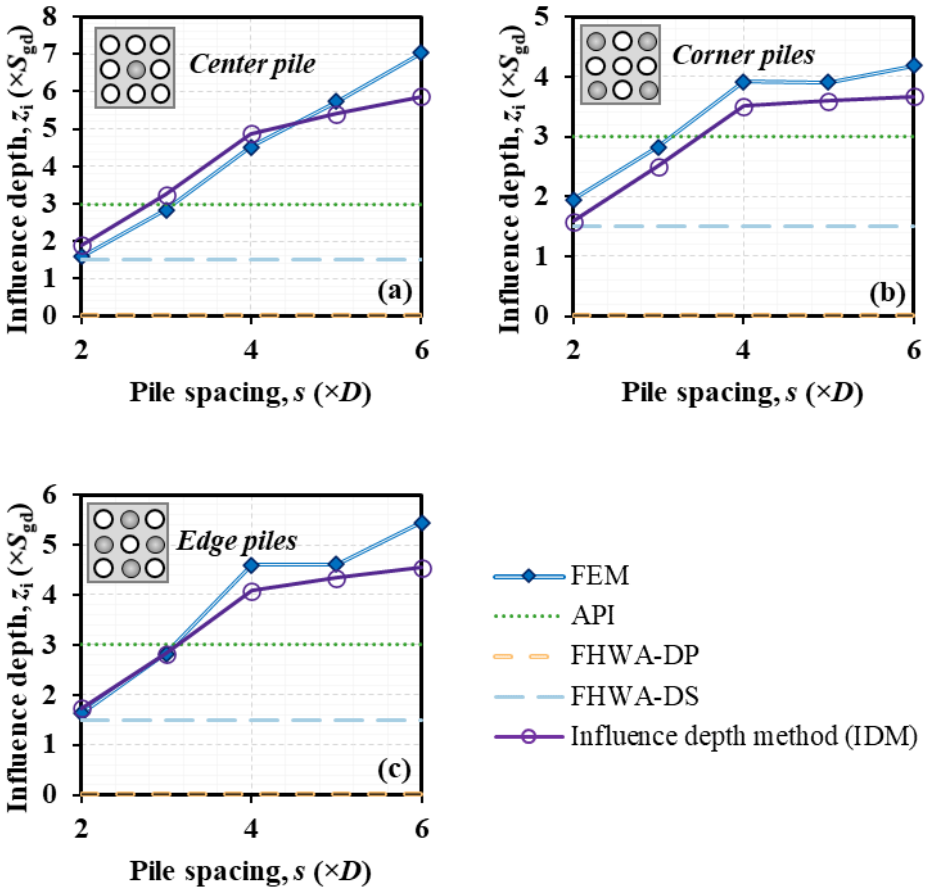

Figure 4.6 Influence depths of (a) center pile, (b) corner piles, and (c) edge piles in a 3×3 pile group vs. pile spacings (S_{gd}=3D, S_{wb}=0, S_{θ}=26.6°)

4.6.2 Post-scour lateral responses of pile groups

For a laterally loaded pile group, geotechnical group effect is usually characterized by p-multiplier, f_m, which can be obtained from load tests, 3D continuum FE analyses; alternatively, typical values of f_m can be referenced to design standards. In this study, f_m was back-calculated from the abovementioned 3D FE results (Lin and Lin, 2020) and compared with the typical values obtained from the field tests (Brown et al., 1988; Mokwa, 1999) and design recommendations (ASSHTO, 2012; FEMA, 2012; Reese et al., 1996; Reese and Van Impe, 2001; U.S. Army Corps of Engineers, 1991) as shown in Figure 4.7.

Overall, the back-calculated f_m was within the range suggested by the design recommendations and field tests. As with Fayyazi et al. (2014), f_m back-calculated from the 3D continuum numerical model was smaller than the recommended values

(ASSHTO, 2012; FEMA, 2012; Reese et al., 1996; Reese and Van Impe, 2001), particularly for the back row. ASSHTO (2012) generally agreed well with f_m obtained from field tests and 3D FEM for $s \leq 4D$ (Fayyazi et al., 2014; Rollins et al., 2005). Contrarily, f_m values per U.S. Army Corps of Engineers (1991) were in general small and conservative, particularly for the leading row. Note that the above back-calculated f_m was obtained in the no-scour condition and was reasonably assumed to remain unchanged after scouring (Lin and Lin, 2020).

In this section, the post-scour lateral responses of pile groups are presented, including the lateral capacity ratio, load share, and bending moment. The effects of scour-hole depth, scour-hole slope angle, soil relative density, pile spacing, and pile group configuration on the post-scour lateral responses were evaluated, with the ranges of input parameters given in Table 4.5.

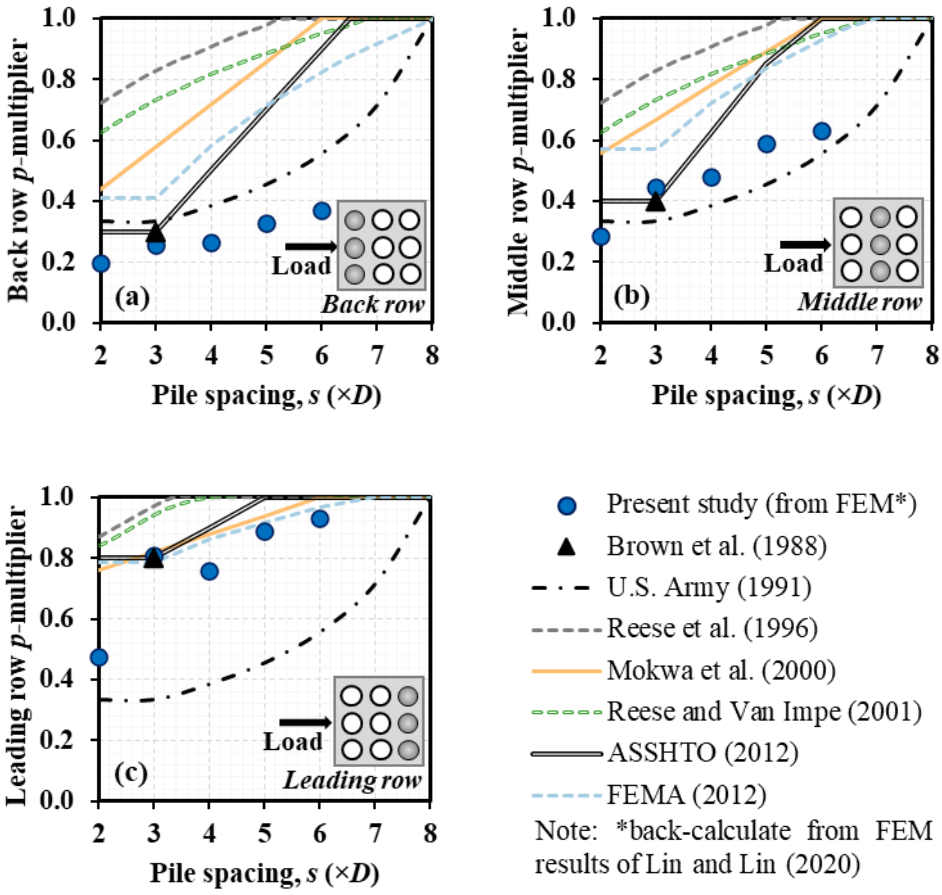

Figure 4.7 Effects of pile spacing on (a) back row, (b) middle row, and (c) leading row *p*-multipliers of a 3×3 pile group

4.6.2.1 Effect of scour-hole depth

Figure 4.8 shows the lateral load-deflection curves at the pile head (3×3 pile group) before and after scouring. Overall, the proposed methods (IAM and IDM) yielded agreeable results with the 3D FEM at different scour depths; In contrast, Lin and Lin's method predicted smaller lateral loads at a given deflection. To assess the effects of scour-hole dimensions, a lateral capacity defined as the post-scour to the pre-scour lateral capacity of a pile group, was adopted. The lateral capacity was the lateral load causing 1-inch deflection at the pile head (Lin and Wu, 2019). Generally, a smaller lateral capacity ratio indicates a greater scour-induced loss in the lateral capacity.

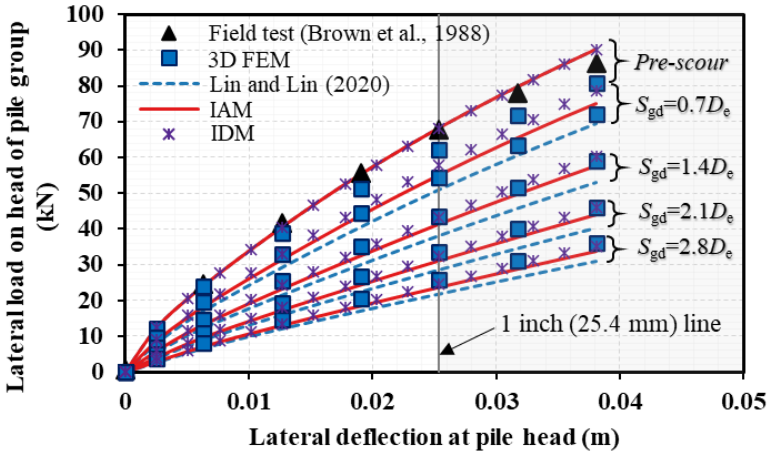

Figure 4.8 Lateral load-deflection curves at pile head (3×3 pile group with 3*D* spacing) under different scour-hole depths (S_{wb}=0, S_θ=26.6°)

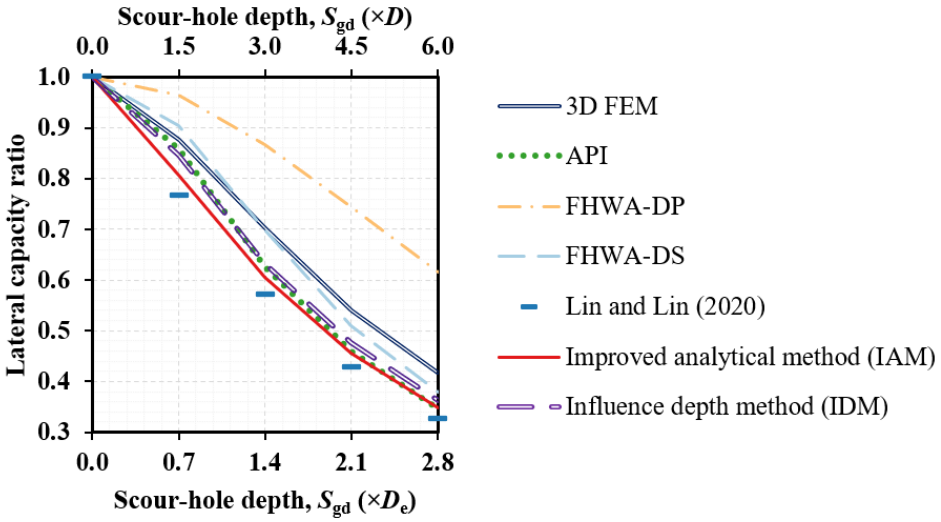

Figure 4.9 Lateral capacity ratio (3×3 pile group with 3*D* spacing) varied with scour-hole depth (S_{wb}=0, S_θ=26.6°)

Figure 4.9 shows the lateral capacity ratio of the 3*D* spaced 3×3 pile group varied

with S_{gd} calculated using different methods. From the 3D FE analyses, the lateral capacity ratio decreased from 1 to 0.42 when S_{gd} increased from 0 to 2.8De (or 6D), indicating a 58% loss in the lateral capacity.

Surprisingly, despite applying only for single piles, FHWA-DS produced the most agreeable results of scoured pile groups as compared with the 3D FEM, with the difference of -4% to 10%. The proposed methods (IAM and IDM) and API also compared well with the 3D FEM, with the difference of 0 to 14%, while the method of Lin and Lin (2020) underestimated the lateral capacity ratio by up to 22%. In contrast, FHWA-DP considerably overestimated the lateral capacity ratio by up to 47% as the neglect of scour-induced loss in the vertical effective stress. The above results demonstrate that all the methods assessed except FHWA-DP are suitable for use when S_θ=26.6°, and the IAM is approved to be an improvement over Lin and Lin (2020).

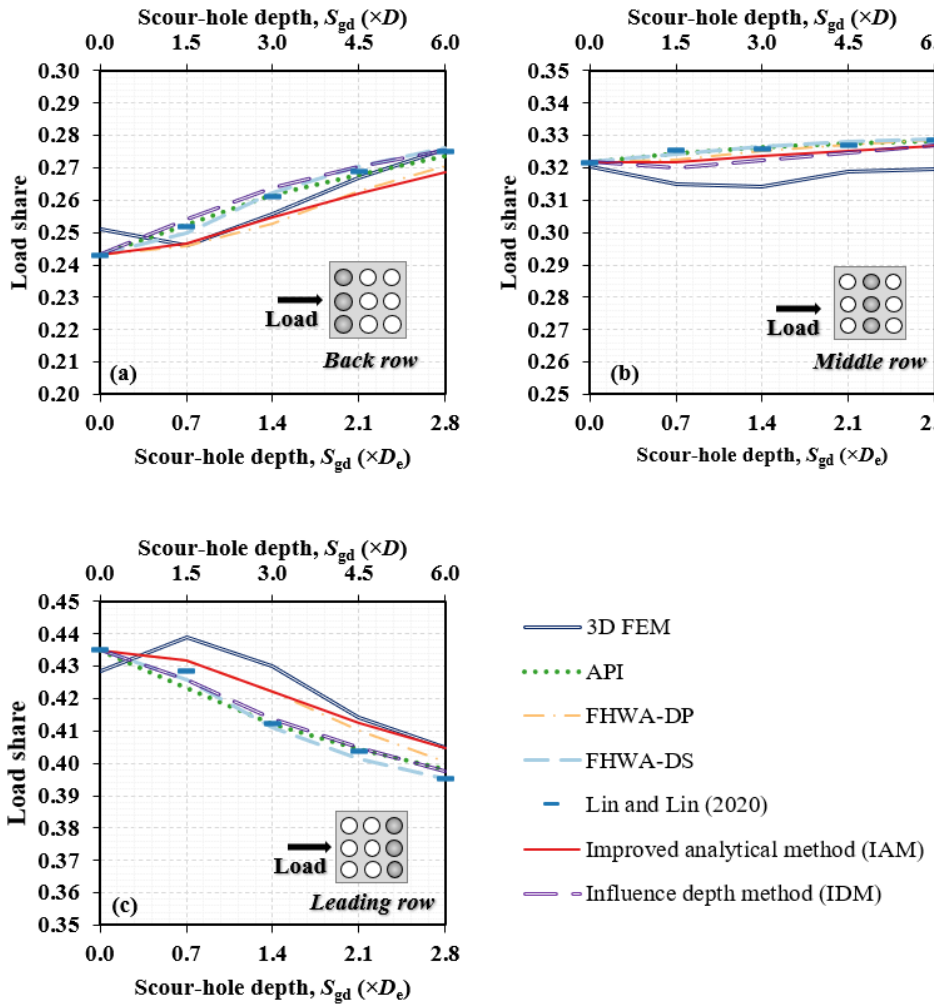

Figure 4.10 Load shares of (a) back row, (b) middle row, and (c) leading row piles under different scour-hole depths (S_{wb}=0, S_θ=26.6°)

Figure 4.10 shows load shares of pile rows varied with S_{gd}. The load share of each row is defined as the lateral load carried by the pile row divided by the total load applied to the pile group that mobilized the pile head laterally by 1 inch. The load share from the 3D FEM increased by10% for the back row but decreased by 6% for the leading row when S_{gd} increased from 0 to $2.8D_e$. This result indicates that as local scour intensified, the back row attracted more lateral load while the leading row took less lateral load. Figure 4.10 also shows that the proposed IAM exhibited a better match with the 3D FEM than the other methods, which indirectly verifies the assumption that f_m remained unchanged with the change in S_{gd} as mentioned in Section 4.6.1. Furthermore, Figures 4.11(a)-(c) profile the bending moment of piles in the back, middle, and leading rows, respectively.

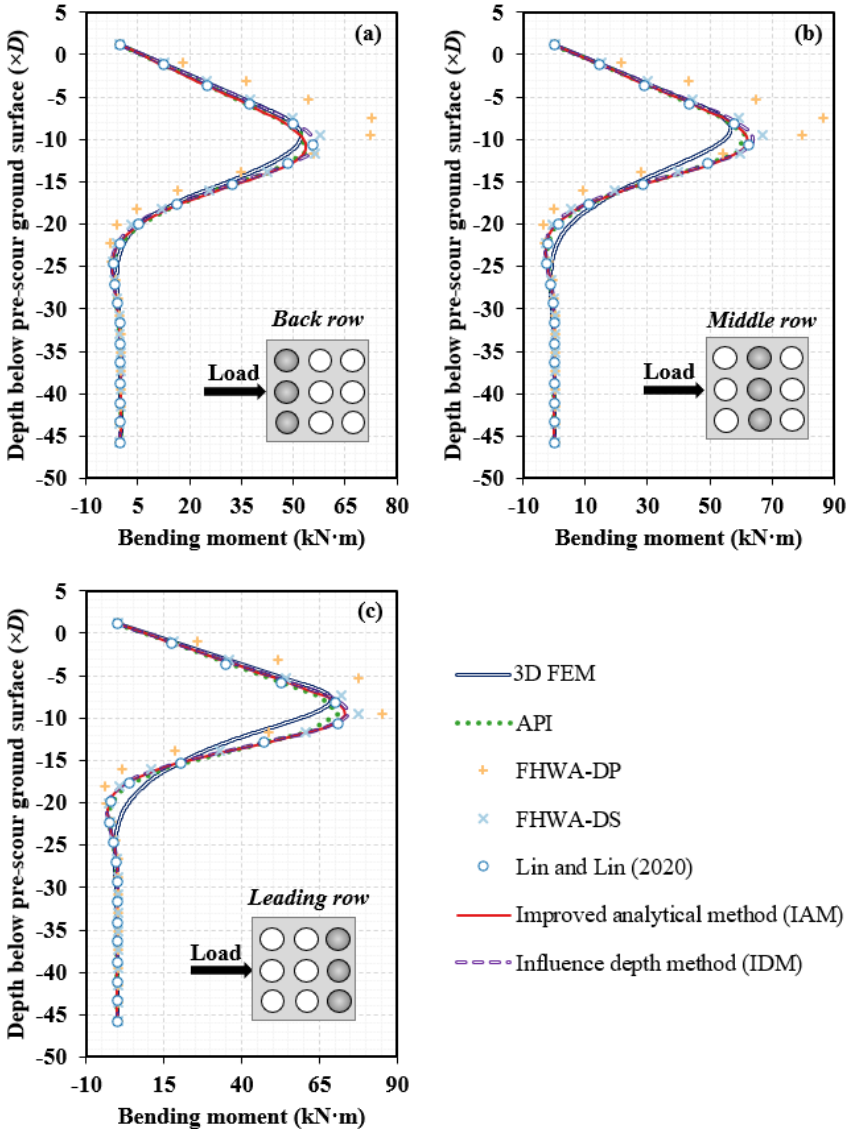

Figure 4.11 Post-scour (S_{gd}=2.8D_e, S_{wb}=0, S_θ=26.6°) bending moments of (a) back row, (b) middle row, and (c) leading row piles (3×3 pile group with 3D spacing)

Compared with the 3D FEM, FHWA-DP overestimated the average bending moments of back-row, middle-row, and leading-row piles by up to 39%, 53%, and 50%, respectively, while all the other methods including IAM and IDM produced consistent and agreeable estimates. In general, maximum bending moments decreased by 17%-20% when S_{gd} increased from $0.7D_e$ to $2.8D_e$ (i.e., $1.5D$ to $6.0D$). Meanwhile, the location of the maximum bending moment moved downward relative to the pile top by $2.4D$-$3.0D$.

4.6.2.2 Effect of scour-hole slope angle

Figure 4.12 shows the lateral capacity ratio for S_θ=0°-42° while the other scour-hole dimensions were maintained constant (S_{gd}=1.4D_e, S_{wb}=0). When S_θ=0°, a local scour turned into a general scour, while the upper bound of the scour-hole slope angle (S_θ=42°) was set to be less than the internal friction angle of sand (ϕ'=43°).

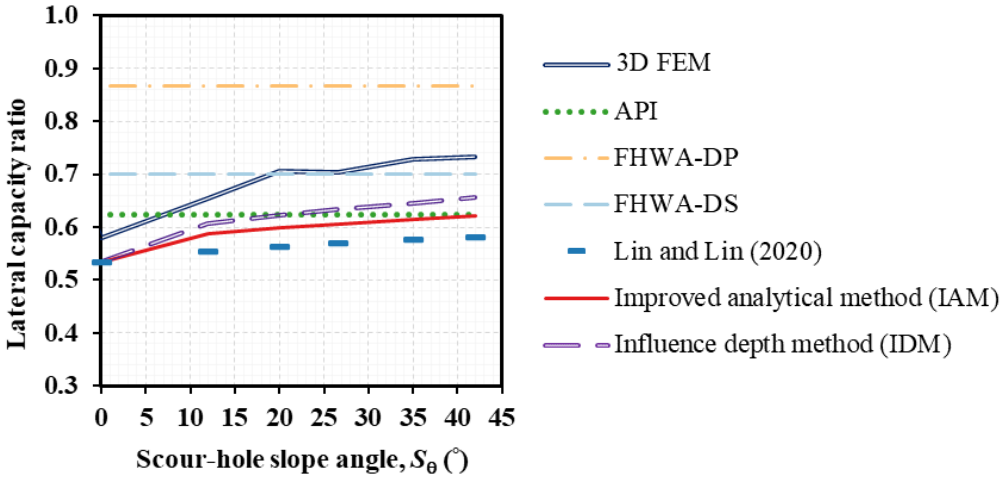

Figure 4.12 Lateral capacity ratio (3×3 pile group with 3*D* spacing) varied with scour-hole slope angle (S_{gd}=1.4D_e, S_{wb}=0)

The results by the proposed methods (IAM and IDM) showed similar trends to the 3D FEM: i.e., the lateral capacity ratios increased with the increase in S_θ, although the magnitudes were slightly lower but conservative, and the difference in the magnitude was attributed to the discrepancy of lateral capacity ratio existed at S_θ=0°. Moreover, both IAM and IDM were superior to Lin and Lin (2020) as compared with the 3D FEM. When S_θ decreased from 26° to 0°, the lateral capacity ratio decreased by 25%. This indicates that simplifying a local scour as a general scour, which is commonly used in practice for foundation design, could underestimate the lateral capacity of a pile group by up to 25%. Contrarily, the results of the

standard methods were all featured by a constant line as they could not consider the changes in S_θ or S_{wb}. FHWA-DP on average overestimated the lateral capacity ratio by 25% when S_θ=0°-42°. Although FHWA-DS compared well with the 3D FEM when S_θ=20°-42°, it overestimated the lateral capacity ratio by up to 20% when S_θ<20°, which is unsafe. For a scoured pile group, the existing data (Table 4.2) showed that S_θ could be less than 15° (Bayram and Larson, 2000; Butch, 1996; Harris and Whitehouse, 2014; Sun et al., 2007). In this circumstance, FHWA-DS could yield an unconservative design. API generally gave conservative results, except $S_\theta \leq 5°$ in which it overestimated the lateral capacity ratio by up to 8%.

Figure 4.13 shows load shares of pile rows varied with S_θ. As previously mentioned, the soil lateral resistance to the leading row is different from that to the back row.

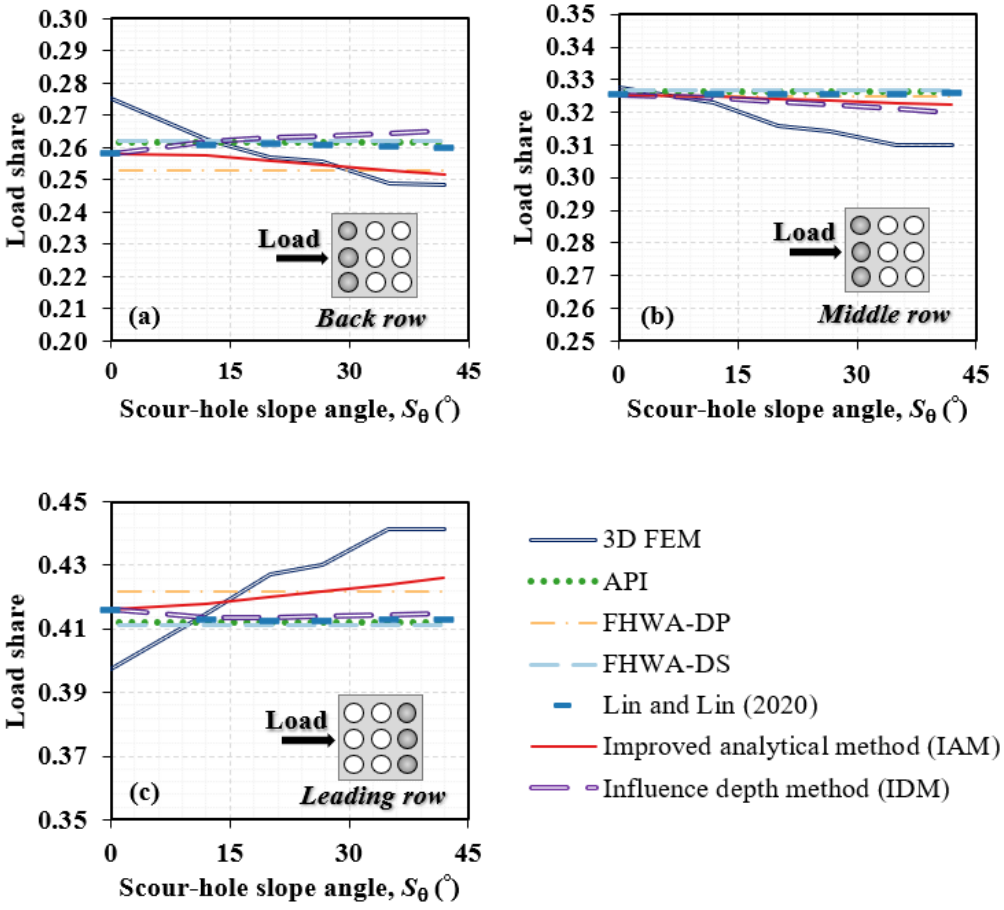

Figure 4.13 Load shares of (a) back row, (b) middle row, and (c) leading row piles (3×3 pile group with 3*D* spacing) under different scour-hole slope angles (S_{gd}=1.4D_e, S_{wb}=0)

In general, the leading row is anticipated to resist more lateral load with increased S_θ as higher passive earth pressures developed in front of it, and the opposite is anticipated for the

back row as higher active pressures developed behind it. This phenomenon was manifested by the 3D FEM and IAM (Figure 4.13), showing a higher lateral load on the leading row but a lower lateral load on the back row as S_θ increased. Although the changes in the load shares estimated by the IAM were slightly narrower than those by the 3D FEM, the trends were similar. However, the other methods gave insignificant or no changes in load share with increased S_θ, which is incorrect. The reason is that the increases in the active earth pressure to the back row and the passive earth pressure to the leading row due to the increased S_θ were not considered in these methods.

4.6.2.3 Effect of soil relative density

Besides the influences of scour-hole dimensions, effects of soil condition on the post-scour lateral responses of pile groups were examined. As shown in Figure 4.14, when S_{gd} increased from 0 to 2.8D_e, scour-induced loss in the lateral capacity was 58%, 50%, and 45% for the pile group in dense, medium dense, and loose sands, respectively from the 3D FEM; similar results were also obtained by the IAM (65%, 57%, and 53%) and IDM (64%, 55%, and 51%).

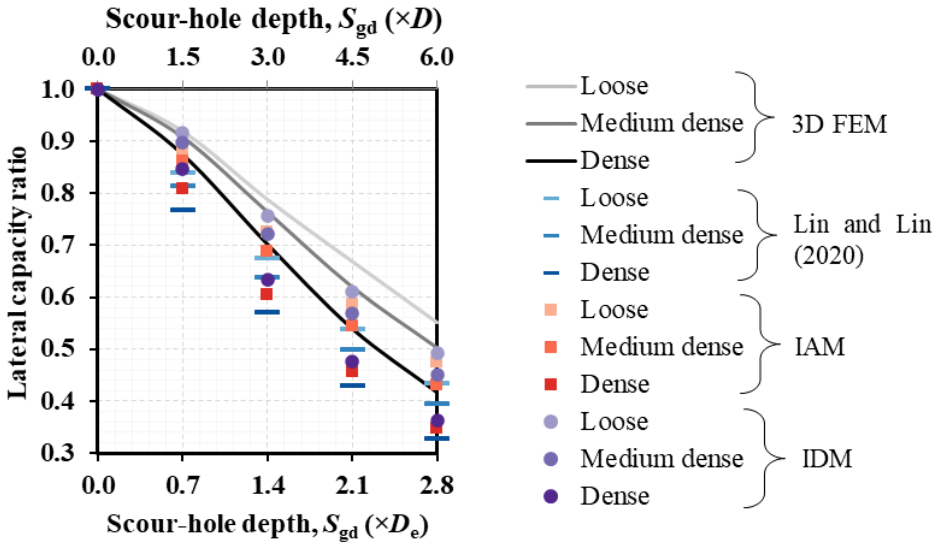

Figure 4.14 Effects of soil relative density on lateral capacity ratios (3×3 pile group with 3*D* spacing) vs. scour-hole depths (S_{wb} = 0, S_θ = 26.6°)

These results indicate that scour caused more loss in the lateral capacity (up to 13%) of the pile group in dense sands than in loose sands, particularly for greater S_{gd}. Overall, the proposed methods (IAM and IDM) provided better estimations of lateral capacity ratio than Lin and Lin (2020). In addition, pile bending moments were profiled in various soil conditions

but under the same scour-hole dimensions (S_{wb}=0, S_{gd}=1.4D_e, S_θ=26.6°). Figure 4.15 shows that the bending moments determined by the IAM and IDM were comparable with those by the 3D FEM.

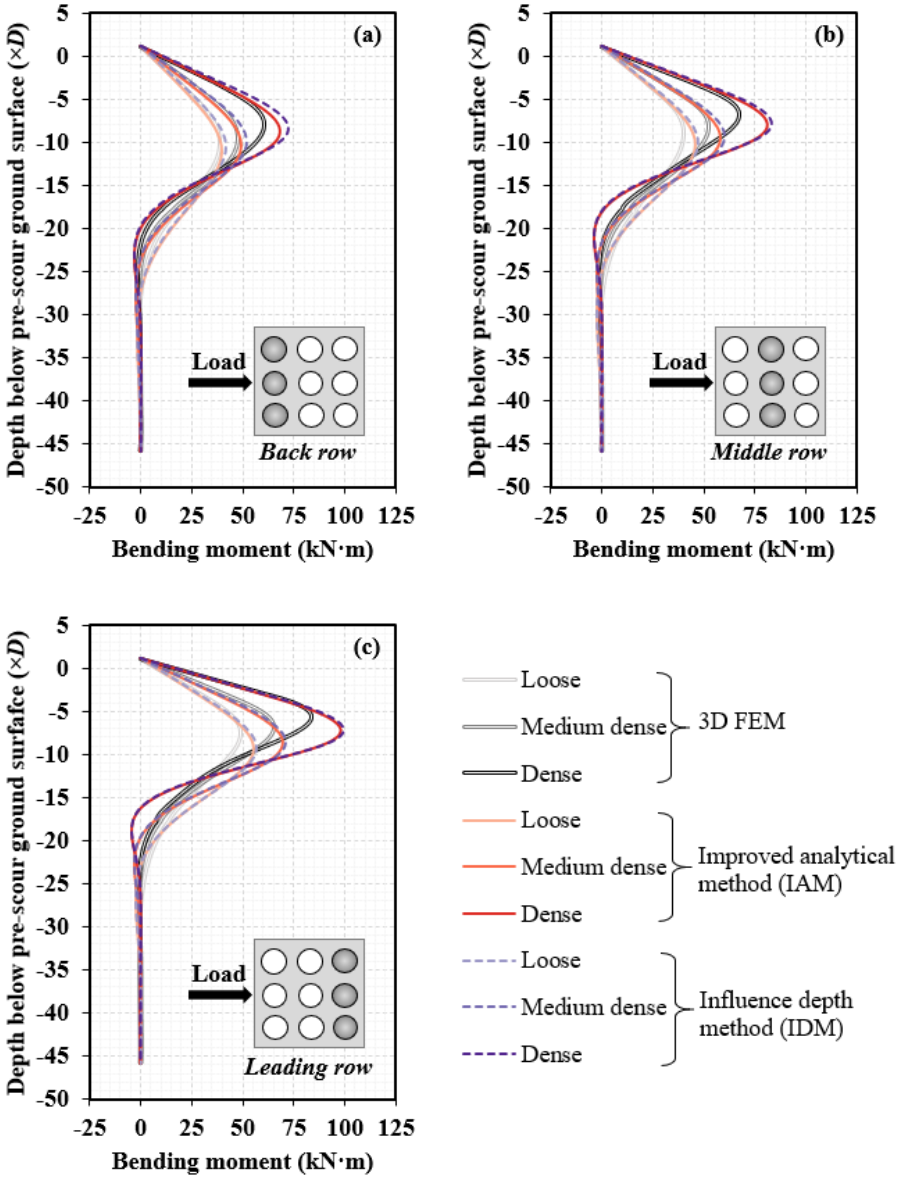

Figure 4.15 Effects of soil relative density on post-scour (S_{gd}=1.4D_e, S_{wb}=0, S_θ=26.6°) bending moments of (a) back row, (b) middle row, and (c) leading row piles (3×3 pile group with 3D spacing)

In general, the maximum bending moment increased with the increased relative density of sands, and the increases were 71%-76% and 57%-70% by the IAM and 3D FEM, respectively. Meanwhile, the location of the maximum bending moment shifted downward by 2.1D when the relative density increased from loose to dense.

4.6.2.4 Effects of pile spacing and number of piles

As mentioned in Section 4.3, in contrast to scour at a single isolated pile, scour at a pile group is influenced not only by hydraulic conditions (e.g., Froude number, Keulegan-Carpenter number, flow direction) but also pile group conditions (e.g., pile spacing, pile number, pile group configuration) due to the hydraulic group effects (i.e., reinforcement, sheltering, shed vortices, and jetting effects). In general, reinforcement and sheltering effects that intensify scour at the upstream pile can be attenuated by increasing the pile spacing in-line with the flow. Likewise, jetting effect that wipes out soils between side-by-side piles as the compression of inner arms of horseshoe vortices can also be weakened by increasing the pile spacing normal to the flow. Moreover, shed vortices that intensify scour at the downstream pile on the path of wake vortices are more significant in a staggered pile group arrangement (Hosseini and Amini, 2015; Lança et al., 2013; Sumer and Fredsøe, 1998). Therefore, the following two sections will focus on the effects of pile spacing, pile number, and pile group configuration on the post-scour responses of pile group.

As indicated by Table 4.1, global scour could develop and dominate the scour-hole geometry at pile groups when s<5.5D. Here, we assume global scour occurred for s=2D-6D, which covers the typical range of spacing in the general design of pile groups. Figure 4.16 shows the lateral capacity ratio varied with the pile spacing when S_{wb}=0, S_{gd}=3D, and S_{θ}=26.6°. Based on the 3D FE analyses, the lateral capacity ratio decreased by 4% as s increased from 2D to 6D. The proposed methods (IAM and IDM) yielded agreeable lateral capacity ratios with the 3D FEM with differences less than 0.1. As with Figure 4.9 and Figure 4.12, API produced similar results to IAM and IDM, while FHWA-DP significantly overestimated the lateral capacity ratio, which is unsafe. Although FHWA-DS produced the best comparable results with the 3D FEM when S_{θ}=26.6°, it could overestimate the lateral capacity ratio when S_{θ}≤20° as shown in Figure 4.12, which is also unsafe.

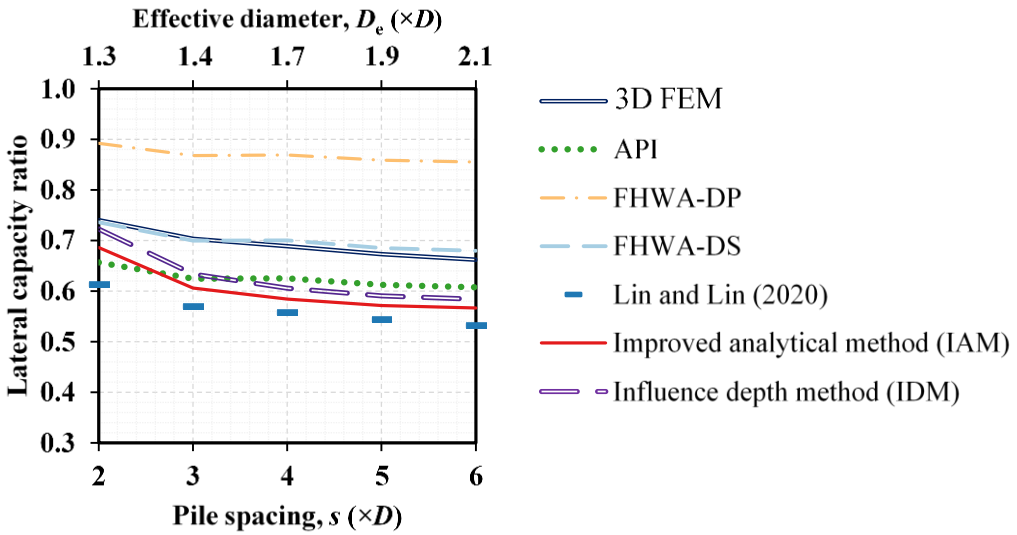

Figure 4.16 Effects of pile spacing on lateral capacity ratios of a 3×3 pile group (S_{gd}=3D, S_{wb}=0, S_θ=26.6°)

Furthermore, the effect of the number of piles on the lateral capacity ratio was investigated by considering three sizes of pile groups: 2×2 (S_{gd}=3D=1.97D_e), 3×3 (S_{gd}=3D=1.40D_e), and 4×4 (S_{gd}=3D=1.05D_e). As shown in Table 4.6, the effect of increasing the number of piles on the lateral capacity ratio was negligible, displaying only a slight increase (4%). Compared with the 3D FEM, IAM and IDM underestimated lateral capacity ratios by 13% and 9%, respectively, while Lin and Lin's method by 18%. However, FHWA-DP overestimated it by 24%. Again, for S_θ=26.6° which is greater than 20°, FHWA-DS agreed best with the 3D FEM, and API yielded similar results to the 3D FEM and IAM.

Table 4.6 Effect of the number of piles on the lateral capacity ratio (S_{gd}=3D, S_{wb}=0, S_θ=26.6°)

Pile group (m×n)	Lateral capacity ratio (S_{gd}=3D, S_{wb}=0, S_θ=26.6°)						
	3D FEM[1]	IAM	IDM	Lin and Lin (2020)	API	FHWA-DP	FHWA-DS
2×2	0.69	0.60	0.63	0.58	0.61	0.86	0.68
3×3	0.70	0.61	0.63	0.57	0.62	0.87	0.70
4×4	0.72	0.63	0.66	0.58	0.66	0.89	0.74

Note: [1]3D FEM results were extracted from Lin and Lin (2020).

4.6.2.5 Effect of pile group configuration

The previous results were determined for the square pile group, a prerequisite assumed by the method of Lin and Lin (2020). The proposed methods (IAM and IDM)

were developed for different shaped pile groups. To assess the effect of pile group configuration, pile groups with three configurations ($m \times n$=6×5, 10×3, 15×2) but the same number of piles (30) and spacing (s=3D) were evaluated using the IAM and IDM under local-scour conditions. For comparison purposes, it is assumed that the standard methods (Figure 4.3) might be applied to the scoured pile groups with rectangular configurations. The p-multipliers used for the three pile groups were evaluated from ASSHTO (2012) (Figure 4.7). The lateral capacity ratios were computed for different scour depths (S_{gd}=0.7D_e-2.8D_e, S_θ=26.6°, S_{wb}=0) (supplementary Figure S4.3) and different scour-hole slope angles (S_θ=0°-26.6°, S_{gd}=2.8D_e, S_{wb}=0) (supplementary Figure S4.4). Figure 4.17 was reduced from supplementary Figure S4.3 and Figure S4.4 by selecting a given scour-hole depth (S_{gd}=1.4D_e) to evaluate the shape effect.

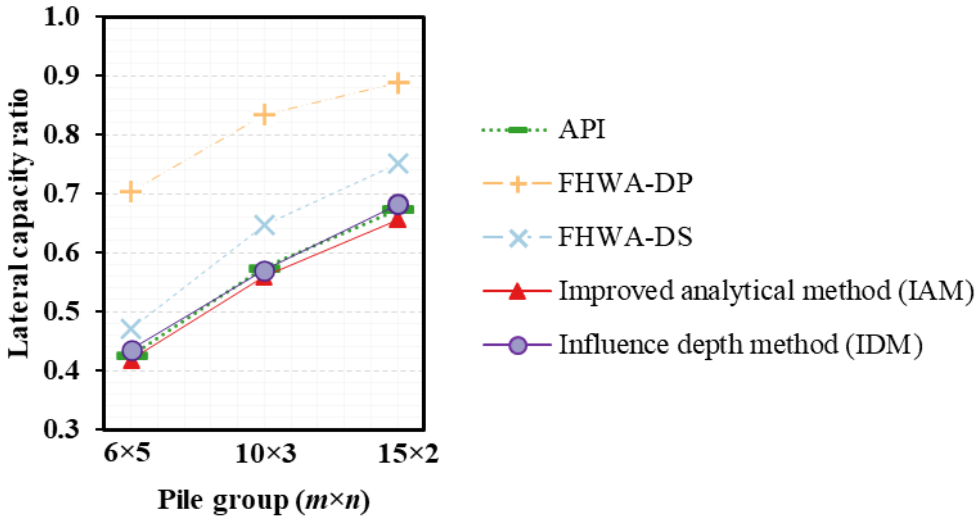

Figure 4.17 Lateral capacity ratios vs. pile group configuration: (a) 6×5, (b) 10×3, and (c) 15×2 (s =3D, S_{gd} =1.4D_e, S_{wb} =0, S_θ =26.6°)

Surprisingly, increasing the aspect ratio of the pile group (approximately equal to m/n) resulted in an increase in the lateral capacity ratio. For the case analyzed, the lateral capacity ratio increased by 57% when m/n increased from 1.2 to 7.5. In other words, given the same number of piles (mn), the square pile group could subject to more scour-induced loss in the lateral capacity than the rectangular pile group. The standard methods (API, FHWA-DP, and FHWA-DS) could also capture this trend, although they might not be technically correct.

4.7 Conclusions

This study proposed a new approach called the improved analytical method (IAM) for analyzing the laterally loaded pile groups under local-scour conditions. Drawing on the IAM and the concept of influence depth in the standard methods (API, FHWA-DP, and FHWA-DS), a simple and practical influence depth method (IDM) was also proposed. The proposed methods (IAM and IDM) were validated against the results of the 3D FE model that was calibrated against a full-scale load test. Two MATLAB programs were developed to implement the IAM and IDM, with which 288 parametric analyses were performed to evaluate the factors (scour-hole depth, scour-hole slope angle, soil relative density, pile spacing, number of piles, and pile group configuration) affecting the post-scour behavior of pile groups in sands. The standard methods and the method of Lin and Lin (2020) were critically assessed in the parametric study. The following conclusions were obtained from this study:

(1) Compared with the 3D FEM, the proposed IAM and IDM produced agreeable and conservative estimates of the lateral capacity and maximum bending moment of pile groups. FHWA-DP significantly overestimated the lateral capacity, which is thus unsafe and not recommended for use. For typical scour-hole dimensions (S_θ=26.6° or 30°) recommended in practices, API and FHWA-DS could be used to yield agreeable prediction of the lateral capacity. However, when S_θ<20° as often encountered in the field per the literature survey, API and FHWA-DS overestimated the lateral capacity, and therefore are unsafe.

(2) The increase in scour-hole depth, S_{gd}, decreased the lateral capacity and maximum bending moment of pile groups, and shifted the location of the maximum bending moment toward the post-scour ground surface. Besides, more lateral loads were transferred to the back row as S_{gd} increased. The proposed IAM yielded a better prediction of the load share as compared with the 3D FEM than the standard methods and Lin and Lin's method.

(3) The lateral capacity and maximum bending moment increased as the scour-hole slope angle, S_θ, increased. The increase in S_θ increased the load share of the leading row but decreased the load share of the back row, which was only captured by the IAM and 3D FEM; while neither the standard methods nor Lin and Lin's method could capture the change in load share with S_θ.

(4) Although adopting a larger pile spacing, *s*, could reduce the geotechnical group effect, scour-induced reduction in the lateral capacity increased as *s* increased given the same local-scour depth. The scour-induced decrease in the lateral capacity was more significant in the square pile group than the rectangular pile group (loading along the length of the pile group) given the same total number of piles. Therefore, the use of a pile group in rectangular configuration is recommended in the foundation design against scour.

4.8 Notation

A_b = area of scour-hole bottom

A_e = area enclosed by the $\sigma'_{z,sc}/\sigma'_{z,int}$ profile and the right vertical axis ($\sigma'_{z,sc}/\sigma'_{z,int}$=1.0) in the depth distribution of vertical stress ratio

$\bar{A}_s$ = static load-type factors dependent on soil depth defined in Reese's *p-y* curve

$\overline{A}_{sa}$ and $\overline{B}_{sa}$ = static load-type factors dependent on z_{ea}/D

$\overline{A}_{sp}$ and $\overline{B}_{sp}$ = static load-type factors dependent on z_{ep}/D

$\bar{B}_s$ = static load-type factors dependent on soil depth defined in Reese's *p-y* curve

D = pile diameter

D_e = effective diameter of a pile group defined by Sheppard (2003)

f_d = factors considering the effect of scour depth in the calculation of η

f_m = *p*-multiplier (usually ≤1.0) that considers geotechnical pile group effect

f_s = factor considering the effect of pile spacing in the calculation of η

h_j = height of soil column defined in the proposed method, j =1, 2, …, J

J = number of soil columns

J_a = number of soil columns within the intermediate-active pressure zone

J_p = number of soil columns within the intermediate-passive pressure zone

K_A = coefficient of active earth pressure, $K_A=\tan^2(45°-\phi'/2)$

K_o = coefficient of earth pressure at rest, taken as $1-\sin\phi'$ for normally consolidated soils

L_b = length of the scour-hole bottom in the proposed method

L_e = post-scour embedded length of pile

L_{ij} = distance between the point of interest in the i^{th} pile to the center of the j^{th} soil column bottom, i= 1, 2, …, mn

m = number of piles in-line with the lateral load direction

n= number of piles normal to the lateral load direction

P_j = weight of the j^{th} soil column, j =1, 2, …, J

p = lateral soil resistance per unit length of a pile

p_m = soil resistance corresponding to y_m in Reese's sand p-y curve, $p_m=\overline{B}_s p_{ult}$

p_u = soil resistance corresponding to y_u in Reese's sand p-y curve, $p_u=\overline{A}_s p_{ult}$

p_{ult} = ultimate lateral soil resistance per unit length of a pile, $p_{ult}=\min\{p_{ult,s}, p_{ult,d}\}$

$p_{ult,d}$ = ultimate lateral soil resistance per unit length of a pile at greater depths

$p_{ult,s}$ = ultimate lateral soil resistance per unit length of a pile at shallow depths

S_{gd} = scour-hole depth around a pile group

S_{sd} = scour-hole depth around a single isolated pile

S_{wb} = scour-hole bottom width around a pile group

S_{wc} = distance from the scour-bottom perimeter to the center pile, $S_{wc}=(A_b/\pi)^{0.5}-0.5D$

S_θ = scour-hole slope angle around a pile group

s = center-to-center pile spacing

y_k = a specific pile deflection in Reese's sand p-y curve that transits the initial linear portion to a parabolic portion

y_m = a specific pile deflection in Reese's sand p-y curve, $y_m=D/60$

y_u = a specific pile deflection in Reese's sand p-y curve, $y_m=3D/80$

W_b = width of the scour-hole bottom in the proposed method

(x_p, y_p) = coordinates of the i^{th} pile

(x_s, y_s) = coordinates of the j^{th} soil column

y = lateral soil displacement

z = depth below post-scour ground surface

z_e = equivalent depth that considers scour effect, $z_e=\sigma'_{z,sc}/\gamma'$

z_{ea} = equivalent depth corresponding to the intermediate-active pressure zone, $z_{ea}=\sigma'_{za,sc}/\gamma'$

z_{ep} = equivalent depth corresponding to the intermediate-passive pressure zone, $z_{ep}=\sigma'_{zp,sc}/\gamma'$

z_i = influence depth that considers scour effect, below which $\sigma'_{z,sc}=\sigma'_{z,int}$

α = angle of the passive failure wedge in the horizontal direction, $\alpha=\phi'/2$

α_f = flow skew angle

β = angle of the passive failure wedge with the ground surface, $\beta=45°+\phi'/2$

γ' = effective unit weight of soil

Δx = width of soil column on x direction in the proposed method

Δy = width of soil column on y direction in the proposed method

$\Delta\sigma'_z$ = vertical effective stress resulting from soil overburden above the post-scour ground surface

$\Delta\sigma'_{za}$ = addition vertical effective stress considering the soil overburden within the intermediate-active pressure zone

$\Delta\sigma'_{zp}$ = addition vertical effective stress considering the soil overburden within the intermediate-passive pressure zone

η = a semi-empirical correction factor to account for the effect of soil-pile interface friction on retaining vertical effective stress in soils after scouring, $\eta=f_d f_s$

λ = parameter used to form the parabolic portion in Reese's sand p-y curve, $\lambda=y_m(p_u-p_m)[p_m(y_u-y_m)]^{-1}$

σ'_z = vertical effective stress resulting from soil overburden below the post-scour ground surface

$\sigma'_{za,sc}$ = post-scour vertical effective stress corresponding to the intermediate-active pressure zone

$\sigma'_{zp,sc}$ = post-scour vertical effective stress corresponding to the intermediate-passive pressure zone

$\sigma'_{z,sc}$ = post-scour vertical effective stress of soil at pile

$\sigma'_{z,int}$ = pre-scour vertical effective stress of soil at pile

ϕ' = effective friction angle of soil

Ψ_{ij} = influence factor depending on L_{ij}

Chapter 5 Scour Effects on Lateral Responses of Pile Groups in Clays

5.1 Abstract

In contrast to single piles, pile groups experience more capacity loss by scour due to not only geotechnical group effect but also hydraulic group effect. However, existing standards only include design considerations for scoured single piles, and scour effects on lateral behavior of pile groups are not fully appreciated. This study proposes a practical method to analyze the lateral behavior of pile groups in soft clays affected by local scour. The proposed method was verified against the results of 3D continuum finite element (FE) models, in which the baseline no-scour 3D model was established based on a reported full-scale load test. Parametric analyses were conducted to investigate the effects of scour-hole dimensions and pile group configurations on the lateral responses of pile groups in soft clays. The suitability of applying the methods specified in the various standards for a scoured single isolated pile to a scoured pile group was assessed by comparing them with the proposed method and 3D FE analyses. The results also highlighted the importance of the hydraulic group effect in the evaluation of lateral behavior of scoured pile groups. This research recommends a rectangular pile group shape with greater pile spacing in the foundation design against scour.

5.2 Introduction

Affected by waves and currents, offshore platforms and bridges are vulnerable to scour as a result of the loss of soil supports to their foundations (Briaud, 2015; Coleman and Melville, 2001; Imhof, 2004; Lagasse et al., 2007; Liang et al., 2017; Watson, 1974; Whitehouse, 1998). The risk of scour-related damages is anticipated to be more severe with climate change, which would not only intensify the extent and frequency of storms and floods but also increase the temperature and acidity of water (Anderson et al., 2014; Nemry and Demirel, 2012). Scour at marine installations includes general scour (a uniform decrease in seabed elevation) and local scour (a localized decrease in seabed elevation, mainly around piles) (Whitehouse, 1998). The local scour at a pile group can

be further classified into global scour (a shallow wide depression covering the footprint of pile group) and localized pit (steep-sided holes formed at individual piles) (Sumer et al., 2005). The mechanisms of scour developed at a pile group involve not only downflow, horseshoe vortex, and lee wake vortices that form at individual piles (Whitehouse, 1998) but also reinforcement, sheltering, shed vortices, and jetting effects (Hannah, 1978; Hosseini and Amini, 2015) that result from a complex flow-structure interaction (i.e., hydraulic group effect). Therefore, scour at pile groups is more complicated and tends to be more severe than at single isolated piles.

Based on an extensive review, Jiang and Lin (2021) recommend that for design purposes, when $s \leq 5D$ (s = pile spacing, D = pile diameter), local scour at a pile group can be characterized by a global scour hole with the shape of an inverted truncated pyramid with a rounded-quadrilateral cross section (Figure 5.1). The scour hole can be described with three dimensions: scour-hole depth, S_{gd}, slope angle, S_θ, and bottom width, S_{wb}. For scour depth at a pile group, S_{gd} is often normalized by an effective diameter, D_e, of a pile group (Sheppard, 2003) to reflect effects of pile group configuration and flow conditions on scour depth (Figure 5.2), and facilitate the comparison of scour severity between a pile group and a single pile. More information about the determination of D_e is presented in Section 5.5. In general, the normalized scour depth for a pile group falls within a range of S_{gd}/D_e=1.2-2.0 (Jiang and Lin, 2021), which is comparable to that for a single isolated pile (S_{sd}/D=1.3-2.5) (API, 2011; DNV, 2014; GL, 2012). The values of S_θ observed at offshore pile groups are 5°-15° (Bayram and Larson, 2000; Sun et al., 2007), which are somehow smaller than the typical values (26.6° and 30°) used in the post-scour design analyses of foundations under bridges (Arneson et al., 2012) and marine structures (Whitehouse, 1998).

In designing laterally loaded piles under local scour, two approaches can be referenced (Lin and Lin, 2019), which are established based on the *p-y* curve framework through modifying the ultimate soil resistance, p_{ult}. The first approach (Lin and Jiang, 2019; Lin and Wu, 2019; H. Zhang et al., 2017) involves the calculation of vertical effective stress of soils at piles after local scour, $\sigma'_{z,sc}$, which is then substituted into the equations for p_{ult} to account for scour effects, while the second approach (Lin et al., 2016, 2014a) involves calculating p_{ult} directly using the wedge failure model with scour hole. The first approach has been mentioned in the design standards such as American Petroleum Institute (API, 2011), U.S. Federal Highway Administration-Drilled Shaft (FHWA-DS) (Brown et al., 2010), and Driven Pile (FHWA-DP) (Patrick et al., 2016),

and details will be given in the next section.

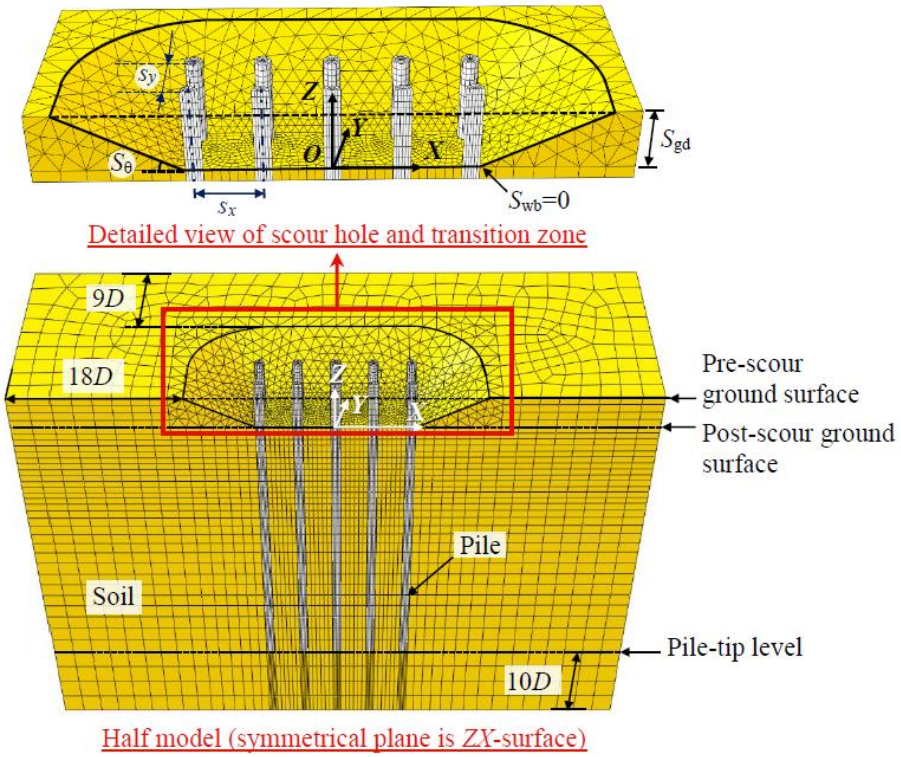

Figure 5.1 Three-dimensional model of a scour hole at a 5×3 pile group

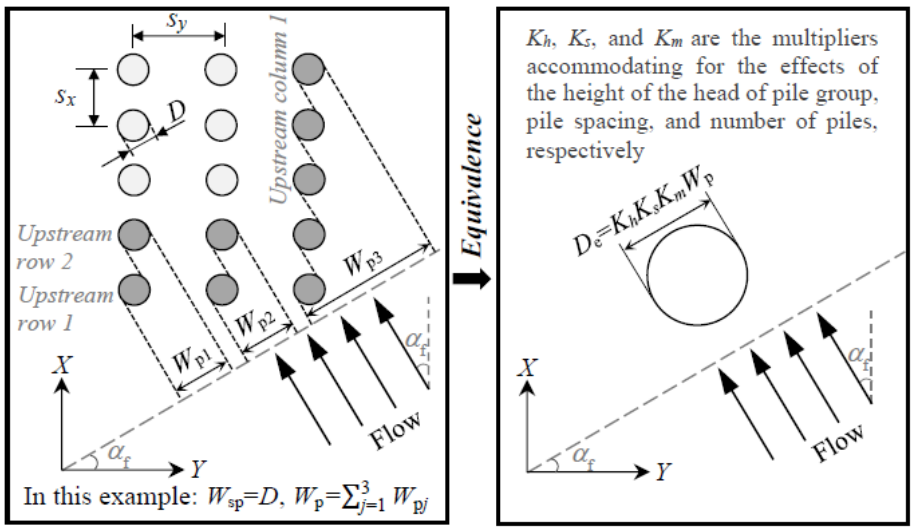

Figure 5.2 Illustration of effective group diameter

The above-mentioned approaches are only applicable for scoured single piles. Nevertheless, piles are typically installed in a group to support a superstructure, and scour susceptibility of pile groups is more significant than single isolated piles due to the dual group effects: hydraulic and geotechnical group effects (Jiang and Lin, 2021).

The hydraulic group effect results in an increased scour depth while the geotechnical group effect causes a reduced average lateral resistance per pile in a pile group as compared with a single isolated pile. Despite a higher risk of pile groups to scour, there is a dearth of studies concerning the lateral behavior of pile groups under scour conditions (Jiang and Lin, 2021; Liang et al., 2020; Lin and Lin, 2020; H. Ma et al., 2018), and in these limited studies, only sandy soils are considered. In fact, scour can develop not only in sands but also in clays (Harris and Whitehouse, 2017).

The overarching goal of this study was to develop a method for analyzing the lateral behavior of pile groups in soft clays under local scour conditions. Firstly, we proposed a practical method for scoured pile groups in soft clays based on the *p*-*y* curve framework by combined application of the first approach (calculation of $\sigma'_{z,sc}$) and the second approach (development of wedge failure model) as previously mentioned. The proposed method was verified against 3D continuum finite element (FE) analyses, in which the baseline no-scour 3D FE model was confirmed with a full-scale lateral load test (Snyder, 2004). With the verified proposed method, a parametric study was conducted to investigate the effects of scour-hole dimensions and pile group configurations on the lateral responses of pile groups. Secondly, we assessed the suitability of applying the standard methods (API, FHWA-DP, and FHWA-DS) that are developed for scoured single isolated piles to analyze scoured pile groups. This mistaken use can occur as a result of lacking specifications for scoured pile groups in the present design standards.

This paper starts with a review of existing solutions for calculation of the vertical effective stresses at piles under local scour conditions, which is required for development of the first approach, followed by development and verification of the proposed method with the aid of 3D FE analyses. Subsequently, the results of 182 cases of parametric analyses for scoured pile groups in soft clays are presented, in which the standard methods are critically assessed, and some design-related issues are discussed.

5.3 Review of standard methods for estimation of post-scour vertical effective stress

For the first approach to the analysis of laterally loaded piles under local scour, the calculation of $\sigma'_{z,sc}$ is the premise. After $\sigma'_{z,sc}$ is estimated for different local-scour

conditions, the *p-y* curves for piles in soft clays can be improved to account for the effect of scour-hole dimensions on the lateral responses of piles. In this section, the standard methods (API, FHWA-DP, and FHWA-DS) for the calculation of $\sigma'_{z,sc}$ for a single isolated pile is first reviewed, which is then extended for a pile group if mistakenly used. The incorporation of $\sigma'_{z,sc}$ to modify *p-y* curves is detailed in the next section.

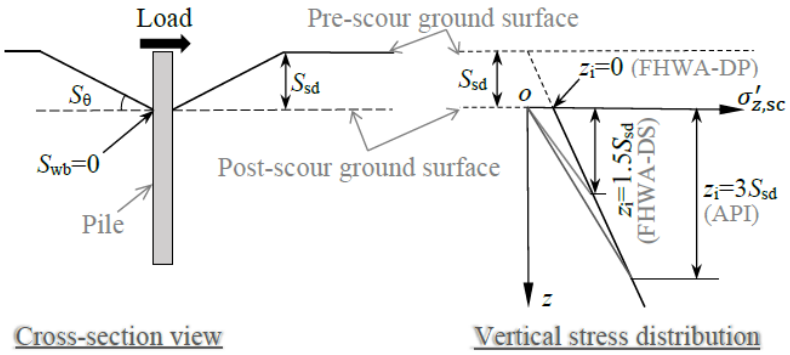

Figure 5.3 Scour-hole model and stress distribution in the standard methods

Figure 5.3 depicts the distribution of $\sigma'_{z,sc}$ calculated based on the standard methods, and the corresponding mathematical expressions are presented in Eq. (5-1). Both API and FHWA-DS acknowledge the scour-induced reduction in the vertical effective stress of soils around the pile (i.e., unloading effect), but the reduction is only restrictive to a certain depth below the post-scour ground surface. This depth is denoted as influence depth, z_i, below which the post-scour vertical effective stress equals the pre-scour one: i.e., $\sigma'_{z,sc} = \sigma'_{z,int}$. FHWA-DS assumes the influence depth to be 1.5 times the scour-hole depth below the post-scour ground surface (z_i=1.5S_{sd}). API suggests the influence depth located at a depth of 6*D* below the pre-scour ground surface, which is equivalent to z_i=3S_{sd} since API also recommends S_{sd}=1.5*D*. In contrast, FHWA-DP neglects the unloading effect in the remaining soils; therefore, the vertical effective stress of soils remains unchanged after scour and z_i=0. By normalizing the post-scour stress to the pre-scour stress, Eq. (5-1) is transformed to Eq. (5-2).

$$\sigma'_{z,sc} = \begin{cases} \gamma' z(1 + S_{sd}/z_i) & \text{for } z < z_i \\ \gamma'(S_{sd} + z) & \text{for } z \geq z_I \end{cases} \tag{5-1}$$

$$\frac{\sigma'_{z,sc}}{\sigma'_{z,int}} = \begin{cases} \frac{z(S_{sd}+z_i)}{z_i(S_{sd}+z)} & \text{for } z < z_i \\ 1.0 & \text{for } z \geq z_I \end{cases} \tag{5-2}$$

where z = depth below the post-scour ground surface; γ' = effective unit weight of soil; S_{sd} = local-scour depth for a single isolated pile. It is important to note that Eq. (5-1) is used only for scoured single piles. However, if it is applied to scoured pile groups, S_{sd} in Eqs. (5-1) and (5-2) may be replaced by the scour-hole depth of the pile group, S_{gd}.

5.4 Development of the proposed method

This study proposes a new method for analyzing the lateral behavior of pile groups in soft clays under local scour conditions through the combined use of the first approach (i.e., calculation of $\sigma'_{z,sc}$) and the second approach (i.e., application of post-scour wedge failure model). The procedure of the first approach was modified from Jiang and Lin (2021) that is established for pile groups in sands. The second approach was established for the leading row of piles only based on the method of Lin et al. (2016). The proposed method is encoded in MATLAB program, which enables calculation of both vertical effective stresses and lateral responses of pile groups in soft clays subjected to local scour.

5.4.1 Post-scour vertical stresses around piles in a pile group

In the proposed method, the scour-hole geometry is slightly modified from rounded edges (Figure 5.1) to sharp edges (Figure 5.4) for mathematical deriving convenience, while both frustums share equivalent bottom area (A_b=$L_b W_b$), length-to-width ratio (L_b/W_b), scour-hole slope angle (S_θ), and scour-hole depth (S_{gd}). Note that L_b and W_b are the length and width of the simplified scour-bottom surface, respectively. This simplified scour-hole shape with sharp edges is also used in centrifuge tests (Kariyawasam et al., 2020). Besides, a Cartesian coordinate system is adopted to define the scour-hole dimensions and pile locations in Figure 5.4, with its origin located at the upper-left corner of the scour-hole bottom and y and z axes pointing toward the lateral load and downward directions, respectively.

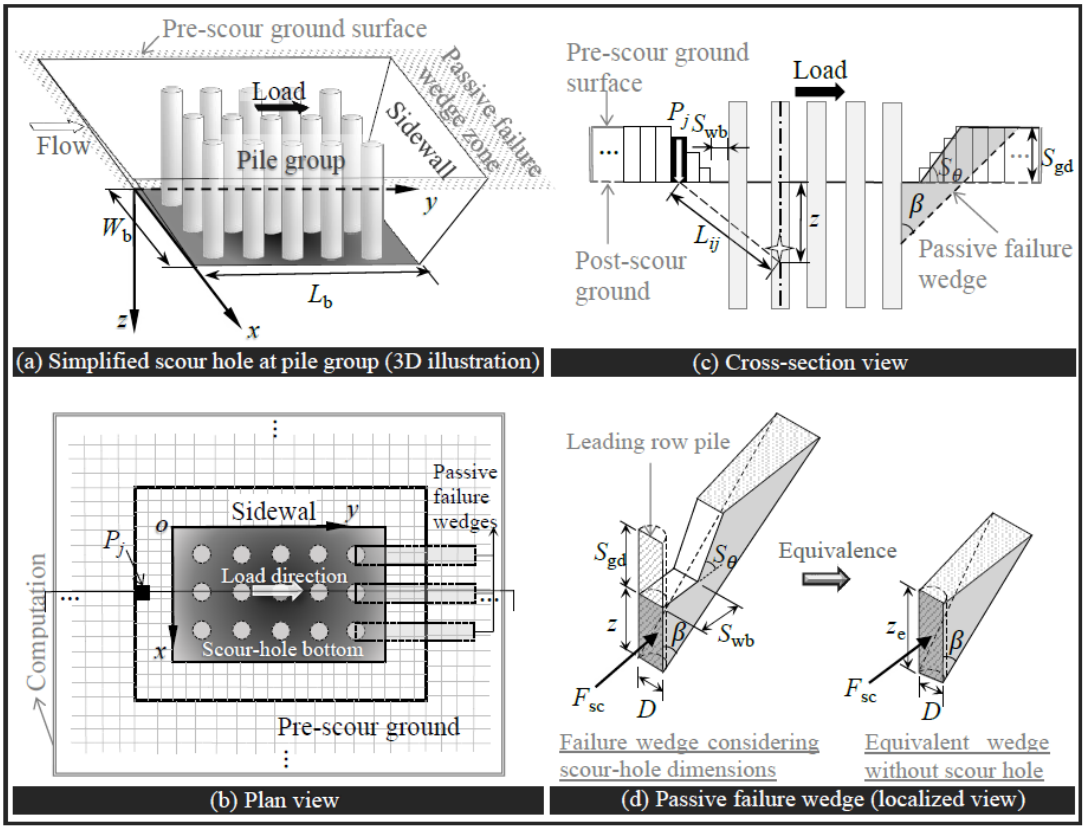

Figure 5.4 (a) 3D illustration, (b) plan view, (c) cross-section view of the proposed model for deriving post-scour vertical stresses at piles, and (d) localized view of passive failure wedge

The $\sigma'_{z,\mathrm{sc}}$ at individual piles in a pile group is the summation of the vertical effective stresses resulting from the soil overburden below and above the post-scour ground surface, i.e., $\sigma'_{z,\mathrm{sc}} = \sigma'_z + \Delta\sigma'_z$. The former can be easily calculated using $\sigma'_z = \gamma' z$ where z refers to the depth below the bottom of scour hole, while the latter (called additional vertical effective stress, $\Delta\sigma'_z$) is calculated based on the discretized soil columns above the post-scour ground surface. As shown in Figures 5.4(b) and (c), the remaining soils above the post-scour ground surface are discretized into a series of soil columns that have a width Δx=Δy=0.02D and varied height h_j=0-S_{gd} within the sloping ground domain (sidewall) but a greater width Δx=Δy=0.5D and constant height h_j=S_{gd} within the leveled pre-scour ground domain. Considering D is sufficiently small relative to the soil domain, individual piles are simplified as vertical lines. Accordingly, $\Delta\sigma'_z$ is derived from the Boussinesq point load solution by integrating the contributions from the self-weight of soil columns. The integration covers a finite area with boundaries located at a distance of 200D from the nearest crest of the scour-hole slope, beyond which soil overburden has no effect on $\Delta\sigma'_z$. Therefore, for an m×n rectangular

pile group, $\Delta\sigma'_z$ for different piles at a given depth, z, below the post-scour ground surface can be expressed as

$$\begin{bmatrix} \Delta\sigma'_{z,1} \\ \Delta\sigma'_{z,2} \\ \vdots \\ \Delta\sigma'_{z,mn} \end{bmatrix}_{mn\times 1} = \begin{bmatrix} \Psi_{1,1} & \Psi_{1,2} & \cdots & \Psi_{1,J} \\ \Psi_{2,1} & \Psi_{2,2} & \cdots & \Psi_{2,J} \\ \vdots & \vdots & \ddots & \vdots \\ \Psi_{mn,1} & \Psi_{mn,2} & \cdots & \Psi_{mn,J} \end{bmatrix}_{mn\times J} \begin{bmatrix} P_1 \\ P_2 \\ \vdots \\ P_J \end{bmatrix}_{mn\times J} \tag{5-3}$$

$$\Psi_{i,j} = \frac{3z^3}{2\pi[(x_\mathrm{p}-x_\mathrm{s})^2+(y_\mathrm{p}-y_\mathrm{s})^2+z^2]^{2.5}} \quad (i = 1,2,\dots,mn \text{ and } j = 1,2,\dots,J) \tag{5-4}$$

where J = number of discretized soil columns; P_j = self-weight of the j^{th} soil column, $P_j = \gamma' h_j \Delta x \Delta y$; $\Psi_{I,j}$ = influence factor depending on the distance (L_{ij}) between the point of interest at the i^{th} pile, (x_p, y_p), and the center of the j^{th} soil column bottom, (x_s, y_s). Subsequently, for a given depth, z, post-scour vertical effective stresses at individual piles in an $m\times n$ group are written as

$$\begin{bmatrix} \sigma'_{z,\mathrm{sc},1} \\ \sigma'_{z,\mathrm{sc},2} \\ \vdots \\ \sigma'_{z,\mathrm{sc},mn} \end{bmatrix}_{mn\times 1} = \eta \left\{ \begin{bmatrix} \gamma' z \\ \gamma' z \\ \vdots \\ \gamma' z \end{bmatrix}_{mn\times 1} + \begin{bmatrix} \Delta\sigma'_{z,1} \\ \Delta\sigma'_{z,2} \\ \vdots \\ \Delta\sigma'_{z,mn} \end{bmatrix}_{mn\times 1} \right\} \leq \begin{bmatrix} \sigma'_{z,\mathrm{int},1} \\ \sigma'_{z,\mathrm{int},2} \\ \vdots \\ \sigma'_{z,\mathrm{int},mn} \end{bmatrix}_{mn\times 1} \tag{5-5}$$

where η is a factor to consider the soil-pile interface adhesion that would resist soil stress release by scour. It was estimated through back-figuring the results of vertical effective stress in a series of 3D FE models simulating local scour (Jiang and Lin, 2021). It is important to note that the η obtained here is for piles in clays, which is different from that in sands (Jiang and Lin, 2021) as the soil-pile interface behavior is dictated by undrained adhesion rather than drained friction. A detailed discussion is given in Section 5.6. Eq. (5-5) can be presented in a normalized form: i.e., vertical stress ratio in Eq. (5-6). The foregoing procedure invoking Eqs. (5-3)-(5-6) constitutes the first step of the proposed method concerning the calculation of $\sigma'_{z,\mathrm{sc}}$ at individual piles in a pile group. The second step is presented in the next section.

$$\begin{bmatrix} \sigma'_{z,\mathrm{sc},1}/\sigma'_{z,\mathrm{int}} \\ \sigma'_{z,\mathrm{sc},2}/\sigma'_{z,\mathrm{int}} \\ \vdots \\ \sigma'_{z,\mathrm{sc},mn}/\sigma'_{z,\mathrm{int}} \end{bmatrix}_{mn\times 1} = \frac{1}{\gamma'(z+S_\mathrm{gd})} \cdot \begin{bmatrix} \sigma'_{z,\mathrm{sc},1} \\ \sigma'_{z,\mathrm{sc},2} \\ \vdots \\ \sigma'_{z,\mathrm{sc},mn} \end{bmatrix}_{mn\times 1} \leq \begin{bmatrix} 1 \\ 1 \\ \vdots \\ 1 \end{bmatrix}_{mn\times 1} \tag{5-6}$$

Since the standard methods are essentially developed based on the influence depth, z_i. Here, z_i for individual piles can be derived from the proposed method by equating

A_e determined by Eqs. (5-6) and (5-7) to that by Eqs. (5-2) and (5-7). The results will be useful in assessing the rationality of different assumptions of z_i by the standard methods.

$$A_e = \int_0^{L_e} \left(1 - \frac{\sigma'_{z,sc}}{\sigma'_{z,int}}\right) dz \tag{5-7}$$

where A_e = area enclosed by the depth distribution of $\sigma'_{z,sc}/\sigma'_{z,int}$ as illustrated in Figure 5.5; L_e = pile embedment relative to the post-scour ground surface. This step allows obtaining a range of z_i for individual piles in scoured pile groups. An example of calculated z_i is presented in Figure 5.5 and the results will be discussed in Section 5.6.

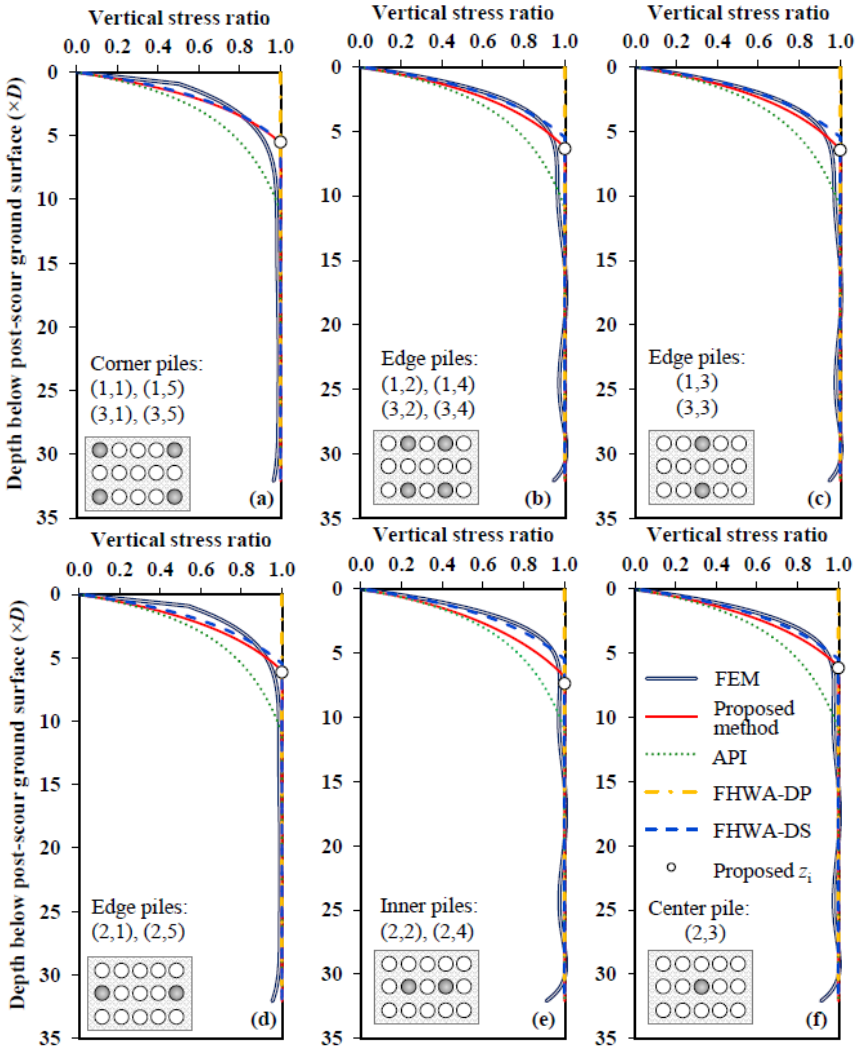

Figure 5.5 Profiles of vertical stress ratios at different pile positions in a 5×3 pile group (S_{gd}=1.5D_e, S_{wb}=0, and S_θ=26.6°)

5.4.2 Post-scour lateral response of pile group

The second step of the proposed method is to modify the existing *p*-*y* curves for soft clays (Matlock, 1970) to be capable of accommodating varying scour-hole dimensions, as expressed in Eqs. (5-8)-(5-10). The key of this step is the modification of the ultimate soil resistance through substituting an equivalent depth, z_e, in Eq. (5-10), where z_e is determined by Eq. (5-11) using $\sigma'_{z,sc}$ determined in the previous section. For a pile group under lateral loading, a reduction factor (also called *p*-multiplier, f_m) is used to account for the geotechnical group effect.

$$p = \begin{cases} 0.5 f_m p_{u,sc} \sqrt[3]{y/y_{50}} & \text{for} \quad y \le 8y_{50} \\ f_m p_{u,sc} & \text{for} \quad y > 8y_{50} \end{cases} \tag{5-8}$$

$$y_{50} = 2.5\varepsilon_{50} D \tag{5-9}$$

$$p_{u,sc} = \min[(3 + \gamma' z_e/c_u + J_s z_e/D)c_u D,\ 9c_u D] \tag{5-10}$$

$$z_e = \sigma'_{z,sc}/\gamma' \tag{5-11}$$

where $p_{u,sc}$ = post-scour ultimate soil resistance per unit length; y_{50} = lateral deflection at one-half of the ultimate soil resistance; ε_{50} = strain at one-half of the maximum stress, typically taken as 0.01; J_s = empirical coefficient, typically taken as 0.5 (Matlock, 1970); c_u = undrained shear strength of clay. The forgoing procedures (steps 1 and 2) comprise the first approach involving the modification of *p*-*y* curves using $\sigma'_{z,sc}$. The limitation of this approach is that it does not account for the shear failure plane that can develop in the remaining soil above the post-scour ground surface because this part of soil is treated as overburden pressures. This would result in an underestimate of lateral ultimate resistance, in particular for the leading row of piles. This is confirmed by Figure 5.6, where both shear stress and displacement contours indicate a potential wedge failure plane that could extend to the slope in front of the leading row. To address this issue, the second approach employing the wedge failure model (in Figure 5.4) was considered to modify the *p*-*y* curve for the leading row of piles when the surrounding soils reach an ultimate state instead of the first approach. Accordingly, z_e of the trailing rows (Row No. ≥2) and the leading row (Row No. =1) were calculated separately, with the former being calculated using the first approach [Eqs. (5-3)-(5-5) plus Eqs. (5-8)-(5-11)] while the latter by the second approach [Eqs.

(5-12)-(5-17) plus Eqs. (5-8)-(5-10)]. Eqs (5-12)-(5-17) are based on the concept of establishing an equivalent failure wedge without scour hole that has the same ultimate soil resistance as that with scour hole [Figure 5.4(d)]. The equivalence allows the equivalent depth, z_e, of the leading row to be determined. Greater details can be referred to Lin et al. (2016).

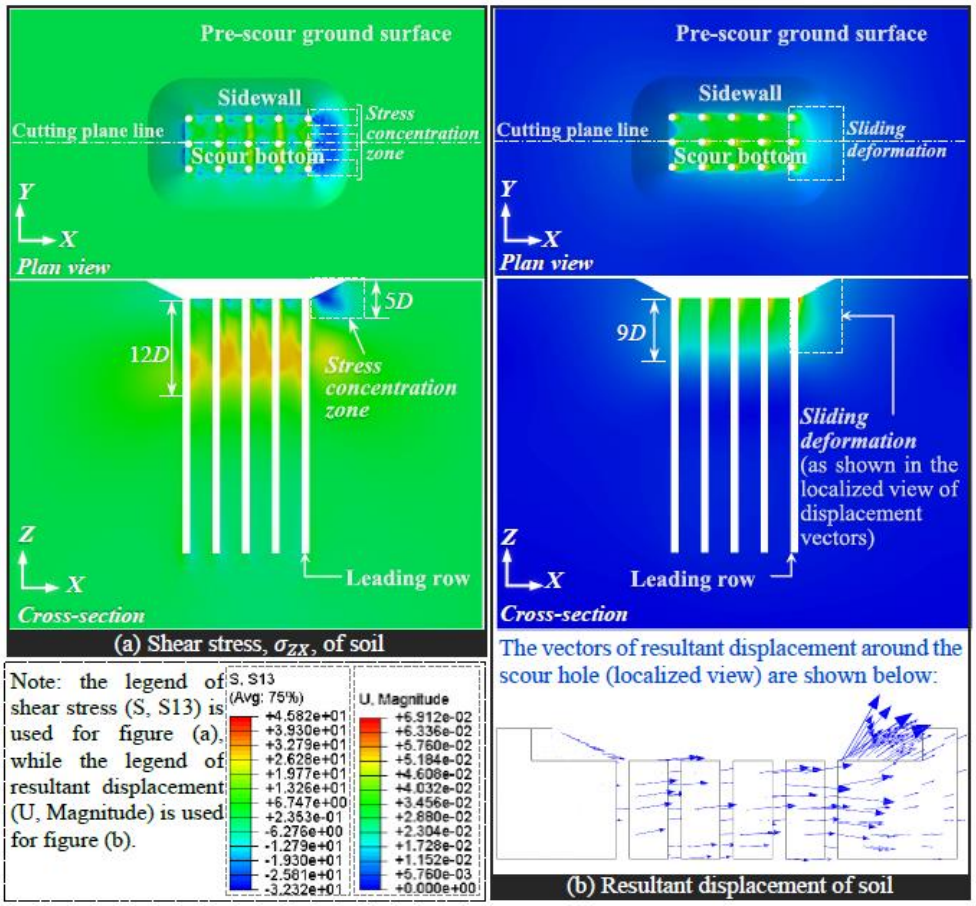

Figure 5.6 Post-scour (a) shear stress and (b) resultant displacement fields of soils around a 5×3 pile group (S_{gd}=1.0D_e, S_{wb}=0, and S_θ=26.6°)

$$F_{sc} = \begin{cases} F_0 & 0 < z \le S_{wb} \\ F_1 & S_{wb} < z \le S_{wb} + S_{gd}/\Theta \\ F_2 & z > S_{wb} + S_{gd}/\Theta \end{cases} \quad \text{and} \quad S_\theta < 90° - \beta = 45° \tag{5-12}$$

$$F_{sc} = \begin{cases} F_0 & 0 < z \le S_{wb} \\ F_2 & z > S_{wb} \end{cases} \quad \text{and} \quad S_\theta \ge 90° - \beta = 45° \tag{5-13}$$

$$F_0 = \left(0.5\gamma' D + \sqrt{2}c_u\right)z^2 + 2c_u Dz \tag{5-14}$$

$$F_1 = \left(0.5\gamma' D + \sqrt{2}c_u\right)[z^2 + \Theta(z - S_{wb})^2] + 2c_u D[z + \Theta(z - S_{wb})] \tag{5-15}$$

$$F_2 = \left(0.5\gamma' D + \sqrt{2}c_u\right)\left[\left(z + S_{gd}\right)^2 - S_{gd}\left(2S_{wb} + S_{gd}\cot S_\theta\right)\right] + 2c_u D\left(z + S_{gd}\right) \quad (5\text{-}16)$$

$$F_{sc} = \left(0.5\gamma' D + \sqrt{2}c_u\right)z_e^2 + 2c_u D z_e \quad (5\text{-}17)$$

where F_{sc} = post-scour ultimate resistive force, taken as F_0, F_1, or F_2 based on the location of the slope failure plane; β = passive failure angle for undrained clays; $\Theta = \tan S_\theta/(1-\tan S_\theta)$.

In summary, the post-scour *p*-*y* curves of the trailing rows of piles and the leading row of piles were developed using z_e, which was obtained by combined use of the first and second approaches. However, for the standard methods, only the first approach was used to generate post-scour *p*-*y* curves for both leading row and trailing rows: i.e., using Eqs. (5-1) and (5-11) to determine z_e, and then invoking Eqs. (5-8)-(5-10).

5.4.3 Implementation and verification

The post-scour *p*-*y* curves generated from the preceding procedures were further incorporated into the Euler-Bernoulli beam equation for piles (Reese and Van Impe, 2001), from which the lateral behavior of a pile group in soft clays under local scour was analyzed. To implement the analysis, a MATLAB script based on the central finite difference algorithm with Newton's iteration was developed and is attached as a supplementary file. Since no experimental test concerning scoured pile groups in soft clays is currently available for comparison, the proposed method was verified against the results of 3D continuum FE analyses in ABAQUS.

5.5 3D Finite element analyses

The 3D FE models included a baseline no-scour model and a series of post-scour models. The baseline FE model was established by comparing the numerical results to those of a full-scale lateral load test. After the baseline model was validated, it was then "scoured" to generate a series of post-scour models with various scour-hole dimensions.

5.5.1 Baseline no-scour model

The full-scale lateral load test of a 5×3 pile group performed at the Salt Lake City International Airport (Snyder, 2004) was used to establish the baseline 3D FE model under a no-scour condition. The piles were steel pipes with 324 mm outer diameter, 9.5 mm thickness, and 12.1 m length, and the pile spacing parallel and normal to the lateral load direction (s_x and s_y) was 3.92D and 3.29D, respectively. The subsurface soil encountered was primarily soft clays and silts in the upper three meters (or 9.3D), followed by sands with interbedded clays. Since the lateral responses of piles are primarily determined by the upper 10D depth of soils, the piles were assumed to be embedded in a single clay layer in this study (Brown et al., 1988; Rollins et al., 1998). During the test, the water table was maintained at the initial ground surface, and the pile head was set as a free-head condition (i.e., free to rotation and translation) since the pile heads were pin jointed with a loading frame. The pile group was laterally loaded to a prescribed displacement of 89 mm (or 0.27D) at the pile head.

During the 3D numerical modeling, the pipe pile was modeled as a solid pile sharing the same flexural rigidity, R_p, and outside diameter, D, as the original pipe pile. The detailed pile parameters are summarized in Table 5.1. The middle pile in each row was equipped with angle iron to protect strain gauges during installation, which increased R_p (and thus elastic modulus, E_p) of the pile by 23% (Snyder, 2004). Because the bending stress was below the yield strength of pile during the test, the piles were simulated with a linear elastic material in the 3D FE models. The soil was modeled as an elastoplastic material with Mohr-Coulomb failure criterion, and the parameters are also shown in Table 5.1. As with Lin et al. (2016), the undrained shear strength used in the FE model (c_{uc}) was taken as 70% of the measured average value (c_u=43.6 kPa) to account for the anisotropic feature and secondary structures of clays (Kulhawy and Mayne, 1990). The undrained modulus, E_s, was taken as 7q_c (q_c = CPT tip resistance) (Bowles, 2012), which is approximately equal to 361c_{uc}. Overall, the values of c_{uc} and E_s were consistent with other studies (c_{uc}=27-40 kPa, E_s=9.7-15 Mpa or 359c_{uc}-375c_{uc}) (Hazzar et al., 2017, 2013; Hussien et al., 2010) where the layered soil profile at the same site was explicitly modeled. The soil-pile interface was simulated with a pressure-overclosure model in the normal direction and a Coulomb model with a friction coefficient of 0.5 in the tangential direction (Achmus and Abdel-Rahman, 2005; Khodair and Abdel-Mohti, 2014; Nicholas, 2014). This helped minimize the soil-pile

interpenetration and simulate the gapping effect. The soil-pile interface connected the master surface (on the pile) with the slave surface (on the soil).

Table 5.1 Parameters of pile and soil

Part	Parameter	Value	Description
Pile (linear elastic)	L (m)	12.1	Total length
	L_{eo} (m)	11.6	Pre-scour embedded length
	D (m)	0.324	Diameter
	I_p (m^4)	5.41×10^{-4}	Moment of inertia
	R_p ($kN\cdot m^2$)	23231 and 28600	Flexural rigidity[1]
	E_p (Gpa)	42.95 and 52.87	Elastic modulus[2]
	M_y (kN·m)	350	Yielding bending moment
	ν_p	0.3	Poisson's ratio
Soil (Mohr-Coulomb)	γ (kN/m^3)	19.1	Total unit weight
	c_{uc} (kPa)	30.5	Undrained shear strength
	E_s (Mpa)	11	Undrained elastic modulus
	ν_s	0.48	Poisson's ratio

Note: [1]the flexural rigidity of the middle pile in each row was increased from 23231 $kN\cdot m^2$ to 28600 $kN\cdot m^2$ to consider the effect of angle iron (Snyder, 2004); [2]accordingly, it was achieved by increasing the elastic modulus in the 3D FEM.

Only half model (Figure 5.1) was established owing to the symmetry of the lateral loads and the model geometry. The bottom of the model was fully constrained, while the vertical boundaries were fixed for all movements except the vertical movement. The side boundaries were set at a distance of 20*D* from the nearest edge of the pile group (Feng et al., 2016; Hazzar et al., 2017) while the bottom boundary (i.e., model base) was 10*D* below the pile tip (Lin and Lin, 2020). A total of 87012 elements were generated in the baseline FE model. Figures 5.7 and 5.8 show the calculated results that are compared with the measured. Overall, the results are agreeable between the numerical modeling and the field measurement, which validates the baseline 3D FE model.

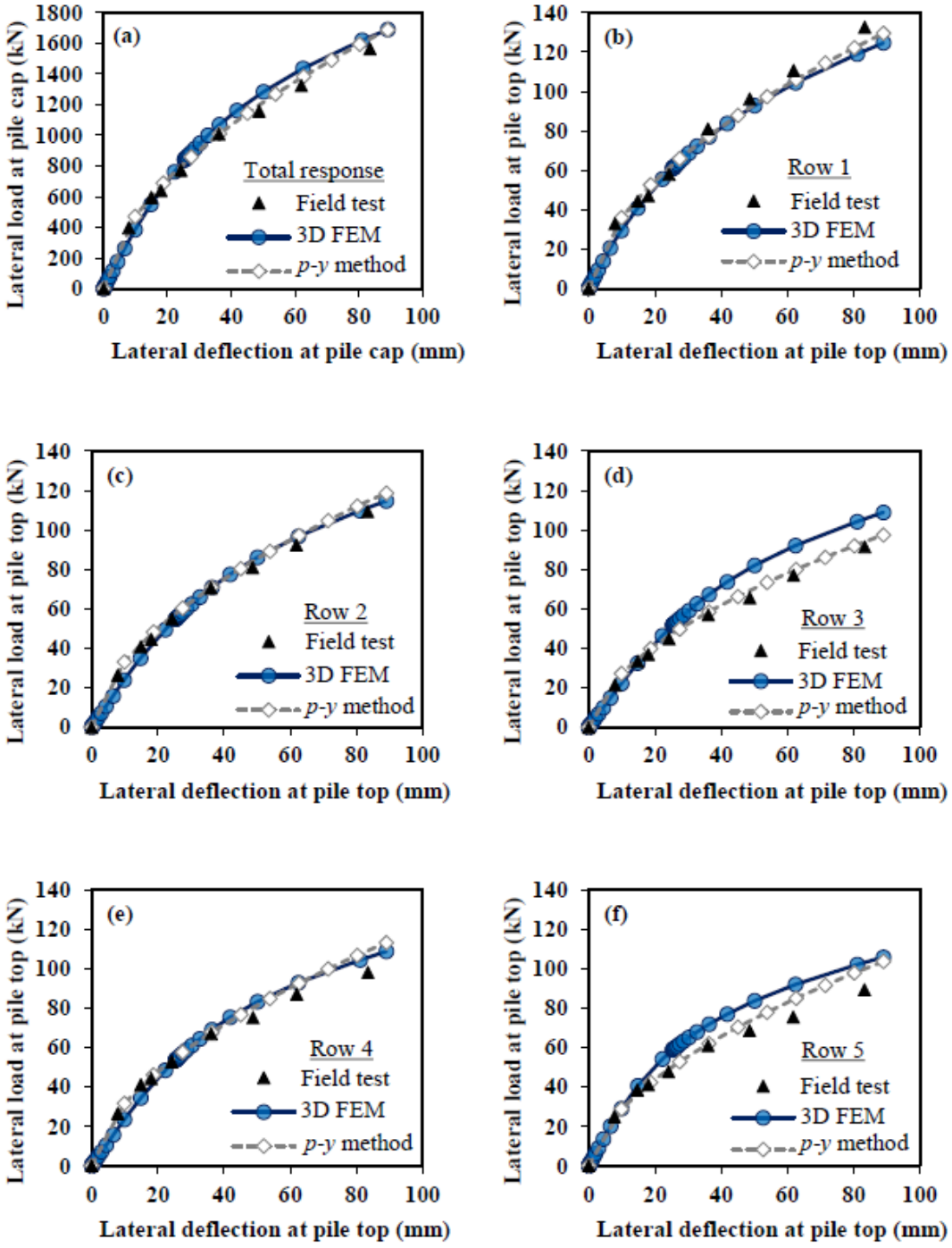

Figure 5.7 Lateral load-deflection curves at the head of (a) pile cap and piles in the (b) 1st, (c) 2nd, (d) 3rd, (e) 4th, and (f) 5th rows of a 5×3 pile group under no-scour condition

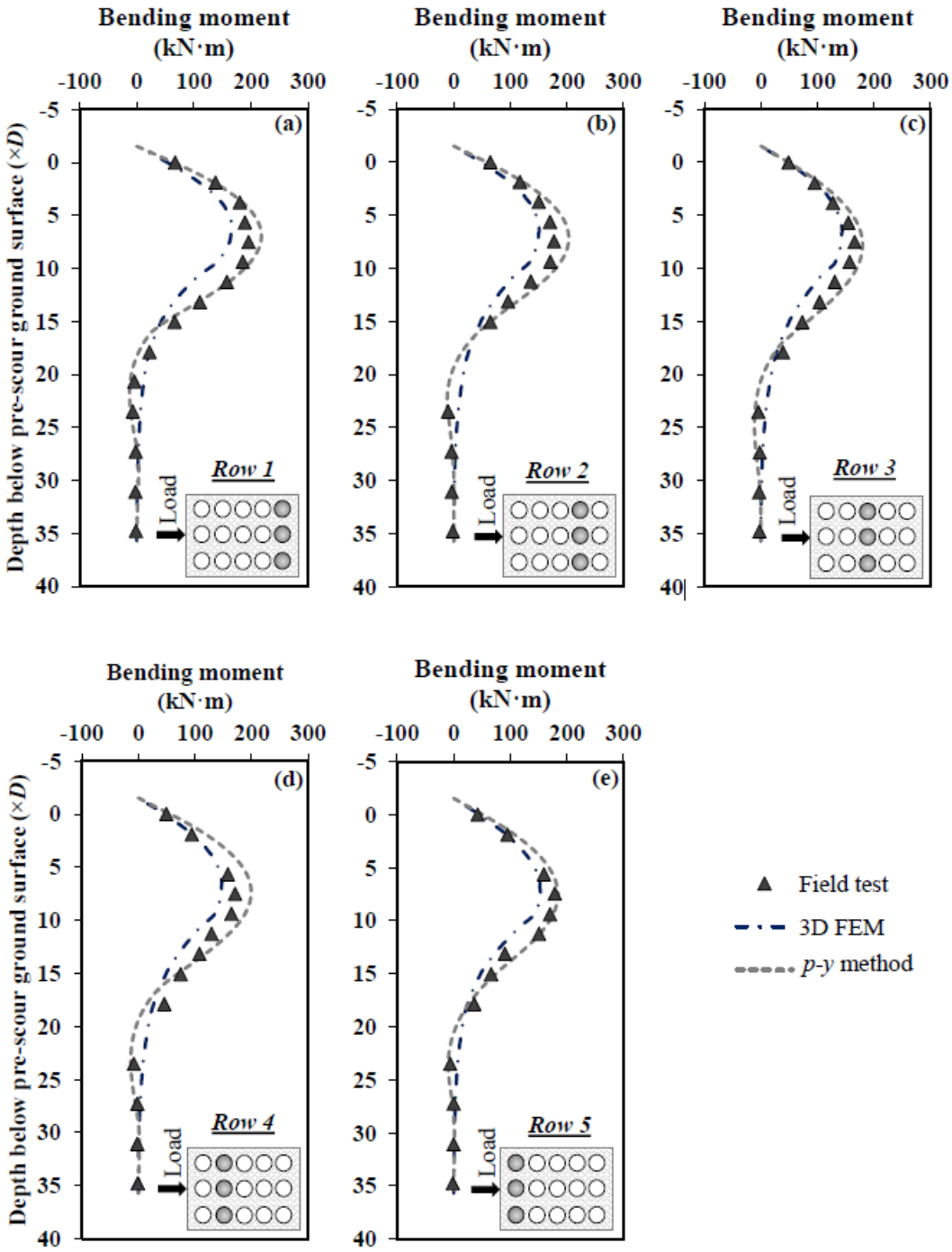

Figure 5.8 Bending moment profiles of the (a) 1st, (b) 2nd, (c) 3rd, (d) 4th, and (e) 5th rows of a 5×3 pile group under no-scour condition

5.5.2 Post-scour FE model

Based on the baseline FE model, post-scour models were developed. The shape of scour hole was modeled as an inverted truncated pyramid with a rounded-quadrilateral cross section (Figure 5.1). Besides creating the scour hole, post-scour models refined

side boundaries and meshing from the baseline model. Firstly, to eliminate boundary effects on scour-induced unloading, the side boundaries of the post-scour FE model were set at a distance of 18*D* (parallel to the lateral load) and 9*D* (perpendicular to the lateral load) from the nearest crest of the scour-hole slope (Figure 5.1). Secondly, soils in the scour hole were simulated using tetrahedral elements to accommodate the complex scour-hole geometry, and a transition mesh zone with tetrahedral elements was defined to connect the scour-hole domain and the surrounding soil domain defined with brick elements. Once the initial stress fields of soil and pile were solved, scour was simulated by deactivating the soil elements and soil-pile interactions within the scour hole. Ten scour scenarios (S_{gd}/D_e=0.5-2.5, S_θ=0°-42°, and S_{wb}=0) were analyzed using the 3D FE models as shown in Table 5.2. The 3D FE analyses were primarily used to verify the proposed method, and therefore, the cases used for the 3D FE model were less than those for the proposed method.

As described previously, to reflect group configuration effect on scour extents, scour depth is normalized by effective group diameter, D_e, which can be determined below and illustrated in Figure 5.2, while greater details can be referred to Sheppard (2003).

$$D_e = K_h K_s K_m W_p \tag{5-18}$$

$$K_s = 1 - \frac{4}{3}\left(1 - \frac{W_{sp}}{W_p}\right)\left[1 - \left(\frac{s}{D}\right)^{-0.6}\right] \tag{5-19}$$

$$K_m = \begin{cases} f_1 f_2 & \text{for } \alpha_f \le 3° \\ 1 & \text{for } \alpha_f > 3° \end{cases} \tag{5-20}$$

$$f_1 = \begin{cases} 0.875 + 0.125m & \text{for } 1 \le m \le 5 \\ 1.5 & \text{for } m > 5 \end{cases} \tag{5-21}$$

$$f_2 = \begin{cases} (0.5 - 0.5/f_1)\, s/D + 1.5/f_1 - 0.5 & \text{for } 1 \le s/D \le 3 \\ (0.143/f_1 - 0.143)\, s/D - 0.429/f_1 + 1.429 & \text{for } 3 < s/D \le 10 \\ 1.001/f_1 - 0.001 & \text{for } s/D > 10 \end{cases} \tag{5-22}$$

where K_h, K_s, and K_m are the multipliers accommodating for the height of the head of pile group, the pile spacing, and the number of piles, respectively; K_h=1 if the head of pile group is above the water level; W_p is the projected width of pile group, which is obtained by summing the unobstructed projected widths of the piles in the first upstream column and the first two upstream rows onto a vertical plane normal to the flow; W_{sp} is

the projected width of an individual pile in the group (W_{sp}=D for a circular pile); α_f is the flow skew angle; s is the pile spacing, taken as the smaller one when $s_x \neq s_y$.

Table 5.2 Details of parametric analyses

Investigated factor	Scour-hole dimensions			Pile group configuration			Analysis method	f_m[1]
	S_{gd} (×D)	S_{gd} (×D_e)	S_θ (°)	m×n	s_x (×D)	s_y (×D)		
Scour-hole slope angle	3.6	1.5	0, 12, 20, 26.6, 35, 42	5×3	3.92	3.29	FEM, proposed method, standard methods	Field test (Snyder, 2004)
Scour-hole depth	1.2, 2.4, 3.6, 4.8, 6.1	0.5, 1.0, 1.5, 2.0, 2.5	26.6	5×3	3.92	3.29		
Number of piles	3.0	2.0 1.4 1.1	26.6	2×2 3×3 4×4	3	3	Proposed method, standard methods	ASSHTO (2012)
	2.1 3.0 4.0	1.4	26.6	2×2 3×3 4×4	3	3		
Pile spacing	3.0	1.4 1.7 1.9 2.1	26.6	3×3	3 4 5 6	3 4 5 6		
	3.0 2.5 2.2 2.0	1.4	26.6	3×3	3 4 5 6	3 4 5 6		
Pile group shape	2.5, 5.1, 7.6, 10.2	0.7, 1.4, 2.1, 2.8 1.0, 2.0, 3.0, 4.0 1.3, 2.5, 3.8, 5.0	26.6	6×5 10×3 15×2	3	3		
	2.5, 5.1, 7.6, 10.2 1.8, 3.6, 5.4, 7.2 1.4, 2.8, 4.3, 5.7	0.7, 1.4, 2.1, 2.8	26.6	6×5 10×3 15×2	3	3		

Note: [1]the p-multiplier, f_m, of the 5×3 pile group was determined from the field test (Snyder, 2004), while the f_m of the other pile groups investigated herein was evaluated from ASSHTO (2012).

5.6 Results and discussion

The parametric analyses were conducted using the proposed method, standard methods, and 3D FE method (FEM) with the details summarized in Table 5.2. The results of post-scour vertical effective stress and influence depth are first presented, followed by lateral responses of pile groups in soft clays considering different scour-hole dimensions and pile group configurations. The discussion is focused on verification of the proposed method and assessment of the suitability of applying the standard methods to analyze scoured pile groups in soft clays.

5.6.1 Post-scour vertical effective stresses around piles

The scour effect on the vertical effective stress of soils around pile is presented using $\sigma'_{z,sc}/\sigma'_{z,int}$. Figure 5.5 shows the depth distribution of $\sigma'_{z,sc}/\sigma'_{z,int}$ for individual piles at different locations in the 5×3 pile group when S_{gd}=1.5D_e (or 3.6D), S_{wb}=0, and S_θ=26.6°. From the 3D FEM, $\sigma'_{z,sc}/\sigma'_{z,int}$ was equal to zero at the post-scour ground surface and gradually increased to one at the influence depth (z_i=10D-15D or 2.8S_{gd}-4.1S_{gd}), beyond which $\sigma'_{z,sc}$ was equal to $\sigma'_{z,int}$ (i.e., the influence of scour on the vertical effective stress ceased). This demonstrated that the influence of scour-induced unloading was limited to a depth of 2.5-4.5 times scour-hole depth. The 3D FE analyses also indicated slight discrepancies of the stress distribution along pile between piles, with the inner piles having a deeper z_i than the outer piles.

Besides the 3D FEM results, Figure 5.5 also shows the results of the proposed method and standard methods. Since FHWA-DP neglects the unloading effect of local scour on soil, the post-scour stress remained the same as the pre-scour stress, and therefore, $\sigma'_{z,sc}/\sigma'_{z,int}$ equaled one at all depths. Contrarily, the other standard methods acknowledge the scour-induced reduction in $\sigma'_{z,sc}$, and produced similar profiles as compared to the 3D FEM, with API giving a more agreeable comparison of z_i to the 3D FEM but FHWA-DS yielding a better match of $\sigma'_{z,sc}/\sigma'_{z,int}$ distribution to the 3D FEM. However, none of these standard methods (API, FHWA-DP, and FHWA-DS) could consider the variation in $\sigma'_{z,sc}/\sigma'_{z,int}$ between different piles. For the proposed method, as discussed previously the soil-pile interface adhesion that could counteract the unloading of soil by local scour was considered. In other words, the scour-induced reduction in $\sigma'_{z,sc}$ was smaller due to the presence of soil-pile interface resistance (Jiang

and Lin, 2021; Lin and Jiang, 2019). To account for this effect, an empirical factor, η, was included in the proposal method [Eq. (5-5)] as did by Jiang and Lin (2021). The value of η was derived from a series of separate 3D FE analyses by merely scouring the soils and then evaluating the soil stress for different scour depths and pile group configurations, and the results are presented in Table 5.3. As with Jiang and Lin (2021), η was primarily affected by scour depth but almost not affected by pile group configurations, and therefore Table 5.3 presents the value of η only as a function of scour depth.

Table 5.3 Correction factor for considering soil-pile interface resistance

S_{gd} ($\times D$)	1	2	4	≥ 6
η	1.1	1.2	1.4	1.6

Table 5.4 Influence depths of a 5×3 pile group under different scour-hole depths (S_{wb}=0 and S_{θ}=26.6°)

S_{gd} ($\times D_e$)	S_{gd} ($\times D$)	Proposed influence depths, z_i ($\times S_g$), of piles at different locations in the group[1]						
		(1,1)	(1,2)	(1,3)	(2,1)	(2,2)	(2,3)	Mean
0.5	1.2	3.46	4.37	4.46	4.21	5.73	5.90	4.69
1.0	2.4	2.07	2.46	2.50	2.38	2.97	3.04	2.57
1.5	3.6	1.51	1.74	1.77	1.69	2.02	2.07	1.80
2.0	4.8	1.20	1.36	1.38	1.32	1.54	1.57	1.39
2.5	6.1	1.00	1.12	1.14	1.09	1.25	1.28	1.15

Note: [1]influence depths are provided for representative piles (1,1), (1,2), (1,3), (2,1), (2,2), and (2,3) as symmetry, as illustrated in the plan view of the 5×3 pile group (Figure 5.5).

Using the proposed method, a series of z_i was calculated as discussed previously. The results are presented in Table 5.4, which is only for the scoured 5×3 pile group. For other configurations of pile group under local scour, z_i values are also provided in Supplementary Tables S5.1-S5.7 for practical use of foundation design against local scour. Overall, for a typical scour depth such as S_{gd}=1.4D_e, z_i fell in a range of 1.3S_{gd}-2.7S_{gd} on average, with the lower and upper bounds closely agreeing with z_i=1.5S_{gd} recommended by FHWA-DS and z_i=3.0S_{gd} by API, respectively. However, for a smaller scour depth (e.g., S_{gd}=0.7D_e), FHWA-DS and API tended to underestimate z_i (as compared with z_i=3.0S_{gd}-4.5S_{gd}), while for a larger scour depth (e.g., S_{gd}=2.8D_e), FHWA-DS and API tended to overestimate z_i (as compared with z_i=1.1S_{gd}-1.5S_{gd}). In general, the calculated z_i increased with increased pile spacing or decreased scour-hole depth. This finding is consistent with that for the scoured pile groups in sands (Jiang and Lin, 2021). Besides, the difference in z_i between the corner pile and the central pile

ranged from $0.2S_{gd}$ to $2.7S_{gd}$. In contrast, the standard methods recommend a constant value of z_i, which was thus independent of different pile spacing, scour-hole depth, or pile position, and apparently, this is technically incorrect.

5.6.2 Post-scour lateral responses of pile groups

Based on the parametric analyses (Table 5.2), the results of post-scour lateral responses of pile groups in soft clays were obtained, which included the lateral load-deflection curves at pile head, lateral load capacity ratio [as defined by (Lin and Lin, 2020)], and bending moment of piles. Figure 5.9 shows the lateral load-deflection curves at the pile head (5×3 pile group) before and after scour. In general, the proposed method produced agreeable and conservative results as compared to the 3D FEM, particularly when the lateral deflection was within the tolerant range for bridge foundations (0.25-2 inch or 6.35-50.8 mm) (Paikowsky et al., 2004). To assess the effect of local scour on the lateral responses of a pile group, the lateral capacity of the pile group at post-scour conditions was compared to that at initial or pre-scour conditions, and a ratio between them is defined as the lateral capacity ratio. The lateral capacity was taken as the lateral load causing 1-inch (25.4 mm) deflection at the head of pile group (Lin and Lin, 2020). Therefore, the lateral capacity ratio should be less than one for scour conditions and a smaller value indicates a greater loss in the lateral capacity caused by scour.

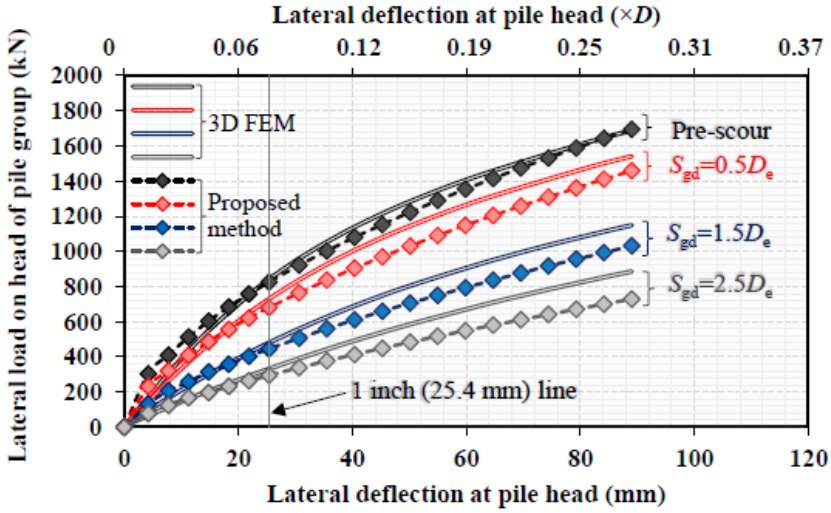

Figure 5.9 Lateral load-deflection curves at the head of pile group under different scour-hole depths (5×3 pile group, S_{wb}=0, and S_θ=26.6°)

In the subsequent sections, the results presented are focused on the lateral capacity

ratio and bending moment. Firstly, the results of the 3D FE analyses were compared with the proposed method and the standard methods for the 5×3 pile group under varying scour-hole slope angles and depths. The purpose of this part was to verify the proposed method considering different scour-hole dimensions. Subsequently, the effects of pile group configurations including the number of piles, pile spacing, and pile group shape were investigated using the proposed method and the standard methods.

5.6.2.1 Effect of scour-hole slope angle

Figure 5.10 shows the lateral capacity ratio of the 5×3 pile group under different S_θ (0°-42°) while S_{gd} and S_{wb} were kept as $1.5D_e$ (or $3.6D$) and 0, respectively. Note that when S_θ=0°, the local scour around the pile group became a general scour. From the 3D FEM, the lateral capacity ratio increased by 18% as S_θ increased from 0° to 42°, and the increase became negligible when $S_\theta \geq 20°$. In other words, the lateral capacity decreased by 15% when S_θ decreased from 42° to 0°, indicating that simplifying local scour (e.g., $S_\theta \geq 20°$) as general scour (S_θ=0°) could underestimate the lateral capacity by 15%. As compared to the 3D FEM, the proposed method underestimated the lateral capacity ratio by no more than 6%.

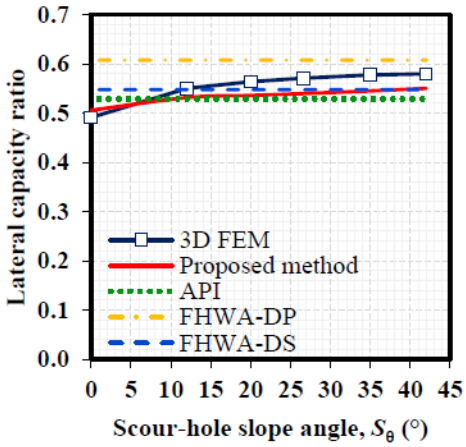

Figure 5.10 Lateral capacity ratio varied with scour-hole slope angle (5×3 pile group, S_{gd}=1.5D_e, and S_{wb}=0)

Moreover, the proposed method properly captured the variation of the lateral capacity ratio with S_θ. This result confirmed the validity of the proposed method. In contrast, the standard methods could not consider the variations of S_θ, and therefore, the results are featured by horizontal lines in Figure 5.10. In comparison with the 3D FEM, FHWA-DP overestimated the lateral capacity ratio by 5%-24% in the entire range

of S_θ examined herein, which is unsafe particularly for small S_θ. Likewise, API and FHWA-DS overestimated the lateral capacity ratio (≤12%) when $S_\theta \leq 12°$, but underestimated the lateral capacity ratio (≤9%) at a larger S_θ. Since $S_\theta \leq 12°$ was also observed in field (Jiang and Lin, 2021), the use of the standard methods could cause an unsafe design in practice.

The effect of S_θ on the maximum bending moment, M_{max}, was found to be more significant in the leading piles than the trailing piles, and the bending moment of the leading row of piles usually dominated the design demand. Therefore, the results of M_{max} of the leading piles (5×3 pile group) are presented here. Technically speaking, M_{max} of the leading piles can increase with S_θ due to an increased passive earth pressure developed in front of them. This is confirmed by the results from the 3D FEM and the proposed method in Figure 5.11, in which the post-scour M_{max} of the leading row of piles was normalized by the pre-scour M_{max} [Figure 5.11(a)] and the post-scour M_{max} at S_θ=0° [Figure 5.11(b)], respectively. Although the proposed method yielded slightly smaller results than the 3D FEM [Figure 5.11(a)], the trend determined from the two methods matched exceptionally well [Figure 5.11(b)], showing an 8% increase in M_{max} as S_θ increased from 0° to 42°. However, the standard methods failed to manifest this trend.

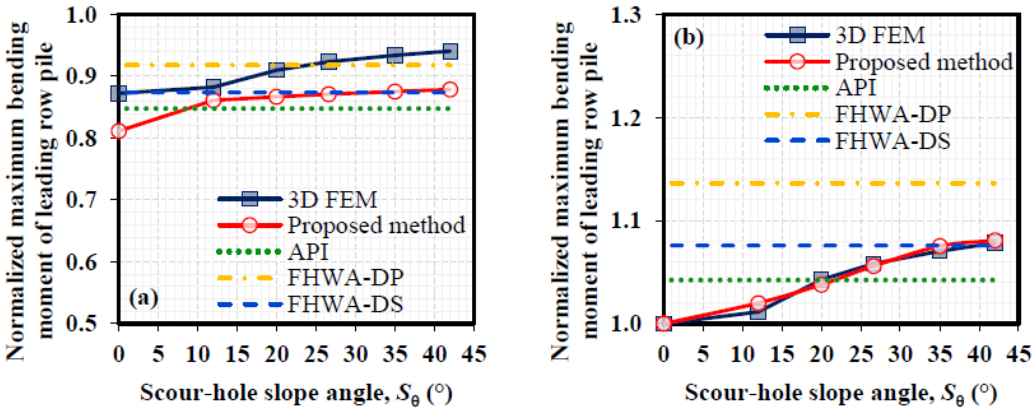

Figure 5.11 Effects of scour-hole slope angle on maximum bending moments of leading row pile normalized by (a) pre-scour value and (b) the value at S_θ=0° (5×3 pile group, S_{gd}=1.5D_e, and S_{wb}=0)

As discussed previously, a stress concentration zone could develop in front of the leading row of piles, which led to a higher lateral soil resistance to the leading piles at this location. Figure 5.12 shows the calculated ultimate lateral soil resistance per unit length, $p_{u,sc}$, at the leading piles varied by S_θ. The results were calculated for a depth of

5D below the post-scour ground surface, where the soil-pile interaction was significant. The increase in S_θ is anticipated to increase the passive earth pressure and ultimate soil resistance at the leading piles. As indicated by the proposed method, $p_{u,sc}$ increased by 27% when S_θ increased from 0° to 42° for the case studied (S_{gd}=1.5D_e and S_{wb}=0). The increase in $p_{u,sc}$ tended to be insignificant when $S_\theta \geq 26.6°$. However, the results of $p_{u,sc}$ from the standard methods were independent of S_θ, which is incorrect.

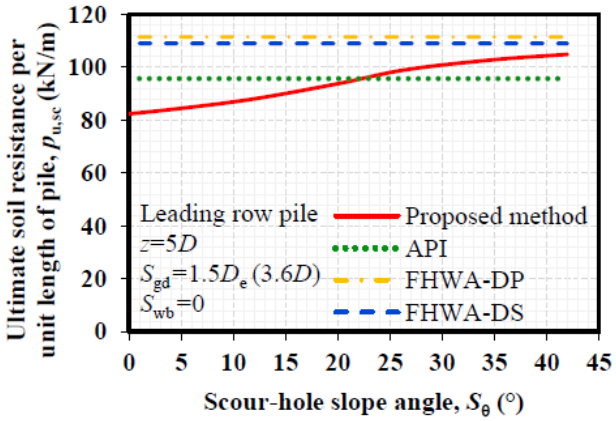

Figure 5.12 Ultimate lateral soil resistance per length of pile (z=5D) in leading row vs. scour-hole slope angles (5×3 pile group, S_{gd}=1.5D_e, and S_{wb}=0)

5.6.2.2 Effect of scour-hole depth

Effect of scour depth was evaluated by varying S_{gd} from 0 to 2.5D_e while keeping the other two dimensions: S_θ=26.6° and S_{wb}=0. As described previously, S_θ=26.6° is often adopted for a scour hole in bridge foundations (Arneson et al., 2012), and therefore it was used herein. Figure 5.13 shows the lateral capacity ratio of the 5×3 pile group with varying S_{gd}. From the 3D FEM, the lateral capacity ratio decreased from 1.0 to 0.39 as S_{gd} increased from 0 to 2.5D_e (or 6.1D), indicating a 61% loss in lateral capacity in soft clays. This amount of loss in lateral capacity was greater than that in sands for a similar scour depth (e.g., a 58% loss as S_{gd} increased from 0 to 2.8D_e) (Jiang and Lin, 2021). In general, the proposed method compared well with the 3D FEM, with an average underestimate of 6%. This confirms that the proposed method was able to consider the effect of S_{gd} on the lateral responses of pile groups. Despite only applying for single isolated piles, API and FHWA-DS produced almost the same results as the proposed method when S_θ=26.6°. Surprisingly, even though it is theoretically incorrect, FHWA-DP also produced agreeable results with the 3D FEM, with an overestimate of <7% when S_{gd}>1.0D_e. This number is much smaller than that for pile groups in sands

(47%) (Jiang and Lin, 2021). This is because as opposed to sands, the undrained properties of soft clays (e.g., undrained shear strength) were insensitive to the scour-induced change in overburden immediately after scour. The undrained properties can be modified by scour if the consolidation (by scour) is allowed to fully complete, which however is a long-term process. In this study, the analyses were only focused on the short-term properties of soils immediately after scour.

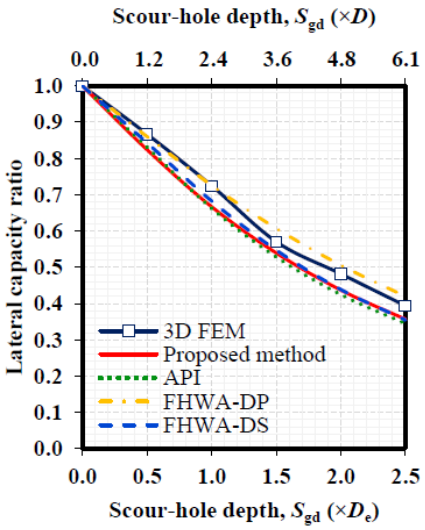

Figure 5.13 Lateral capacity ratio varied with scour-hole depth (5×3 pile group, S_{wb}=0, and S_θ=26.6°)

Figures 5.14(a) and (b) show the magnitude and location of the maximum bending moment (M_{max} and $z_{M,max}$) determined by the 3D FE analyses, when the lateral deflection at the pile head was 25.4 mm. The magnitude of M_{max} decreased by 20%-37% as S_{gd} increased from 0 to 2.5D_e (or 6.1D), with a lower decrease found at the leading row of piles and a larger decrease at the trailing-most row (Row 5). The magnitude at the leading row was approximately 12%-28% higher than the average value of the trailing rows under different S_{gd}. This was expected as the lateral loads carried by the leading piles increased when S_{gd} increased, resulting in a larger passive failure wedge to be mobilized in front of them. Figure 5.14(b) shows that the location of M_{max} also varied with S_{gd}. Overall, the location moved toward the post-scour ground surface by a distance equal to D_e (or 2.5D) as S_{gd} increased from 0 to 2.5D_e. Similar results were obtained by the proposed method as compared to the 3D FEM, as shown in Figure 5.15 where the post-scour M_{max} was normalized by the pre-scour one. Except FHWA-DP, both API and FHWA-DS produced agreeable results with the proposed method; therefore, only results from FHWA-DP are presented in Figure 5.15.

In summary, based on the discussion in the previous two sections, the proposed method could provide agreeable results as compared to the 3D FEM. Therefore, credence is given to the proposed method. In the following sections, the results were obtained from the proposed method and the standard methods, focusing on the effects of the number of piles, pile spacing, and pile group shape.

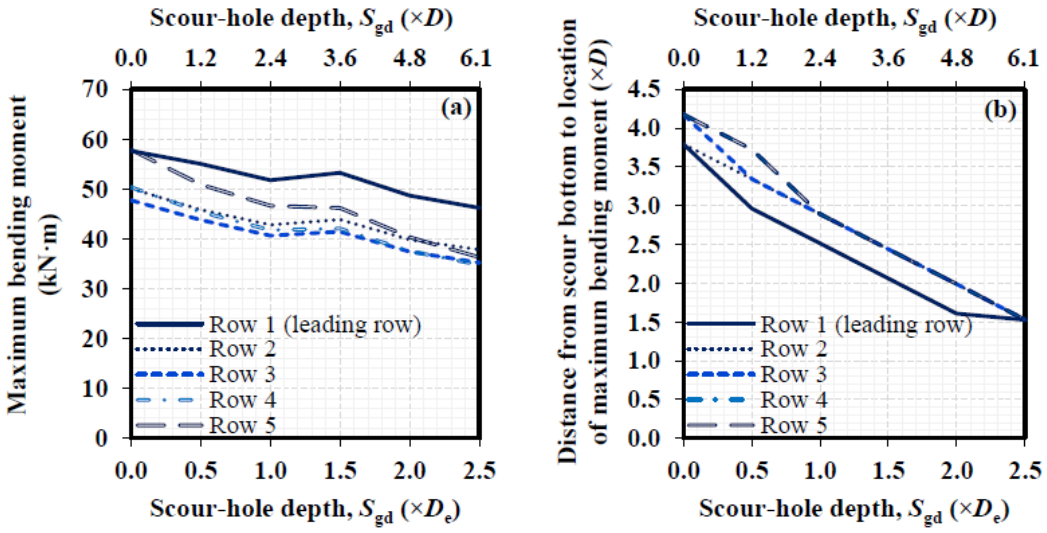

Figure 5.14 Effects of scour-hole depth on (a) maximum bending moment and (b) location corresponding to the maximum bending moment of different pile rows (5×3 pile group, S_{wb}=0, and S_θ=26.6°)

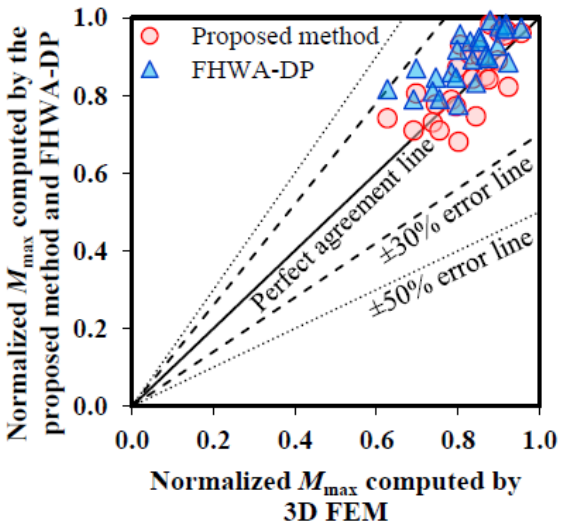

Figure 5.15 Comparison of the normalized maximum bending moment computed by different methods (S_{gd}=0.5D_e-2.5D_e, S_{wb}=0, and S_θ=26.6°)

5.6.2.3 Effects of number of piles and pile spacing

The dual group effects for a scoured pile group are dependent on the pile group configuration (i.e., number of piles, pile spacing, and group shape). The hydraulic group effect was indicated by relating the scour depth to the effective diameter, D_e (Sheppard, 2003) while the geotechnical group effect was considered using the *p*-multiplier evaluated from ASSHTO (2012). As such, the scour depth expressed as S_{gd} ($\times D_e$) allows examining both hydraulic and geotechnical group effects, while that expressed as S_{gd} ($\times D$) only manifests the sole geotechnical group effect because the *p*-multiplier is already included in the lateral response analyses for the pile group regardless of which way to normalize the scour depth.

Table 5.5 first shows at the same S_{gd} ($\times D$), the lateral capacity ratios of three pile groups with the spacing of 3D but different sizes: 2×2 (S_{gd}=3D=2D_e), 3×3 (S_{gd}=3D=1.4D_e), and 4×4 (S_{gd}=3D=1.1D_e). It shows that the proposed method and the standard methods except FHWA-DP produced similar results, and an increase in the number of piles had a negligible effect on the geotechnical group effect. This was expected as the average *p*-multiplier per pile suggested by ASSHTO (2012) was not varied considerably by the size of pile group. Note that the above results were calculated for the same S_{gd} ($\times D$), which precluded the hydraulic group effect. This is not realistic in practice as a square pile group with a greater number of piles tends to develop a deeper scour hole (Table 5.2). To include the hydraulic group effect, the scour depth was expressed using the effective group diameter, i.e., S_{gd} ($\times D_e$), and the three pile groups were reanalyzed using S_{gd}=1.4D_e (i.e., S_{gd}=2.1D, 3.0D, and 4.0D for 2×2, 3×3, and 4×4, respectively). The results of the lateral capacity ratios for the same S_{gd}=1.4D_e are also shown in Table 5.5. Again, all the methods except FHWA-DP produced similar results. As indicated by the proposed method, the lateral capacity ratio decreased by 24% as the number of piles increased from 4 to 16, showing an opposite trend as compared with that under the same S_{gd} ($\times D$). This is because that the value of D_e was larger for a larger size of square pile group, which thus resulted in a greater S_{gd} when S_{gd}/D_e was kept constant. This result indicated that when the dual group effects were considered, the variation in the lateral capacity ratio became more significant. In other words, the hydraulic group effect prevailed over the geotechnical group effect.

Table 5.5 Effect of number of piles on the lateral capacity ratio (S_{gd}=3.0D vs. S_{gd}=1.4D_e)

Pile group (m×n)	Lateral capacity ratio (S_{gd}=3.0D, S_{wb}=0, and S_θ=26.6°)				Lateral capacity ratio (S_{gd}=1.4D_e, S_{wb}=0, and S_θ=26.6°)			
	Proposed method	API	FHWA-DP	FHWA-DS	Proposed method	API	FHWA-DP	FHWA-DS
2×2	0.62	0.60	0.68	0.62	0.72	0.73	0.77	0.73
3×3	0.63	0.62	0.69	0.64	0.63	0.62	0.69	0.64
4×4	0.64	0.63	0.70	0.65	0.55	0.54	0.63	0.56

As described in the introduction section, when the pile spacing s≤5D, local scour can be approximated with global scour. Herein, for completeness, a typical range of pile spacing (s=3D-6D) for a pile group used in practice was considered. For 5D<s≤6D, the global scour was conservatively assumed to develop to the bottom of the localized pit. Figure 5.16(a) shows the lateral capacity ratio of a 3×3 pile group with varying pile spacing when S_{gd}=3D, in which only geotechnical group effect was examined. All the methods produced similar results except FHWA-DP which overestimated the lateral capacity ratio by 10%.

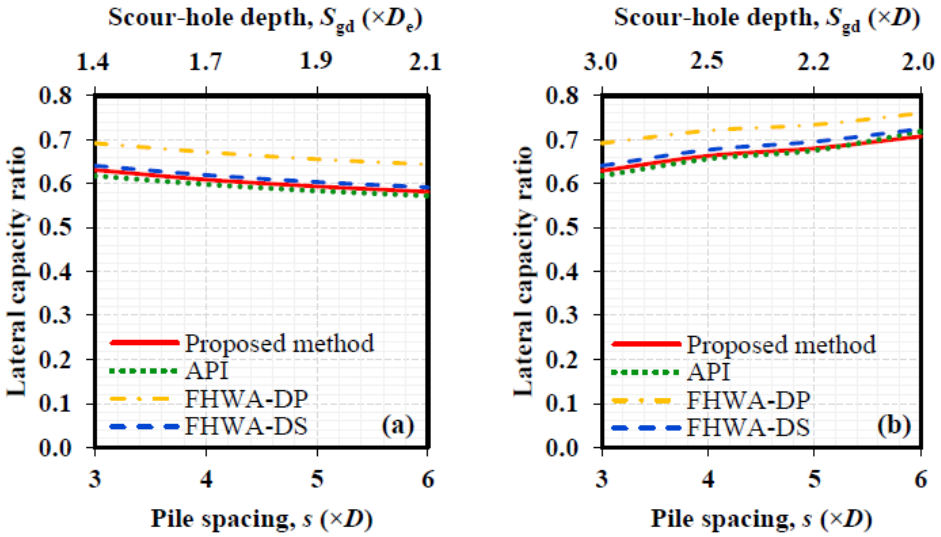

Figure 5.16 Effects of pile spacing on lateral capacity ratios of a 3×3 pile group when (a) S_{gd}=3.0D and (b) S_{gd}=1.4D_e (S_{wb}=0 and S_θ=26.6°)

Overall, these results were found to be consistent with that of scoured pile groups in sands (Jiang and Lin, 2021; Lin and Lin, 2020). From the proposed method, the lateral capacity ratio decreased by 8% as the pile spacing increased from 3D to 6D, indicating a slightly more loss in the lateral capacity. However, this change was small, and thus scour-related geotechnical group effect was small with the changes in pile

spacing. To consider the dual hydraulic and geotechnical group effects, the analyses were conducted by considering S_{gd}=1.4D_e and the results are presented in Figure 5.16(b). In this case, the lateral capacity ratio increased by 12% as s increased from 3D to 6D, showing an opposite trend as compared with Figure 5.16(a). Note that an increase in s for the 3×3 pile group resulted in a decrease in D_e; therefore, the increase in s decreased S_{gd} when S_{gd}=1.4D_e as seen in Table 5.2. The reduction in D_e was up to 34% for the range of s investigated. The above results also demonstrated that the hydraulic group effect governed scour effect on the lateral response of pile groups. This result also implied that increasing pile spacing could attenuate the dual group effects, and therefore, mitigate the scour-induced loss in the lateral capacity.

5.6.2.4 Effect of pile group shape

The effect of pile group shape was investigated for three pile groups with different arrangements (m×n=6×5, 10×3, 15×2) but the same number of piles (30) and pile spacing (s=3D). The results are presented in Figure 5.17.

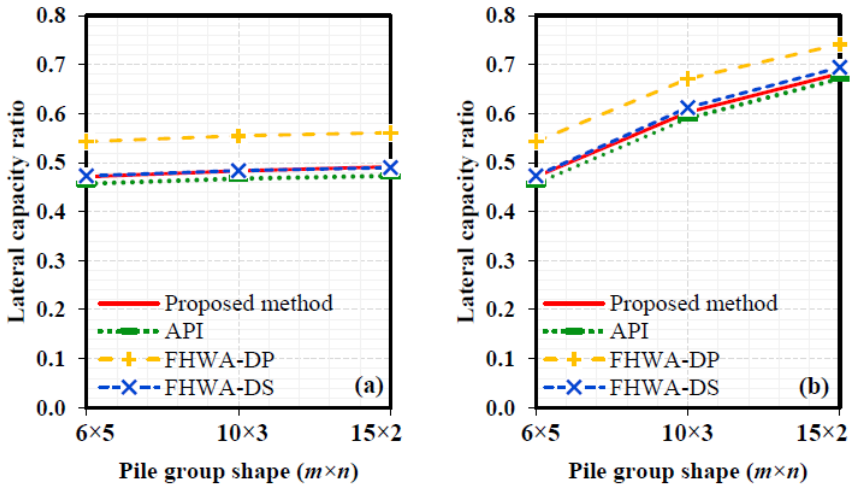

Figure 5.17 Effects of pile group shape (6×5, 10×3, and 15×2) on lateral capacity ratios when (a) S_{gd}=5.1D and (b) S_{gd}=1.4D_e (S_{wb}=0 and S_θ=26.6°)

All the methods developed similar results except FHWA-DP. As shown in Figure 5.17(a), when the hydraulic group effect was precluded, the effect of increasing the aspect ratio of pile group (approximately equal to m/n) on the lateral capacity ratio was slight, e.g., only 4% increase as m/n increased from 1.2 to 7.5. Figure 5.17(b) shows the lateral capacity ratio when S_{gd}=1.4D_e to account for the dual hydraulic and geotechnical group effects. Compared with Figure 5.17(a), the variation in the lateral

capacity ratio became more significant. This is due to the incorporation of the hydraulic group effect. The increase in m/n caused a decrease in D_e and therefore S_{gd} value when S_{gd}/D_e was fixed (as shown in Table 5.2). The lateral capacity ratio increased by 45% when m/n increased from 1.2 to 7.5. The above results also highlighted the dominant role of the hydraulic group effect. As with Jiang and Lin (2021), the use of a rectangular pile group (i.e., increasing m/n) could reduce the scour-induced loss in the lateral capacity.

Note that Figure 5.17 only presents the lateral capacity ratio calculated for the selected S_{gd}. To assess the beneficial effect of increasing m/n at varying S_{gd}, Figures 5.18(a) and (b) exhibit the percent increase in the lateral capacity ratio when m/n was increased from 1.2 to 7.5 under different S_{gd} ($\times D$) and S_{gd} ($\times D_e$), respectively. In general, the lateral capacity ratio increased from 2.5% to 6.1% for the prescribed increase in m/n when S_{gd} increased from 2.5D to 10.2D. However, the increase was more pronounced when the hydraulic group effect was incorporated, showing a 20%-100% increase due to the prescribed increase in m/n when S_{gd} increased from 0.7D_e to 2.8D_e. The results demonstrated that the beneficial effect of employing a rectangular pile group could be more remarkable for a greater scour depth.

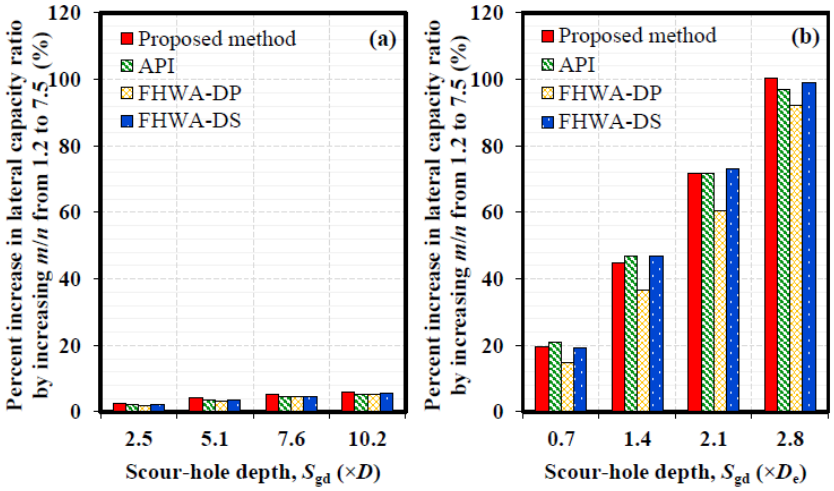

Figure 5.18 The percent increase in lateral capacity ratio due to the increase of m/n varied with scour-hole depths normalized by (a) pile diameter and (b) effective group diameter (S_{wb}=0 and S_θ=26.6°)

In general, the lateral capacity ratio increased from 3% to 6% for the increase in m/n when S_{gd} increased from 2.5D to 10.2D. However, the increase was more pronounced when the hydraulic group effect was incorporated, showing 20%-100%

increase due to the increase in m/n for S_{gd}=0.7D_e-2.8D_e. The results demonstrated that the beneficial effect of employing a rectangular pile group could be more significant in increased scour extent with greater S_{gd}.

5.7 Conclusions

This study proposed a practical method to facilitate the design of laterally loaded pile groups in soft clays under local scour conditions. Moreover, the standard methods (API, FHWA-DP, and FHWA-DS) were also critically assessed by comparing them with the proposed method. The following conclusions were obtained from this study:

(1) The results from the proposed method agreed well with those from the 3D FEM, which verified the proposed method. The normalized influence depth, z_i/S_{gd}, determined from the proposed method was found to increase with the increase in pile spacing or the decrease in scour depth. It also varied with the pile position in a pile group with a larger influence depth at the inner piles than at the perimeter piles. For typically used scour-hole dimensions (S_{gd}=1.4D_e, S_θ=26.6°, S_{wb}=0), z_i/S_{gd} ranged between 1.3 and 2.7, which was approximately bounded by the values recommended by FHWA-DS (z_i/S_{gd} =1.5) and API (z_i/S_{gd} =3.0).

(2) For a typical scour-hole shape (S_θ=26.6° or 30°) used in practice, all the three standard methods (API, FHWA-DS, and FHWA-DP) could be used to predict the lateral capacity ratio of pile groups in soft clays with the margin of error <8%. However, they overestimated the lateral capacity ratio when S_θ<12°, which could result in an unsafe design, and the overestimation was most considerable for FHWA-DP (up to 24%).

(3) The increase in scour-hole depth decreased the lateral capacity and maximum bending moment of the pile group, and shifted the location of the maximum bending moment upward relative to the post-scour ground surface. Contrarily, the increase in the scour-hole slope angle increased the passive earth pressure in front of the leading row of piles, and therefore increased the lateral capacity and maximum bending moment of the pile group.

(4) The post-scour lateral responses of pile groups were dependent on both hydraulic group effect and geotechnical group effect, in which the hydraulic group effect was found to be more profound. When the dual group effects were considered, the

scour-induced loss in the lateral capacity could be reduced by increasing the pile spacing and decreasing the number of piles. However, ignoring the hydraulic group effect produced an opposite trend.

(5) Given the same number of piles, the scour-induced loss in the lateral capacity was more significant in a square pile group than a rectangular pile group. This effect was intensified with the increase in the scour extent. Therefore, a rectangular pile group is recommended in the design of pile groups against scour.

5.8 Notation

A_b = area of scour-hole bottom

A_e = area enclosed by the $\sigma'_{z,sc}/\sigma'_{z,int}$ profile and the right vertical axis ($\sigma'_{z,sc}/\sigma'_{z,int}$=1.0) in the depth distribution of vertical stress ratio

c_u = undrained shear strength of clay

c_{uc} =undrained shear strength of clay used in 3D FEM

D = pile diameter

D_e = effective diameter of a pile group defined by Sheppard (2003)

E_p = elastic modulus of pile

E_s = undrained elastic modulus of soil

F_0 = post-scour ultimate soil resistance in force units when $0<z\leq S_{wb}$

F_1 = post-scour ultimate soil resistance in force units when $S_{wb}<z\leq S_{wb}+S_{gd}/\Theta$ and $S_\theta<45°$

F_{sc} = post-scour ultimate soil resistance in force units when $z>S_{wb}+S_{gd}/\Theta$ and $S_\theta<45°$ or when $z>S_{wb}$ and $S_\theta\geq 45°$

f_m = p-multiplier (usually ≤1.0) that considers geotechnical pile group effect

h_j = height of soil column defined in the proposed method, j =1, 2, …, J

J = number of soil columns

J_s = empirical coefficient in Matlock's p-y curve for soft clay, typically taken as 0.5

K_h= multiplier accommodating for the height of the pile top in the determination of D_e

K_m= multiplier accommodating for the number of piles in the determination of D_e

K_s= multiplier accommodating for the pile spacing in the determination of D_e

L = pile length

L_b = length of the scour-hole bottom in the proposed method

L_e = pre-scour embedded length of pile

L_{ij} = distance between the point of interest in the i^{th} pile to the center of the j^{th} soil

column bottom, i= 1, 2, …, mn

I_p = moment of inertia of pile

M_{max} = maximum bending moment of pile

M_y = yielding bending moment of pile

m = number of piles in-line with the lateral load direction

n= number of piles normal to the lateral load direction

P_j = weight of the j^{th} soil column, j =1, 2, …, J

R_p = flexural rigidity of pile

p = lateral soil resistance per unit length of a pile

p_{ult} = ultimate lateral soil resistance per unit length of a pile

$p_{u,sc}$ = post-scour ultimate lateral soil resistance

q_c = cone penetration resistance

S_{gd} = scour-hole depth around a pile group

S_{sd} = scour-hole depth around a single isolated pile

S_{wb} = scour-hole bottom width around a pile group

S_θ = scour-hole slope angle around a pile group

s = center-to-center pile spacing (s is used when s_x=s_y)

s_x = center-to-center pile spacing in-line with the lateral load direction

s_y = center-to-center pile spacing normal to the lateral load direction

W_b = width of the scour-hole bottom in the proposed method

W_p = projected width of pile group in the determination of D_e

W_{sp} = projected width of an individual pile in the pile group in the determination of D_e

(x_p, y_p) = coordinates of the i^{th} pile

(x_s, y_s) = coordinates of the j^{th} soil column

y = lateral soil displacement

y_{50} = lateral displacement of pile at one-half of the ultimate lateral soil resistance

z = depth below post-scour ground surface

z_e = equivalent depth that considers scour effect, z_e= $\sigma'_{z,sc}/\gamma'$

z_i = influence depth that considers scour effect, below which $\sigma'_{z,sc} = \sigma'_{z,int}$

$z_{M,max}$ = distance from scour bottom to location of the maximum bending moment

α_f = flow skew angle

β = angle of the passive failure wedge with the ground surface, β=45° for undrained clay

γ' = effective unit weight of soil

γ_s =saturated unit weight of soil

Δx = width of soil column on x direction in the proposed method

Δy = width of soil column on y direction in the proposed method

$\Delta\sigma'_z$ = vertical effective stress resulting from soil overburden above the post-scour ground surface

ε_{50} = strain corresponding to one-half of the maximum principal stress difference, typically taken as 0.01

η = a semi-empirical correction factor to account for the effect of soil-pile interface friction on retaining vertical effective stress in soils after scouring

Θ = a pramaeter given by $\tan S_\theta/(1-\tan S_\theta)$

ν_p = poison's ratio of pile

ν_s = Poisson's ratio of soil

σ'_z = vertical effective stress resulting from soil overburden below the post-scour ground surface

$\sigma'_{z,sc}$ = post-scour vertical effective stress of soil at pile

Ψ_{ij} = influence factor depending on L_{ij}

Chapter 6 Future Work

This research investigated the scour effects on the vertical effective stresses of single piles and pile groups, the lateral responses of the monopile-supported offshore wind turbines (OWTs) under seismic loading, and the lateral responses of the pile groups under static loading. Further research can be conducted on the following topics:

(1) Using the developed computer scripts based on the proposed methods in Chapters 2 and 3, seismic fragility analysis can be performed for the monopile-supported OWTs under scoured conditions. The fragility curves can serve as a more convenient indicator for the seismic design against scour.

(2) A further study is needed to modify the rotational springs and base shear springs for a large diameter pile (e.g., monopile) under the local scour condition. This allows incorporating the scour effect into the PISA design model, which is a new method developed in the Pile Soil Analysis Project (PISA) and is deemed as a more rigorous design method for the monopile.

(3) Based on the post-scour vertical effective stress evaluated in Chapters 4 and 5, post-scour t-z and q-z springs for a pile group can be developed to further investigate the vertical behavior of pile groups under local scour conditions.

(4) The dynamic behavior of pile groups under the combined effects of local scour and earthquakes can be investigated by incorporating the proposed methods in Chapters 4 and 5 into the framework of dynamic soil-structure interactions.

(5) Analytical methods and numerical simulations are also needed to investigate the scour effect on the lateral and/or vertical responses of single piles and pile groups in layered soils.

References

Abhinav, K.A., Saha, N., 2016. Effect of scouring in sand on monopile-supported offshore wind turbines. Mar. Georesources Geotechnol. 35, 817–828. https://doi.org/10.1080/1064119X.2016.1255687.

Achmus, M., Abdel-Rahman, K., 2005. Numerical modeling of vertical piles in clay under inclined compression loading. Presented at the Frontiers in Offshore Geotechnics, Taylor & Francis, Perth, Australia, pp. 391–396.

Achmus, M., Kuo, Y.S., Abdel-Rahman, K., 2010. Numerical investigation of scour effect on lateral resistance of windfarm monopiles. Presented at the 20th International Offshore and Polar Engineering Conference, International Society of Offshore and Polar Engineers, Beijing, China.

Afacan, K.B., Yniesta, S., Shafiee, A., Stewart, J.P., Brandenberg, S.J., 2019. Total stress analysis of soft clay ground response in centrifuge models. J. Geotech. Geoenvironmental Eng. 145, 04019061. https://doi.org/10.1061/(ASCE)GT.1943-5606.0002115

Ali, A., Risi, R.D., Sextos, A., Goda, K., Chang, Z., 2020. Seismic vulnerability of offshore wind turbines to pulse and non-pulse records. Earthq. Eng. Struct. Dyn. 49, 24–50. https://doi.org/10.1002/eqe.3222

Amini, A., Melville, B.W., Ali, T.M., 2014. Local scour at piled bridge piers including an examination of the superposition method. Can. J. Civ. Eng. 41, 461–471. https://doi.org/10.1139/cjce-2011-0389

Amini, A., Melville, B.W., Ali, T.M., Ghazali, A.H., 2012. Clear-water local scour around pile groups in shallow-water flow. J. Hydraul. Eng. 138, 177–185. https://doi.org/10.1061/(ASCE)HY.1943-7900.0000488

Anderson, I.A., Dewoolkar, M.M., Rizzo, D.M., Huston, D.R., 2014. Scour related Vermont bridge damage from tropical storm Irene. Presented at the Structures Congress 2014, American Society of Civil Engineers (ASCE), Boston, Massachusetts, United States, pp. 505–515. https://doi.org/10.1061/9780784413357.046

API, 2011. API RP 2GEO: Recommended practice, geotechnical and foundation design considerations, ANSI/API recommended practice 2GEO. American Petroleum

Institute (API), Washington, D.C., USA.

API, 2000. Recommended practice for planning, designing and constructing fixed offshore platforms-working stress design [Report No. RP 2A-WSD (21st ed.)]. American Petroleum Institute (API), Washington, D.C., USA.

Arany, L., Bhattacharya, S., Macdonald, J., Hogan, S.J., 2017. Design of monopiles for offshore wind turbines in 10 steps. Soil Dyn. Earthq. Eng. 92, 126–152. https://doi.org/10.1016/j.soildyn.2016.09.024

Arneson, L.A., Zevenbergen, L.W., Lagasse, P.F., Clopper, P.E., 2012. Evaluating scour at bridges (Report No. FHWA-HIF-12-003, HEC-18). Federal Highway Administration, U.S. Department of Transportation, Washington, D.C., USA.

ASSHTO, 2012. ASSHTO LRFD bridge design specifications (Report No. LRFDUS-6). American Association of State Highway and Transportation Officials (AASHTO), Washington, D.C., USA.

Ataie-Ashtiani, B., Beheshti, A.A., 2006. Experimental investigation of clear-water local scour at pile groups. J. Hydraul. Eng. 132, 1100–1104. https://doi.org/10.1061/(ASCE)0733-9429(2006)132:10(1100)

Baffer, B., 2013. Relationship between small strain shear modulus and undrained shear strength in direct simple shear (M.Sc. thesis). Department of Ocean Engineering, The University of Rohde Island, Kinston, Rohde Island, USA.

Baker, J.W., Lin, T., Shahi, S.K., Jayaram, N., 2011. New ground motion selection procedures and selected motions for the PEER transportation research program. Pacific Earthquake Engineering Research Center (PEER), Berkeley, CA, USA.

Bayram, A., Larson, M., 2000. Analysis of scour around a group of vertical piles in the field. J. Waterw. Port Coast. Ocean Eng. 126, 215–220. https://doi.org/10.1061/(ASCE)0733-950X(2000)126:4(215)

Berger, E., Mahi, S.A., Pyke, R., 1977. Simplified method for evaluating soil-pile-structure interaction effects. Presented at the 9th Annual Offshore Technology Conference, Offshore Technology Conference, Houston, Texas, USA, pp. 589–598. https://doi.org/10.4043/2954-MS

Bhattacharya, S., 2019. Design of foundations for offshore wind turbines, 1st ed. John Wiley & Sons Ltd, West Sussex, UK.

Bhattacharya, S., De Risi, R., Lombardi, D., Ali, A., Demirci, H.E., Haldar, S., 2021.

On the seismic analysis and design of offshore wind turbines. Soil Dyn. Earthq. Eng. 145, 106692. https://doi.org/10.1016/j.soildyn.2021.106692

Bhattacharya, S., Lombardi, D., Muir Wood, D., 2011. Similitude relationships for physical modelling of monopile-supported offshore wind turbines. Int. J. Phys. Model. Geotech. 11, 58–68. https://doi.org/10.1680/ijpmg.2011.11.2.58

Bhattacharya, S., Nikitas, N., Garnsey, J., Alexander, N.A., Cox, J., Lombardi, D., Muir Wood, D., Nash, D.F.T., 2013. Observed dynamic soil–structure interaction in scale testing of offshore wind turbine foundations. Soil Dyn. Earthq. Eng. 54, 47–60. https://doi.org/10.1016/j.soildyn.2013.07.012

Boulanger, R.W., Curras, C.J., Bruce, B.L., Wilson, D.W., Abghari, A., 1999. Seismic soil-pile-structure interaction experiments and analyses. J. Geotech. Geoenvironmental Eng. 125, 750–759. https://doi.org/10.1061/(ASCE)1090-0241(1999)125:9(750)

Boulanger, R.W., Kutter, B.L., Brandenberg, S.J., Singh, P., Chang, D., 2003. Pile foundations in liquefied and laterally spreading ground during earthquakes: centrifuge experiments and analyses (Report No. UCD/CGM-03/01). University of California, Davis, Davis, California, USA.

Bowles, J.E., 2012. Foundation analysis and design, 5th ed. McGraw-Hill Education.

Bowles, J.E., 1997. Foundation analysis and design, 15th ed. The McGraw-Hill Companies, Inc., Peoria, Illinois, USA.

Brandenberg, S.J., Zhao, M., Boulanger, R.W., Wilson, D.W., 2013. *p-y* plasticity model for nonlinear dynamic analysis of piles in liquefiable soil. J. Geotech. Geoenvironmental Eng. 139, 1262–1274. https://doi.org/10.1061/(ASCE)GT.1943-5606.0000847

Briaud, J.L., 2015. Scour depth at bridges: method including soil properties. I: maximum scour depth prediction. J. Geotech. Geoenvironmental Eng. 141, 04014104. https://doi.org/10.1061/(ASCE)GT.1943-5606.0001222

Brown, D., Morrison, Reese, L.C., 1988. Lateral load behavior of pile group in sand. J. Geotech. Eng. 114, 1261–1276. https://doi.org/10.1061/(ASCE)0733-9410(1988)114:11(1261)

Brown, D.A., Turner, J.P., Castelli, R.J., 2010. Drilled shafts: Construction procedures and LRFD design methods (Report No. FWHA-NHI-10-016). Federal Highway

Administration, U.S. Department of Transportation, Washington, D.C., USA.

Butch, G.K., 1996. Scour-hole dimensions at selected bridge piers in New York. Presented at the North American water and environment congress & destructive water, American Society of Civil Engineers (ASCE), Anaheim, California, USA.

Capraro, I., 2018. Damage, collapse potential and long duration effects of subduction ground motions on structural systems. The University of British Columbia. https://doi.org/10.14288/1.0368712

Carter, J.M.F., 2007. North Hoyle offshore wind farm: design and build. Proc. Inst. Civ. Eng. - Energy 160, 21–29. https://doi.org/10.1680/ener.2007.160.1.21

Chin, C.O., Chiew, Y.M., Lim, S.Y., Lim, F.H., 1996. Jet scour around vertical pile. J. Waterw. Port Coast. Ocean Eng. 122, 59–67. https://doi.org/10.1061/(ASCE)0733-950X(1996)122:2(59)

Chopra, A.K., 2011. Dynamics of structures, 4th ed. Prentice-Hall International Series in Civil Engineering and Engineering Mechanics. Prentice Hall, Upper Saddle River, New Jersey, USA.

Coleman, S.E., Melville, B.W., 2001. Case study: New Zealand bridge scour experiences. J. Hydraul. Eng. 127, 535–546. https://doi.org/10.1061/(ASCE)0733-9429(2001)127:7(535)

Couldrey, A.J., Benson, T., Knaapen, M.A.F., Marten, K.V., Whitehouse, R.J.S., 2020. Morphological evolution of a barchan dune migrating past an offshore wind farm foundation. Earth Surf. Process. Landf. 45, 2884–2896. https://doi.org/10.1002/esp.4937

Darendeli, M.B., 2001. Development of a new family of normalized modulus reduction and material damping curves (Ph.D. thesis). The University of Texas, Austin, TX, USA.

De Risi, R., Bhattacharya, S., Goda, K., 2018. Seismic performance assessment of monopile-supported offshore wind turbines using unscaled natural earthquake records. Soil Dyn. Earthq. Eng. 109, 154–172. https://doi.org/10.1016/j.soildyn.2018.03.015

Dean, E.T.R., 2010. Offshore geotechnical engineering. Thomas Telford Ltd. https://doi.org/10.1680/oge.36413

Di Laora, R., de Sanctis, L., 2013. Piles-induced filtering effect on the foundation input

motion. Soil Dyn. Earthq. Eng. 46, 52–63. https://doi.org/10.1016/j.soildyn.2012.12.007

DNV, 2014. Design of offshore wind turbine structures. Det Norske Veritas (DNV), Oslo, Norway.

Doherty, P., Gavin, K., 2012. Laterally loaded monopile design for offshore wind farms. Proc. Inst. Civ. Eng. - Energy 165, 7–17. https://doi.org/10.1680/ener.11.00003

Esfeh, P.K., Kaynia, A.M., 2020. Earthquake response of monopiles and caissons for offshore wind turbines founded in liquefiable soil. Soil Dyn. Earthq. Eng. 136, 106213. https://doi.org/10.1016/j.soildyn.2020.106213

Fayyazi, M.S., Taiebat, M., Finn, W.D.L., 2014. Group reduction factors for analysis of laterally loaded pile groups. Can. Geotech. J. 51, 758–769. https://doi.org/10.1139/cgj-2013-0202

FEMA, 2012. Foundation analysis and design (Report No. FEMA P-751), NEHRP recommended provisions: design examples. Federal Emergency Management Agency (FEMA). National Institute of Building Sciences, Building Seismic Safety Council, Washington, D.C., USA.

FEMA, 2009. Quantification of building seismic performance factors (Report No. FEMA P695). Federal Emergency Management Agency (FEMA), Redwood City, CA, USA.

Feng, J., Zhang, J., Zhu, M., Jiang, N., 2016. Characteristic study of horizontal bearing capacity and pile group effect coefficient of laterally loaded high pile group foundation for bridge in soft soil. Rock Soil Mech. 37, 103–113. https://doi.org/10.16285/j.rsm.2016.S2.011

Fischenich, C., Landers, M., 1999. Computing scour. EMRRP SR-05 technical note. U.S. Army Engineer Research and Development Center, Vicksburg, MS, USA.

Fleming, K., Weltman, A., Randolph, M., Elson, K., 2009. Piling engineering, 3rd ed. Taylor & Francis Group, Abingdon, UK.

Fleming, W., Weltman, A., Randolph, M., Elson, W., 1992. Piling engineering, 2nd ed. Taylor & Francis Group, London, UK.

Garala, T.K., Madabhushi, G.S.P., 2019. Seismic behaviour of soft clay and its influence on the response of friction pile foundations. Bull. Earthq. Eng. 17, 1919–1939. https://doi.org/10.1007/s10518-018-0508-4

Gazetas, G., Dobry, R., 1984. Simple radiation damping model for piles and footings. J. Eng. Mech. 110, 937–956. https://doi.org/10.1061/(ASCE)0733-9399(1984)110:6(937)

Ghosn, M., Moses, F., Wang, J., 2003. National Cooperative Highway Research Program (NCHRP): Design of highway bridges for extreme events (Report No. 489). Transportation Research Board, Washington, D.C., USA.

Gilbert, R.B., Wang, S.T., Senanayake, A., Rendon, E., 2015. Design of wind turbine monopiles for lateral loads. Bureau of Safety and Environment Enforcement (BSEE), U.S. Department of the Interior, Washington, D.C., USA.

GL, 2012. Guideline for the certification of offshore wind turbines. Germanischer Lloyd (GL) Renewables Certification, Hamburg, Germany.

Gouw, T.L., 2014. Common mistakes on the application of Plaxis 2D in analyzing excavation problems. Int. J. Appl. Eng. Res. 9, 8291–8311.

Goyal, A., Chopra, A.K., 1989a. Earthquake analysis of intake-outlet towers including tower-water-foundation-soil interaction. Earthq. Eng. Struct. Dyn. 18, 325–344. https://doi.org/10.1002/eqe.4290180303

Goyal, A., Chopra, A.K., 1989b. Simplified evaluation of added hydrodynamic mass for intake towers. J. Eng. Mech. 115, 1393–1412. https://doi.org/10.1061/(ASCE)0733-9399(1989)115:7(1393)

Groholski, D.R., Hashash, Y.M.A., Kim, B., Musgrove, M., Harmon, J., Stewart, J.P., 2016. Simplified model for small-strain nonlinearity and strength in 1D seismic site response analysis. J. Geotech. Geoenvironmental Eng. 142, 04016042. https://doi.org/10.1061/(ASCE)GT.1943-5606.0001496

Guan, D., Chiew, Y.M., Melville, B.W., Zheng, J., 2019. Current-induced scour at monopile foundations subjected to lateral vibrations. Coast. Eng. 144, 15–21. https://doi.org/10.1016/j.coastaleng.2018.10.011

GWEC, 2021. Global wind report 2021. Global Wind Energy Council (GWEC), Brussels, Belgium.

GWEC, 2020. Global wind report 2019. Global Wind Energy Council (GWEC), Brussels, Belgium.

Haldar, S., Patra, S.K., 2021. Dynamic response of monopile supported offshore wind turbine in liquefied soil, in: Sitharam, T.G., Jakka, R., Kolathayar, S. (Eds.), Latest

Developments in Geotechnical Earthquake Engineering and Soil Dynamics, Springer Transactions in Civil and Environmental Engineering. Springer, Singapore, pp. 525–538. https://doi.org/10.1007/978-981-16-1468-2_27

Hamidi, A., Siadatmousavi, S.M., 2018. Numerical simulation of scour and flow field for different arrangements of two piers using SSIIM model. Ain Shams Eng. J. 9, 2415–2426. https://doi.org/10.1016/j.asej.2017.03.012

Hannah, C.R., 1978. Scour at pile groups (Master's thesis). The University of Canterbury, Canterbury, New Zealand.

Hardin, B.O., Drnevich, V.P., 1972. Shear modulus and damping in soils: measurement and parameter effects (Terzaghi lecture). J. Soil Mech. Found. Div. 98, 603–624.

Harris, J., Whitehouse, R.J.S., 2014. Marine scour: lessons from nature's laboratory. Presented at the 7th International Conference on Scour and Erosion, International Conference on Scour and Erosion, Crawley, Australia. https://doi.org/10.1201/b17703-4

Harris, J.M., Whitehouse, R.J.S., 2017. Scour development around large-diameter monopiles in cohesive soils: Evidence from the field. J. Waterw. Port Coast. Ocean Eng. 143, 04017022. https://doi.org/10.1061/(ASCE)WW.1943-5460.0000414

Hashash, Y.M.A., Musgrove, M.I., Harmon, J.A., Ilhan, O., Groholski, D.R., Phillips, C.A., Park, D., 2017. DEEPSOIL 7.0, User Manual. Board of Trustees of the University of Illinois at Urbana-Champaign.

Hazzar, L., Hussien, M.N., Karray, M., 2017. On the behaviour of pile groups under combined lateral and vertical loading. Ocean Eng. 131, 174–185. https://doi.org/10.1016/j.oceaneng.2017.01.006

Hazzar, L., Karray, M., Hussien, M., Bouassida, M., 2013. Three dimensional modeling of a pile group under static lateral loading using finite differences method, in: 66th Canadian Geotechnical Conference. Presented at the GéoMontréal 2013, Canadian Geotechnical Society, Montreal, Quebec, Canada.

He, B., Lai, Y., Wang, L., Hong, Y., Zhu, R., 2019. Scour effects on the lateral behavior of a large-diameter monopile in soft clay: role of stress history. J. Mar. Sci. Eng. 7, 170. https://doi.org/10.3390/jmse7060170

Hochi, Y., Murono, Y., Saitoh, M., Goit, C.S., 2019. Earthquake motion filtering effect by pile foundations considering nonlinearity of soil and piles. Soil Dyn. Earthq.

Eng. 125, 105748. https://doi.org/10.1016/j.soildyn.2019.105748

Hosseini, R., Amini, A., 2015. Scour depth estimation methods around pile groups. KSCE J. Civ. Eng. 19, 2144–2156. https://doi.org/10.1007/s12205-015-0594-7

Hussien, M.N., Tobita, T., lai, S., Rollins, K.M., 2010. Soil-pile separation effect on the performance of a pile group under static and dynamic lateral loads. Can. Geotech. J. 47, 1234+. https://doi.org/10.1139/T10-026

Idriss, I.M., 1991. Earthquake ground motions at soft soil sites. Presented at the 2nd International Conference on Recent Advances in Geotechnical Earthquake Engineering and Soil Dynamics, 2nd International Conference on Recent Advances in Geotechnical Earthquake Engineering and Soil Dynamics, Missouri, USA, p. 9.

Ilankatharan, M., 2008. Centrifuge modeling for soil-pile-bridge systems with numerical simulations accounting for soil-container-shaker interaction (Ph.D. thesis). University of California, Davis, Davis, California, USA.

Imhof, D., 2004. Risk assessment of existing bridge structures (Ph.D. thesis). University of Cambridge. https://doi.org/10.17863/CAM.19092

Isenhower, W.M., Wang, S.T., Vasquez, L.G., 2020. LPILE V2019 Technical manual: a program for the analysis of deep foundations under lateral loading. Ensoft, Inc., Austin, TX, USA.

Ji, C., Zhang, J., Zhang, Q., Li, M., Chen, T., 2018. Experimental investigation of local scour around a new pile-group foundation for offshore wind turbines in bi-directional current. China Ocean Eng. 32, 737–745. https://doi.org/10.1007/s13344-018-0075-0

Jia, N., Ding, H., Zhang, P., Liu, J., 2017. The seismic response of composite bucket foundation for offshore wind turbines under scour conditions. Presented at the 27th International Ocean and Polar Engineering Conference, International Society of Offshore and Polar Engineers, San Francisco, California, USA.

Jiang, W., Lin, C., 2021. Scour effects on vertical effective stresses and lateral responses of pile groups in sands. Ocean Eng. 229, 109017. https://doi.org/10.1016/j.oceaneng.2021.109017

Jiang, W., Lin, C., 2020. Seismic responses of monopile in sands under scour conditions. Presented at the GeoVirtual 2020 Resilience and Innovation, Canada.

Jiang, W., Lin, C., Sun, M., 2021. Seismic responses of monopile-supported offshore

wind turbines in soft clays under scoured conditions. Soil Dyn. Earthq. Eng. 142, 106549. https://doi.org/10.1016/j.soildyn.2020.106549

Joyner, W.B., Chen, A.T.F., 1975. Calculation of nonlinear ground response in earthquakes. Bull. Seismol. Soc. Am. 65, 1315–1336.

Kampitsis, A.E., Sapountzakis, E.J., Giannakos, S.K., Gerolymos, N.A., 2013. Seismic soil-pile-structure kinematic and inertial interaction-a new beam approach. Soil Dyn. Earthq. Eng. 55, 211–224. https://doi.org/10.1016/j.soildyn.2013.09.023

Kariyawasam, K.D., Middleton, C.R., Madabhushi, G., Haigh, S.K., Talbot, J.P., 2020. Assessment of bridge natural frequency as an indicator of scour using centrifuge modelling. J. Civ. Struct. Health Monit. 10, 861–881. https://doi.org/10.1007/s13349-020-00420-5

Khodair, Y., Abdel-Mohti, A., 2014. Numerical analysis of pile-soil interaction under axial and lateral loads. Int. J. Concr. Struct. Mater. 8, 239–249. https://doi.org/10.1007/s40069-014-0075-2

Khosravifar, A., Boulanger, R.W., Kunnath, S.K., 2014. Effects of liquefaction on inelastic demands on extended pile shafts. Earthq. Spectra 30, 1749–1773.

Kim, D.H., Lee, S.G., Lee, I.K., 2014. Seismic fragility analysis of 5 MW offshore wind turbine. Renew. Energy, SI:AFORE 2012 65, 250–256. https://doi.org/10.1016/j.renene.2013.09.023

Kim, H.S., Nabi, M., Kimura, I., Shimizu, Y., 2014. Numerical investigation of local scour at two adjacent cylinders. Adv. Water Resour. 70, 131–147. https://doi.org/10.1016/j.advwatres.2014.04.018

Klinkvort, R.T., Hededal, O., 2013. Lateral response of monopile supporting an offshore wind turbine. Proc. Inst. Civ. Eng. - Geotech. Eng. 166, 147–158. https://doi.org/10.1680/geng.12.00033

Krabbenhoft, S., Andersen, A., Damkilde, L., 2008. The tensile capacity of bored piles in frictional soils. Can. Geotech. J. 45, 1715–1722. https://doi.org/10.1139/T08-086

Kramer, S.L., 1996. Geotechnical earthquake engineering, 1st ed. Prentice-Hall international series in civil engineering and engineering mechanics. Pearson Education, Upper Saddle River, New Jersey, USA.

Kramer, S.L., Sideras, S.S., Greenfield, M.W., 2016. The timing of liquefaction and its

utility in liquefaction hazard evaluation. Soil Dyn. Earthq. Eng., 6ICEGE – Earthquake Geotechincal Engineeering 91, 133–146. https://doi.org/10.1016/j.soildyn.2016.07.025

Kulhawy, F.H., Mayne, P.W., 1990. Manual on estimating soil properties for foundation design (Report No. EL-6800). Electric Power Research Institute, Palo Alto, California, USA.

Lagasse, P.F., Zevenbergen, L.W., Schall, J.D., 2007. Countermeasures to protect bridge piers from scour (Report No. NCHRP Report 593). Transportation Research Board, Washington, D.C. https://doi.org/10.17226/17612

Lança, R., Cristina, F., Rodrigo, M., Pêgo, J.P., Cardoso, A.H., 2013. Clear-water scour at pile groups. J. Hydraul. Eng. 139, 1089–1098. https://doi.org/10.1061/(ASCE)HY.1943-7900.0000770

Li, H., Ong, M.C., Leira, B.J., Myrhaug, D., 2018. Effects of soil profile variation and scour on structural response of an offshore monopile wind turbine. J. Offshore Mech. Arct. Eng. 140. https://doi.org/10.1115/1.4039297

Li, Q., Prendergast, L.J., Askarinejad, A., Chortis, G., Gavin, K., 2020. Centrifuge modeling of the impact of local and global scour erosion on the monotonic lateral response of a monopile in sand. Geotech. Test. J. 43, 1084–1100. https://doi.org/10.1520/GTJ20180322

Liang, F., Liang, X., Zhang, H., Wang, C., 2020. Seismic response from centrifuge model tests of a scoured bridge with a pile-group foundation. J. Bridge Eng. 25, 04020054. https://doi.org/10.1061/(ASCE)BE.1943-5592.0001594

Liang, F., Wang, C., Huang, M., Wang, Y., 2017. Experimental observations and evaluations of formulae for local scour at pile groups in steady currents. Mar. Georesources Geotechnol. 35, 245–255. https://doi.org/10.1080/1064119X.2016.1147510

Liang, F., Wang, C., Yu, X. (Bill), 2019. Widths, types, and configurations: influences on scour behaviors of bridge foundations in non-cohesive soils. Mar. Georesources Geotechnol. 37, 578–588. https://doi.org/10.1080/1064119X.2018.1460644

Liang, F., Zhang, H., Chen, S., 2018. Effect of vertical load on the lateral response of offshore piles considering scour-hole geometry and stress history in marine clay. Ocean Eng. 158, 64–77. https://doi.org/10.1016/j.oceaneng.2018.03.070

Liang, F., Zhang, H., Huang, M., 2015. Extreme scour effects on the buckling of bridge piles considering the stress history of soft clay. Nat. Hazards 77, 1143–1159. https://doi.org/10.1007/s11069-015-1647-4

Liaw, C.Y., Chopra, A.K., 1974. Dynamics of towers surrounded by water. Earthq. Eng. Struct. Dyn. 3, 33–49. https://doi.org/10.1002/eqe.4290030104

Lin, C., 2017. The loss of pile axial capacities due to scour: vertical stress distribution. Presented at the 2017 International Conference on Transportation Infrastructure and Materials (ICTIM 2017), Qingdao, China.

Lin, C., Bennett, C., Han, J., Parsons, R.L., 2010. Scour effects on the response of laterally loaded piles considering stress history of sand. Comput. Geotech. 37, 1008–1014. https://doi.org/10.1016/j.compgeo.2010.08.009

Lin, C., Han, J., Bennett, C., Parsons, R.L., 2016. Analysis of laterally loaded piles in soft clay considering scour-hole dimensions. Ocean Eng. 111, 461–470. https://doi.org/10.1016/j.oceaneng.2015.11.029

Lin, C., Han, J., Bennett, C., Parsons, R.L., 2014a. Analysis of laterally loaded piles in sand considering scour hole dimensions. J. Geotech. Geoenvironmental Eng. 140, 04014024. https://doi.org/10.1061/(ASCE)GT.1943-5606.0001111

Lin, C., Han, J., Bennett, C., Parsons, R.L., 2014b. Behavior of laterally loaded piles under scour conditions considering the stress history of undrained soft clay. J. Geotech. Geoenvironmental Eng. 140, 06014005. https://doi.org/10.1061/(ASCE)GT.1943-5606.0001112

Lin, C., Jiang, W., 2019. Evaluation of vertical effective stress and pile tension capacity in sands considering scour-hole dimensions. Comput. Geotech. 105, 94–98. https://doi.org/10.1016/j.compgeo.2018.09.013

Lin, C., Wu, R., 2019. Evaluation of vertical effective stress and pile lateral capacities considering scour-hole dimensions. Can. Geotech. J. 56, 135–143. https://doi.org/10.1139/cgj-2017-0644

Lin, Y., Lin, C., 2020. Scour effects on lateral behavior of pile groups in sands. Ocean Eng. 208, 107420. https://doi.org/10.1016/j.oceaneng.2020.107420

Lin, Y., Lin, C., 2019. Effects of scour-hole dimensions on lateral behavior of piles in sands. Comput. Geotech. 111, 30–41. https://doi.org/10.1016/j.compgeo.2019.02.028

Liu, R., Yan, S., Li, Z., 2009. Soil plug effect prediction and pile driveability analysis for large-diameter steel piles in ocean engineering. China Ocean Eng. 23, 107–118.

Lombardi, D., Bhattacharya, S., Muir Wood, D., 2013. Dynamic soil-structure interaction of monopile supported wind turbines in cohesive soil. Soil Dyn. Earthq. Eng. 49, 165–180. https://doi.org/10.1016/j.soildyn.2013.01.015

Lysmer, J., Kuhlemeyer, R.L., 1969. Finite dynamic model for infinite media. J. Eng. Mech. Div. 95, 859–878.

Ma, H., Yang, J., Chen, L., 2018. Effect of scour on the structural response of an offshore wind turbine supported on tripod foundation. Appl. Ocean Res. 73, 179–189. https://doi.org/10.1016/j.apor.2018.02.007

Ma, L., Wang, L., Guo, Z., Jiang, H., Gao, Y., 2018. Time development of scour around pile groups in tidal currents. Ocean Eng. 163, 400–418. https://doi.org/10.1016/j.oceaneng.2018.06.035

MATLAB, 2019. MATLAB R2019b. The MathWorks Inc., Natick, Massachusetts, USA.

Matlock, H., 1970. Correlation for design of laterally loaded piles in soft clay. Presented at the Offshore Technology Conference, Offshore Technology Conference, Houston, Texas, USA. https://doi.org/10.4043/1204-MS

McKenna, F., 2011. OpenSees: a framework for earthquake engineering simulation. Comput. Sci. Eng. 13, 58–66. https://doi.org/10.1109/MCSE.2011.66

Mehrzad, B., Jafarian, Y., Lee, C.J., Haddad, A.H., 2018. Centrifuge study into the effect of liquefaction extent on permanent settlement and seismic response of shallow foundations. Soils Found. 58, 228–240. https://doi.org/10.1016/j.sandf.2017.12.006

Meymand, P.J., 1998. Shaking table scale model tests of nonlinear soil-pile-superstructure interaction in soft clay (Ph.D. thesis). University of California, Berkeley, Berkeley, California, USA.

Miyamoto, J., Sassa, S., Tsurugasaki, K., Sumida, H., 2021. Wave-induced liquefaction and instability of offshore monopile in a drum centrifuge. Soils Found. 61, 35–49. https://doi.org/10.1016/j.sandf.2020.10.005

Mo, R., Kang, H., Li, M., Zhao, X., 2017. Seismic fragility analysis of monopile offshore wind turbines under different operational conditions. Energies 10, 1037.

https://doi.org/10.3390/en10071037

Mokwa, R.L., 1999. Investigation of the resistance of pile caps to lateral loading (Ph.D. thesis). Virginia Polytechnic Institute and State University, Blacksburg, Virginia, USA.

Mosher, R.L., 1984. Load-transfer criteria for numerical analysis of axially loaded piles in sand. Part I: load-transfer criteria (Report No. K-84-1). U.S. Army Engineer Waterways Experiment Station, Vicksburg, MS, USA.

Mueller, D.S., Wagner, C.R., 2005. Field observations and evaluations of streambed scour at bridges (Report No. FHWA-RD-03-052). Federal Highway Administration, U.S. Department of Transportation, McLean, VA, USA.

Mullins, G., Winters, D., Dapp, S., 2006. Predicting end bearing capacity of post-grouted drilled shaft in cohesionless soils. J. Geotech. Geoenvironmental Eng. 132, 478–487. https://doi.org/10.1061/(ASCE)1090-0241(2006)132:4(478)

Myers, A.T., Gupta, A., Ramirez, C.M., Chioccarelli, E., 2012. Evaluation of the seismic vulnerability of tubular wind turbine towers. Presented at the 15th World Conference on Earthquake Engineering, The 15th World Conference on Earthquake Engineering, Lisbon, Portugal, p. 9.

Nemry, F., Demirel, H., 2012. Impacts of climate change on transport: a focus on road and rail transport infrastructures (Report No. EUR 25553 EN, JRC72217), EUR - Scientific and Technical Research Reports. Publications Office of the European Union, Luxembourg (Luxembourg).

Ni, X., Xue, L., An, C., 2021. Experimental investigation of scour around circular arrangement pile groups. Ocean Eng. 219, 108096. https://doi.org/10.1016/j.oceaneng.2020.108096

Nicholas, S., 2014. Modeling of soil and structure interaction subsea (Master's thesis). Chalmers University of Technology, Göteborg, Sweden.

NRCC, 2015. National building code of Canada 2015. National Research Council of Canada (NRCC), Ottawa, Canada.

Paikowsky, S.G., Birgisson, B., McVay, M., Nguyen, T., Kuo, C., Baecher, G., Ayyub, B., Stenerson, K., O'Malley, K., Chernauskas, L., O'Neil, M., 2004. Load and resistance factor design (LRFD) for deep foundations (Report No. NCHRP 507). Transportation Research Board, National Research Council, Washington, D.C.,

USA.

Palmer, H.D., 1969. Wave-induced scour on the sea floor, in: Proceedings of Civil Engineering in the Oceans II. American Society of Civil Engineers (ASCE), New York, USA, pp. 703–716.

Passon, P., Branner, K., Larsen, S.E., Rasmussen, J.H., 2015. Offshore wind turbine foundation design (Ph.D. thesis). The Technical University of Denmark, Kongens Lyngby, Denmark.

Patrick, J.H., Frank, R., Garland, E.L., Brent, R.R., Matthew, L.B., 2016. Design and construction of driven pile foundations (Report No. FHWA-NHI-16-009), Geotechnical engineering circular No.12-volume 1. Federal Highway Administration, U.S. Department of Transportation, Washington, D.C., USA.

Phillips, C., Hashash, Y.M.A., 2009. Damping formulation for nonlinear 1D site response analyses. Soil Dyn. Earthq. Eng. 29, 1143–1158. https://doi.org/10.1016/j.soildyn.2009.01.004

Prendergast, L.J., Gavin, K., Doherty, P., 2015. An investigation into the effect of scour on the natural frequency of an offshore wind turbine. Ocean Eng. 101, 1–11. https://doi.org/10.1016/j.oceaneng.2015.04.017

Rathje, E.M., Abrahamson, N.A., Bray, J.D., 1998. Simplified frequency content estimates of earthquake ground motions. J. Geotech. Geoenvironmental Eng. 124, 150–159. https://doi.org/10.1061/(ASCE)1090-0241(1998)124:2(150)

Reese, L.C., O'Neil, M., 1988. Drilled shafts: Construction and design (Report No. FHWA-HI-88-42). Federal Highway Administration, U.S. Department of Transportation, Washington, D.C., USA.

Reese, L.C., Van Impe, W., 2001. Single piles and pile groups under lateral loading, 2nd ed. CRC Press/Balkema, Leiden, The Netherlands. https://doi.org/10.1201/b17499

Reese, L.C., Wang, S.T., Arrellaga, J.A., Hendrix, J., 1996. GROUP version 4.0 for Windows users manual. Ensoft, Inc., Austin, TX, USA.

REN21, 2019. Renewables 2019 global status report. Renewable Energy Policy Network for the 21st Century (REN21) Secretariat, Paris, France.

Rezaei, R., Duffour, P., Fromme, P., 2018. Scour influence on the fatigue life of operational monopile-supported offshore wind turbines. Wind Energy 21, 683–696.

https://doi.org/10.1002/we.2187

Rollins, K.M., Lane, J.D., Gerber, T.M., 2005. Measured and computed lateral response of a pile group in sand. J. Geotech. Geoenvironmental Eng. 131, 103–114. https://doi.org/10.1061/(ASCE)1090-0241(2005)131:1(103)

Rollins, K.M., Peterson, K.T., Weaver, T.J., 1998. Lateral load behavior of full-scale pile group in clay. J. Geotech. Geoenvironmental Eng. 124, 468–478. https://doi.org/10.1061/(ASCE)1090-0241(1998)124:6(468)

Santos, J., 2000. Behavior of piles under lateral static and dynamic loading (Ph.D. thesis). Technical University of Lisbon, Portugal.

Schofield, A., Wroth, P., 1968. Critical state soil mechanics, 1st edition. ed. McGraw-Hill, London, UK.

Seed, H.B., Wong, R.T., Idriss, I.M., Tokimatsu, K., 1986. Moduli and damping factors for dynamic analyses of cohesionless soils. J. Geotech. Eng. 112, 1016–1032. https://doi.org/10.1061/(ASCE)0733-9410(1986)112:11(1016)

Shang, Y., Xu, Y., Ye, A., Alipour, A., 2016. Experimental investigation on seismic response of bridges considering scour effect. Presented at the Civil Engineering Conference in the Asian Region CECAR7, Civil Engineering Conference in the Asian Region CECAR7, Waikiki, Oahu, Hawaii, USA.

Sheppard, D.M., 2003. Scour at complex piers. Florida Department of Transportation (FDOT), Tallahassee, FL, USA.

Snyder, J.L., 2004. Full-scale lateral-load tests of a 3×5 pile group in soft clays and silts (Master's thesis). Brigham Young University, Provo, Utah, USA.

Solaimani, N., Amini, A., Banejad, H., Ghazvinei, P.T., 2017. The effect of pile spacing and arrangement on bed formation and scour hole dimensions in pile groups. Int. J. River Basin Manag. 15, 219–225. https://doi.org/10.1080/15715124.2016.1274321

Søren, P.H.S., Lars Bo, I., 2013. Assessment of foundation design for offshore monopiles unprotected against scour. Ocean Eng. 63, 17–25. https://doi.org/10.1016/j.oceaneng.2013.01.016

Sumer, B.M., Bundgaard, K., Fredsøe, J., 2005. Global and local scour around a group of piles. Presented at the 15th International Offshore and Polar Engineering Conference (ISOPE), ISOPE, Seoul, Korea, pp. 577–583.

Sumer, B.M., Fredsøe, J., 1998. Wave scour around group of vertical piles. J. Waterw. Port Coast. Ocean Eng. 124, 248–256. https://doi.org/10.1061/(ASCE)0733-950X(1998)124:5(248)

Sumer, B.M., Hatipoglu, F., Fredsøe, J., 2007. Wave scour around a pile in sand, medium dense, and dense silt. J. Waterw. Port Coast. Ocean Eng. 133, 14–27. https://doi.org/10.1061/(ASCE)0733-950X(2007)133:1(14)

Sun, Y., Song, Y., Bian, S., 2007. Scour process around the pile foundation of marine platforms and analysis of scour mechanics. Period. Ocean Univ. China 636–640.

Taboada-Urtuzuastegui, V.M., Martinez-Ramirez, G., Abdoun, T., 2002. Centrifuge modeling of seismic behavior of a slope in liquefiable soil. Soil Dyn. Earthq. Eng. 22, 1043–1049. https://doi.org/10.1016/S0267-7261(02)00129-X

Tempel, J. van der, Zaaijer, M.B., Subroto, H., 2004. The effects of scour on the design of offshore wind turbines. Presented at the 3rd International Conference on Marine Renewable Energy (MAREC 2004), The East of England Energy Group (EEEGR), Newcastle, UK.

Tokimatsu, K., Suzuki, H., Sato, M., 2005. Effects of inertial and kinematic interaction on seismic behavior of pile with embedded foundation. Soil Dyn. Earthq. Eng., 11th International Conference on Soil Dynamics and Earthquake Engineering (ICSDEE): Part 1 25, 753–762. https://doi.org/10.1016/j.soildyn.2004.11.018

Tseng, W.C., Kuo, Y.S., Chen, J.W., 2017. An investigation into the effect of scour on the loading and deformation responses of monopile foundations. Energies 10, 1190. https://doi.org/10.3390/en10081190

Tseng, W.C., Kuo, Y.S., Lu, K.C., Chen, J.W., Chung, C.F., Chen, R.C., 2018. Effect of scour on the natural frequency responses of the meteorological mast in the Taiwan Strait. Energies 11, 823. https://doi.org/10.3390/en11040823

Turner, B.J., Brandenberg, S.J., Stewart, J.P., 2017. Influence of kinematic SSI on foundation input motions for bridges on deep foundations (Report No. PEER 2017/08). Pacific Earthquake Engineering Research Center (PEER), LA, USA.

U.S. Army Corps of Engineers, 1991. Engineering and design: design of pile foundations (Report No. EM 1110-2-2906). U.S. Army Corps of Engineers, Washington, D.C., USA.

Uthayakumar, M., Naesgaard, E., 2004. Ground response analysis for seismic design in

Fraser River Delta, British Columbia. Presented at the 13th World Conference on Earthquake Engineering, World Conference on Earthquake Engineering, Vancouver, B.C., Canada.

Van de Putte, V., 2018. Dynamic analysis of a monopile offshore wind support structure subjected to earthquakes: A comparative study between the responses of an elastic and an inelastic soil-structure interaction model through incremental dynamic analysis (Master's thesis). Delft University of Technology, Delft, Netherlands.

Van den Brink, F., 2014. Influence of liquefaction on scour around offshore monopile foundations (Master's thesis). Delft University of Technology, Delft, Netherlands.

Vijayvergiya, V.N., 1977. Load-movement characteristics of piles, in: Ports '77. 4th Annual Symposium of the American Society of Civil Engineers, Waterway, Port, Coastal and Ocean Division. American Society of Civil Engineers (ASCE), CA, USA, pp. 269–284.

Wang, C., Liang, F., Yu, X., 2017. Experimental and numerical investigations on the performance of sacrificial piles in reducing local scour around pile groups. Nat. Hazards 85, 1417–1435. https://doi.org/10.1007/s11069-016-2634-0

Wang, H., Tang, H., Xiao, J., Wang, Y., Jiang, S., 2016. Clear-water local scouring around three piers in a tandem arrangement. Sci. China Technol. Sci. 59, 888–896. https://doi.org/10.1007/s11431-015-5905-1

Wang, P., Zhao, M., Du, X., Liu, J., Xu, C., 2018. Wind, wave and earthquake responses of offshore wind turbine on monopile foundation in clay. Soil Dyn. Earthq. Eng. 113, 47–57. https://doi.org/10.1016/j.soildyn.2018.04.028

Wang, S., Kutter, B.L., Chacko, M.J., Wilson, D.W., Boulanger, R.W., Abghari, A., 1998. Nonlinear seismic soil-pile structure interaction. Earthq. Spectra 14, 377–396. https://doi.org/10.1193/1.1586006

Wang, S.C., Liu, K.Y., Chen, C.H., Chang, K.C., 2015. Experimental investigation on seismic behavior of scoured bridge pier with pile foundation. Earthq. Eng. Struct. Dyn. 44, 849–864. https://doi.org/10.1002/eqe.2489

Wang, X., Ji, B., Ye, A., 2020. Seismic behavior of pile-group-supported bridges in liquefiable soils with crusts subjected to potential scour: insights from shake-table tests. J. Geotech. Geoenvironmental Eng. 146, 04020030. https://doi.org/10.1061/(ASCE)GT.1943-5606.0002250

Wang, X., Luo, F., Su, Z., Ye, A., 2017. Efficient finite-element model for seismic response estimation of piles and soils in liquefied and laterally spreading ground considering shear localization. Int. J. Geomech. 17, 06016039. https://doi.org/10.1061/(ASCE)GM.1943-5622.0000835

Wang, X., Ye, A., Shang, Y., Zhou, L., 2019. Shake-table investigation of scoured RC pile-group-supported bridges in liquefiable and nonliquefiable soils. Earthq. Eng. Struct. Dyn. 48, 1217–1237. https://doi.org/10.1002/eqe.3186

Wang, Z., Dueñas-Osorio, L., Padgett, J.E., 2013. Seismic response of a bridge-soil-foundation system under the combined effect of vertical and horizontal ground motions. Earthq. Eng. Struct. Dyn. 42, 545–564. https://doi.org/10.1002/eqe.2226

Watson, T.N., 1974. Scour in the North Sea. J. Pet. Technol. 26, 289–293. https://doi.org/10.2118/4324-PA

Wehnert, M., Vermeer, P., 2004. Numerical analyses of load tests on bored piles. Presented at the Numerical methods in geomechanics-NUMOG IX, Ottawa, Canada.

Whitehouse, R., 1998. Scour at marine structures: a manual for practical applications, 1st ed. Thomas Telford Publications, London, UK.

Whitehouse, R.J.S., Harris, J.M., Sutherland, J., Rees, J., 2011. The nature of scour development and scour protection at offshore windfarm foundations. Mar. Pollut. Bull. 62, 73–88. https://doi.org/10.1016/j.marpolbul.2010.09.007

Wilson, D.W., Boulanger, R.W., Kutter, B.L., 1997. Soil-pile-superstructure interaction at soft or liquefiable soils sites - centrifuge data report for CSP3 (Report No. UCD/CGMDR-97/04). University of California, Davis, Davis, California, USA.

WindEurope, 2019. Offshore wind in Europe: key trends and statistics 2018. WindEurope, Brussels, Belgium.

Yagci, O., Yildirim, I., Celik, M.F., Kitsikoudis, V., Duran, Z., Kirca, V.S.O., 2017. Clear water scour around a finite array of cylinders. Appl. Ocean Res. 68, 114–129. https://doi.org/10.1016/j.apor.2017.08.014

Yang, Y., Bashir, M., Li, C., Wang, J., 2019a. Analysis of seismic behaviour of an offshore wind turbine with a flexible foundation. Ocean Eng. 178, 215–228. https://doi.org/10.1016/j.oceaneng.2019.02.077

Yang, Y., Li, C., Bashir, M., Wang, J., Yang, C., 2019b. Investigation on the sensitivity

of flexible foundation models of an offshore wind turbine under earthquake loadings. Eng. Struct. 183, 756–769. https://doi.org/10.1016/j.engstruct.2019.01.050

Yang, Yifan, Melville, B.W., Macky, G.H., Shamseldin, A.Y., 2020. Experimental study on local scour at complex bridge pier under combined waves and current. Coast. Eng. 160, 103730. https://doi.org/10.1016/j.coastaleng.2020.103730

Yang, Yilin, Qi, M., Wang, X., Li, J., 2020. Experimental study of scour around pile groups in steady flows. Ocean Eng. 195, 106651. https://doi.org/10.1016/j.oceaneng.2019.106651

Yang, Z., 2000. Numerical modeling of earthquake site response including dilation and liquefaction (Ph.D. thesis). Columbia University, New York, USA.

Yee, E., Stewart, J.P., Tokimatsu, K., 2013. Elastic and large-strain nonlinear seismic site response from analysis of vertical array recordings. J. Geotech. Geoenvironmental Eng. 139, 1789–1801. https://doi.org/10.1061/(ASCE)GT.1943-5606.0000900

Yim, S.C., Olsen, M., Cheung, K.F., Azadbakht, M., 2014. Tsunami modeling, fluid load simulation, and validation using geospatial field data. J. Struct. Eng. 140, A4014012. https://doi.org/10.1061/(ASCE)ST.1943-541X.0000940

Yu, H., Zeng, X., Li, B., Lian, J., 2015. Centrifuge modeling of offshore wind foundations under earthquake loading. Soil Dyn. Earthq. Eng. 77, 402–415. https://doi.org/10.1016/j.soildyn.2015.06.014

Zaaijer, M.B., 2006. Foundation modelling to assess dynamic behaviour of offshore wind turbines. Appl. Ocean Res. 28, 45–57. https://doi.org/10.1016/j.apor.2006.03.004

Zhang, H., Chen, S., Liang, F., 2017. Effects of scour-hole dimensions and soil stress history on the behavior of laterally loaded piles in soft clay under scour conditions. Comput. Geotech. 84, 198–209. https://doi.org/10.1016/j.compgeo.2016.12.008

Zhang, Q., Zhou, X.L., Wang, J.H., 2017. Numerical investigation of local scour around three adjacent piles with different arrangements under current. Ocean Eng. 142, 625–638. https://doi.org/10.1016/j.oceaneng.2017.07.045

Zhang, X., Yao, W., Liu, Y., Chen, B., 2015. Research on identification method of scour depth for bridge based on ERA and SVM. Shock Vib. 2015, 1–8.

https://doi.org/10.1155/2015/346820

Zheng, X.Y., Li, H., Rong, W., Li, W., 2015. Joint earthquake and wave action on the monopile wind turbine foundation: an experimental study. Mar. Struct. 44, 125–141. https://doi.org/10.1016/j.marstruc.2015.08.003

Zhou, Y.G., Chen, J., Chen, Y.M., Kutter, B.L., Zheng, B.L., Wilson, D.W., Stringer, M.E., Clukey, E.C., 2017. Centrifuge modeling and numerical analysis on seismic site response of deep offshore clay deposits. Eng. Geol., New Advances in Coastal Engineering Geology and Geotechnics 227, 54–68. https://doi.org/10.1016/j.enggeo.2017.01.008

Zhu, B., Wu, X., Wang, Y., Chen, Y., 2020. Centrifuge modeling for seismic response of fixed-end model piles considering local scour. J. Waterw. Port Coast. Ocean Eng. 146, 04020041. https://doi.org/10.1061/(ASCE)WW.1943-5460.0000604

Appendices

Firstly, Appendix A presents the supplementary figures discussed in Chapter 3. Subsequently, Appendices B and C present the supplementary tables and supplementary figures, respectively, for Chapter 4. Lastly, Appendix D presents the supplementary tables discussed in Chapter 5.

The developed computer scripts discussed in Chapters 2 to 5 are available from Mendeley Data: Jiang, W., 2021, Developed Computer Scripts for "Static and Seismic Responses of Pile-Supported Marine Structures under Scoured Conditions". Mendeley Data, V1, doi: 10.17632/5btcx9fdjv.1. Alternatively, these computer codes may also be acquired by contacting the authors via the UVic emails: wenyujiang@uvic.ca; chenglin918@uvic.ca.

Appendix A: Supplementary Figures of Chapter 3

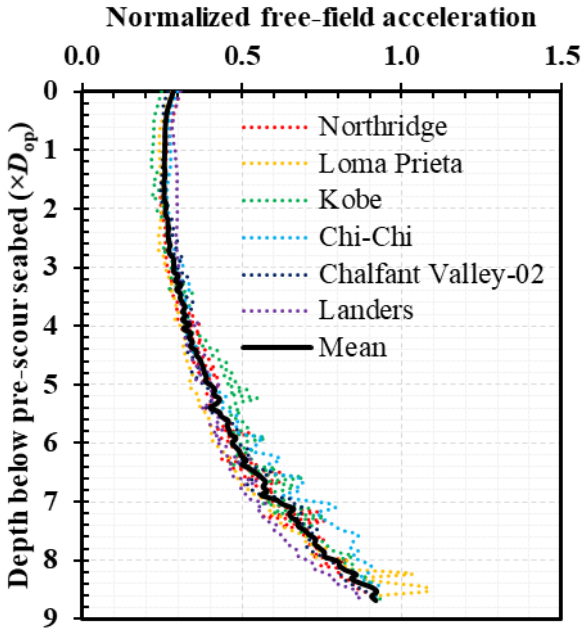

Figure S3.1 Profiles of pre-scour normalized free-field accelerations

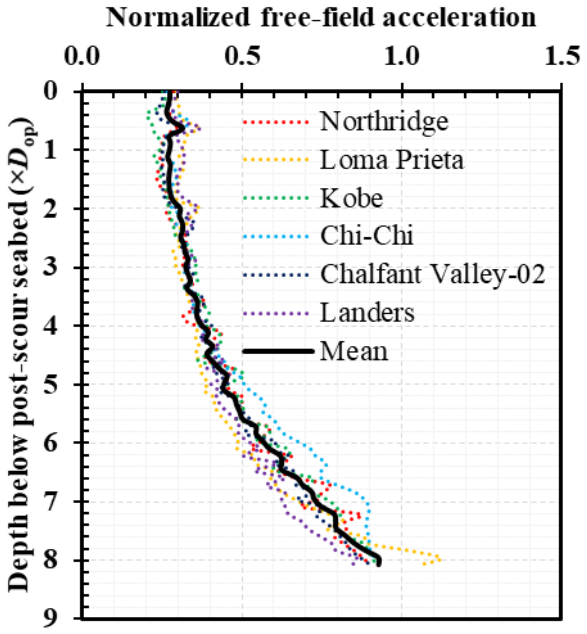

Figure S3.2 Profiles of post-scour normalized free-field accelerations (S_{dl}=0.5D_{op}, S_{wb}=0, S_{θ}=30°, and S_{dg}=0.1S_{dl})

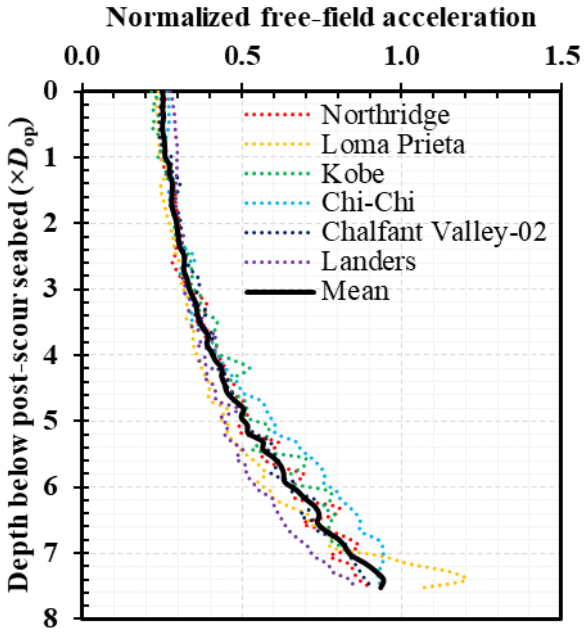

Figure S3.3 Profiles of post-scour normalized free-field accelerations (S_{dl}=1.0D_{op}, S_{wb}=0, S_{θ}=30°, and S_{dg}=0.1S_{dl})

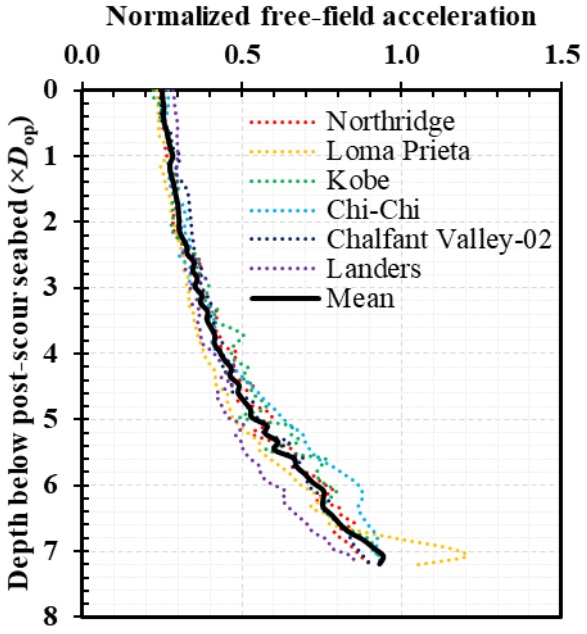

Figure S3.4 Profiles of post-scour normalized free-field accelerations (S_{dl}=1.3D_{op}, S_{wb}=0, S_{θ}=30°, and S_{dg}=0.1S_{dl})

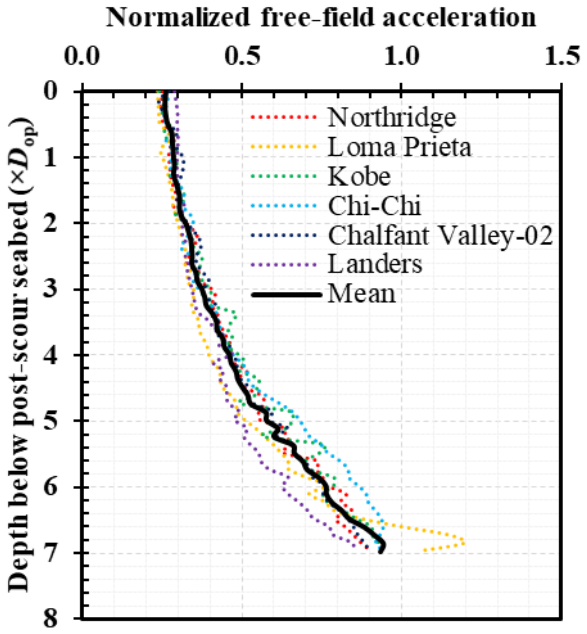

Figure S3.5 Profiles of post-scour normalized free-field accelerations (S_{dl}=1.5D_{op}, S_{wb}=0, S_{θ}=30°, and S_{dg}=0.1S_{dl})

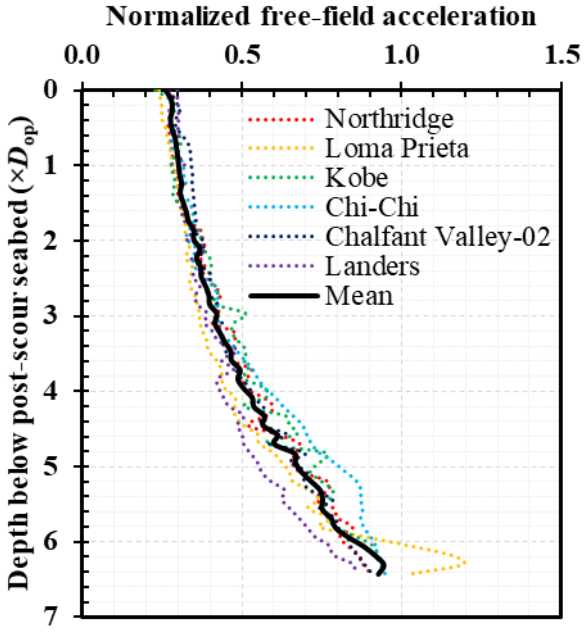

Figure S3.6 Profiles of post-scour normalized free-field accelerations (S_{dl}=2.0D_{op}, S_{wb}=0, S_{θ}=30°, and S_{dg}=0.1S_{dl})

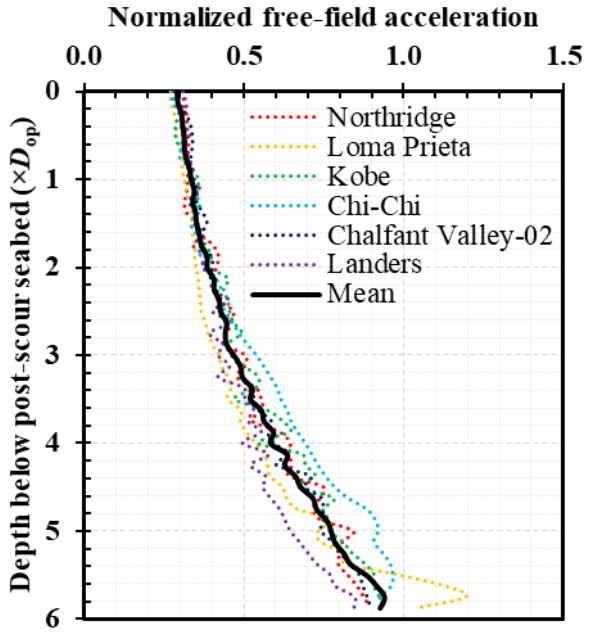

Figure S3.7 Profiles of post-scour normalized free-field accelerations (S_{dl}=2.5D_{op}, S_{wb}=0, S_{θ}=30°, and S_{dg}=0.1S_{dl})

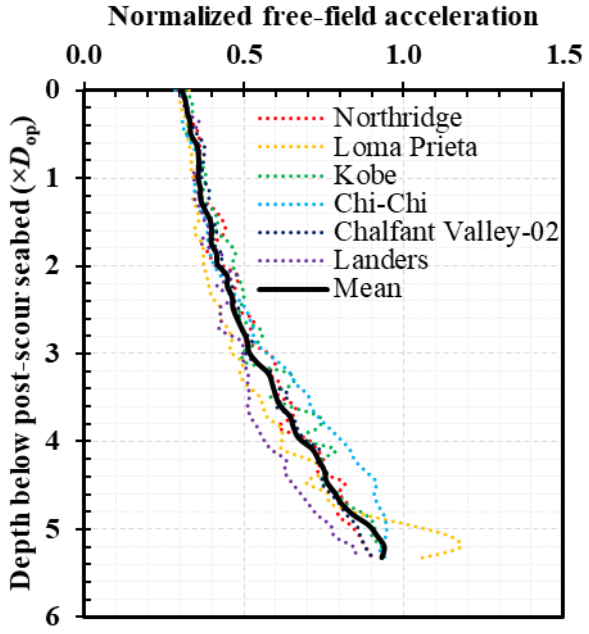

Figure S3.8 Profiles of post-scour normalized free-field accelerations (S_{dl}=3.0D_{op}, S_{wb}=0, S_{θ}=30°, and S_{dg}=0.1S_{dl})

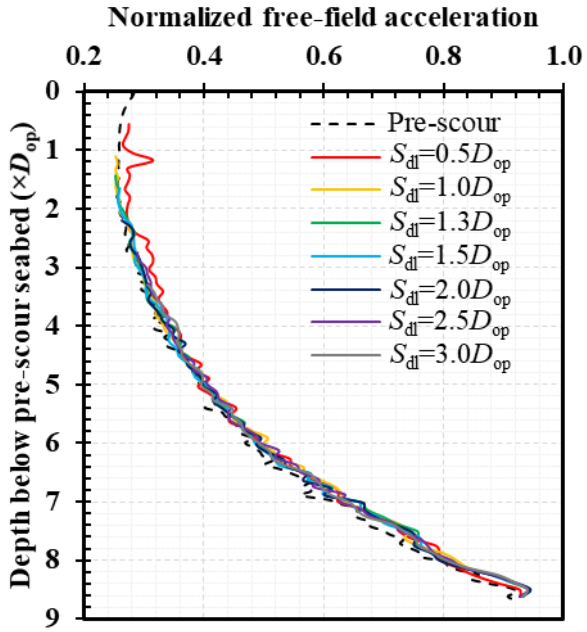

Figure S3.9 Comparison of mean profiles of normalized free-field accelerations before and after scour

Appendix B: Supplementary Tables of Chapter 4

Table S4.1 Measured dimensions of scour holes around pile groups in sands from literature (entire table)

Type	Reference	Flow condition	α_f (°)	Pile group ($m \times n$)	s ($\times D$)	D_e ($\times D$)	S_{gd} ($\times D$)	S_{gd} ($\times D_e$)
Field survey	Sun et al. (2007)	Wave and current	N/A	2×2	N/A	N/A	1.67-1.92	N/A
	Bayram and Larson (2000)	Oscillatory wave	<10	2×2 (rhombus shape)	4.45	1.33	1.00-3.50	0.75-2.63
Flume test	L. Ma et al. (2018)	Live-bed steady current	0	49 piles (dumbbell shape)	2.37	N/A	3.57	N/A
		Live-bed tidal current					2.39-2.90	
	Liang et al. (2017)	Clear-water steady current	0	1×2	1	2.00	1.33	0.67
					2	1.55	1.23	0.80
					4	1.25	1.13	0.91
					8	1.05	1.10	1.05
				2×1	1	1.00	1.06	1.23
					2	1.06	0.92	1.10
					4	1.11	0.85	1.02
					8	1.04	0.84	1.06
				3×3	1	3.00	1.67	0.56
					2	1.81	1.17	0.64
	Wang et al. (2016a)	Clear-water steady current	0	2×1	2	1.06	1.10-1.25	1.04-1.18
					3	1.13	0.95-1.15	0.84-1.02
					4	1.11	0.72-1.08	0.65-0.98
					6	1.07	1.13-1.18	1.06-1.10
					8	1.04	1.00-1.28	0.97-1.24
					10	1.00	1.00-1.22	1.00-1.22
	Wang et al. (2016b)	Clear-water steady current	0	3×1	2	1.13	1.27	1.13
					3	1.25	1.37	1.09
					4	1.21	1.57	1.29
					5	1.18	1.47	1.24
					6	1.14	1.47	1.28
					8	1.07	1.43	1.34
					10	1.00	1.43	1.43
	Amini et al. (2014)	Clear-water steady current	0	2×2	2	1.64	2.13	1.30
				(3, 4, 3)×3	In-line: 3.05 normal[4]: 2.95	2.23	3.18	1.43
				4×2	2	1.84	2.57	1.40
				4×2	2.48	1.84	2.29	1.25
				5×2	in-line: 3.83, normal[4]: 0.17	1.82	2.50	1.38
	Lança et al. (2013)	Clear-water steady current	0	4×1	1	1.00	3.06	3.06
					2	1.19	3.20	2.69
					3	1.38	3.04	2.21
					4.5	1.29	2.98	2.30
					6	1.21	2.72	2.24
			15		1	1.80	3.14	1.74
					2	1.87	3.04	1.62
					3	1.86	3.24	1.75
					4.5	1.62	3.66	2.26
					6	1.37	3.40	2.49
			30		1	2.60	4.92	1.89
					2	2.64	4.84	1.83
					3	2.07	4.24	2.05
					4.5	1.62	3.96	2.44
					6	2.37	3.54	2.59

(To be continued on the next page)

Table S1. (*Continued.*)

Type	Reference	Flow condition	α_f (°)	Pile group ($m\times n$)	s ($\times D$)	D_e ($\times D$)	S_{gd} ($\times D$)	S_{gd} ($\times D_e$)
Flume test	Lança et al. (2013)	Clear-water steady current	45	4×1	1	3.20	6.32	1.98
					2	2.64	3.50	1.33
					3	2.07	3.12	1.51
					4.5	1.62	3.16	1.95
					6	1.37	2.88	2.11
			90		1	4.00	7.08	1.77
					2	2.64	3.80	1.44
					3	2.07	3.50	1.69
					4.5	1.62	3.18	1.96
					6	1.37	2.51	1.86
			0	4×2	1	2.00	5.22	2.61
					2	1.84	3.70	2.01
					3	1.87	3.66	1.96
					4.5	1.56	2.92	1.87
					6	1.36	3.12	2.29
			15		1	2.80	5.98	2.14
					2	2.64	4.80	1.82
					3	2.50	3.66	1.47
					4.5	2.04	4.10	2.01
					6	1.61	4.08	2.54
			30		1	3.80	6.32	1.66
					2	3.19	6.62	2.08
					3	2.43	5.56	2.29
					4.5	1.83	4.34	2.37
					6	1.49	4.00	2.69
			45		1	3.80	6.70	1.76
					2	3.19	5.14	1.61
					3	2.43	4.88	2.01
					4.5	1.83	3.78	2.07
					6	1.49	3.54	2.38
			90		1	4.00	7.38	1.85
					2	2.64	4.24	1.61
					3	2.07	3.78	1.83
					4.5	1.62	3.56	2.19
					6	1.37	2.82	2.07
			0	4×3	1	3.00	6.54	2.18
					2	2.49	4.22	1.70
					3	2.36	4.16	1.77
					4.5	1.83	4.36	2.38
					6	1.51	2.78	1.84
			15		1	3.80	5.68	1.49
					2	3.51	4.80	1.37
					3	3.07	4.22	1.38
					4.5	2.45	3.56	1.45
					6	1.85	3.16	1.71
			30		1	4.20	6.94	1.65
					2	4.50	7.56	1.68
					3	3.49	5.60	1.60
					4.5	2.45	4.74	1.93
					6	1.85	4.56	2.46
			45		1	4.60	7.18	1.56
					2	3.73	6.58	1.76
					3	2.78	5.58	2.01
					4.5	2.04	3.64	1.79
					6	1.61	3.20	1.99
			90		1	4.00	6.56	1.64
					2	2.64	5.10	1.93
					3	2.07	3.74	1.81
					4.5	1.62	3.02	1.86
					6	1.37	2.90	2.12
	Sumer et al. (2005)	Live-bed steady current	0	4×4	2	3.13	0.66	0.21
					2.5	2.96	0.63	0.21
					3	2.85	0.68	0.24
	Zhao and Sheppard (1998)	Steady current	0	8×3	3	2.57	2.14	0.83

Note: [1]effective diameters of pile group with matrix configuration ($m\times n$) were computed according to Sheppard (2003) for both steady current flow and wave flow (Butch, 1996), while the effective diameter of circular configuration was evaluated

according to Butch (1996). [2]top width and [3]side slope angle were estimated by assuming a cone-shape scour hole. According to Sun et al. (2007), S_{wt}=7.5D-10.87D and S_{θ}=12°-15°; according to Bayram and Larson (2000), S_{wt}=3.75D-11.25D and S_{θ}=5°-15°; [4]pile spacing in-line with the flow and normal to flow are different, and effective diameter was computed using the pile spacing in-line with the flow (Sheppard, 2003). Besides the literature provided in the manuscript, two other studies are referenced here, including: Wang, H., Tang, H., Liu, Q., Wang, Y., 2016a. Local scouring around twin bridge piers in open-channel flows. J. Hydraul. Eng. 142, 06016008. https://doi.org/10.1061/(ASCE)HY.1943-7900.0001154; Wang, H., Tang, H., Xiao, J., Wang, Y., Jiang, S., 2016b. Clear-water local scouring around three piers in a tandem arrangement. Sci. China Technol. Sci. 59, 888–896. https://doi.org/10.1007/s11431-015-5905-1

Table S4.2 Scour-hole characteristics of four different scenarios

Case No.	Method	Investigated factor	Global scour-hole dimensions[1]			Localized pit dimensions	
			$S_{gd,g}$ ($\times D$)[2]	S_θ (°)[3]		$S_{gd,l}$ ($\times D$)[4]	$S_{\theta l}$ (°)[5]
				upstream	downstream		
1	FEM	Unequal slope angles	3.00	26.6	13.3	N/A	N/A
2		Uneven scour bottom	1.65	26.6	26.6	1.35 (leading row), 0.9 (middle row), 0.45 (back row)	42
3		Unequal slope angle and uneven scour bottom	1.65	26.6	13.3	1.35 (leading row), 0.9 (middle row), 0.45 (back row)	42
4		Symmetrical and uniform scour hole	3.00	26.6	26.6	N/A	N/A

Note: [1]scour-hole bottom widths were assumed to be zero at individual piles as no experimental data is available; [2]$S_{gd,g}$ and [3]S_θ are depth and side slope angle of global scour at pile group, respectively, S_θ was taken as 26.6° upstream (Arneson et al., 2012) but 13.3° downstream (Harris and Whitehouse, 2014) in Case 1; [4]$S_{gd,l}$ and [5]$S_{\theta l}$ are depth and side slope angle of localized pits at individual piles, and $S_{\theta l}$ was set to be less than the internal friction angle of sand (43°) but large enough to avoid forming crests between localized pits for numerical stability; the ratio of $S_{gd,g}$ to the maximum value of $S_{gd,l}$ was taken as 1.22 in Cases 2 and 3, falling within a typical range of 0.44-1.41 (Sumer et al., 2005).

Table S4.3 Influence depths of 2×2 pile groups under different pile spacings and scour-hole depths

s (×D)	D_e (×D)	S_{gd} (×D_e)	z_i (×S_{gd})[1]
2	1.6	0.7	2.4
		1.4	1.9
		2.1	1.7
		2.8	1.4
3	1.5	0.7	4.2
		1.4	3.0
		2.1	2.5
		2.8	2.2
4	1.4	0.7	7.1
		1.4	4.6
		2.1	3.6
		2.8	2.9

Note: [1]indicates influence depth of corner pile in a 2×2 (square configuration) pile group.

Table S4.4 Influence depths of 3×3 pile groups under different pile spacings and scour-hole depths

s (×D)	D_e (×D)	S_{gd} (×D_e)	z_i (×S_{gd})[1]			
			(1,1)	(1,2)	(2,2)	mean
2	2.4	0.7	2.2	2.4	2.8	2.5
		1.4	1.7	1.8	2.0	1.8
		2.1	1.5	1.6	1.7	1.6
		2.8	1.4	1.4	1.5	1.4
3	2.1	0.7	3.0	4.6	3.6	3.7
		1.4	2.5	3.3	2.8	2.9
		2.1	2.2	2.6	2.4	2.4
		2.8	2.0	2.3	2.1	2.1
4	1.8	0.7	6.7	8.6	11.5	8.9
		1.4	4.3	5.1	6.2	5.2
		2.1	3.3	3.8	4.3	3.8
		2.8	2.8	3.1	3.5	3.1

Note: [1]influence depths of a 3×3 (square configuration) pile group are provided for representative piles as symmetry, as illustrated in the plan view of the pile group.

(1,1)	(1,2)	(1,3)
(2,1)	(2,2)	(2,3)
(3,1)	(3,2)	(3,3)

Table S4.5 Influence depths of 4×4 pile groups under different pile spacings and scour-hole depths

s (×D)	D_e (×D)	S_{gd} (×D_e)	z_i (×S_{gd})[1]			
			(1,1)	(1,3)	(2,2)	mean
2	3.1	0.7	1.8	2.0	2.4	2.1
		1.4	1.5	1.6	1.8	1.7
		2.1	1.4	1.4	1.6	1.5
		2.8	1.3	1.4	1.5	1.4
3	2.9	0.7	3.1	3.8	4.8	3.9
		1.4	2.6	2.9	3.4	3.0
		2.1	2.1	2.3	2.6	2.3
		2.8	2.0	2.1	2.3	2.2
4	2.3	0.7	6.1	8.0	11.1	8.4
		1.4	3.8	4.6	5.8	4.7
		2.1	3.0	3.4	4.0	3.5
		2.8	2.6	2.9	3.3	2.9

Note: [1]influence depths of a 4×4 (square configuration) pile group are provided for representative piles as symmetry, as illustrated in the plan view of the pile group.

(1,1)	(1,2)	(1,3)	(1,4)
(2,1)	(2,2)	(2,3)	(2,4)
(3,1)	(3,2)	(3,3)	(3,4)
(4,1)	(4,2)	(4,3)	(4,4)

Table S4.6 Influence depths of 6×5 pile groups under different pile spacings and scour-hole depths

s	D_e	S_{gd}	z_i ($\times S_{gd}$)[1]									
($\times D$)	($\times D$)	($\times D_e$)	(1,1)	(1,2)	(1,3)	(2,1)	(2,2)	(2,3)	(3,1)	(3,2)	(3,3)	mean
2	4.0	0.7	1.8	2.1	2.1	2.1	2.4	2.5	2.1	2.5	2.6	2.2
		1.4	1.4	1.5	1.6	1.5	1.7	1.7	1.5	1.7	1.8	1.6
		2.1	1.3	1.4	1.4	1.4	1.5	1.5	1.4	1.5	1.6	1.4
		2.8	1.4	1.4	1.5	1.4	1.5	1.5	1.4	1.5	1.6	1.5
3	3.6	0.7	2.6	3.1	3.3	3.1	4.0	4.2	3.2	4.2	4.5	3.6
		1.4	2.0	2.3	2.4	2.3	2.7	2.8	2.4	2.8	2.9	2.5
		2.1	1.9	2.1	2.2	2.1	2.3	2.4	2.1	2.4	2.5	2.2
		2.8	1.9	2.0	2.1	2.0	2.2	2.3	2.1	2.3	2.3	2.1
4	2.8	0.7	4.9	6.4	6.9	6.4	9.0	9.8	6.7	9.6	10.5	7.8
		1.4	3.0	3.7	3.9	3.7	4.6	4.9	3.8	4.8	5.2	4.2
		2.1	2.6	3.0	3.1	3.0	3.5	3.7	3.1	3.7	3.9	3.3
		2.8	2.6	3.0	3.1	3.0	3.4	3.5	3.0	3.5	3.6	3.2

Note: [1]influence depths of a 6×5 (square configuration) pile group are provided for representative piles as symmetry, as illustrated in the plan view of the pile group.

(1,1)	(1,2)	(1,3)	(1,4)	(1,5)	(1,6)
(2,1)	(2,2)	(2,3)	(2,4)	(2,5)	(2,6)
(3,1)	(3,2)	(3,3)	(3,4)	(3,5)	(3,6)
(4,1)	(4,2)	(4,3)	(4,4)	(4,5)	(4,6)
(5,1)	(5,2)	(5,3)	(5,4)	(5,5)	(5,6)

Table S4.7 Influence depths of 10×3 pile groups under different pile spacings and scour-hole depths

s	D_e	S_{gd}	z_i ($\times S_{gd}$)[1]										
($\times D$)	($\times D$)	($\times D_e$)	(1,1)	(1,2)	(1,3)	(1,4)	(1,5)	(2,1)	(2,2)	(2,3)	(2,4)	(2,5)	mean
2	2.6	0.7	2.1	2.4	2.5	2.5	2.5	2.3	2.7	2.8	2.9	2.9	2.6
		1.4	1.7	1.9	2.0	2.0	2.0	1.8	2.1	2.1	2.2	2.2	2.0
		2.1	1.5	1.6	1.7	1.7	1.7	1.6	1.7	1.8	1.8	1.8	1.7
		2.8	1.4	1.5	1.6	1.6	1.6	1.5	1.6	1.6	1.7	1.7	1.6
3	2.6	0.7	3.6	4.4	4.7	4.7	4.8	4.3	5.4	5.8	5.9	5.9	4.9
		1.4	2.6	3.1	3.2	3.3	3.3	2.9	3.5	3.7	3.7	3.8	3.3
		2.1	2.2	2.5	2.6	2.6	2.7	2.4	2.7	2.9	2.9	2.9	2.6
		2.8	2.0	2.2	2.3	2.4	2.4	2.2	2.4	2.5	2.6	2.6	2.4
4	2.1	0.7	6.3	8.5	9.2	9.4	9.5	8.0	11.4	12.4	12.7	12.9	10.0
		1.4	3.8	4.7	5.0	5.2	5.2	4.4	5.7	6.1	6.3	6.4	5.3
		2.1	3.1	3.6	3.8	3.9	4.0	3.4	4.2	4.4	4.5	4.6	4.0
		2.8	2.6	3.0	3.2	3.2	3.3	2.9	3.4	3.5	3.6	3.7	3.2

Note: [1]influence depths of a 10×3 pile group are provided for representative piles as symmetry, as illustrated in the plan view of the pile group.

(1,1)	(1,2)	(1,3)	(1,4)	(1,5)	(1,6)	(1,7)	(1,8)	(1,9)	(1,10)
(2,1)	(2,2)	(2,3)	(2,4)	(2,5)	(2,6)	(2,7)	(2,8)	(2,9)	(2,10)
(3,1)	(3,2)	(3,3)	(3,4)	(3,5)	(3,6)	(3,7)	(3,8)	(3,9)	(3,10)

Table S4.8 Influence depths of 15×2 pile groups under different pile spacings and scour-hole depths

s	D_e	S_{gd}	z_i ($\times S_{gd}$)[1]								
($\times D$)	($\times D$)	($\times D_e$)	(1,1)	(1,2)	(1,3)	(1,4)	(1,5)	(1,6)	(1,7)	(1,8)	mean
2	1.9	0.7	1.4	2.1	2.4	2.4	2.5	2.5	2.5	2.5	2.5
		1.4	2.7	1.9	2.1	2.1	2.2	2.2	2.2	2.2	2.2
		2.1	4.1	1.5	1.7	1.7	1.7	1.8	1.8	1.8	1.8
		2.8	5.4	1.4	1.6	1.6	1.6	1.6	1.6	1.6	1.6
3	2.0	0.7	1.4	2.7	3.4	3.5	3.6	3.6	3.6	3.6	3.6
		1.4	2.8	2.3	2.7	2.8	2.8	2.9	2.9	2.9	2.9
		2.1	4.3	2.0	2.3	2.4	2.4	2.4	2.4	2.4	2.4
		2.8	5.7	1.8	2.0	2.0	2.1	2.1	2.1	2.1	2.1
4	1.8	0.7	1.2	6.7	9.0	9.5	9.7	9.7	9.8	9.8	9.8
		1.4	2.5	4.2	5.2	5.4	5.5	5.6	5.6	5.6	5.6
		2.1	3.7	3.2	3.8	4.0	4.1	4.1	4.2	4.2	4.2
		2.8	5.0	2.7	3.1	3.3	3.3	3.4	3.4	3.4	3.4

Note: [1]influence depths of a 15×2 pile group are provided for representative piles as symmetry, as illustrated in the plan view of the pile group.

(1,1)	(1,2)	(1,3)	(1,4)	(1,5)	(1,6)	(1,7)	(1,8)	(1,9)	(1,10)	(1,11)	(1,12)	(1,13)	(1,14)	(1,15)
(2,1)	(2,2)	(2,3)	(2,4)	(2,5)	(2,6)	(2,7)	(2,8)	(2,9)	(2,10)	(2,11)	(2,12)	(2,13)	(2,14)	(2,15)

Appendix C: Supplementary Figures of Chapter 4

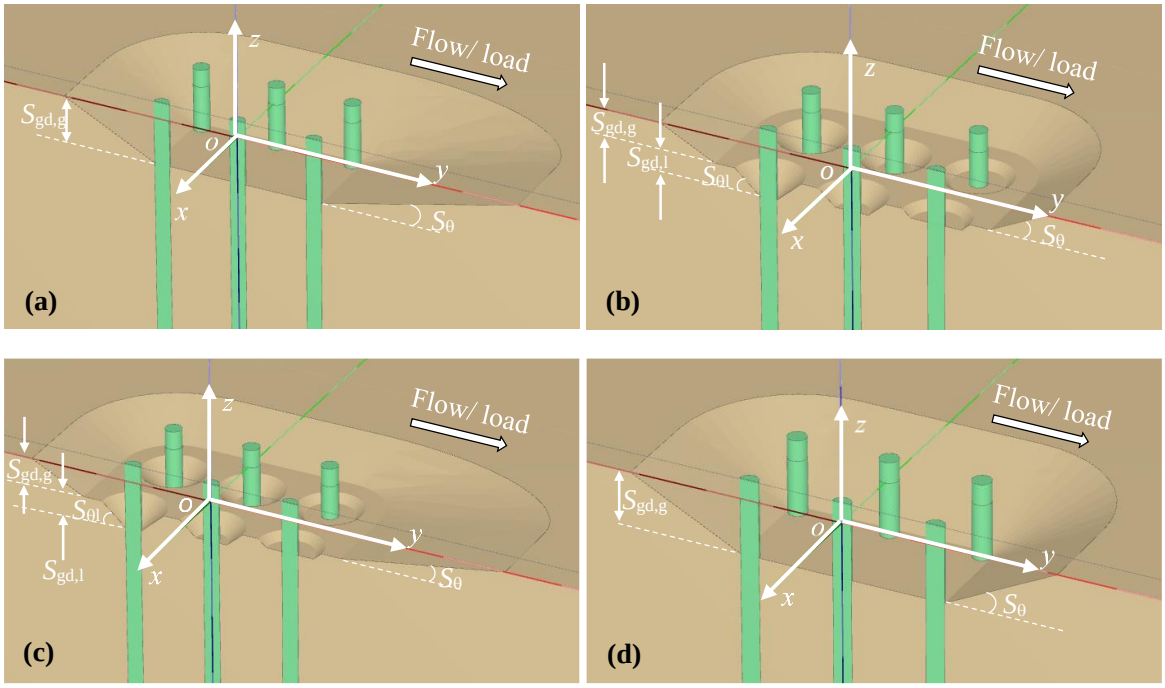

Figure S4.1 3D FE model of four scour-hole scenarios at a 3×3 pile group (half model): (a) Case 1, (b) Case 2. (c) Case 3, and (d) Case 4

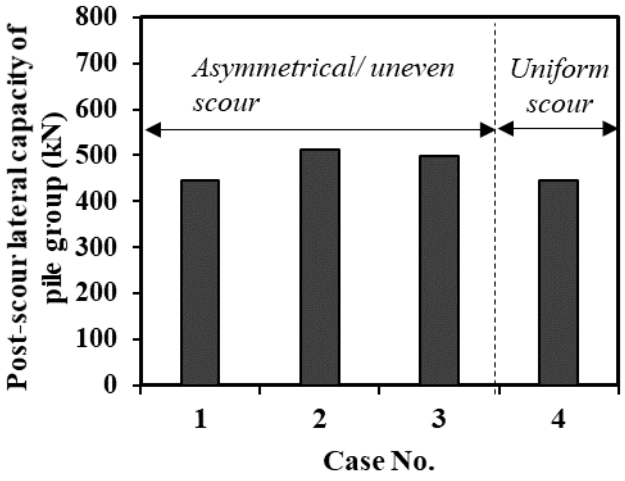

Figure S4.2 Lateral capacities of a 3×3pile group (*s*=5*D*) under four scour-hole scenarios

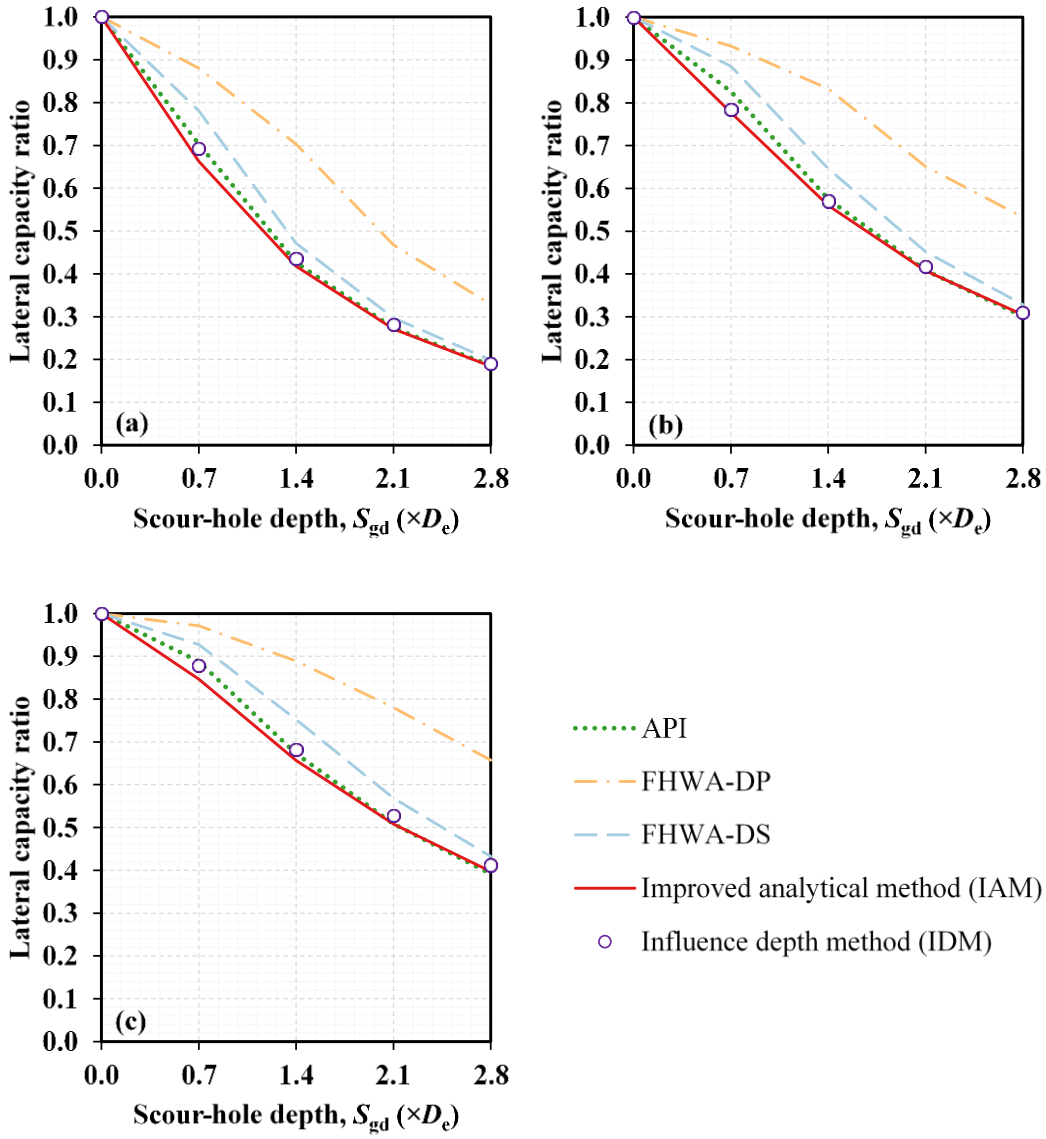

Figure S4.3 Lateral capacity ratios of (a) 6×5, (b) 10×3, and (c) 15×2 pile groups (s=3D) under different scour-hole depths (S_{wb}=0, S_θ=0° and 26.6°)

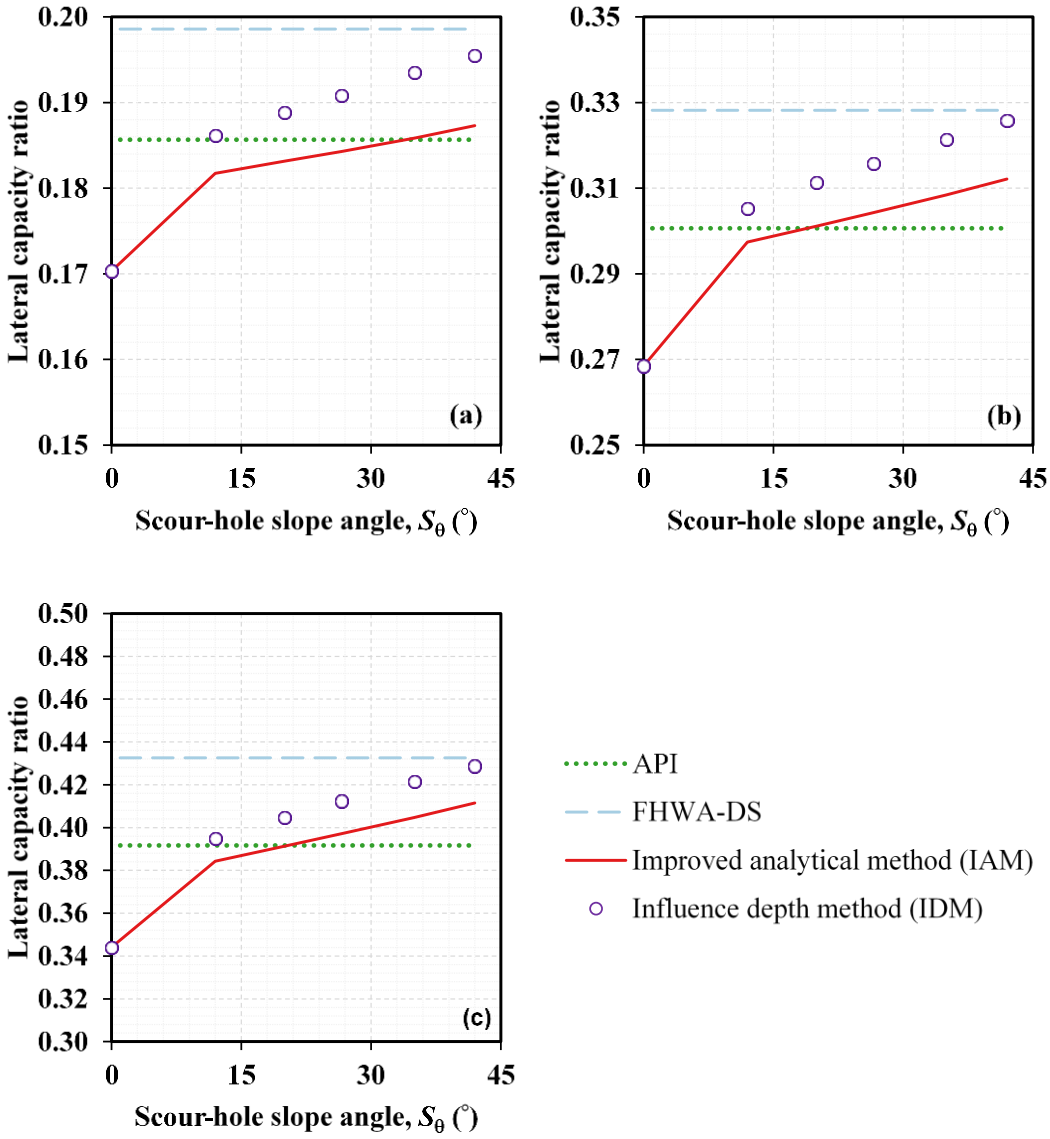

Figure S4.4 Lateral capacity ratios of (a) 6×5, (b) 10×3, and (c) 15×2 pile groups (s=3D) under different scour-hole slope angles (S_{gd}=2.8D_e, S_{wb}=0)

Appendix D: Supplementary Tables of Chapter 5

Table S5.1 Influence depths of 2×2 pile groups under different pile spacings and scour-hole depths

s (×D)	D_e (×D)	S_{gd} (×D_e)	z_i (×S_{gd})[1]
3	1.5	0.7	3.7
		1.4	2.2
		2.1	1.6
		2.8	1.3
4	1.4	0.7	3.3
		1.4	2.3
		2.1	1.8
		2.8	1.3
5	1.3	0.7	3.9
		1.4	2.5
		2.1	1.8
		2.8	1.4

Note: [1]indicates influence depth of corner pile in a 2×2 (square configuration) pile group.

Table S5.2 Influence depths of 3×3 pile groups under different pile spacings and scour-hole depths

s (×D)	D_e (×D)	S_{gd} (×D_e)	z_i (×S_{gd})[1]			
			(1,1)	(1,2)	(2,2)	Mean
3	2.1	0.7	2.9	3.4	4.2	3.5
		1.4	1.7	1.9	2.2	1.9
		2.1	1.2	1.3	1.5	1.4
		2.8	1.0	1.1	1.2	1.1
4	1.8	0.7	2.9	3.7	4.9	3.8
		1.4	1.9	2.3	2.7	2.3
		2.1	1.5	1.7	1.9	1.7
		2.8	1.2	1.3	1.5	1.4
5	1.6	0.7	3.2	4.1	5.9	4.4
		1.4	2.1	2.5	3.3	2.6
		2.1	1.6	1.9	2.3	1.9
		2.8	1.3	1.5	1.8	1.5

Note: [1]influence depths of a 3×3 (square configuration) pile group are provided for representative piles as symmetry, as illustrated in the plan view of the pile group.

(1,1)	(1,2)	(1,3)
(2,1)	(2,2)	(2,3)
(3,1)	(3,2)	(3,3)

Table S5.3 Influence depths of 4×4 pile groups under different pile spacings and scour-hole depths

s (×D)	D_e (×D)	S_{gd} (×D_e)	z_i (×S_{gd})[1]			
			(1,1)	(1,3)	(2,2)	Mean
3	2.8	0.7	2.5	2.9	3.6	3.0
		1.4	1.4	1.6	1.9	1.7
		2.1	1.0	1.1	1.3	1.2
		2.8	1.0	1.1	1.2	1.1
4	2.3	0.7	2.6	3.3	4.1	3.3
		1.4	1.7	2.0	2.5	2.1
		2.1	1.2	1.4	1.6	1.4
		2.8	1.0	1.2	1.3	1.2
5	1.9	0.7	3.2	4.0	5.8	4.3
		1.4	1.9	2.3	2.9	2.4
		2.1	1.4	1.6	2.0	1.6
		2.8	1.1	1.2	1.5	1.3

Note: [1]influence depths of a 4×4 (square configuration) pile group are provided for representative piles as symmetry, as illustrated in the plan view of the pile group.

(1,1)	(1,2)	(1,3)	(1,4)
(2,1)	(2,2)	(2,3)	(2,4)
(3,1)	(3,2)	(3,3)	(3,4)
(4,1)	(4,2)	(4,3)	(4,4)

Table S5.4 Influence depths of 5×3 pile groups under different pile spacings and scour-hole depths

s (×D)	D_e (×D)	S_{gd} (×D_e)	z_i (×S_{gd})[1]					
			(1,1)	(1,2)	(2,1)	(2,2)	(2,3)	Mean
3	2.6	0.7	2.5	3.0	2.9	3.7	3.8	3.2
		1.4	1.5	1.7	1.6	1.9	2.0	1.7
		2.1	1.1	1.3	1.2	1.4	1.4	1.3
		2.8	1.0	1.1	1.1	1.2	1.2	1.1
4	2.1	0.7	2.9	3.6	3.5	4.8	4.9	4.0
		1.4	1.7	2.0	2.0	2.4	2.5	2.1
		2.1	1.2	1.4	1.4	1.6	1.7	1.5
		2.8	1.0	1.2	1.2	1.3	1.4	1.2
5	1.8	0.7	3.0	3.9	3.8	5.5	5.6	4.4
		1.4	2.0	2.4	2.3	3.0	3.1	2.6
		2.1	1.5	1.8	1.7	2.1	2.2	1.9
		2.8	1.1	1.3	1.3	1.5	1.6	1.4

Note: [1]influence depths of a 5×3 pile group are provided for representative piles as symmetry, as illustrated in the plan view of the pile group.

(1,1)	(1,2)	(1,3)	(1,4)	(1,5)
(2,1)	(2,2)	(2,3)	(2,4)	(2,5)
(3,1)	(3,2)	(3,3)	(3,4)	(3,5)

Table S5.5 Influence depths of 6×5 pile groups under different pile spacings and scour-hole depths

s	D_e	S_{gd}	z_i ($\times S_{gd}$)[1]									
($\times D$)	($\times D$)	($\times D_e$)	(1,1)	(1,2)	(1,3)	(2,1)	(2,2)	(2,3)	(3,1)	(3,2)	(3,3)	Mean
3	3.6	0.7	2.0	2.3	2.4	2.3	2.8	3.0	2.4	2.9	3.1	2.6
		1.4	1.1	1.2	1.3	1.2	1.4	1.5	1.3	1.5	1.5	1.3
		2.1	1.0	1.1	1.1	1.1	1.3	1.3	1.1	1.3	1.3	1.2
		2.8	1.0	1.1	1.1	1.1	1.2	1.2	1.1	1.2	1.2	1.1
4	2.8	0.7	2.5	3.0	3.1	3.0	4.0	4.2	3.1	4.1	4.4	3.5
		1.4	1.5	1.7	1.7	1.7	2.1	2.1	1.7	2.1	2.2	1.9
		2.1	1.0	1.2	1.2	1.2	1.4	1.4	1.2	1.4	1.5	1.3
		2.8	1.0	1.1	1.2	1.1	1.3	1.4	1.2	1.3	1.4	1.2
5	2.3	0.7	2.7	3.4	3.4	3.4	4.8	5.0	3.4	5.0	5.2	4.0
		1.4	1.7	2.1	2.1	2.1	2.6	2.7	2.1	2.7	2.8	2.3
		2.1	1.2	1.4	1.4	1.4	1.7	1.8	1.4	1.8	1.8	1.5
		2.8	1.1	1.2	1.2	1.2	1.5	1.5	1.2	1.5	1.5	1.3

Note: [1]influence depths of a 6×5 pile group are provided for representative piles as symmetry, as illustrated in the plan view of the pile group.

(1,1)	(1,2)	(1,3)	(1,4)	(1,5)	(1,6)
(2,1)	(2,2)	(2,3)	(2,4)	(2,5)	(2,6)
(3,1)	(3,2)	(3,3)	(3,4)	(3,5)	(3,6)
(4,1)	(4,2)	(4,3)	(4,4)	(4,5)	(4,6)
(5,1)	(5,2)	(5,3)	(5,4)	(5,5)	(5,6)

Table S5.6 Influence depths of 10×3 pile groups under different pile spacings and scour-hole depths

s	D_e	S_{gd}	z_i ($\times S_{gd}$)[1]										
($\times D$)	($\times D$)	($\times D_e$)	(1,1)	(1,2)	(1,3)	(1,4)	(1,5)	(2,1)	(2,2)	(2,3)	(2,4)	(2,5)	Mean
3	2.6	0.7	2.5	3.0	3.1	3.2	3.2	3.0	3.7	3.9	3.9	4.0	3.4
		1.4	1.5	1.7	1.7	1.8	1.8	1.6	1.9	2.0	2.0	2.0	1.8
		2.1	1.2	1.3	1.3	1.3	1.3	1.3	1.4	1.5	1.5	1.5	1.3
		2.8	1.0	1.1	1.1	1.2	1.2	1.1	1.2	1.3	1.3	1.3	1.2
4	2.1	0.7	2.9	3.6	3.7	3.7	3.7	3.5	4.8	5.0	5.0	5.0	4.1
		1.4	1.7	2.0	2.1	2.1	2.1	2.0	2.5	2.5	2.6	2.6	2.2
		2.1	1.2	1.4	1.5	1.5	1.5	1.4	1.7	1.7	1.7	1.7	1.5
		2.8	1.0	1.2	1.2	1.2	1.2	1.2	1.3	1.4	1.4	1.4	1.2
5	1.8	0.7	3.0	3.9	3.9	4.0	4.0	3.8	5.5	5.7	5.7	5.7	4.5
		1.4	2.0	2.4	2.4	2.4	2.4	2.3	3.0	3.1	3.2	3.2	2.7
		2.1	1.5	1.8	1.8	1.8	1.8	1.7	2.1	2.2	2.2	2.2	1.9
		2.8	1.1	1.3	1.3	1.3	1.3	1.3	1.5	1.6	1.6	1.6	1.4

Note: [1]influence depths of a 10×3 pile group are provided for representative piles as symmetry, as illustrated in the plan view of the pile group.

(1,1)	(1,2)	(1,3)	(1,4)	(1,5)	(1,6)	(1,7)	(1,8)	(1,9)	(1,10)
(2,1)	(2,2)	(2,3)	(2,4)	(2,5)	(2,6)	(2,7)	(2,8)	(2,9)	(2,10)
(3,1)	(3,2)	(3,3)	(3,4)	(3,5)	(3,6)	(3,7)	(3,8)	(3,9)	(3,10)

Table S5.7 Influence depths of 15×2 pile groups under different pile spacings and scour-hole depths

s	D_e	S_{gd}	z_i ($\times S_{gd}$)[1]								
($\times D$)	($\times D$)	($\times D_e$)	(1,1)	(1,2)	(1,3)	(1,4)	(1,5)	(1,6)	(1,7)	(1,8)	mean
3	2.0	0.7	2.7	3.2	3.3	3.4	3.4	3.4	3.4	3.4	3.3
		1.4	1.7	2.0	2.0	2.1	2.1	2.1	2.1	2.1	2.0
		2.1	1.3	1.5	1.5	1.5	1.5	1.5	1.5	1.5	1.5
		2.8	1.1	1.2	1.2	1.2	1.2	1.2	1.2	1.2	1.2
4	1.8	0.7	2.8	3.6	3.7	3.7	3.7	3.7	3.7	3.7	3.6
		1.4	1.9	2.2	2.2	2.3	2.3	2.3	2.3	2.3	2.2
		2.1	1.4	1.6	1.7	1.7	1.7	1.7	1.7	1.7	1.6
		2.8	1.1	1.3	1.3	1.3	1.3	1.3	1.3	1.3	1.3
5	1.6	0.7	3.2	4.1	4.2	4.2	4.2	4.2	4.2	4.2	4.0
		1.4	2.1	2.5	2.6	2.6	2.6	2.6	2.6	2.6	2.5
		2.1	1.6	1.9	1.9	1.9	1.9	1.9	1.9	1.9	1.9
		2.8	1.3	1.5	1.5	1.5	1.5	1.6	1.6	1.6	1.5

Note: [1]influence depths of a 15×2 pile group are provided for representative piles as symmetry, as illustrated in the plan view of the pile group.

(1,1)	(1,2)	(1,3)	(1,4)	(1,5)	(1,6)	(1,7)	(1,8)	(1,9)	(1,10)	(1,11)	(1,12)	(1,13)	(1,14)	(1,15)
(2,1)	(2,2)	(2,3)	(2,4)	(2,5)	(2,6)	(2,7)	(2,8)	(2,9)	(2,10)	(2,11)	(2,12)	(2,13)	(2,14)	(2,15)